

## **Final Report**

# **Distribution of End Bearing and Tip Shear on Drilled Shafts Founded in Florida Limestone**

**BD-545, RPWO # 59**  
**UF Project # 00057247**

### **Submitted by:**

Dr. Michael C. McVay, Principal Investigator, University of Florida  
Dr. David Bloomquist P.E., Co-Principal Investigator, University of Florida  
Jeongsoo Ko, Researcher, University of Florida  
Dr. Haki Klammler, Researcher, University of Florida  
Johanna Otero, Researcher, University of Florida

**Department of Civil and Coastal Engineering**  
**University of Florida**  
**Gainesville, Florida 32611**

### **Developed for the**



Peter Lai, P.E., Project Manager  
May 2008

## **Disclaimer**

The opinions, findings, and conclusions expressed in this publication are those of the author and not necessarily those of the State of Florida Department of Transportation.

## SI (MODERN METRIC) CONVERSION FACTORS (FROM FHWA)

Table 0-1. Approximate Conversions to SI Units

SYMBOL	WHEN YOU KNOW	MULTIPLY BY	TO FIND	SYMBOL
LENGTH				
in	inches	25.4	millimeters	Mm
ft	feet	0.305	meters	M
yd	yards	0.914	meters	M
mi	miles	1.61	kilometers	Km
SYMBOL	WHEN YOU KNOW	MULTIPLY BY	TO FIND	SYMBOL
AREA				
in <sup>2</sup>	Square inches	645.2	square millimeters	mm <sup>2</sup>
ft <sup>2</sup>	Square feet	0.093	square meters	m <sup>2</sup>
yd <sup>2</sup>	square yard	0.836	square meters	m <sup>2</sup>
ac	acres	0.405	hectares	Ha
mi <sup>2</sup>	square miles	2.59	square kilometers	km <sup>2</sup>
SYMBOL	WHEN YOU KNOW	MULTIPLY BY	TO FIND	SYMBOL
VOLUME				
fl oz	fluid ounces	29.57	milliliters	ml
gal	gallons	3.785	liters	L
ft <sup>3</sup>	cubic feet	0.028	cubic meters	m <sup>3</sup>
yd <sup>3</sup>	cubic yards	0.765	cubic meters	m <sup>3</sup>
NOTE: volumes greater than 1000 L shall be shown in m <sup>3</sup>				
SYMBOL	WHEN YOU KNOW	MULTIPLY BY	TO FIND	SYMBOL
MASS				
oz	ounces	28.35	grams	G
lb	pounds	0.454	kilograms	Kg
T	short tons (2000 lb)	0.907	megagrams (or "metric ton")	Mg (or "t")
SYMBOL	WHEN YOU KNOW	MULTIPLY BY	TO FIND	SYMBOL
TEMPERATURE (exact degrees)				
°F	Fahrenheit	5 (F-32)/9 or (F-32)/1.8	Celsius	°C
SYMBOL	WHEN YOU KNOW	MULTIPLY BY	TO FIND	SYMBOL
ILLUMINATION				
fc	foot-candles	10.76	lux	Lx
fl	foot-Lamberts	3.426	candela/m <sup>2</sup>	cd/m <sup>2</sup>
SYMBOL	WHEN YOU KNOW	MULTIPLY BY	TO FIND	SYMBOL
FORCE and PRESSURE or STRESS				
lbf	Pound force	4.45	newtons	N
lbf/in <sup>2</sup>	Pound force per square inch	6.89	kilopascals	kPa

Table 0-2. Approximate Conversions to English Units

SYMBOL	WHEN YOU KNOW	MULTIPLY BY	TO FIND	SYMBOL
LENGTH				
mm	millimeters	0.039	inches	In
m	meters	3.28	feet	Ft
m	meters	1.09	yards	Yd
km	kilometers	0.621	miles	Mi
SYMBOL	WHEN YOU KNOW	MULTIPLY BY	TO FIND	SYMBOL
AREA				
mm <sup>2</sup>	square millimeters	0.0016	square inches	in <sup>2</sup>
m <sup>2</sup>	square meters	10.764	square feet	ft <sup>2</sup>
m <sup>2</sup>	square meters	1.195	square yards	yd <sup>2</sup>
ha	hectares	2.47	acres	Ac
km <sup>2</sup>	square kilometers	0.386	square miles	mi <sup>2</sup>
SYMBOL	WHEN YOU KNOW	MULTIPLY BY	TO FIND	SYMBOL
VOLUME				
mL	milliliters	0.034	fluid ounces	fl oz
L	liters	0.264	gallons	Gal
m <sup>3</sup>	cubic meters	35.314	cubic feet	ft <sup>3</sup>
m <sup>3</sup>	cubic meters	1.307	cubic yards	yd <sup>3</sup>
SYMBOL	WHEN YOU KNOW	MULTIPLY BY	TO FIND	SYMBOL
MASS				
g	grams	0.035	ounces	Oz
kg	kilograms	2.202	pounds	Lb
Mg (or "t")	megagrams (or "metric ton")	1.103	short tons (2000 lb)	T
SYMBOL	WHEN YOU KNOW	MULTIPLY BY	TO FIND	SYMBOL
TEMPERATURE (exact degrees)				
°C	Celsius	1.8C+32	Fahrenheit	°F
SYMBOL	WHEN YOU KNOW	MULTIPLY BY	TO FIND	SYMBOL
ILLUMINATION				
lx	lux	0.0929	foot-candles	Fc
cd/m <sup>2</sup>	candela/m <sup>2</sup>	0.2919	foot-Lamberts	Fl
SYMBOL	WHEN YOU KNOW	MULTIPLY BY	TO FIND	SYMBOL
FORCE and PRESSURE or STRESS				
N	newtons	0.225	Pound force	Lbf
kPa	kilopascals	0.145	Pound force per square inch	lbf/in <sup>2</sup>

\*SI is the symbol for the International System of Units. Appropriate rounding should be made to comply with Section 4 of ASTM E380.(Revised March 2003

Table 0-3. Technical Report Documentation Page

1. Report No.	2. Government Accession No.	3. Recipient's Catalog No.	
4. Title and Subtitle Distribution of End Bearing and Tip Shear on Drilled Shafts Founded in Florida Limestone BD-545, RPWO # 59 UF Project 00057247		5. Report Date May 2008	
		6. Performing Organization Code 4910-4504-725-12	
7. Author(s) Drs. McVay, Bloomquist, Mssrs. J.S. Ko, J. Otero		8. Performing Organization Report No.	
9. Performing Organization Name and Address Department of Civil and Coastal Engineering 365 Weil Hall University of Florida Gainesville, Florida 32611		10. Work Unit No. (TRAIS)	
		11. Contract or Grant No. BD-545, RPWO #59	
12. Sponsoring Agency Name and Address Florida Department of Transportation 605 Suwannee Street, MS 30 Tallahassee, FL 32399 Program Manager: Peter Lai, P.E.		13. Type of Report and Period Covered Final Draft Report 8/2005 – 5/2008	
		14. Sponsoring Agency Code	
15. Supplementary Notes			
16. Abstract <p>This study investigated the behavior of large diameter drilled shafts embedded short distances in Florida Limestone (i.e. <math>L/D = 1</math> &amp; <math>3</math>). The work was performed via laboratory (centrifuge) tests and at two field sites (17<sup>th</sup> Street and Fuller Warren Bridges). The work focused on the modeling the axial, shear and moment response of shafts subject to combined axial and lateral loading in uniform and variable strength/modulus limestone.</p> <p>The study found that O'Neill's method of assessing tip resistance vs. displacement was accurate if the Harmonic or Geometric Mass Modulus of the rock is assessed within three diameters below the shaft's tip. In the case of tip shear, it was found that a bilinear elastic plastic model with failure assessed from Mohr-Coulomb provided good results. For tip rotation, the model proposed by Bell (1991) gave very reasonable results even though it requires assessment of tip shear and lateral tip displacement.</p> <p>An important finding from the field investigation was the variability of the LRFD resistance factors, <math>\phi</math>, from the spatial variability of the rock at the two sites. Using standard Geostatistics measures, Variogram, covariance, etc., the Variance of the Geometric Mass Modulus 3D below a shaft was assessed, along with tip resistance, and its associated variability. LRFD resistance factors based on FOSM were calculated with reliability values of 2.5 &amp; 3.0. An Excel spreadsheet is provided for LRFD assessment and design for other sites.</p>			
17. Key Words Drilled Shafts, End-Bearing, Tip Shear, Tip Rotation, LRFD resistance factors, $\phi$ , Lime-Rock, Tip Moment		18. Distribution Statement No restrictions.	
19. Security Classif. (of this report) Unclassified.	20. Security Classif. (of this page) Unclassified.	21. No. of Pages 178	22. Price N/A

- 17<sup>th</sup> street: This is bascule Replacement Bridge for the old movable bridge on S.E. 17<sup>th</sup> street Causeway over the intercostals waterway in Fort Lauderdale, located on Broward County, FL.
- Fuller Warren Bridge: It is localized over the St. Johns River in downtown Jacksonville on the Interstate Highway 95 (I-95). It replaced the old Gilmore Street Bridge.
- FHWA: Federal Highway Administration
- FOSM: First-Order-Second-Moment
- LRFD: Load and Resistance Factored Design

## EXECUTIVE SUMMARY

Due primarily to economics, large diameter drilled shafts have become more popular for supporting large bridges and tall structures. The benefits of reducing the number of piles, say in a group and associated pile cap dimensions, as well as noise and vibration abatement, makes drilled shaft design and construction very appealing. In addition, Florida's geology, with its limestone varying from the ground surface to depths of 150 feet, provides five to ten times more axial capacity as compared to a similar size driven pile. Transferring lateral loads to deeper, competent material is readily accomplished by simply increasing a shaft's diameter. Consequently, four to nine individual shafts beneath a single bridge pier have evolved down to two and more recently to just a single, large diameter shaft per pier.

The use of eight to twelve foot diameter drilled shafts, embedded ten to twenty feet (for typical shaft geometry's length to diameter ratio of one to three) in Florida Limestone, will lead to vertical and lateral tip translations as well as rotations. In addition, axial tip resistance increases quadratically versus side shear (linearly) as a shaft's diameter increases. Unfortunately, current FDOT and FHWA design methodologies were developed for four and six foot diameter shafts (embedded ten to twenty feet), which exhibit little if any tip translation or rotation. Consequently, early designs counted on minimal end bearing and its use offset by reducing the axial shaft's LRFD phi factors.

This project focused on developing improved axial, shear and moment models for large diameter drilled shafts embedded in Florida limestone. Impacting both the shear-lateral translation and moment-rotation models was the axial tip-vertical displacement model. The axial tip resistance is controlled by the compressibility or Young's Modulus of the limestone. In Florida, limestone is both voided and highly variable or layered. To study the latter, thirty two

combined axial and lateral centrifuge tests were performed on drilled shafts embedded in homogeneous, as well as layered rock formations. To characterize the reduced recoveries (e.g. 30% and 50%), synthetic limestone with micropores made from perlite was created.

Based on the laboratory centrifuge results, the research found that the FHWA's end bearing approach of O'Neill gave acceptable axial tip resistance versus tip displacement, if either the rock's Harmonic or Geometric Mean Modulus is used as its mass modulus, within three diameters below the shaft tip. The research also found that the mass modulus may be directly related to the rock's recovery.

In the case of tip shear under combined axial and lateral loading, the study proposes the use of an elastic plastic model. Specifically, for lateral tip displacements less than failure, an elastic stiffness based on the rock's Young's Modulus or shear strength is proposed. However, for displacements beyond failure, a limiting or constant shear resistance is maintained. Shear failure is based on Mohr-Coulomb strength criterion which is a function of normal tip stress and the cohesion of the rock. It should be noted that typical Florida limestone's shear strength is highly dependent on normal stresses, with angles of internal friction between 25 and 55 degrees.

For large diameter drilled shafts embedded short distances into limestone, the transfer of moment at the tip of shaft was found to be significant and must be modeled to ensure proper shaft reinforcement design. The model developed by Bell (1992) which considers both axial and tip shear resistance was found to yield reasonable results compared to the centrifuge results.

Finally, with axial end bearing varying from 25% to 50% of a shaft's total capacity, the development of appropriate LRFD resistance factors is important. Presently, one set of resistance factors are used for drilled shafts in limestone depending on inclusion or exclusion of end bearing. However, the axial tip resistance is a function of the rock's Harmonic or Geometric

Mean Modulus near the tip, which in turn depends on a site's coefficient of variability and spatial covariance function. Thus, using Geostatistics, a First Order Second Moment LRFD methodology was created. The resulting Excel spreadsheet, using Monte Carlo simulation, allows designers to assign LRFD phi values for specific sites. Assessment of LRFD resistance factors for two separate field sites, the 17<sup>th</sup> Street and Fuller Warren Bridges, showed phi values varying from 0.3 to 0.6.

## TABLE OF CONTENTS

	<u>page</u>
SI (MODERN METRIC) CONVERSION FACTORS (from FHWA).....	iii
EXECUTIVE SUMMARY .....	vii
LIST OF TABLES.....	xii
LIST OF FIGURES .....	xiii
CHAPTERS:	
1. INTRODUCTION .....	1
1.1 Background.....	1
1.1.1 Design.....	1
1.1.2 Background – Centrifuge Testing .....	4
1.1.3 Background – Spatial Variability .....	5
1.2 Scope.....	7
1.2.1 Laboratory .....	7
1.2.1.1. Loading (Axial and Lateral).....	7
1.2.1.2. Shaft Diameter.....	7
1.2.1.3. Length to Diameter (L/D) Ratio.....	8
1.2.1.4. Influence of Rock Voids or Limestone Recoveries.....	8
1.2.2 LRFD Assessment and Field Verification.....	9
2. CENTRIFUGE TESTING SETUP AND MATERIAL .....	10
2.1 Background.....	10
2.2 Hardware & Instrumentation .....	11
2.3 Material.....	14
2.3.1 Synthetic Rock.....	14
2.3.2 Concrete Grout .....	18
2.3.2.1 Mix with Silica Sand.....	19
2.3.2.2 Mix with Granite Sand .....	20
3. CENTRIFUGE Test DATA REDUCTION.....	21
3.1 Axial Loading .....	21
3.1.1 Axial Loading –Side Shear.....	23
3.1.2 Axial Loading – End Bearing.....	25
3.2 Lateral Loading in Combination with Axial Loading .....	29
3.2.1 Lateral Centrifuge Data Reduction.....	29
4. MEASURED VERSUS PREDICTED SHAFT TIP RESPONSE.....	41

4.1 Axial Test Results.....	41
4.2 Lateral Test Result - Tip Shear Model .....	45
4.3 Lateral Test Results - Moment-Rotation Model.....	50
5. INFLUENCE OF THREE DIMENSIONAL SOIL/ROCK SPATIAL VARIABILITY ON A SHAFT’S CAPACITY .....	60
5.1 Soil and Rock Variability Using Geostatistics .....	60
5.1.1 (Semi) variogram.....	61
5.1.2 Semivariogram models.....	63
5.1.3 Covariance and Correlogram.....	68
5.1.4 Kriging.....	69
5.1.5 Stochastic Simulation using Sequential Gaussian Simulation .....	72
5.1.6 WINGSLIB Stochastic Software.....	74
5.2 Numerical Analysis of Shaft Capacity – FLAC3D .....	75
5.3 Simulation of an Axial Loaded Drilled Shaft.....	77
6. LRFD RESISTANCE FACTORS, $\phi$ , FOR END BEARING .....	81
6.1 Spatial Correlation and Its Influence on LRFD resistance factors, $\phi$ .....	81
6.2 Development of LRFD resistance factors, $\phi$ for End Bearing and the 17 <sup>th</sup> Street Bridge Case Study.....	84
6.3 LRFD resistance factors, $\phi$ for End Bearing at the Fuller Warren Bridge .....	97
7. CONCLUSIONS AND RECOMMENDATIONS .....	104
REFERENCES .....	111
APPENDIX A.....	113
Compressive Force (Q) along Depth from Each Pair of Strain Gage with Trend Line.....	113
APPENDIX B .....	123
Output Voltage (Volt on Y-Axis) from Gages vs. Time (Sec on X-Axis) with Loadings..	123
APPENDIX C .....	133
Moment Curve.....	133
APPENDIX D.....	143
Shear Curve .....	143
APPENDIX E .....	154
Example for LRFD resistance factors, $\phi$ to Be Calculated From Field Test.....	154

## LIST OF TABLES

<u>Table</u>	<u>page</u>
Table 1.1 Recommended Tests for End Bearing and Unit Tip Shear.....	9
Table 2.1 Centrifuge Test Matrix.....	10
Table 2.2 Conversions between Prototype and Model for Shafts Tested.....	11
Table 2.3 Proportion of Component for Synthetic Limestone.....	16
Table 2.4 Ratio of $E_m$ (with perlite) / $E_i$ (no perlite).....	18
Table 2.5 Amount of Component for Mixing Concrete with Silica Sand .....	19
Table 2.6 Result of Unconfined Compression Strength Test .....	19
Table 2.7 Amount of Component for Mixing Concrete with Granite Sand .....	20
Table 2.8 Result of Unconfined Compression Strength Test .....	20
Table 3.1 Estimation of $E_m/E_i$ Based on RQD (Load Transfer for Drilled Shafts in Intermediate Geomaterials, 1996).....	26
Table 4.1 Comparison of Axial Tip Stresses .....	47

## LIST OF FIGURES

<u>Figure</u>	<u>page</u>
Figure 1.1 Field Load Transfer in Soil/Rock .....	2
Figure 1.2 Reconstructed P-Y Curves for 80 ksf Rock .....	3
Figure 1.3 Combined Axial and Lateral Load Test (McVay,2004).....	4
Figure 1.4 Instrumented Drilled Shafts to Monitor Axial, Moment and Shear .....	5
Figure 2.1 New Cylindrical Sample Container.....	12
Figure 2.2 Instrumentation for Measuring Lateral & Vertical Forces and Deformation.....	13
Figure 2.3 Slotted Steel Pipe (Axial Reinforcement) & Strain Gages.....	13
Figure 2.4 Mixture of Synthetic Rock (10 tsf) for Axial Load Test in Centrifuge.....	14
Figure 2.5 Grain Size Distribution for Limerock Aggregate .....	15
Figure 2.6 Strength Testing for Concrete and Rock .....	16
Figure 2.7 Synthetic Limestone with 5 mm Perlite Spheres Occupying 30 % Volume.....	17
Figure 2.8 Stress-Strain Response Voided and non-Voided Limestone.....	18
Figure 3.1 Strain Gage Layout for $L/D = 1$ .....	21
Figure 3.3 Mobilized Skin Friction vs. Axial Displacement .....	23
Figure 3.4 Measured Skin Friction Comparing Lila (2003) and McVay (1992).....	24
Figure 3.5 Measured Skin Friction Comparing Lila (2003) and McVay (1992).....	24
Figure 3.6 O'Neil $E_m/E_i$ vs. RQD and UF $E_m/E_i$ vs. Recovery.....	27
Figure 3.7 Two Layer System and Equivalent Modulus (Ueshita and Meyerhof, 1967).....	28
Figure 3.8 Layered Moduli Beneath a Drilled Shaft.....	28
Figure 3.9 Output Voltage from Gages vs. Time.....	30
Figure 3.10 Total Axial and Bending Strains along the Shaft Cross-Section.....	31
Figure 3.11 Moment-Curvature Relationship for 9ft Diameter from a Pair of Strain Gages above Rock Surface. ....	32

Figure 3.12a Moment Distribution along a 9 ft Diameter, 30% Styrofoam at 1D below Tip of Shaft in 10 tsf Limestone.....	33
Figure 3.12b Moment Distribution along a 9 ft Diameter, 30% Styrofoam at 1D below Tip of Shaft in 45 tsf Limestone.....	34
Figure 3.12c Moment Distribution along 9 ft Shaft without Styrofoam below Tip in 35 tsf Rock .....	35
Figure 3.13 Increase in Tip Shear with Increasing Lateral Load, $L/D = 1$ .....	36
Figure 3.14 Increasing Tip Shear with Increasing Rock Strength.....	37
Figure 3.15 Shaft Shear at Failure with and without an Underlying Soft Layer .....	37
Figure 3.16 Assessing Rotation from the Moment-Curvature Relationship.....	39
(a)Moment versus Depth (b)Moment-Curvature Relationship.....	39
Figure 3.17 Typical Lateral Deflection (y) vs. Depth.....	40
Figure 4.1a Tip Resistance (Model vs.O’Neill’s Equation with Harmonic Average Method (left) and Geometric Average Method (right) for 10 tsf Rock with 50% Recovery at 1D.....	42
Figure 4.1b Tip Resistance (Model vs.O’Neill’s Equation with Harmonic Average Method (left) and Geometric Average Method (right) for 30 tsf Rock with 50% Recovery at 1D.....	42
Figure 4.1c Tip Resistance (Model vs. O’Neill’s Equation) with Harmonic Average Method (left) and Geometric Average Method(right) for 9 ft / 9 ft - 10 tsf Rock .....	42
Figure 4.1d Tip Resistance (Model vs.O’Neill’s) Equation with Harmonic Average Method (left) and Geometric Average Method (right) for 9 ft / 9 ft - 30 tsf Rock .....	43
Figure 4.1e Tip Resistance (Model vs. O’Neill’s Equation) with Harmonic Average Method (left) and Geometric Average Method (right) for 6 ft / 6ft - 10 tsf Rock .....	43
Figure 4.1f Tip Resistance (Model vs. O’Neill’s Equation) with Harmonic Average Method (left) and Geometric Average Method (right) for 6 ft / 6ft - 30 tsf Rock .....	43
Figure 4.1g Tip Resistance (Model vs. O’Neill’s Equation) with Harmonic Average Method (left) and Geometric Average Method (right) for 9ft / 27 ft -10 tsf Rock .....	44
Figure 4.1h Tip Tip Resistance (Model vs. O’Neill’s Equation) with Harmonic Average Method (left) and Geometric Average Method (right) for 9ft / 27 ft -30 tsf Rock.....	44
Figure 4.1i Tip Resistance (Model vs. O’Neill’s Equation) with Harmonic Average Method (left) and Geometric Average Method (right) for 6 ft /18 ft -10 tsf Rock .....	44

Figure 4.1j Tip Resistance (Model vs. O’Neill’s Equation) with Harmonic Average Method (left) and Geometric Average Method (right) for 6ft / 18ft - 30 tsf Rock .....	45
Figure 4.2 Tip Shear Stress vs. Tip Lateral Displacement .....	45
Figure 4.3 Tip Shear Stress vs. Tip Lateral Displacement .....	46
Figure 4.4 Shear in Shafts vs. Depth with and without Underlying Softer Layer .....	47
Figure 4.5 Moment in Shafts vs. Depth with and without Underlying Softer Layer.....	47
Figure 4.6 Tip Shear Minus Rock Strength Divided by Normal Tip Stress vs. Normalized Lateral Displacement .....	48
Figure 4.7 Tip Shear minus Rock Strength Divided by Normal Tip Stress vs. Normalized Lateral Displacement .....	48
Figure 4.8 Mohr-Coulomb Strength of Florida limestone .....	49
Figure 4.9 Tip Shear Model (a) Tip Shear Model Scheme (b) Tip Shear Model.....	50
Figure 4.10 Tip Moment Transfer as Function of Tip Rotation .....	51
Figure 4.11 Tip Moment Transfer as Function of Tip Rotation .....	51
Figure 4.12 Embedded Shaft.....	53
Figure 4.13 Calculated vs. Measured Rotation using Bell (1991) - Trend line is in red .....	55
Figure 4.14 Calculated vs. Measured Rotation using Bell (1991) with Trend line in red.....	55
Figure 4.15 Doherty and Deeks (2006) on left, Bell (1991) on Right.....	56
Figure 4.16 Stiffness Coefficient, K, from Doherty and Deeks (2006).....	57
Figure 4.17 Calculated vs. Measured Rotation in 10 tsf Rock using Doherty and Deeks (2006) with Trend Line in Red .....	58
Figure 4.18 Calculated vs. Measured Rotation in 30 tsf Rock using Doherty and Deeks (2006) with Trend Line in red.....	58
Figure 4.19 Recommended Tip Rotations vs. Moment Model from Bell (1991).....	59
(a) Tip Rotation Model Scheme (b) Tip Rotation Model.....	59
Figure 5.1 Typical Geostatistics Semivariogram.....	62
Figure 5.2 Location Map of Core Borings B4 through B9 at 17 <sup>th</sup> Street Bridge: Inside Parentheses are Means and Standard Deviations of Measured $q_s$ per Boring. ....	64

Figure 5.3 17 <sup>th</sup> Street Bridge Depth Profiles of $q_s$ for Borings B4 through B9. ....	65
Figure 5.4 17 <sup>th</sup> Street Bridge Histogram of $q_s$ with Log-Normal Distribution Fit.....	66
Figure 5.5 Normalized (Unity Sill) Experimental Variograms (Connected Dots) of $q_s$ with Different Variogram Model Fits (no dots) $\gamma_A$ & $\gamma_B$ . Solid line is Horizontal Direction and Dashed Lines are Vertical. Lag Interval in (a) and (b) is 2 ft, X-Axis is in ft. ....	66
Figure 5.6 Simulation of Rock Strength (i.e., Cohesion) – Red Highest and Blue Lowest.....	76
Figure 5.7 Young’s Modulus, E, vs. Rock Cohesion.....	78
Figure 5.8 Variability of Shaft Total Capacity with Spatial Correlation Length.....	80
Figure 6.1 Thick Solid Contour Lines Represent $\alpha = \sigma_s^2/\sigma^2$ for $a/D = [0, 20]$ and $L/D =$ $[0,10]$ . Thick Dashed Contour Lines Represent $\alpha = f(L/a)$ for $D = 0$ . Thin Dotted Lines are Parabolas, Along Which $A = \text{const}$ . ....	84
Figure 6.2 LRFD resistance factors, $\phi$ , as a Function of Reliability Index $\beta$ and $\text{COV}_R$ .....	85
Figure 6.3 O’Neil $E_m/E_i$ vs. RQD and UF $E_m/E_i$ vs. Recovery.....	87
Figure 6.4 Secant vs. Tangent Young’s Modulus on 17 <sup>th</sup> Street Bridge Data from LTSO4 .....	88
Figure 6.5 Tangent Mass Modulus of 17 <sup>th</sup> Street Bridge (118 Values).....	89
Figure 6.6 Secant Mass Modulus of 17 <sup>th</sup> Street Bridge (118 values) .....	89
Figure 6.7 Geometric Mean Modulus, $E_g$ , Assuming Correlation Length, $a = 5$ ft from 17 <sup>th</sup> Street Bridge Data.....	91
Figure 6.8 Geometric Mean Modulus, $E_g$ , Assuming Correlation Length, $a = 10$ ft from 17 <sup>th</sup> Street Bridge Data.....	92
Figure 6.9 Geometric Mean Modulus, $E_g$ , Assuming Correlation Length, $a = 15$ ft from 17 <sup>th</sup> Street Bridge Data.....	92
Figure 6.10 Histogram/PDF of Contact Stress, $q_b$ , Using $E_g$ with Correlation Length, $a = 5$ ft from 17 <sup>th</sup> Street Bridge Data.....	94
Figure 6.11 Histogram/PDF of Contact Stress, $q_b$ , Using $E_g$ with Correlation Length, $a = 10$ ft from 17 <sup>th</sup> Street Bridge Data .....	95
Figure 6.12 Histogram/PDF of Contact Stress, $q_b$ , Using $E_g$ with Correlation Length, $a = 15$ ft from 17 <sup>th</sup> Street Bridge Data .....	95
Figure 6.13 Secant Mass Modulus of Fuller Warren Bridge (96 values).....	96
Figure 6.14 Tangent Mass Modulus of Fuller Warren Bridge (96 values).....	96

Figure 6.15 Tangent Mass Modulus for the Fuller Warren Bridge Site (96 values) .....	98
Figure 6.16 Geometric Mean Modulus, $E_g$ , Assuming a Correlation Length, $a = 5$ ft from Fuller Warren Bridge Data.....	98
Figure 6.17 Geometric Mean Modulus, $E_g$ , Assuming a Correlation Length, $a = 10$ ft from Fuller Warren Bridge Data.....	99
Figure 6.18 Geometric Mean Modulus, $E_g$ , Assuming a Correlation Length, $a = 15$ ft from Fuller Warren Bridge Data.....	99
Figure 6.19 Histogram/PDF of Contact Stress, $q_b$ , Using $E_g$ with a Correlation Length, $a = 5$ ft from Fuller Warren Bridge Data .....	101
Figure 6.20 Histogram/PDF of Contact Stress, $q_b$ , Using $E_g$ with a Correlation Length, $a = 10$ ft from Fuller Warren Bridge Data .....	101
Figure 6.21 Histogram/PDF of Contact Stress, $q_b$ , Using $E_g$ with a Correlation Length, $a = 15$ ft from Fuller Warren Bridge Data .....	102
Figure 7.1 Ratio of Mass Modulus, $E_m$ to Intact Young's Modulus, $E_i$ , for Florida Limestone .	105
Figure 7.2 Tip Resistance from Field Data vs. Tip Resistance from O'Neill's Equation with Harmonic Average Method (left) and Geometric Average Method (right) for 10 tsf Rock with 50% Recovery at 1D.....	106
Figure 7.3 Drilled Shaft Tip Shear Model in Florida Limestone.....	106
Figure 7.4 The Tip Rotation Model .....	107
Figure 7.5 Drilled Shaft Tip Model .....	108
Figure 7.6 Estimated Variability of Geometric Mean Modulus at 17 <sup>th</sup> Street Bridge .....	109
Figure 7.7 Histogram/PDF of Contact Stress, $q_b$ , Using $E_g$ with Correlation Length, $a = 10$ ft at 17 <sup>th</sup> Street Bridge .....	110
Figure A.1 Result from 9 ft Diameter 9 ft Embedded Length in 10 tsf Rock with 50 % Styrofoam Layering below 1D below from Tip of Shaft a) Test No. 1 b)Test No. 2.....	113
Figure A.2 Result from 9 ft Diameter 9 ft Embedded Length in 30 tsf Rock with 50 % Styrofoam Layering below 1D below from Tip of Shaft a) Test No. 1 b)Test No. 2.....	114
Figure A.3 Result from 9 ft Diameter 9 ft Embedded Length in 10 tsf Rock a) Test No. 1 b) Test No. 2.....	115
Figure A.4 Result from 9 ft Diameter 9 ft Embedded Length in 30 tsf Rock a) Test No. 1 b) Test No. 2.....	116

Figure A.5 Result from 6 ft Diameter 6 ft Embedded Length in 10 tsf Rock a) Test No. 1 b) Test No. 2.....	117
Figure A.6 Result from 6 ft Diameter 6 ft Embedded Length in 30 tsf Rock a) Test No. 1 b) Test No. 2.....	118
Figure A.7 Result from 9 ft Diameter 27 ft Embedded Length in 10 tsf Rock a) Test No. 1 b) Test No. 2.....	119
Figure A.8 Result from 9 ft Diameter 27 ft Embedded Length in 30 tsf Rock a) Test No. 1 b) Test No. 2.....	120
Figure A.9 Result from 6 ft Diameter 18 ft Embedded Length in 10 tsf Rock a) Test No. 1 b) Test No. 2.....	121
Figure A.10 Result from 6 ft Diameter 18 ft Embedded Length in 30 tsf Rock a) Test No. 1 b) Test No. 2 .....	122
Figure B.1 Output Voltage from 9 ft Diameter 9 ft Embedded Length in 10 tsf Rock with 50 % Styrofoam Layering below 1D below from Tip of Shaft a) Test No. 1 b)Test No. 2.....	123
Figure B.2 Output Voltage from 9 ft Diameter 9 ft Embedded Length in 30 tsf Rock with 50 % Styrofoam Layering below 1D below from Tip of Shaft a) Test No. 1 b)Test No. 2.....	124
Figure B.3 Output Voltage from 9 ft Diameter 9 ft Embedded Length in 10 tsf Rock a) Test No. 1 b) Test No. 2.....	125
Figure B.4 Output Voltage from 9 ft Diameter 9 ft Embedded Length in 30 tsf Rock a) Test No. 1 b) Test No. 2.....	126
Figure B.5 Output Voltage from 6 ft Diameter 6 ft Embedded Length in 10 tsf Rock a) Test No. 1 b) Test No. 2.....	127
Figure B.6 Output Voltage from 6 ft Diameter 6 ft Embedded Length in 30 tsf Rock a) Test No. 1 b) Test No. 2.....	128
Figure B.7 Output Voltage from 9 ft Diameter 27 ft Embedded Length in 10 tsf Rock a) Test No. 1 b) Test No. 2.....	129
Figure B.8 Output Voltage from 9 ft Diameter 27 ft Embedded Length in 30 tsf Rock a) Test No. 1 b) Test No. 2.....	130
Figure B.9 Output Voltage from 6 ft Diameter 18 ft Embedded Length in 10 tsf Rock a) Test No. 1 b) Test No. 2.....	131

Figure B.10 Output Voltage from 6 ft Diameter 18 ft Embedded Length in 30 tsf Rock a) Test No. 1 b) Test No. 2.....	132
Figure C.1 Moment Curve with Different Top Lateral Displacement from 9 ft Diameter 9 ft Embedded Length in 10 tsf Rock with 50 % Styrofoam Layering below 1D below from Tip of Shaft a) Test No. 1 b) Test No. 2 .....	133
Figure C.2 Moment Curve with Different Top Lateral Displacement from 9 ft Diameter 9 ft Embedded Length in 30 tsf Rock with 50 % Styrofoam Layering below 1D below from Tip of Shaft a) Test No. 1 b) Test No. 2 .....	134
Figure C.3 Moment Curve with Different Top Lateral Displacement from 9 ft Diameter 9 ft Embedded Length in 10 tsf Rock a) Test No. 1 b) Test No. 2.....	135
Figure C.4 Moment Curve with Different Top Lateral Displacement from 9 ft Diameter 9 ft Embedded Length in 30 tsf Rock a) Test No. 1 b) Test No. 2.....	136
Figure C.5 Moment Curve with Different Top Lateral Displacement from 6 ft Diameter 6 ft Embedded Length in 10 tsf Rock a) Test No. 1 b) Test No. 2.....	137
Figure C.6 Moment Curve with Different Top Lateral Displacement from 6 ft Diameter 6 ft Embedded Length in 30 tsf Rock a) Test No. 1 b) Test No. 2.....	138
Figure C.7 Moment Curve with Different Top Lateral Displacement from 9 ft Diameter 27 ft Embedded Length in 10 tsf Rock a) Test No. 1 b) Test No. 2.....	139
Figure C.8 Moment Curve with Different Top Lateral Displacement from 9 ft Diameter 27 ft Embedded Length in 30 tsf Rock a) Test No. 1 b) Test No. 2.....	140
Figure C.9 Moment Curve with Different Top Lateral Displacement from 6 ft Diameter 18 ft Embedded Length in 10 tsf Rock a) Test No. 1 b) Test No. 2.....	141
Figure C.10 Moment Curve with Different Top Lateral Displacement from 6 ft Diameter 18 ft Embedded Length in 30 tsf Rock a) Test No. 1 b) Test No. 2 .....	142
Figure D.1 Shear Curve with Different Top Lateral Displacement from 9 ft Diameter 9 ft Embedded Length in 10 tsf Rock with 50 % Styrofoam Layering below 1D below from Tip of Shaft a) Test No. 1 b) Test No. 2 .....	143
Figure D.2 Shear Curve with Different Top Lateral Displacement from 9 ft Diameter 9 ft Embedded Length in 30 tsf Rock with 50 % Styrofoam Layering below 1D below from Tip of Shaft a) Test No. 1 b) Test No. 2 .....	144
Figure D.3 Shear Curve with Different Top Lateral Displacement from 9 ft Diameter 9 ft Embedded Length in 10 tsf Rock a) Test No. 1 b) Test No. 2.....	145
Figure D.4 Shear Curve with Different Top Lateral Displacement from 9 ft Diameter 9 ft Embedded Length in 30 tsf Rock a) Test No. 1 b) Test No. 2.....	146

Figure D.5 Shear Curve with Different Top Lateral Displacement from 6 ft Diameter 6 ft Embedded Length in 10 tsf Rock a) Test No. 1 b) Test No. 2.....	147
Figure D.6 Shear Curve with Different Top Lateral Displacement from 6 ft Diameter 6 ft Embedded Length in 30 tsf Rock a) Test No. 1 b) Test No. 2.....	148
Figure D.7 Shear Curve with Different Top Lateral Displacement from 9 ft Diameter 27 ft Embedded Length in 10 tsf Rock a) Test No. 1 b) Test No. 2.....	149
Figure D.8 Shear Curve with Different Top Lateral Displacement from 9 ft Diameter 27 ft Embedded Length in 30 tsf Rock a) Test No. 1 b) Test No. 2.....	150
Figure D.9 Shear Curve with Different Top Lateral Displacement from 6 ft Diameter 18 ft Embedded Length in 10 tsf Rock a) Test No. 1 b) Test No. 2.....	151
Figure D.10 Shear Curve with Different Top Lateral Displacement from 6 ft Diameter 18 ft Embedded Length in 30 tsf Rock a) Test No. 1 b) Test No. 2.....	152

# CHAPTER 1 INTRODUCTION

## 1.1 Background

### 1.1.1 Design

Over the past decades, drilled shafts have become the deep foundation of choice for bridges and tall structures. Due to their large diameters and associated large moments of inertia, they are able to resist large lateral loads induced by hurricanes and ship impacts. In addition, installation involves a minimal foundation footprint addressing right of way issues and the need to minimize construction noise and vibrations in urban areas. Finally, there are economic benefits of replacing a large number of piles in a group with a single or several drilled shafts.

In the late 1980s, drilled shaft designs for bridges in Florida (e.g., Port Orange, Gandy, etc.) utilized shafts with diameters of between four and six feet, with rock embedments exceeding 25 ft (i.e., rock socket Length/Diameter or  $L/D > 5$  diameters). Typical axial load transfer was based solely on skin friction with virtually no contribution from tip resistance. Subsequently, with the use of shaft inspection devices, field load tests (e.g., Osterberg or Statnamic) as well as new end bearing design approaches (e.g., FHWA – O’Neill), end-bearing resistance in design has become more common place (e.g., Ringling Bridge). Moreover, in order to reduce foundation costs and minimize their footprint, shaft diameters have steadily increased, with six to ten feet now the norm (e.g., Apalachicola, Ringling, New River, etc.).

Unfortunately, the size of drilled shafts has a profound effect on their load resistance behavior. For instance, under lateral loading, large diameter shafts develop a significant moment or couple from the shear transfer on the side of the shaft, as shown in Figure 1.1. The side shear shown in Figure 1.1 thus influences the back calculated P-Y curves. For example, Figure 1.2

(McVay et al., 2004) shows back calculated P-Y curves if side shear is accounted for (i.e., labeled ‘corrected’ in Figure 1.2). It is apparent that the error in estimating the lateral resistance may be as high as 26% for a 12 foot diameter shaft. Consequently, the new release of FB-PIER, Version 4, accounts for the side shear and its influence on shaft moments.

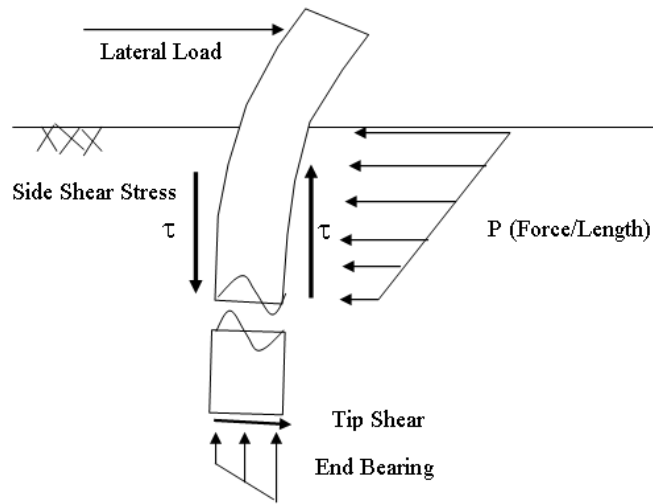


Figure 1.1 Field Load Transfer in Soil/Rock

Besides side shear, the tip behavior of large diameter shafts (i.e., 8 ft or greater) is greatly influenced by embedment length. For instance, at typical embedment depths of 20 ft or less, it is expected that these shafts will exhibit lateral tip displacement and rotation, especially for  $L/D < 3$ . The rotations will develop significant moments and shear at the shaft tip, especially in Florida limestone. These shears and moments will correspondingly change the shaft’s internal shears and moments and therefore must be accounted for in shaft design (i.e., steel reinforcement requirements).

Besides shears and moments within the shaft, large diameter shafts are also strongly influenced by spatial variability within the tip zone (3D). For example, voids, weak zones, and variable soil properties (modulus, strength etc.) all must be taken into account. For instance, an

eight foot diameter shaft would have a zone of influence of 24 feet which could include layering as well as highly variable rock properties and voids. Any LRFD design methodology must account for spatial variability on a site by site basis.

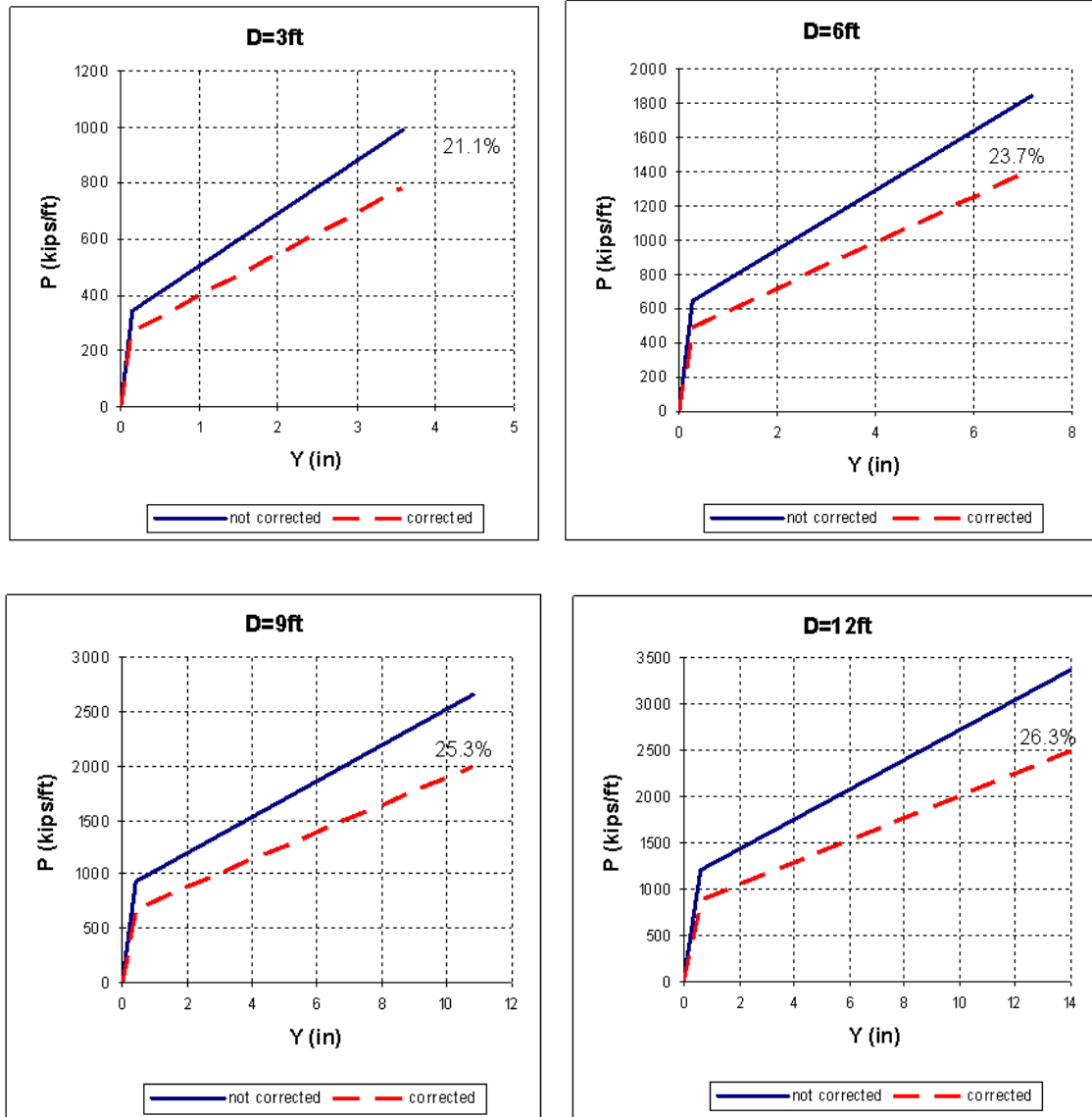


Figure 1.2 Reconstructed P-Y Curves for 80 ksf Rock

### 1.1.2 Background – Centrifuge Testing

Recently, the researchers successfully tested large diameter drilled shafts embedded in variable strength limestone. The testing was conducted using UF’s centrifuge facility, in which small scale models are subjected to large scale field stresses. Since Florida limestone is highly variable, both horizontally and vertically, it was obvious that there would be insufficient duplicate samples needed for the testing program. Consequently, synthetic rock, which is homogeneous and isotropic with strengths similar to Florida limestone, was developed. The rock was produced by mixing ground limestone, cement and water in various proportions to obtain prescribed unconfined strengths. Axial and lateral tests of shafts in this “rock” produced similar load-deformation response as natural limestone (McVay, 2004).

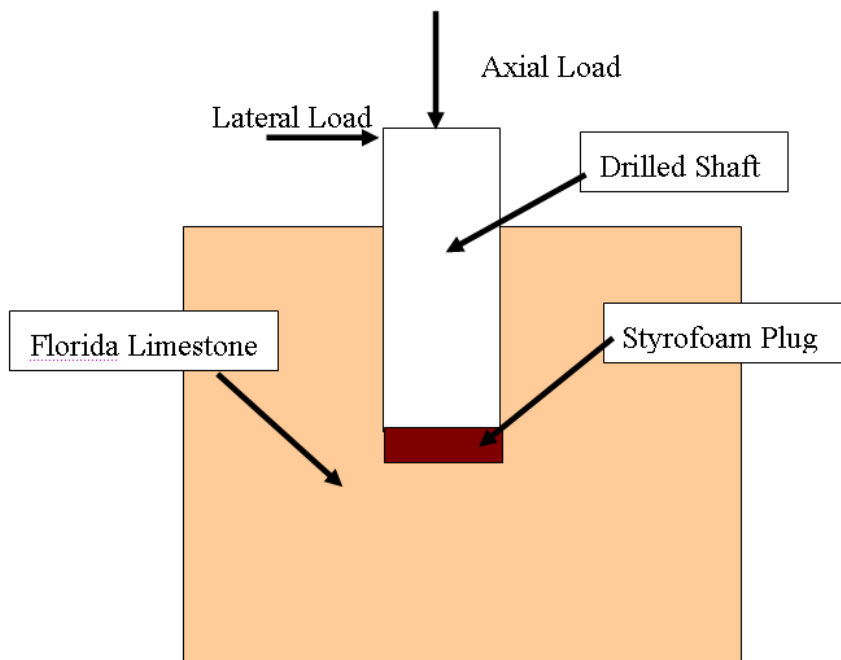


Figure 1.3 Combined Axial and Lateral Load Test (McVay, 2004)

In this prior research (McVay, 2004), the end bearing contribution was removed by using a Styrofoam plug as shown in Figure 1.3. Thus, only side shear contributed to the lateral resistance (P-Y curves) of the shaft.

For the current research project, the Styrofoam plug was removed and the various shafts shortened to  $L/D < 3$ . In addition, the unit end bearing and tip shear as a function of axial tip displacement and rotation had to be measured. Thus, strain gages used in the prior research, and shown in Figure 1.4, were used in assessing the axial and lateral shears, moments and lateral resistances as a function of shaft displacement and rotation. However, as the prior research performed axial and lateral load tests independently of one another, these tests needed to apply both axial and lateral loads concurrently. A range of lateral loads, representative of typical Florida designs with variable axial loading (i.e., develop tip resistance vs. displacements) were used.



Figure 1.4 Instrumented Drilled Shafts to Monitor Axial, Moment and Shear

### 1.1.3 Background – Spatial Variability

Since tip resistance is a function of tip compressibility, the effects of voids found in Florida limestone, i.e., Karst materials where recoveries range between 40 to 80% must be considered. For this study, the use of perlite spheres mixed in with the synthetic limestone (30%

to 50% by volume) was used to represent typical rock recoveries. It is important to note that the current design methods by O'Neill and FHWA in FB-DEEP model the effects of voids through the Mass Modulus of the rock,  $E_m$ . This is always smaller than the intact Young's Modulus,  $E_i$  and is generally related to Recovery or RQD.

The results of the laboratory centrifuge work was the development of a tip model (i.e., axial, shear, and moment) for short shafts ( $L/D < 3$ ) as a function of tip displacements, rotations, rock strength ( $q_u, q_t$ ), stiffness ( $E_i$ ) and Recoveries. Another important point to consider is that current design software (FB-Pier, FB-Deep, FHWA, etc.) identifies tip resistance only as a function of tip displacement, stiffness ( $E_i$ ) and RQD.

Due to the loss of foundation redundancy and the trend toward larger single shaft construction (e.g., Cross-Town Expressway, New River Bridge, Ringling Bridge, etc.), field coring of rock near as-built non-redundant shafts is now required (FDOT Structures Bulletin, 2005). However, to accurately predict skin and end bearing of a new shaft during the design phase is also of strong interest. For instance, the thickness of limestone layers, recoveries (voids), strength and compressibility near the proposed shaft may significantly improve the LRFD resistance factors,  $\phi$ , for design. Consequently, there is a need to assess the LRFD resistance factors based on the frequency distribution of strengths, recoveries and compressibility data for an entire site rather than for a specific shaft location.

Fortunately, probabilistic based LRFD resistance factors can be used to address these issues. For example, using Monte Carlo or Bayesian theory, strength, compressibility, etc., statistical properties can be generated from core and laboratory data near a specific shaft or over the entire site. Using simple random sampling, end bearing, skin friction, etc. may be computed for a specific shaft or for any other shafts on site. For instance, (McVay 2004) used the latter

approach to assess LRFD skin friction resistance factors. This technique had not been used previously and it is expected that the difference in LRFD resistance factors for end bearing will be significant when applied at a specific location versus the entire site.

## **1.2 Scope**

### **1.2.1 Laboratory**

In order to develop end bearing and tip shear for large diameter short shafts ( $L/D < 5$ ), two different rock strengths, 10 tsf and 30 tsf, were used. For each of the rock strengths, the following conditions were varied in order to develop end bearing and tip shear relationships.

#### **1.2.1.1. Loading (Axial and Lateral)**

Initially, axial load tests only were performed to assess existing lab/field unit tip resistance models (O'Neill FHWA, FB-Pier) as a function of tip displacement (e.g., Osterberg results). These tests were used to identify the peak axial force for a given rock strength, Young's Moduli, and L/D embedment. Next, the maximum lateral capacity of the test shaft was established using FB-Pier. In strong rock, the lateral capacity was controlled by its moment capacity for the longer shafts ( $L/D = 3$ ), but the rock strength controlled the shorter shafts ( $L/D = 1$ ). The shafts' axial tip displacement and end bearing, as well as tip translation and shear were recorded.

#### **1.2.1.2. Shaft Diameter**

The effects of short shaft tip rotation was more pronounced for larger diameter shafts, e.g., over eight feet. Consequently, two different shaft diameters were tested to quantify influences of shaft diameter. Diameters of six and nine feet were studied since they are representative of medium and large diameter Florida drilled shafts.

### **1.2.1.3. Length to Diameter (L/D) Ratio**

For each shaft diameter, two different L/D ratios were tested to investigate the effect of embedment depth on the distribution of end bearing and tip shear. The embedment depth strongly influences the magnitude of displacement and rotation of the shaft as well as its tip normal pressure and shear distribution. Long shafts (i.e.,  $L/D > 5$ ) are generally controlled by shaft's moment capacity, whereas the soil/rock lateral resistance controls shorter shaft response. L/D ratios between 1 and 3, Table 1.1, were tested, since they represent typical Florida embedment depths.

### **1.2.1.4. Influence of Rock Voids or Limestone Recoveries**

Of particular interest was the influence of karst channels or rock voids (Recoveries < 100%) on end bearing. To account for the effect of voids on a shaft's ultimate tip resistance as well as tip shear, perlite (Styrofoam) spheres, 30% to 50% by volume, were mixed with the synthetic limestone. Since voids are more of a concern for short shafts, the studies focused on shafts with a length to diameter ratio of one and were tested in weak and strong limestone as shown in Table 1.1.

In addition, since shafts may be embedded in limited thick layers, e.g., Fort Thompson, Jacksonville, etc., the extent and quality of rock below the shaft tip becomes extremely important. Current design practice assumes uniform rock properties to a depth below the tip of three diameters, which may or may not be conservative. To investigate this possibility, reduced modulus rock, located one and three diameters below the shaft tip (see Table 1.1) were used to quantify its influence on end bearing capacities.

Table 1.1 shows a summary of all 32 tests performed to quantify end bearing and tip shear for large diameter short shafts. Note, there were 16 different scenarios (i.e., rock strength, embedment, voids etc.), but each test had to be repeated twice to ensure accuracy.

### 1.2.2 LRFD Assessment and Field Verification

Current assessment of drilled shaft skin and tip resistance is performed using core samples recovered from the site and tested in the laboratory (unconfined compression, split tension, and intact Young’s Modulus). Generally, all the samples are averaged over the entire site and either a log normal distribution or arithmetic mean is assumed, while discarding those values one standard deviation above and below. Unfortunately, these methods don’t consider spatial variability and associated correlation (i.e., covariance), which is important for end bearing. A probabilistic approach (Monte Carlo), which does consider spatial variability and associated correlation at a specific pier or entire site is more appropriate. For instance, the designer should have the option of developing specific LRFD resistance factors for a specific shaft/pier based on adjacent data (summary statistics, covariance, etc.) or by using the entire site data for general LRFD assessment values. Obviously, it is expected that the  $\phi$  values developed on a pier by pier basis should be much higher. However this is offset by the higher cost of additional field testing. Examples of predicted tip response, as well as LRFD  $\phi$  factors using spatial variability and correlation is presented for two FDOT sites: 17<sup>th</sup> Street and Fuller Warren Bridges.

Table 1.1 Recommended Tests for End Bearing and Unit Tip Shear

10 tsf	W/O Styrofoam	Diameter	9 ft	L/D = 1	
				L/D = 3	
		Diameter	6 ft	L/D = 1	
				L/D = 3	
	W/ Styrofoam	Diameter	9 ft	1 D Below	30%
					50%
3 D Below			30%		
			50%		
30 tsf	W/O Styrofoam	Diameter	9 ft	L/D = 1	
				L/D = 3	
		Diameter	6 ft	L/D = 1	
				L/D = 3	
	W/ Styrofoam	Diameter	9 ft	1 D Below	30%
					50%
3 D Below			30%		
			50%		

CHAPTER 2  
CENTRIFUGE TESTING SETUP AND MATERIAL

**2.1 Background**

The chapter focuses on the development of a tip shear, end bearing and tip rotation model for drilled shafts in Florida limestone using centrifuge results. Specifically, the influence of tip translation and rotation, limestone strength and stiffness, as well as voids and layering were investigated. For the model development, the recommended tests, outlined in Table 1.1 were adopted and are re-shown in Table 2.1 below.

Table 2.1 Centrifuge Test Matrix

10 tsf	W/O Styrofoam	Diameter	9 ft	L/D = 1	
				L/D = 3	
	Diameter	6 ft	L/D = 1		
			L/D = 3		
	W/ Styrofoam	Diameter	9 ft	1 D Below	30%
					50%
3 D Below		30%			
		50%			
30 tsf	W/O Styrofoam	Diameter	9 ft	L/D = 1	
				L/D = 3	
	Diameter	6 ft	L/D = 1		
			L/D = 3		
	W/ Styrofoam	Diameter	9 ft	1 D Below	30%
					50%
3 D Below		30%			
		50%			

The tests were selected to encompass both soft and medium strength rock for both short and intermediate embedment. Also, since Florida limestone typically contains voids, it results in a variable modulus. To model this aspect, 1.5 mm diameter perlite spheres were used to capture the mass modulus,  $E_m$ . A total of 32 centrifuge tests were conducted based on Table 2.1, i.e., duplicate 16 tests for repeatability. A discussion of the centrifuge testing and results follows.

## 2.2 Hardware & Instrumentation

The tests were performed in the newly constructed axial/lateral test box shown in Figure 2.1. The circular steel container holds the cast limestone specimen. The aluminum superstructure provides the necessary reaction for both axial and lateral loading of the models. Mounted to the top of the container are two load cells for axial and lateral loading as well as two displacement transducers ( LVDTs) for axial displacement and one for lateral displacement. The test setup is shown Figure 2.2.

Since the sample container is 12 inches tall and 17 inches in diameter, in order to model a prototype foundation embedment of 27 feet, the centrifuge tests were conducted at 67 gravities. To minimize the end effects, seven inches were maintained between the model's tip and bottom of container. The basic centrifuge scaling relationships is as follows. The length dimension is scaled by 1/67 (i.e., the model diameter equals the prototype diameter divided by the number of gravities). By applying this scaling factor, model and field stresses are equal. A comparison of Prototype (Field) to centrifuge model dimensions is shown in Table 2.2.

Table 2.2 Conversions between Prototype and Model for Shafts Tested

Prototype Size	6 ft	9 ft
Modeled Size	1.07 in	1.61 in

Each model shaft had steel reinforcing oriented in the axial direction for lateral loading, as shown in Figure 2.3. Attached to opposite sides of the reinforcing were four to six pairs of strain gages depending on the L/D ratio. The steel reinforcing was modeled with a 0.75 inch diameter steel pipe for the 6 ft diameter and a 1.32 inch diameter steel pipe for the 9 ft diameter shaft.

Both were slotted, and roughened to aid bonding with the concrete. The strain gages were obtained from Micro Measurements with 350 Ohm resistance.



Figure 2.1 New Cylindrical Sample Container



Figure 2.2 Instrumentation for Measuring Lateral & Vertical Forces and Deformation

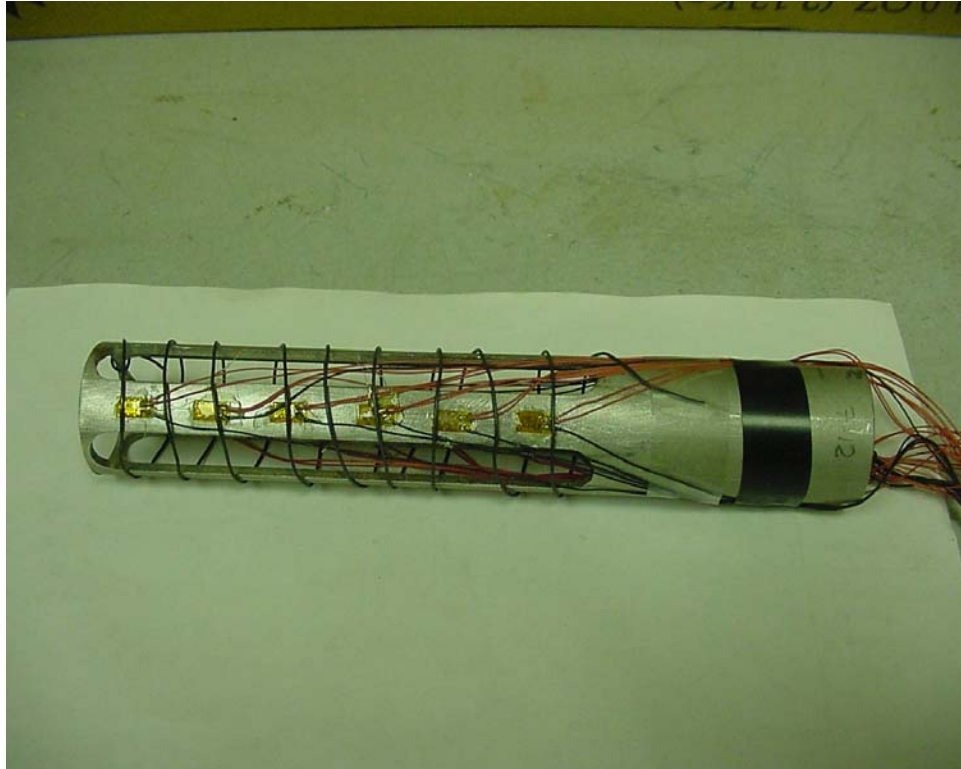


Figure 2.3 Slotted Steel Pipe (Axial Reinforcement) & Strain Gages

The axial forces in the shaft were obtained from the average strain gage readings at discrete locations multiplied by the shaft modulus and cross-sectional area. To assess bending and thus flexure, the bending strains are measured from which the curvature is compute and bending moments obtained. Note the moment-curvature relationship may be nonlinear for cracked cross-sections. Once the bending moment distribution along a shaft is known, the shear distribution (i.e., derivative of moment with depth) is also known. Not only were the shear and bending moments determined along the shaft, but at the tip as well.

## 2.3 Material

### 2.3.1 Synthetic Rock

The limestone used in the experiments, Figure 2.4, was reconstituted material (synthetic limestone), i.e., a mixture of crushed limestone, cement, and water (McVay et al. 2004). Perlite spheres were added to characterize voids associated with typical recoveries from the field. Of primary interest is the influence of void sizes on rock properties, i.e., modulus and strength. The current practice (i.e., FHWA intermediate geomaterials) is to reduce modulus as a function of RQD or Recovery values.



Figure 2.4 Mixture of Synthetic Rock (10 tsf) for Axial Load Test in Centrifuge

For this work, crushed limerock was obtained from a quarry in Newberry (Florida Limestone Products Inc.) by the SMO and delivered to UF in bulk (approximate 2 tons). For volume considerations, i.e., centrifuge testing, the limerock was subsequently sieved through a No. 10 standard sieve. Its grain size distribution is shown in Figure 2.5 and as seen in the Figure, the aggregate is well graded.

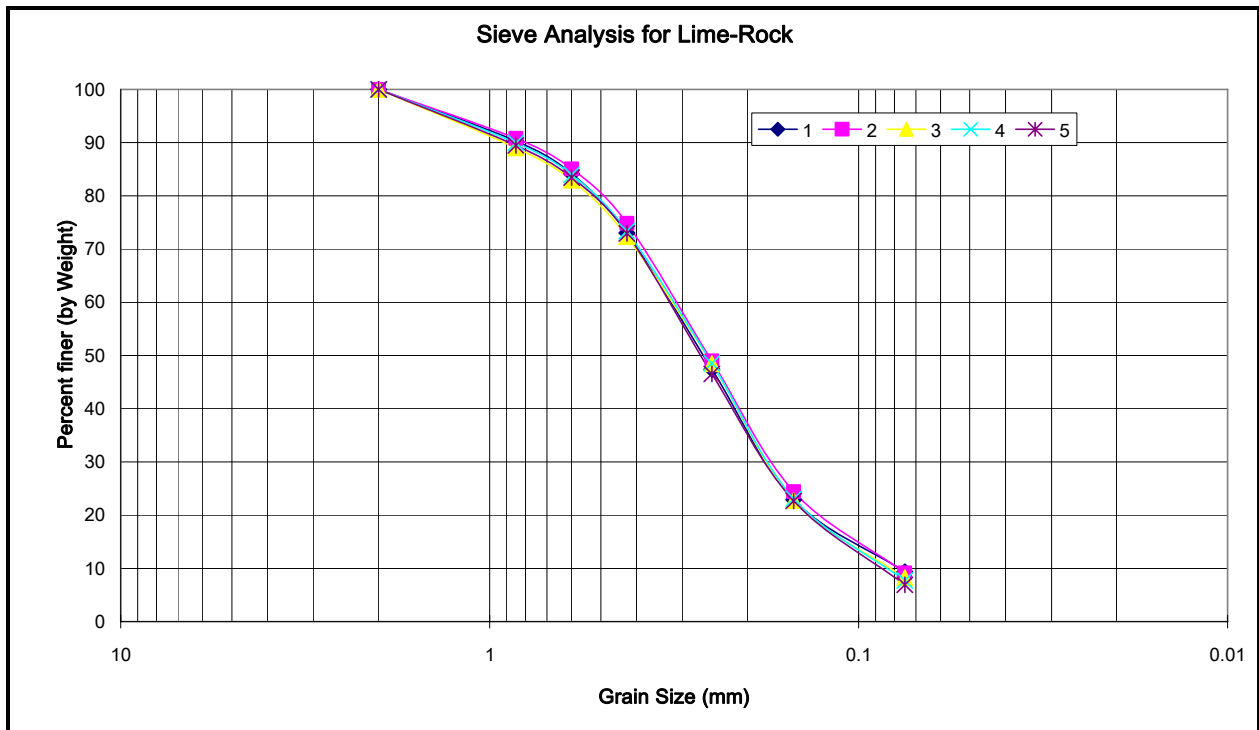


Figure 2.5 Grain Size Distribution for Limerock Aggregate

To minimize the affect of natural moisture in the material, it was dried for at least 24 hours. Next, the synthetic limestone was batched by mixing Portland cement and water in differing proportions. Cylindrical samples (2 inch diameter and 4 inches high) were cast and cured at room temperature for 14 days before unconfined compressive tests were run. To obtain the desired strength, multiple trials of different proportions of limerock, cement and water were

used and are shown Table 2.3. Once the desired strength was achieved, the tests were repeated at least three times to verify repeatability. Limestone specimens with and without Styrofoam were also cast in 2" x 4" cylinders to identify the influence of voids on rock properties, i.e., strength and modulus, shown in Figure 2.6. The unconfined compression strength testing was performed in accordance with ASTM D 2938. An ISTRON, compression testing machine, was used to obtain both the unconfined compression strength, as well as the modulus.



Figure 2.6 Strength Testing of Concrete and Rock

Table 2.3 Proportion of Component for Synthetic Limestone

Required Strength	Percentage, %, (by weight)		
	Limestone	Cement	Water
$q_u$ (tsf)			
10	75	5	20
20	72.5	7.5	20
30	70	10	20

As discussed previously, perlite spheres cast with the synthetic limestone specimens attempted to mimic voids found in natural occurring rock (Figure 2.7). Figure 2.8 shows the stress strain response of intact (i.e., no perlite) versus 30% by volume perlite specimens. Both small (5 mm) and larger (10 mm) spheres were investigated. Evident from the Figure, a significant reduction (>50 %) in strength and compressibility (i.e., the slope of stress vs. strain) occurred with the addition of the perlite. Interestingly, the size of the perlite spheres (i.e., small vs. large) was not an issue, suggesting that the karst nature of limestone could be characterized through sphere inclusion. Table 2.4 shows the comparison of voided modulus to non-voided modulus based on volume or recovery.



Figure 2.7 Synthetic Limestone with 5 mm Perlite Spheres Occupying 30 % Volume

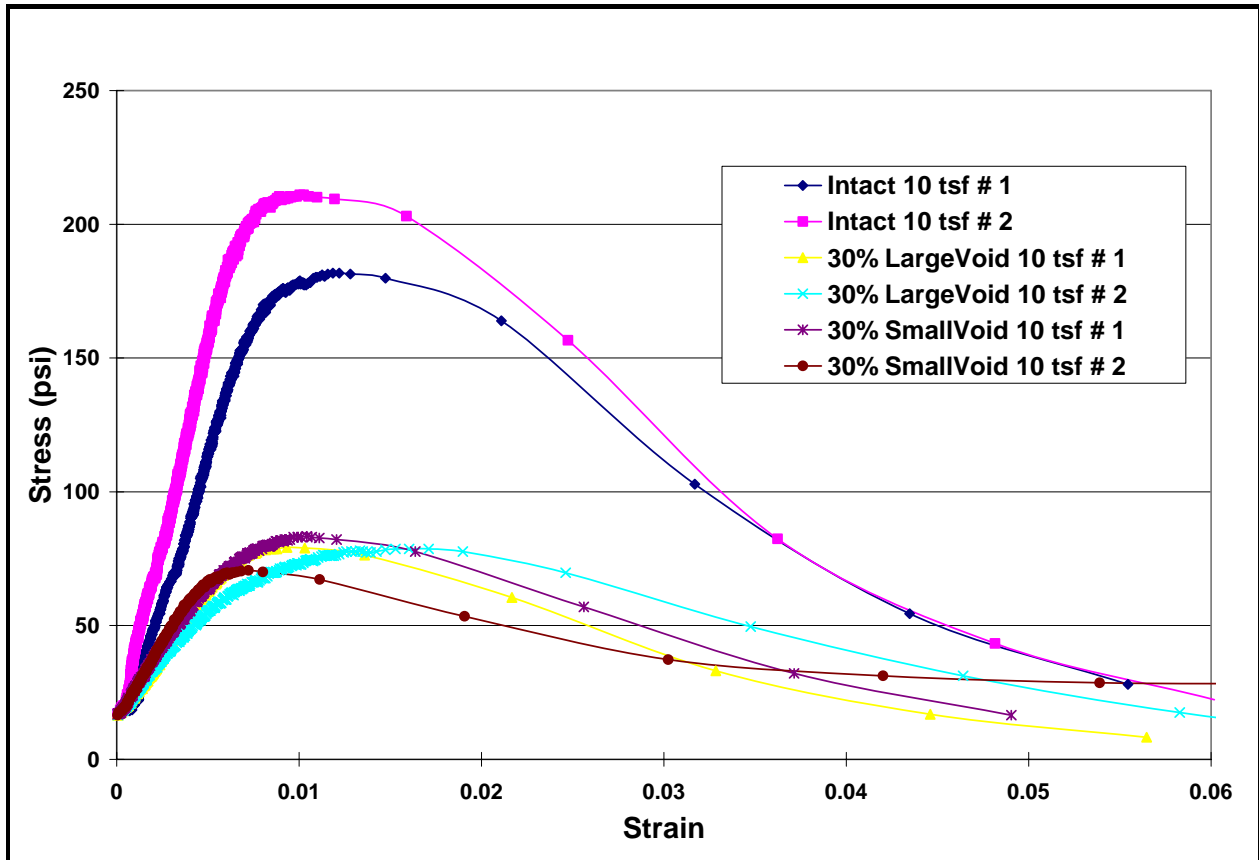


Figure 2.8 Stress-Strain Response Voided and non-Voided Limestone

Table 2.4 Ratio of  $E_m$  (with perlite) /  $E_i$  (no perlite)

Recovery	Modulus Ration ( $E_m/E_i$ )
70%	0.29
50%	0.065

### 2.3.2 Concrete Grout

Since the rock strength used in the centrifuge tests are as high as 30 tsf (417 psi), the concrete strengths had to be sufficient enough to ensure a limestone failure instead of the concrete. This is because the study focused on rotations of the drilled shaft models, as well as translations, i.e., tip shear. To ensure the latter, a concrete strength of 360 tsf (5000 psi) which is typical for drilled shafts in Florida, was used. Due to model size of the shafts, the concrete

aggregate was limited in size to 2 mm and below. Several trial mixes were tested, incorporating five components; Portland cement type I, sand, silica fume, super-plasticizer, and water. The silica fume and super-plasticizer provide an increase in strength by reducing the water cement (w/c) ratio. The influence of sand particle size, were investigated as follows.

### 2.3.2.1 Mix with Silica Sand

Several trials mixes using w/c ratios of 0.35 to 0.4 and 0.5 to 0.6, with final strength values of 3 ksi to 4 ksi were obtained. After several trials to obtain 5,000 psi, w/c ratio was reduced to 0.3 for higher strengths; unfortunately the target strength, i.e., 5 ksi, couldn't be obtained. Table 2.5 shows the amount of each component. The amounts of each component were for 5 samples. Table 2.6 shows the dimensions of the samples and the maximum load applied to each. The samples were tested after 4 days of curing at room temperature.

Table 2.5 Amount of Component for Mixing Concrete with Silica Sand

W/C	Water (g)	Cement (g)	SP (oz)	SF (g)	C/A	Aggregate (g)
0.3	213.8	712.7	0.45	60.6	0.5	1425.5

Table 2.6 Result of Unconfined Compression Strength Test

Sample #	1	2	3
Average Length (in)	4.06	4.063	4.055
Average Diameter (in)	2	2	2
Weight (g)	471	472	469
Unit Weight (pcf)	140.7	140.9	140.2
Max. Load (lbf)	15003	10996	13691
Strength (psi)	4776	3500	4358

### 2.3.2.2 Mix with Granite Sand

Table 2.7 shows the amount of each component weights required to make 4 samples. Table 2.8 shows the size of sample and the maximum load on each sample. The samples were tested 4 days after curing at room temperature. As evident by Table 2.8, the expected strength, i.e., 5 ksi, was obtained and was used to make the model shafts.

Table 2.7 Amount of Component for Mixing Concrete with Granite Sand

W/C	Water (g)	Cement (g)	S-P (oz)	S-F (g)	C/A	Aggregate (g)
0.35	213.8	611	0.5	52	0.5	1221.9

Table 2.8 Result of Unconfined Compression Strength Test

Sample #	1	2	3
Average Length (in)	3.965	4	3.97
Average Diameter (in)	2	2	2
Weight (g)	456	462	453
Unit Weight (pcf)	139.4	140	138.4
Max. Load (lbf)	15229	15866	16248
Strength (psi)	4847.5	5050.3	5171.9

Consequently, the mix design outlined in Tables 2.7 & 2.8 was used for the drilled shafts construction, as well as the instrumentation and Testing Matrix outlined in Table 2.1 for a total of 32 instrumented tests.

## CHAPTER 3 CENTRIFUGE TEST DATA REDUCTION

### 3.1 Axial Loading

The standard testing procedure consisted of first applying an axial load to each shaft until settlement reached 3% to 5% of the models' diameters. This was then followed by the lateral loading. The axial loading was representative of the vertical live and dead loads under service conditions. The data from the axial loading was used to develop the tip displacement vs. tip stress model. The reduction of the data is as follows.

From several pairs of strain gage readings (Figure 3.1) in concert with axial LVDT displacements and load cell output at the top of shaft, the transferred skin friction along the shaft and tip resistance were computed. Specifically, from each pair of strain gage, the axial strain or compressive strain for each applied axial load state was found.

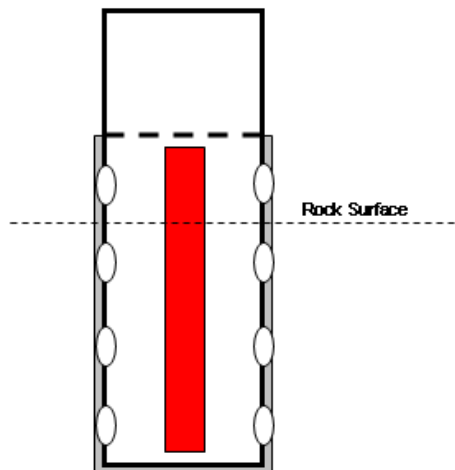


Figure 3.1 Strain Gage Layout for  $L/D = 1$

The compressive strain is given by:

$$\varepsilon_a = \frac{(\varepsilon_{left} + \varepsilon_{right})}{2} \quad \text{Eq.3.1}$$

Next, the transformed Young's Modulus of the shaft was assessed from the pair of strain gages located above the rock surface along with the applied axial load. The Young's Modulus of the shaft is given by:

$$E = \frac{P}{\pi \times r^2 \times \varepsilon_a} \quad \text{Eq.3.2}$$

Where, P is the applied axial load.

Subsequently, from each axial strain, the compressive force (Q) with depth may be assessed:

$$Q = E \times \varepsilon_a \times A \quad \text{Eq.3.3}$$

Where, A is Gross Shaft Area.

Figure 3.2 shows the typical axial force, Q, distribution within a shaft for various applied axial loads.

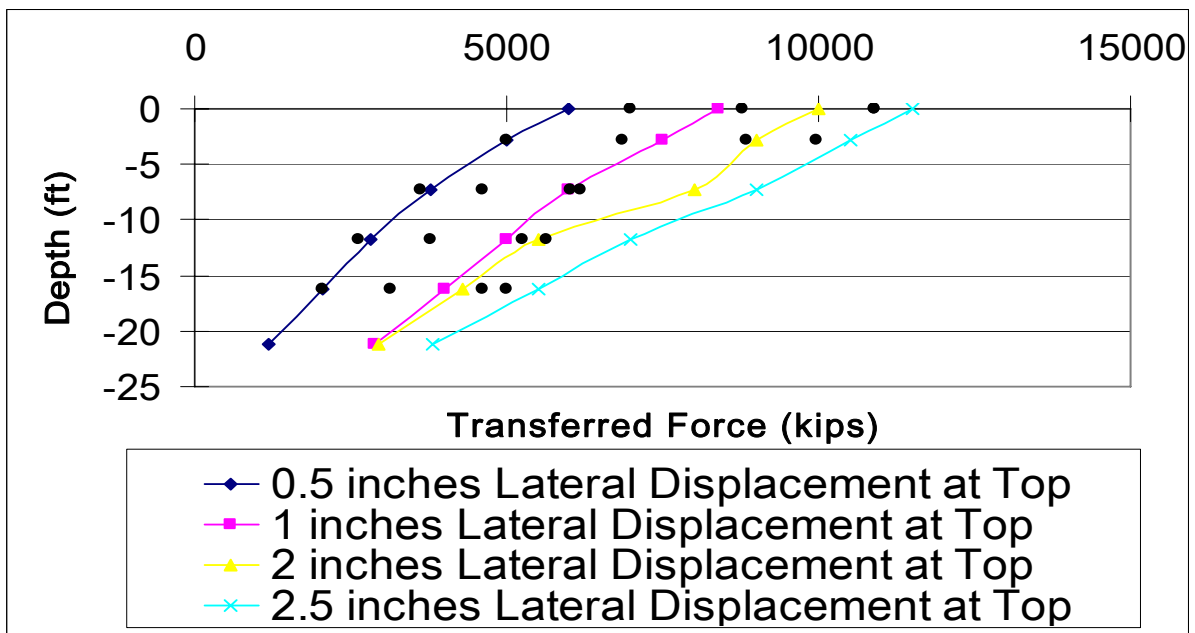


Figure 3.2 Compressive Force (Q) vs. Depth

### 3.1.1 Axial Loading –Side Shear

Once the axial force distribution along the shaft for a particular top displacement and set of strains along the shaft is determined, the T ( $f_s$ ) versus Z curve for the shaft can be computed by:

$$f_s = \frac{\Delta Q}{\pi \times D \times L} \quad \text{Eq.3.4}$$

Where, L is the interval length between adjacent pairs of strain gages.

Figure 3.3 shows typical  $f_s$  vs. Z curve for test shafts.

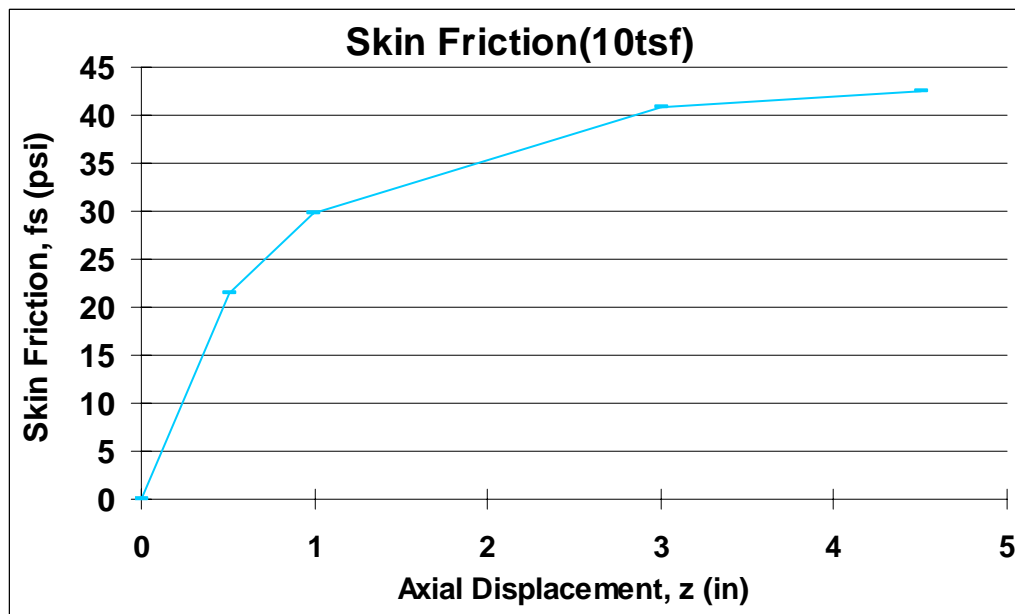


Figure 3.3 Mobilized Skin Frictions vs. Axial Displacement

For any applied axial load, a corresponding axial displacement and skin friction can be calculated at each elevation. However, due to the homogenous nature of the rock, the skin friction was expected to be uniform along the shaft as well as within range of the FDOT design values (McVay, 1992) and of previous centrifuge tests (Lila, 2003). Shown in Figures 3.4 and 3.5 are all the T-Z curves for the axial load portions of the centrifuge tests. Figure 3.4 shows the results for 10 tsf strength rock and Figure 3.5 shows the 30 tsf strength results. The results show

that the FDOT design criteria is quite good, however slightly conservative. The latter is attributed to the linear assumption of the strength envelope in assessing cohesion from  $\frac{1}{2} \text{sqrt}(q_u) \text{sqrt}(q_t)$ .

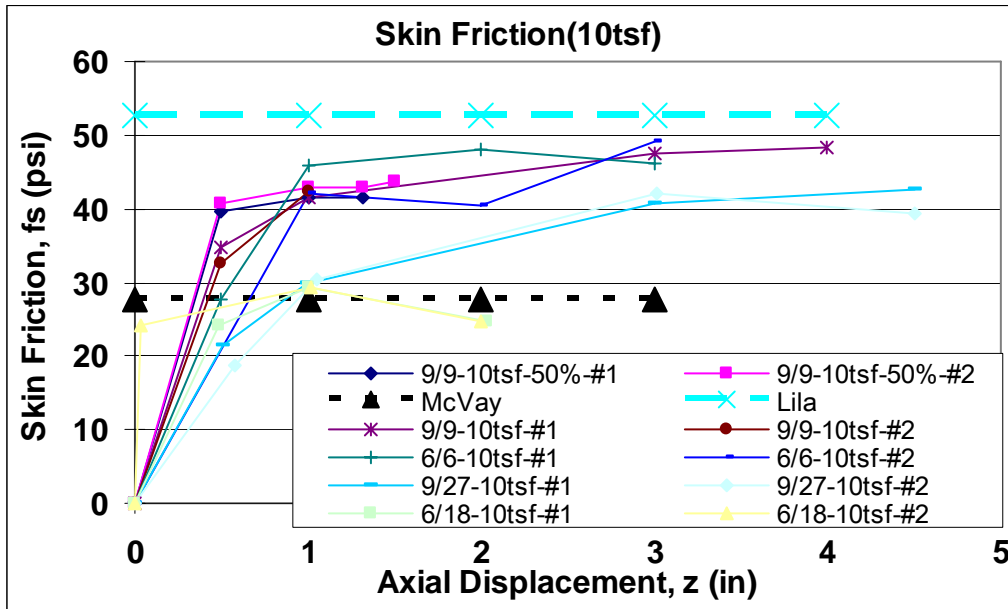


Figure 3.4 Measured Skin Friction Comparing Lila (2003) and McVay (1992)

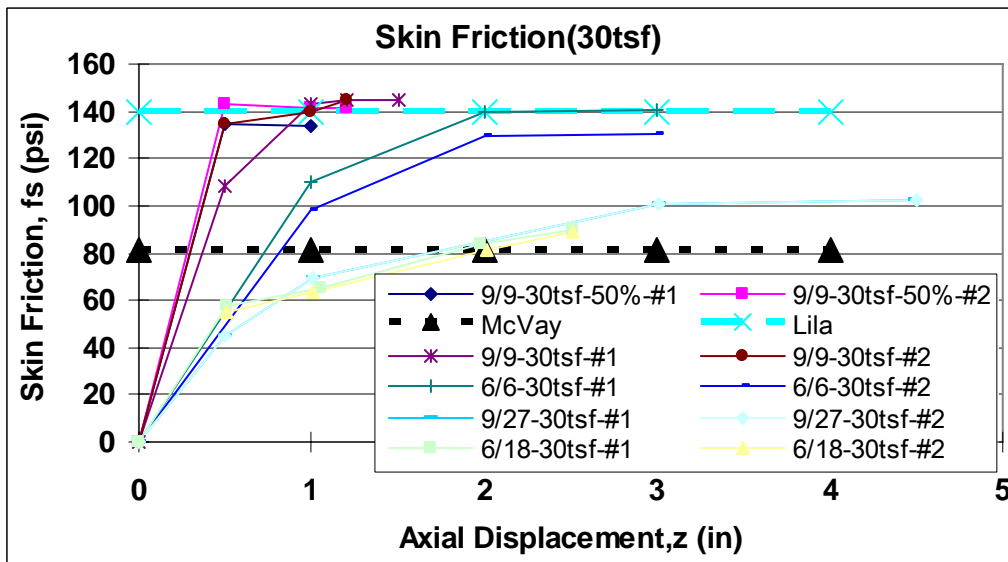


Figure 3.5 Measured Skin Friction Comparing Lila (2003) and McVay (1992)

The T-Z curves shown in Figures 3.4 and 3.5 agree very well with Lila's results which have subsequently been implemented into FB-MultiPier.

### 3.1.2 Axial Loading – End Bearing

A major focus of this research involves end bearing and specifically mobilized tip resistance as a function of tip displacement. Currently, FB-DEEP and FB-MultiPIER employ the FHWA model formulated by O' Neill which characterizes tip resistance,  $q_b$  as:

$$q_b = \Lambda W_t^{0.67} \quad \text{Eq.3.5}$$

Where  $\Lambda$ (Lambda) = Elastic compressibility parameter;

$W_t$  = Displacement at top of shaft (value assumed)

The elastic compressibility parameters,  $\Lambda$ (Lambda),  $\Gamma$ (Gamma), and  $\Omega$ (Omega), may be computed as:

$$\Gamma = 0.37 \left( \frac{L}{D} \right)^{0.5} - 0.15 \left[ \left( \frac{L}{D} \right)^{0.5} - 1 \right] \log_{10} \left( \frac{E_c}{E_m} \right) + 0.13 \quad \text{Eq.3.6}$$

$$\Omega = 1.14 \left( \frac{L}{D} \right)^{0.5} - 0.05 \left[ \left( \frac{L}{D} \right)^{0.5} - 1 \right] \log_{10} \left( \frac{E_c}{E_m} \right) - 0.44 \quad \text{Eq.3.7}$$

Leading to

$$\Lambda = 0.0134 E_m \frac{\left( \frac{L}{D} \right)}{\left( \frac{L}{D} + 1 \right)} \left\{ \frac{200 \left[ \left( \frac{L}{D} \right)^{0.5} - \Omega \right] \left[ \frac{L}{D} + 1 \right]}{\pi L \Gamma} \right\}^{0.67} \quad \text{Eq.3.8}$$

The Young's Modulus in Eqs. 3.4 to 3.6 is the mass modulus,  $E_m$ , and is of significant importance. The latter is different from the Young's modulus of intact rock samples,  $E_i$ , measured in the laboratory (ASTM D3148). The rock mass Young's Modulus,  $E_m$ , represents the

whole mass including fissures, voids, slip planes, etc. O'Neill suggests a correlation (Table 3.1) between the  $E_i$  and  $E_m$  based on Rock Quality Designation (RQD). If RQD values are less than 20 percent, the 20 percent's RQD correlation was used (Load Transfer for Drilled Shafts in Intermediate Geomaterials, 1996).

Table 3.1 Estimation of  $E_m/E_i$  Based on RQD (Load Transfer for Drilled Shafts in Intermediate Geomaterials, 1996)

Estimation of $E_m/E_i$ based on RQD		
RQD	$E_m/E_i$	$E_m/E_i$
%	Closed Joint	Open Joint
100	1	0.6
70	0.7	0.1
50	0.15	0.1
20	0.05	0.05

Of interest was the relationship between Florida limestone's Mass Modulus and intact Young's Modulus,  $E_i$  as reported in Table 2.4. Shown in Figure 3.6 are the  $E_m/E_i$  ratios as reported by O'Neil and UF. It shows that the UF data falls between O'Neil's open and closed joint data. Also, there exists a linear relationship between  $E_m/E_i$  for Recoveries above 50 % and below this value there is a sharp drop off.

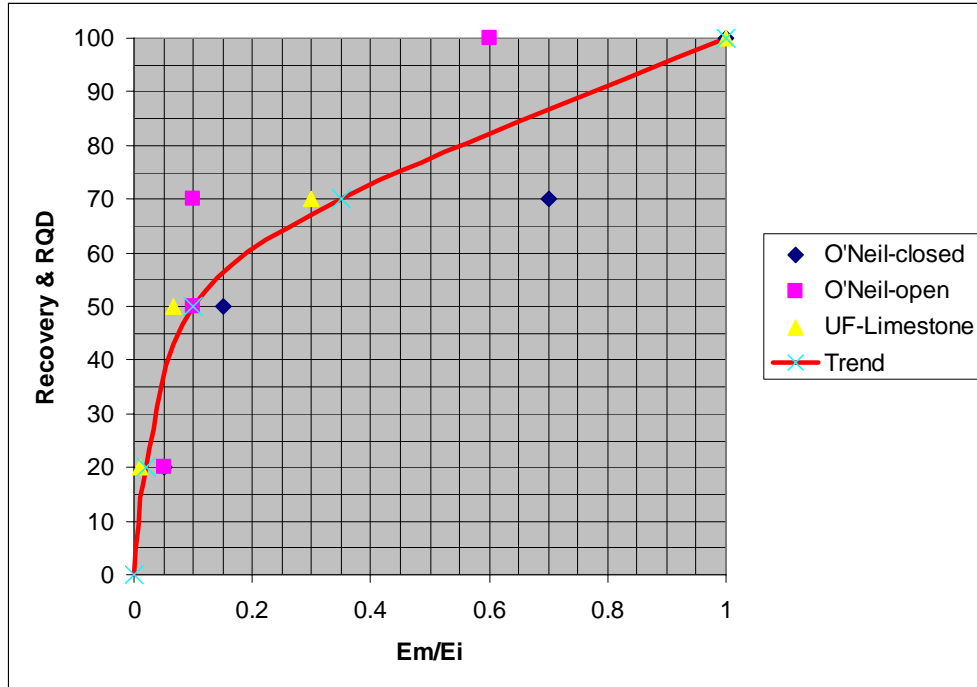


Figure 3.6 O'Neil  $E_m/E_i$  vs. RQD and UF  $E_m/E_i$  vs. Recovery

Next in importance for estimating tip resistance is the influence of layered systems (Example Table 2.1). The first researchers to address this were Ueshita and Meyerhof (1967) whose results are shown in Figure 3.7. Their theoretical solution for settlement or stress were found in terms of an Equivalent Modulus,  $E_e = K E_1$  shown in Figure 3.7.

Others have suggested the harmonic mean  $E_h$  (i.e. Menard), or:

$$E_{harmonic} = \frac{N}{\left(\frac{1}{E_1} + \frac{1}{E_2} + \dots + \frac{1}{E_N}\right)} \quad \text{Eq.3.9}$$

Where N is number of layers and  $E_N$  is the modulus of each layer.

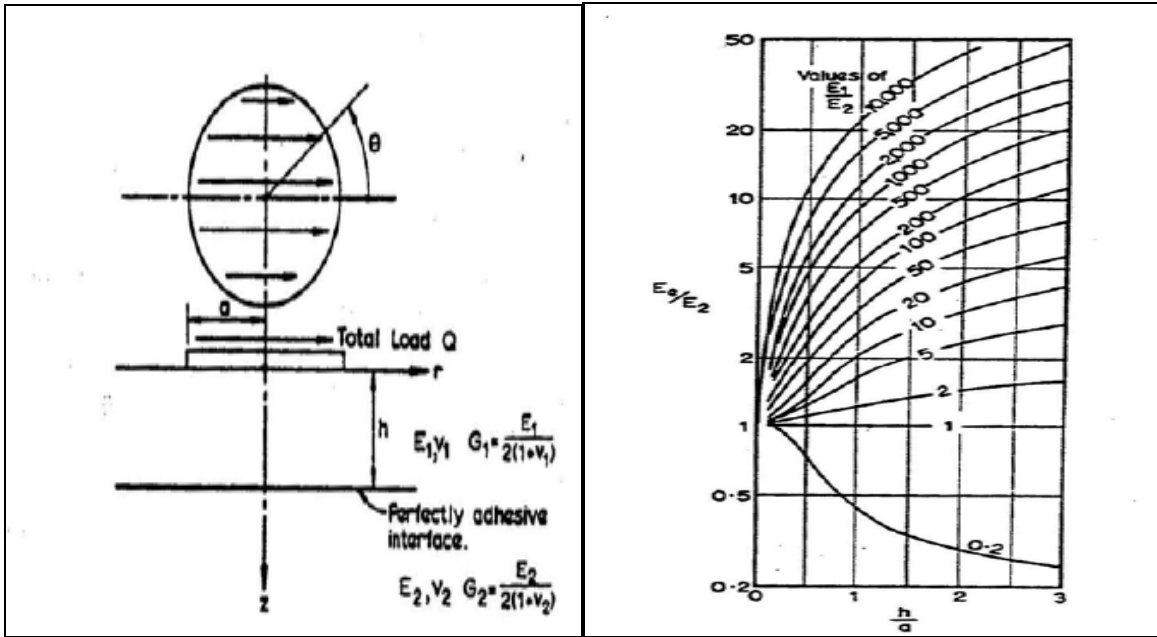


Figure 3.7 Two Layer System and Equivalent Modulus (Ueshita and Meyerhof, 1967)

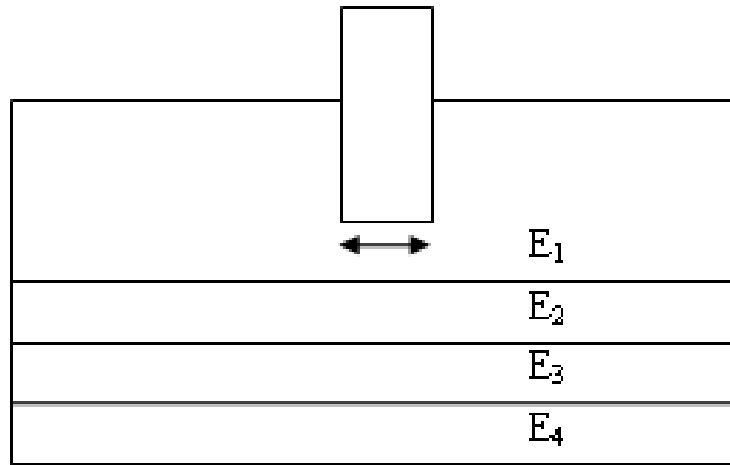


Figure 3.8 Layered Moduli beneath a Drilled Shaft

Recently, the geometric averaging method,  $E_g$ , to account for spatial variability (i.e., covariance) provided an excellent correlation with an FEM analysis (Fenton and Griffiths, 2005).

The latter may be expressed as:

$$E_g = \exp\left(\frac{1}{n} \sum_{i=1}^4 \ln E_i\right) \quad \text{Eq.3.10}$$

Both the Harmonic and Geometric means were used to estimate the tip resistance,  $q_b$  vs. displacement (Eq.3.5) for all axial centrifuge tests. The results are presented in Figure 4.1.

### 3.2 Lateral Loading in Combination with Axial Loading

The first phase of the research was to conduct lateral load tests in combination with axial loading to obtain moment, shear and tip rotation of the shafts. Variables that were used include: rock strength (10 tsf and 30 tsf), diameter (6 ft and 9 ft) and embedment ratio (L/D ratio of 1 and 3). Based on the latter tests, tip shear and rotation models were developed. A discussion on how the data reduction was performed is presented in the following section.

#### 3.2.1 Lateral Centrifuge Data Reduction

As discussed earlier, instrumentation was used to assess the lateral load and displacements at the top of shaft. The strain gage output was found by:

$$\varepsilon = \frac{4 \times \Delta V}{G \times E} \quad \text{Eq.3.11}$$

Where,  $\varepsilon$  is the strain (inches per inch)

$\Delta V$  is the change in bridge output voltage (mV)

G is the gage factor (2.05)

E is bridge excitation voltage (10 V)

It was assumed that the relationship between strain gage resistance and voltage, i.e., Eq.3.11 was linear. Figure 3.9 shows a typical output voltage from the strain gages located at the rock surface for the entire loading sequence (i.e., axial and subsequent axial with lateral). As

expected, from 0 to 600 seconds, the individual gages on each side of the shaft indicated no bending since only an axial load was being applied. However after 600 seconds when the lateral load was applied the gage values diverged. A positive output voltage indicates tension and negative voltage, compression. Note that the voltage relationship is linear with the first application of the lateral load, but then becomes non-linear due to concrete cracking.

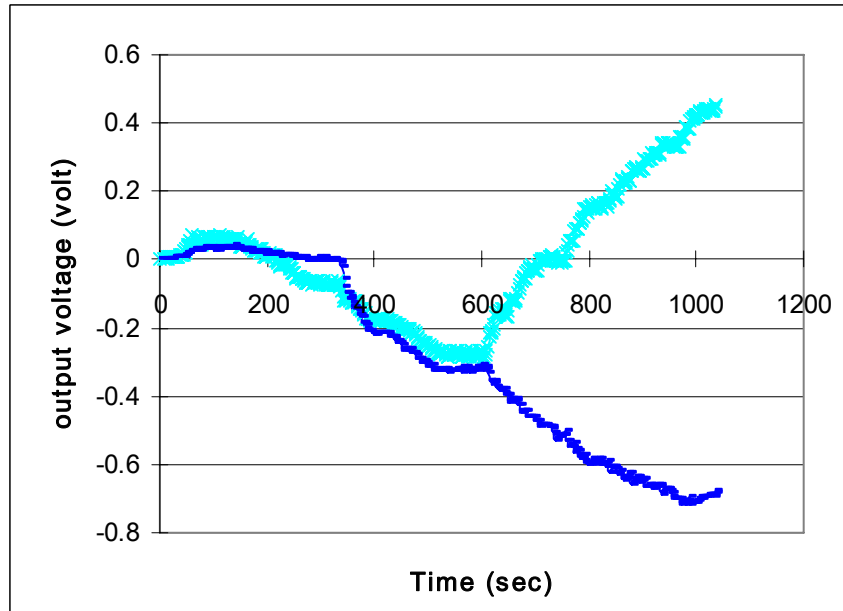


Figure 3.9 Output Voltage from Gages vs. Time

At each strain gage elevation, the bending strain may be computed from the gage values on each side of the shaft as:

$$\varepsilon_b = \frac{\varepsilon_{left} - \varepsilon_{right}}{2} \quad \text{Eq.3.12}$$

Summing the axial strains (Eq.3.1) and the bending strains will result in the measured strain on each side of the shaft, i.e.,  $\varepsilon_a$  and  $\varepsilon_b$  as shown in Figure 3.10.

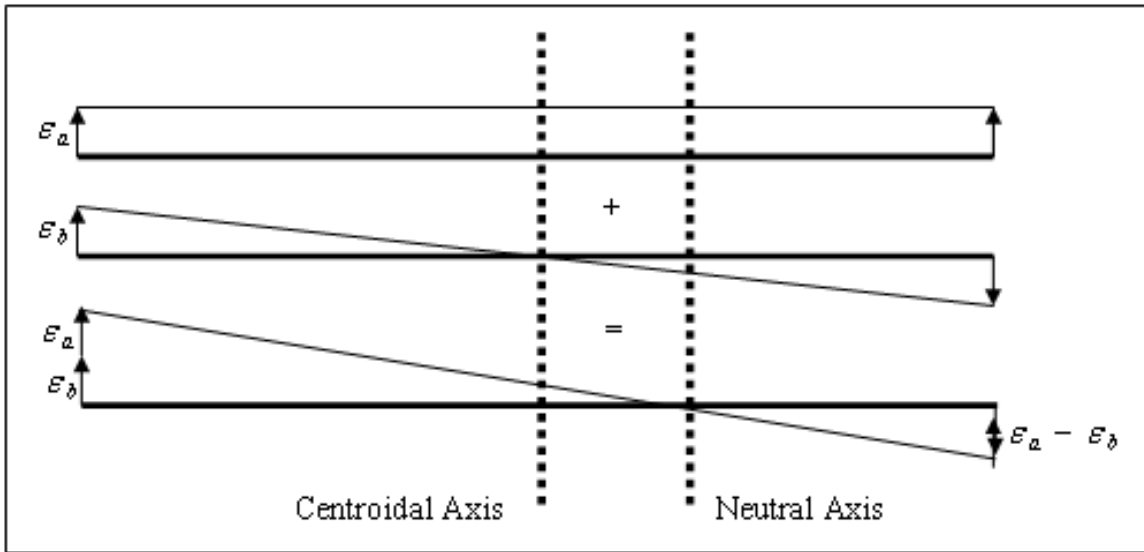


Figure 3.10 Total Axial and Bending Strains along the Shaft Cross-Section

Also of great interest was the moment-curvature relationship of the shaft's cross-section. The latter was used in assessing the moments, shears, rotations and lateral translations of the shaft below the rock surface. That relationship is:

$$M = EI \frac{\epsilon_b}{r} = EI\phi \quad \text{Eq.3.13}$$

where E = Young's Modulus of the shaft

I = Moment of Inertia of cross-section

r = Shaft's radius

$\phi$  = Curvature of the cross-section (i.e., change in rotation)

The moment curvature relationship may be simply expressed as  $M=B\phi$  where B is the nonlinear relationship of EI. The latter may be obtained readily from the strain gage data in the shaft at the rock surface elevation where the moment is readily known (lateral load x height

above rock). The curvature, Eq.3.13 is also obtained from strain gage data. A typical moment-curvature expression is shown in Figure 3.11.

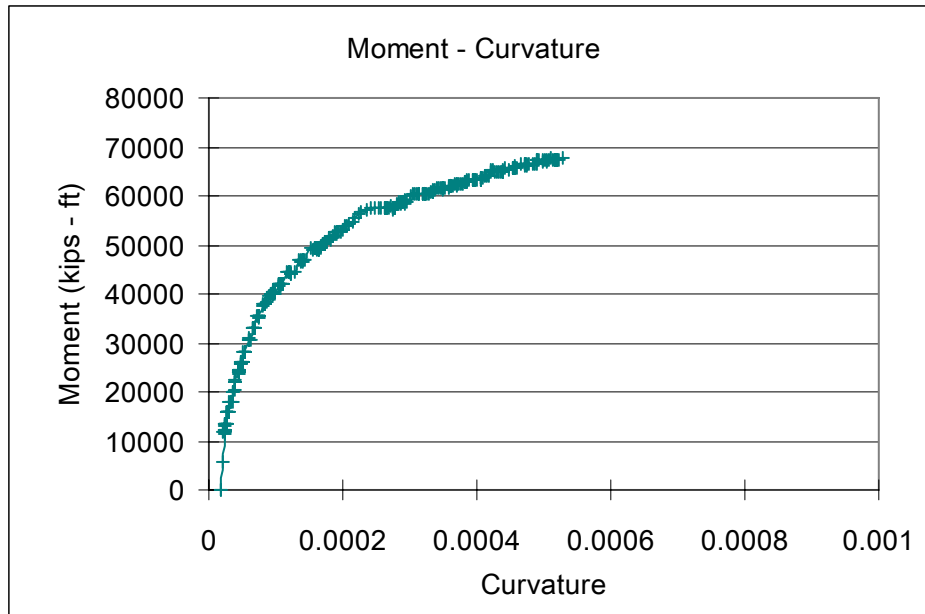


Figure 3.11 Moment-Curvature Relationship for 9 ft Diameter from a Pair of Strain Gages above Rock Surface.

From the moment – curvature relationship, the moment distribution along the length of the shaft may be found from Eq.3.13 by using the bending strains from the gage pairs along the shaft. Figure 3.12 a, b, and c show a number of moment distribution curves along the length of the shafts under multiple lateral loading states.

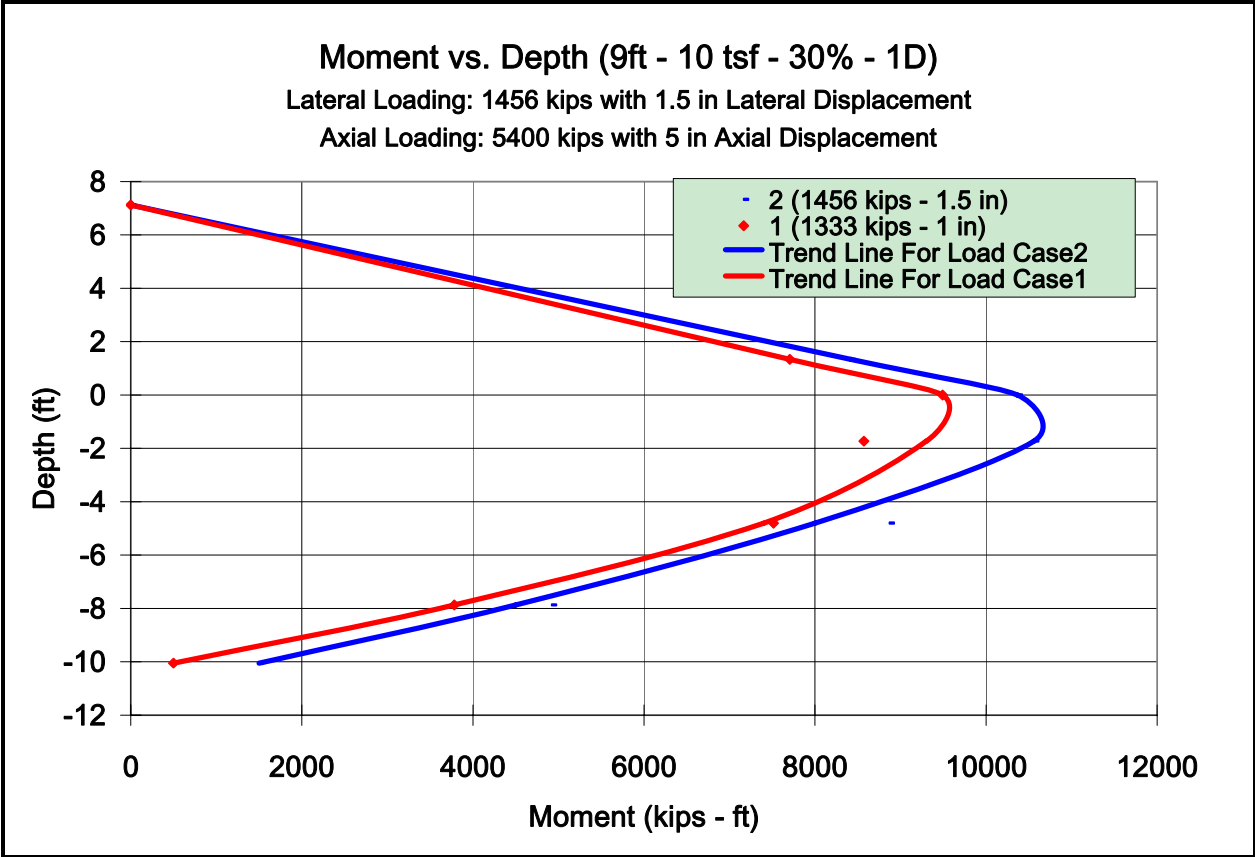


Figure 3.12a Moment Distribution along a 9 ft Diameter, 30% Styrofoam at 1D below Tip of Shaft in 10 tsf Limestone

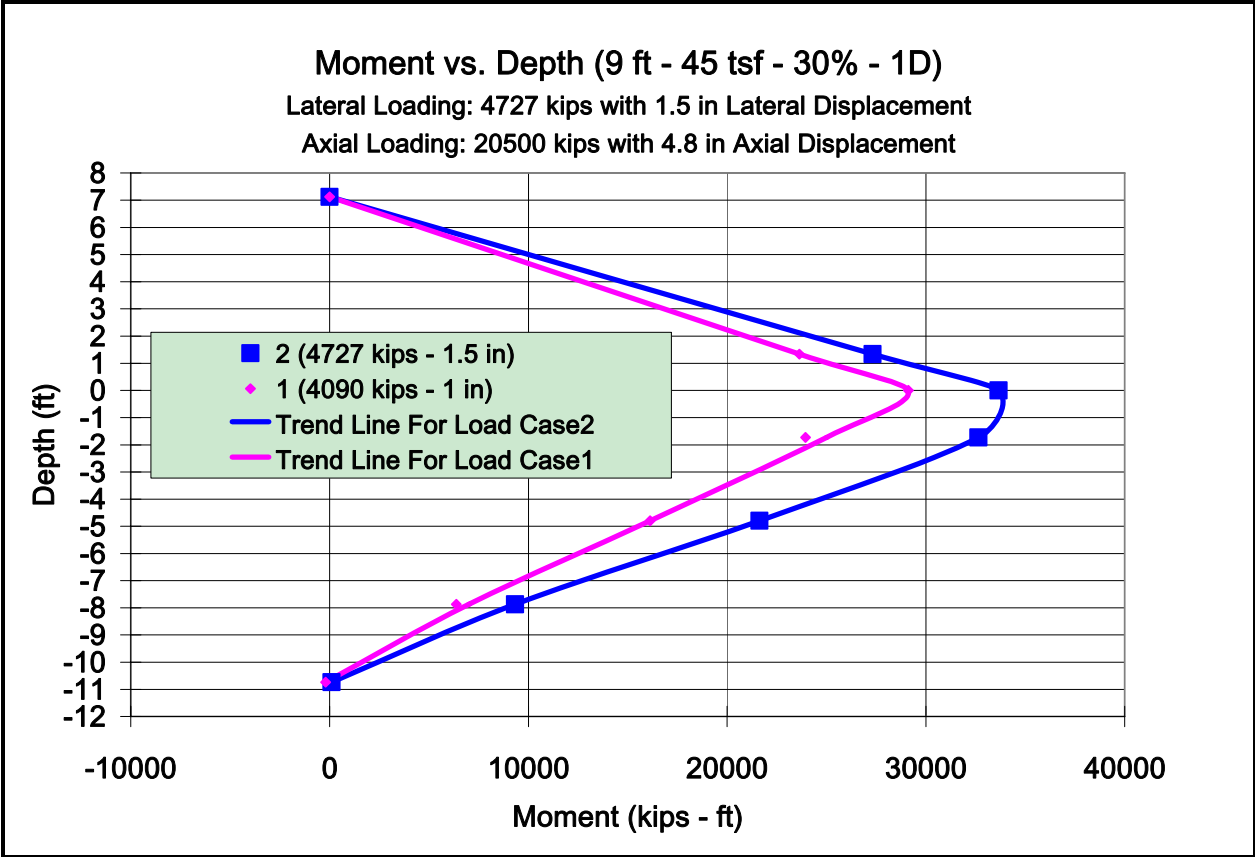


Figure 3.12b Moment Distribution along a 9 ft Diameter, 30% Styrofoam at 1D below Tip of Shaft in 45 tsf Limestone

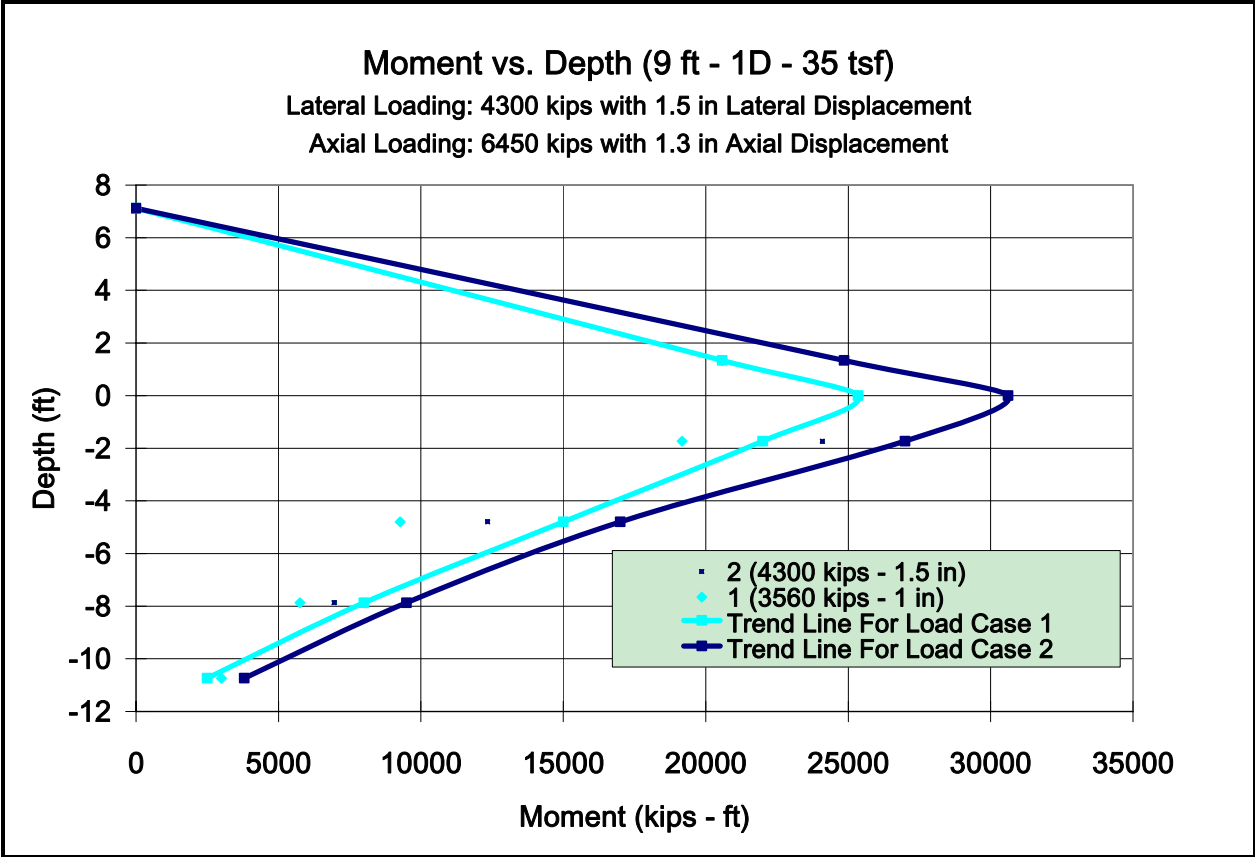


Figure 3.12c Moment Distribution along 9 ft Shaft without Styrofoam below Tip in 35 tsf Rock

From a study of Figure 3.12, the moment distribution along the shaft starts at zero at the top and increases linearly down to the rock surface (i.e., maximum moment) whereupon it starts to decrease due to the rock’s resistance. The moment at the tip is a function of shaft length and rock strength.

After the moment distribution along the shaft is found, the shear distribution within the shaft may be readily determined from:

$$V = \frac{dM}{dz} \tag{Eq.3.14}$$

Shown in Figure 3.13 is the increase in shear with increased lateral loading. The axial load is maintained at approximately 80% of the ultimate capacity. The rock had an unconfined compressive strength of 11 tsf, and the shaft was 9 ft in diameter and embedded 9 ft in the rock ( $L/D = 1$ ). The shear at the bottom of the shaft represents the tip shear and is the force transferred to the rock at the bottom. From the Figure it is evident that the tip shear transfer increases with lateral load due to increased lateral displacement, suggesting a model which mobilizes tip shear based on tip lateral deformation.

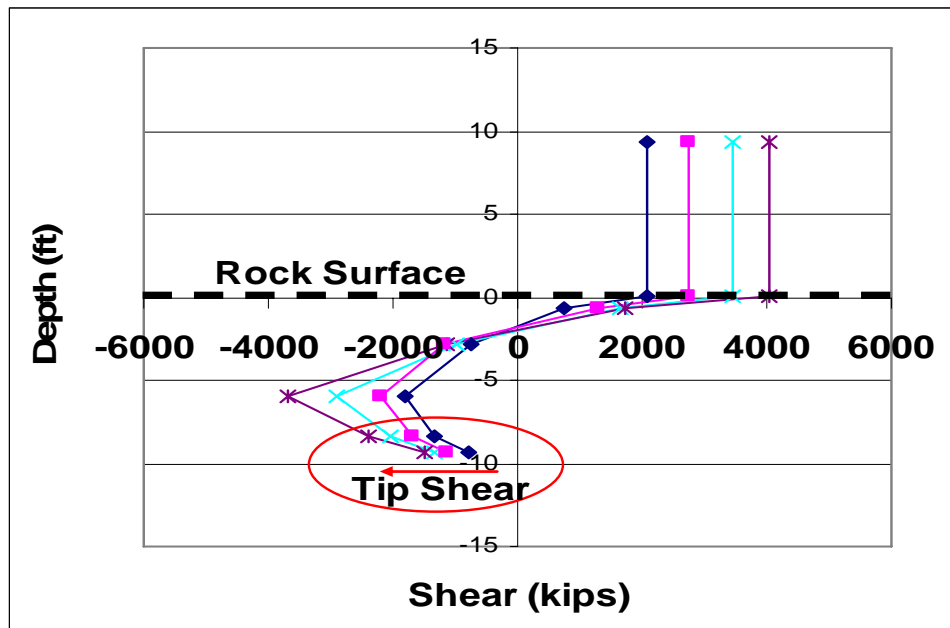


Figure 3.13 Increase in Tip Shear with Increasing Lateral Load,  $L/D = 1$

Increasing the rock strength ( $q_u = 35$  tsf vs. 11 tsf) increases the available tip shear for comparable deformations. The results are shown in Figure 3.14. Both tests involved 9 foot diameter shafts embedded 9 feet into limestone under constant axial and varying lateral loads. Shown in the Figure is the shear distribution in the shafts under the same lateral top displacements. Note that failure occurred at 5% of the shaft's diameter or 5.4 inches.

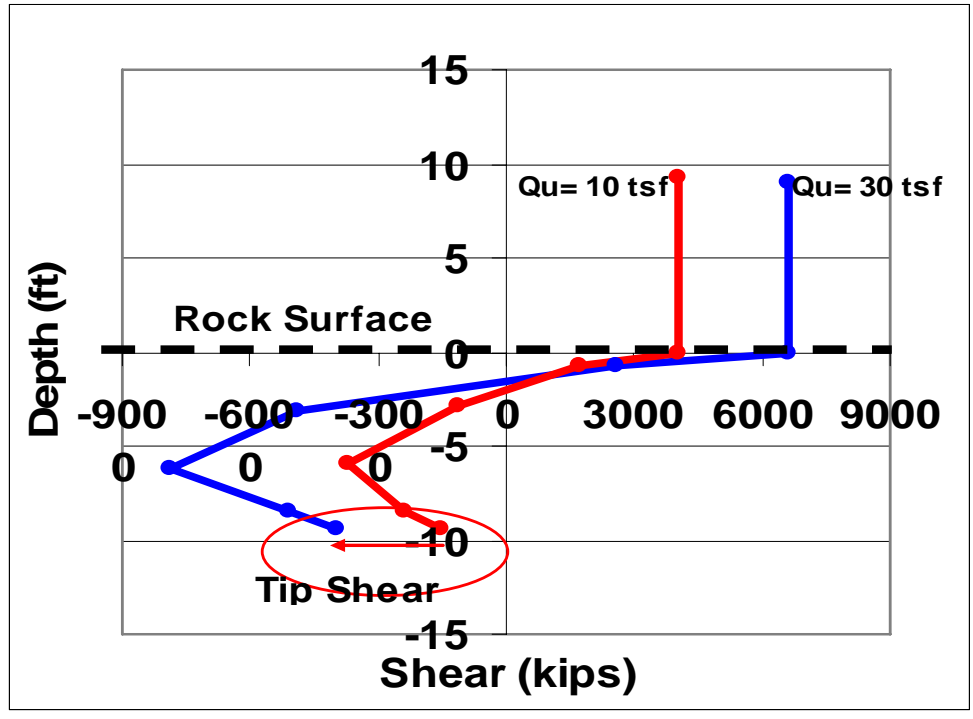


Figure 3.14 Increasing Tip Shear with Increasing Rock Strength

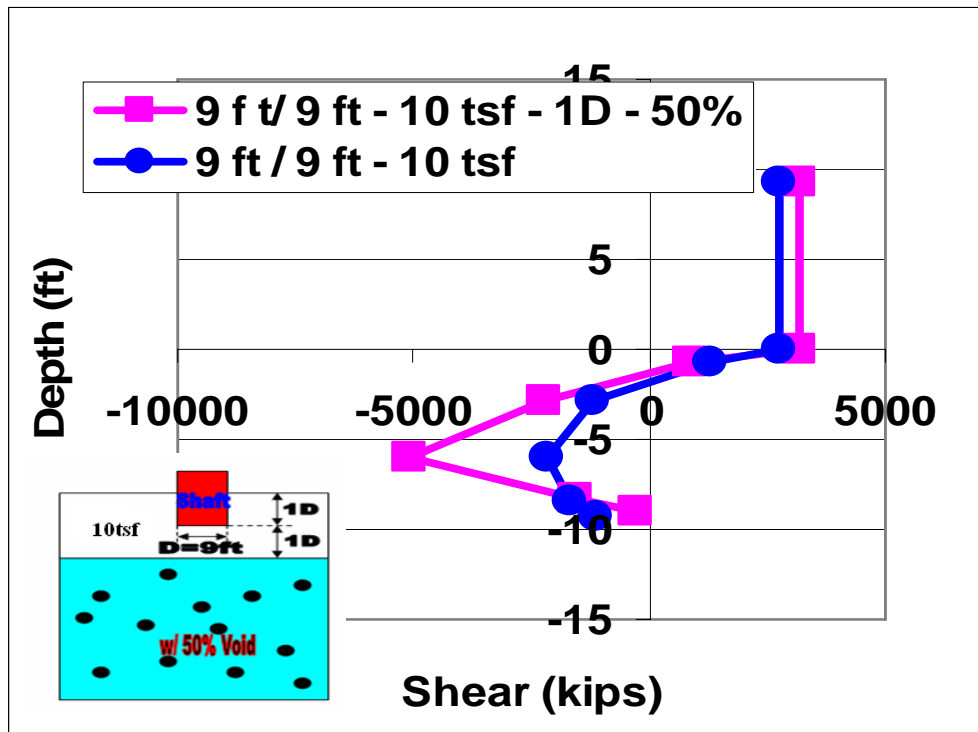


Figure 3.15 Shaft Shear at Failure with and without an Underlying Soft Layer

Shown in Figure 3.15 is the influence of a soft limestone layer (i.e., 50 % voids) one diameter below the tip of the shaft in 10 tsf strength rock. This is reflected by the shear crossing the axis (i.e., zero shear or lateral resistance) as well as the shear distribution along the length of the shaft as it reduces at the shaft's tip.

In order to develop a tip shear model, the lateral translation of shaft tip was necessary. This was accomplished by evaluating the lateral displacement and rotation along the entire length of the shaft. The procedure used is as follows:

1. Choose a depth along shaft as shown Figure 3.16a;
2. From the Moment trend line, assess the moment from the selected depth;
3. With the known Moment, go to the Moment-Curvature relationship, 3.16b, to obtain the curvature (i.e., change in slope);
4. Repeat steps 1 through 3 for several points along the shaft making sure the tip is also selected;
5. Identify where there is zero lateral translation of the shaft, i.e.,  $y = 0$ , by checking for zero lateral resistance, i.e.,  $P = dV/dX = 0$  in Figure 3.17
6. From the curvature, the rotation at the top of shaft ( $\theta$ ) is found;

$$\Delta\theta = \frac{\varepsilon_{bt} + \varepsilon_{bb}}{2r} \times L \quad \text{Eq.3.15}$$

where,  $\varepsilon_{bt}$  and  $\varepsilon_{bb}$  are the bending strains at the top and bottom of each segment respectively,  $r$  is the shaft radius and  $L$  is the segment length;

7. Using the latter estimate of  $\theta$ , the segment rotations,  $\Delta\theta$  at each point are obtained along the shaft (i.e.,  $\theta_2 = \theta_1 - \Delta\theta_1$ ,  $\theta_3 = \theta_2 - \Delta\theta_2$ , etc.)

8. The computed  $\theta_i$  (step 7) at each point represents the slope of the deflected shape at their respective positions ( $dy/dz_i = \theta_i$ ). Thus, the lateral displacement at each point can be calculated using  $dy = \theta_i * dz_i$ .
9. Steps 5 to 9 were repeated until the line passed through or was very close to the point of zero deflection and  $P = 0$ .
10. After shaft rotations and displacements are assessed for the top half of the shaft, i.e., above  $y = 0$ , the bottom half of the shaft values are determined, especially for the shaft tip.

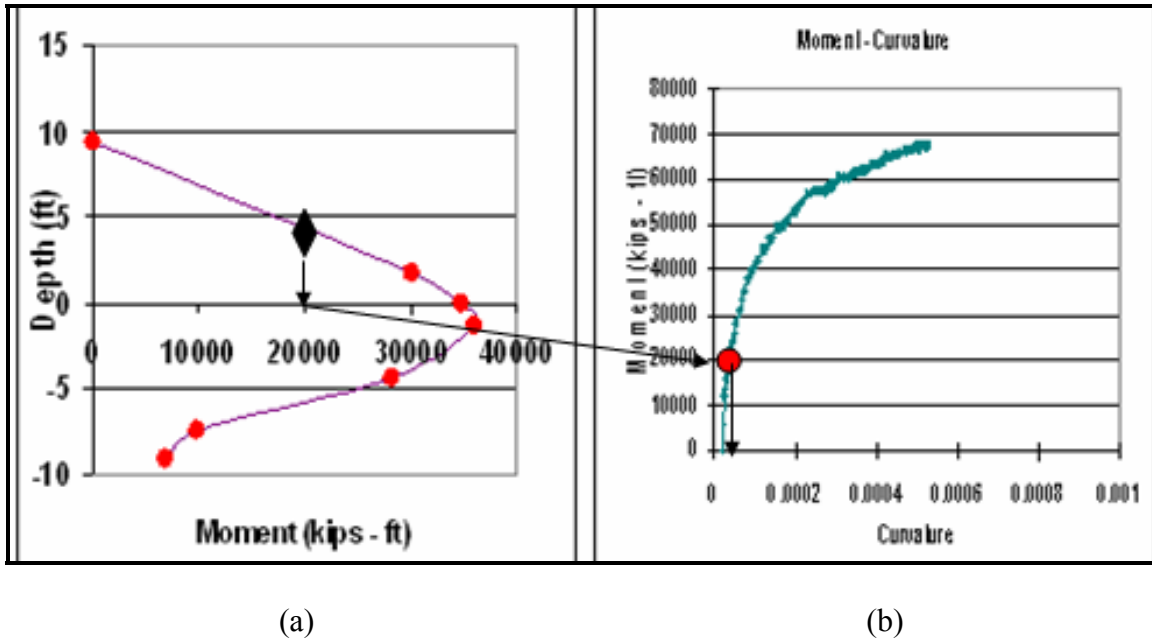


Figure 3.16 Assessing Rotation from the Moment-Curvature Relationship  
 (a) Moment versus Depth (b) Moment - Curvature Relationship

Shown in Figure 3.17 is a typical displacement vs. depth for a shaft using this method. The next chapter presents the shear versus tip displacement for all tests conducted and presents the proposed shear tip model.

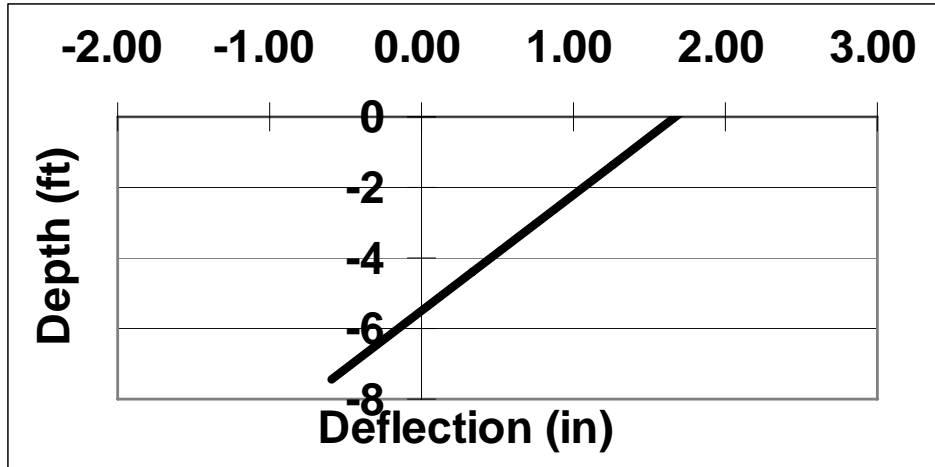


Figure 3.17 Typical Lateral Deflections (y) vs. Depth

## CHAPTER 4 MEASURED VERSUS PREDICTED SHAFT TIP RESPONSE

The focus of this research was to validate or develop reliable methods to predict the axial, shear, and moment response of a drilled shaft tip founded in Florida limestone under combined axial and lateral loads. A number of models to characterize tip response were investigated (e.g., O'Neill, Bell, Doherty, Ueshita, etc.). Some had been developed specifically for rock (O'Neill), while others were applicable for general elastic materials (e.g., Bell, & Doherty). However, none had tested Florida limestone with its associated variability (see Chapters 5 and 6). For the lateral tip shear response, the work focused on extending the existing FDOT side friction model (McVay 1992) to account for normal stress and shaft diameter. A discussion of axial loading is presented next, followed by shear and then moment computations. This sequence was followed because shear results use axial data and moment results require shear resistance).

### **4.1 Axial Test Results**

Figures 4.1a through 4.1j show the measured axial tip response for all shafts founded in 10 tsf and 30 tsf strength rock with and without layering. Also shown in each Figure is the predicted axial tip response using O'Neill's (Eqs. 3.5 to 3.8) model incorporating either the harmonic mean modulus,  $E_m$ , or geometric mean modulus,  $E_g$ . Analysis of Figures 4.1a through 4.1j reveals that both the harmonic and geometric modulus in combination with the O'Neill's tip resistance model shows good agreement with the experimental response. Since the geometric modulus,  $E_g$ , gave slightly better results, it was used in the LRFD resistance assessment.

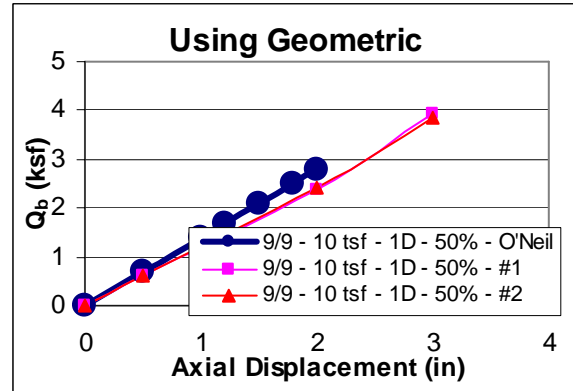
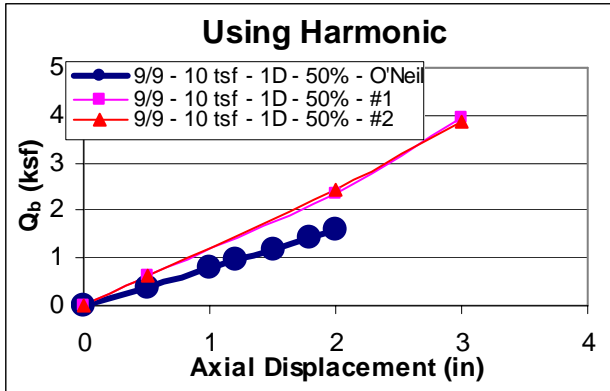


Figure 4.1a Tip Resistance (Model vs.O'Neill's Equation with Harmonic Average Method (left) and Geometric Average Method (right) for 10 tsf Rock with 50% Recovery at 1D

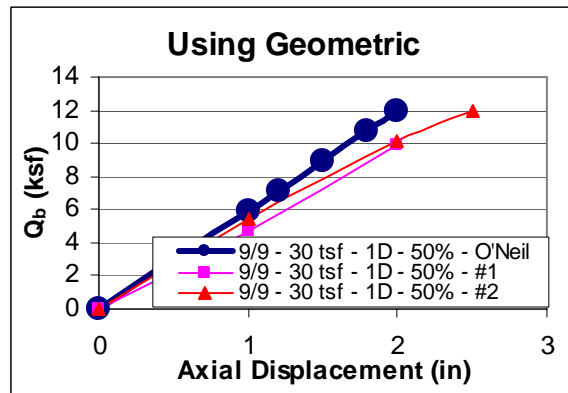
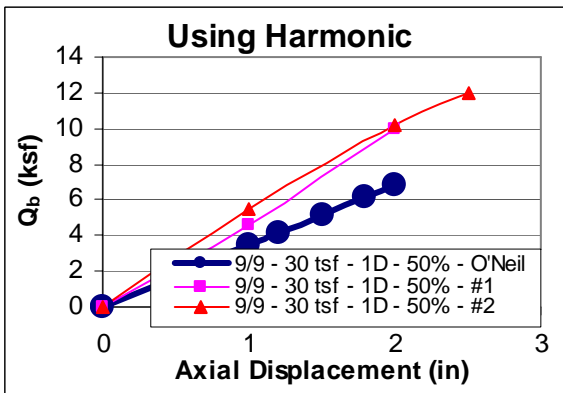


Figure 4.1b Tip Resistance (Model vs.O'Neill's Equation with Harmonic Average Method (left) and Geometric Average Method (right) for 30 tsf Rock with 50% Recovery at 1D

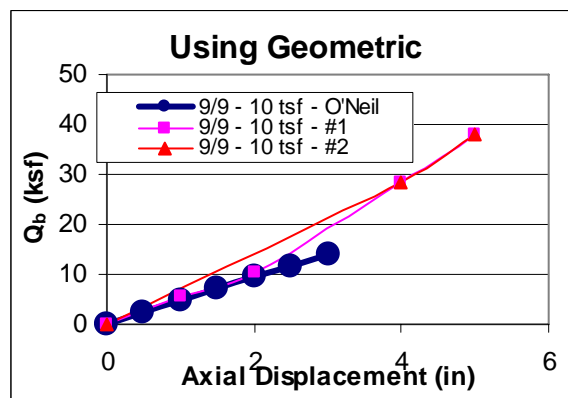
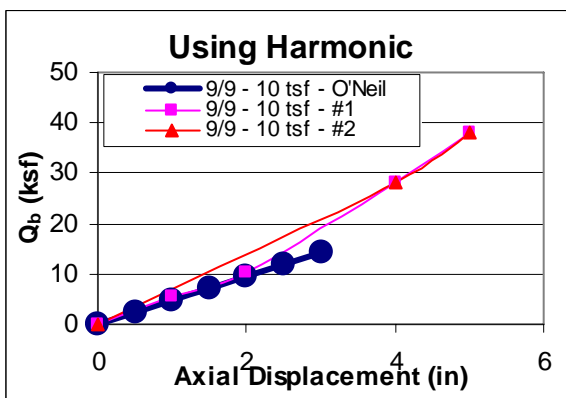


Figure 4.1c Tip Resistance (Model vs. O'Neill's Equation) with Harmonic Average Method (left) and Geometric Average Method (right) for 9 ft / 9 ft - 10 tsf Rock

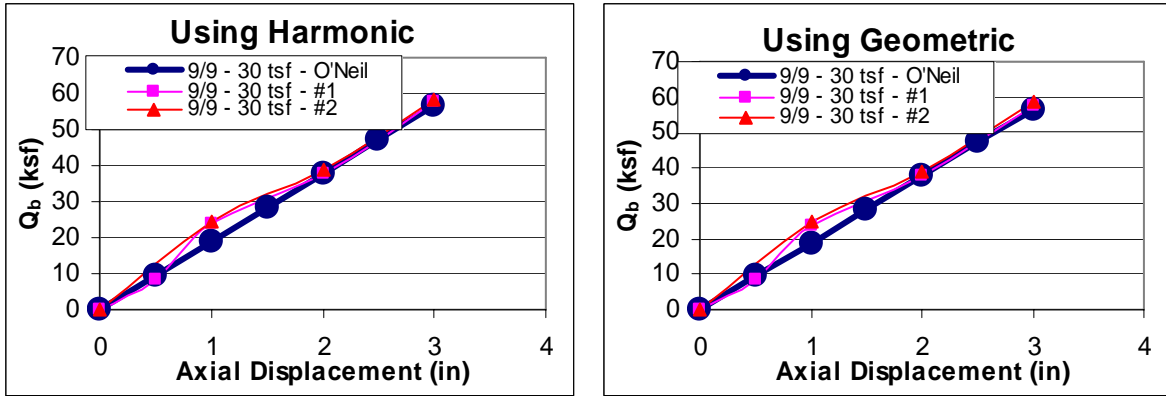


Figure 4.1d Tip Resistance (Model vs. O'Neill's Equation with Harmonic Average Method (left) and Geometric Average Method (right) for 9 ft / 9 ft - 30 tsf Rock

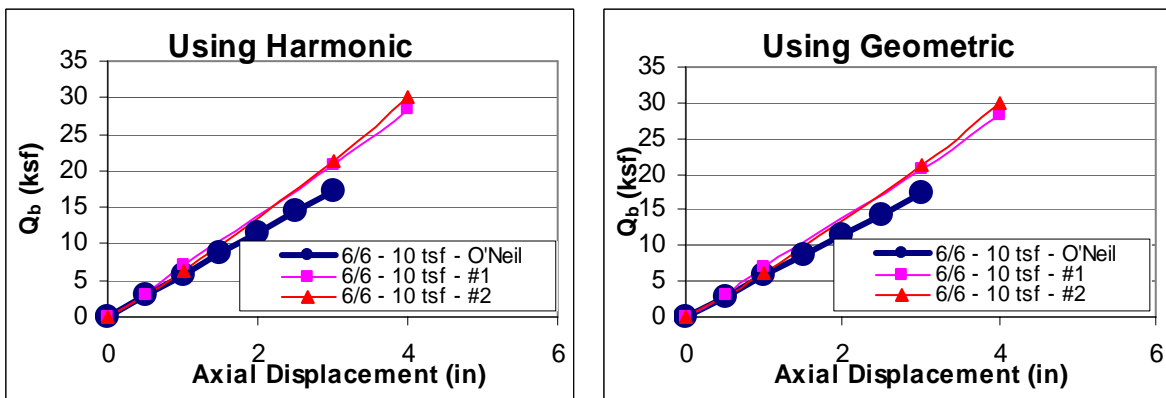


Figure 4.1e Tip Resistance (Model vs. O'Neill's Equation) with Harmonic Average Method (left) and Geometric Average Method (right) for 6 ft / 6 ft - 10 tsf Rock

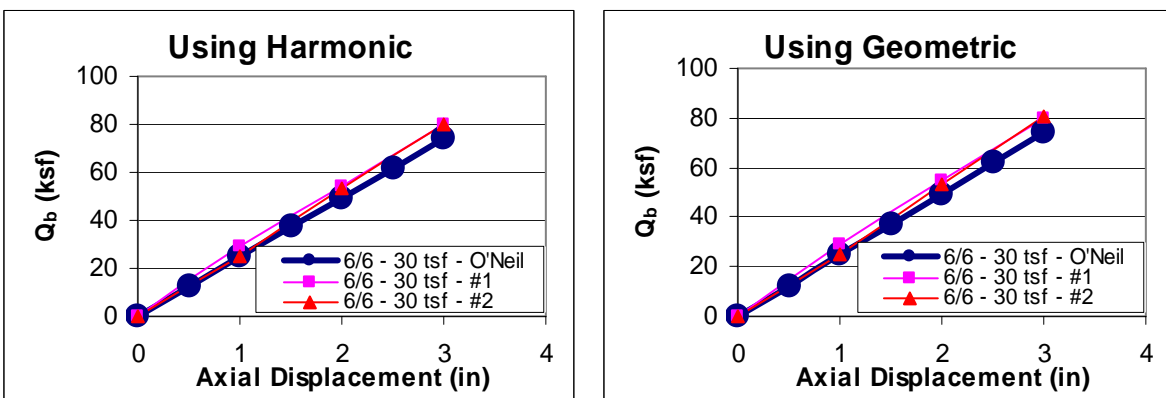


Figure 4.1f Tip Resistance (Model vs. O'Neill's Equation) with Harmonic Average Method (left) and Geometric Average Method (right) for 6 ft / 6 ft - 30 tsf Rock

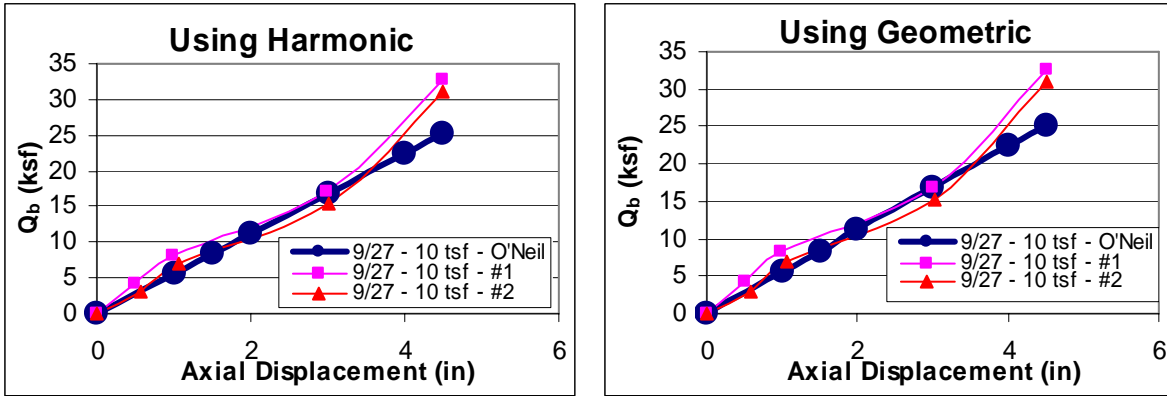


Figure 4.1g Tip Resistance (Model vs. O'Neil's Equation) with Harmonic Average Method (left) and Geometric Average Method (right) for 9ft / 27 ft -10 tsf Rock

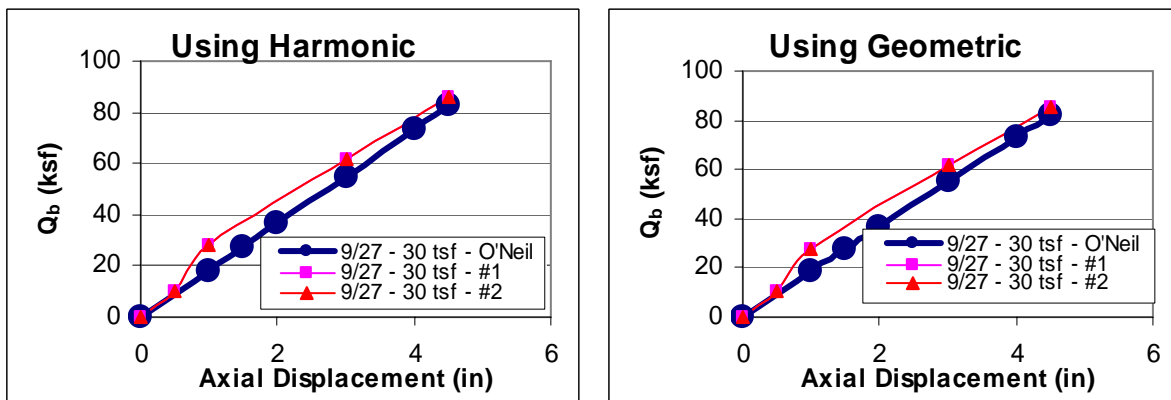


Figure 4.1h Tip Tip Resistance (Model vs. O'Neil's Equation) with Harmonic Average Method (left) and Geometric Average Method (right) for 9ft / 27 ft -30 tsf Rock

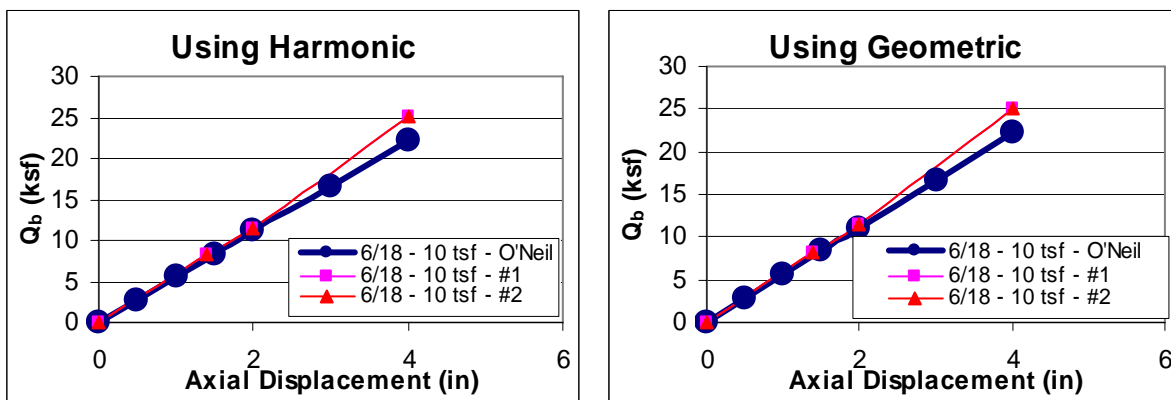


Figure 4.1i Tip Resistance (Model vs. O'Neil's Equation) with Harmonic Average Method (left) and Geometric Average Method (right) for 6 ft / 18 ft -10 tsf Rock

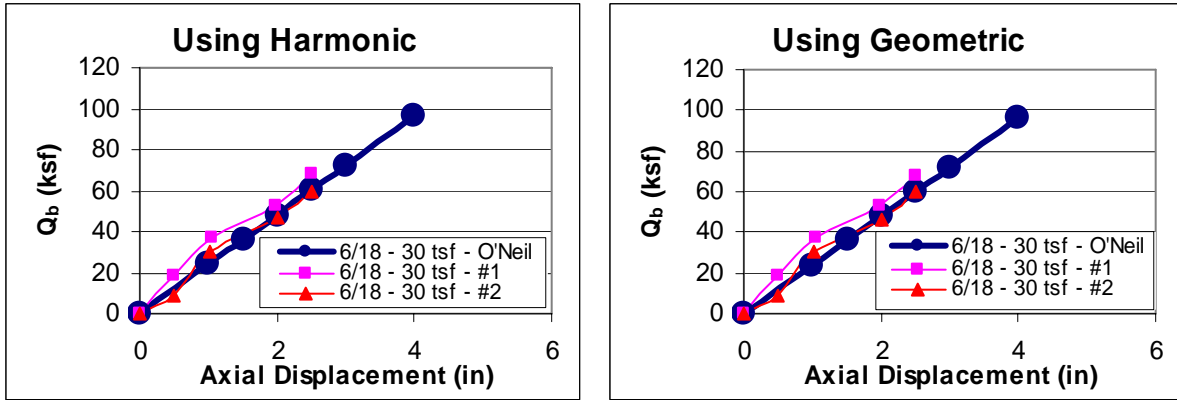


Figure 4.1j Tip Resistance (Model vs. O’Neill’s Equation) with Harmonic Average Method (left) and Geometric Average Method (right) for 6ft / 18ft - 30 tsf Rock

#### 4.2 Lateral Test Result - Tip Shear Model

Figures 4.2 and 4.3 show the measured mobilized shear stress versus tip lateral displacement for all centrifuge tests. Figure 4.2 identifies the lower strength (10 tsf) response and Figure 4.3 the higher (30 tsf) strength rock results. Also included in each Figure (Red Lines/Diamonds Dots) are the results for the layered system, i.e., 50% recovery rock located one diameter below the tip of the shafts.

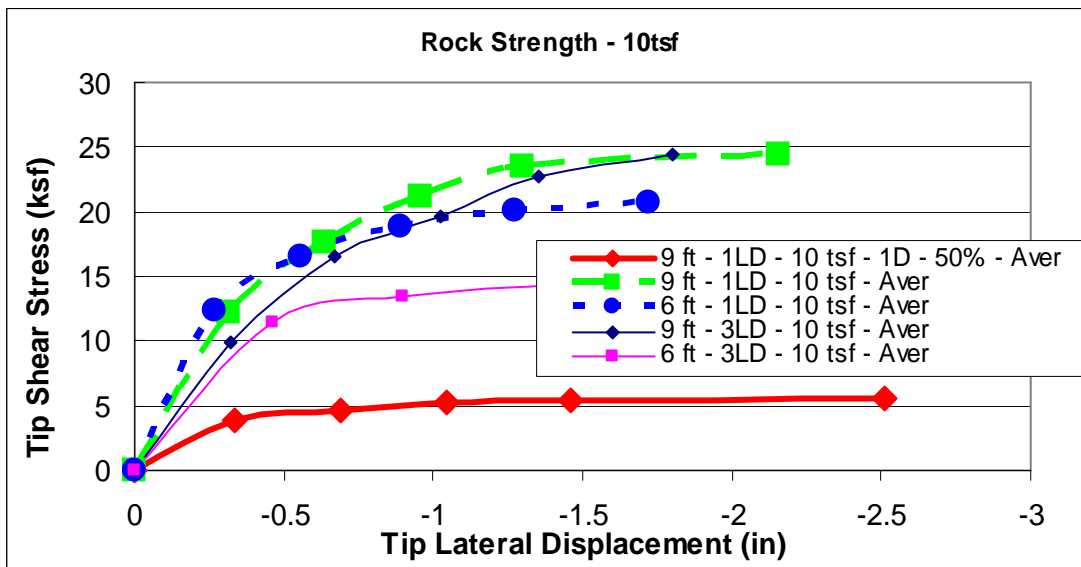


Figure 4.2 Tip Shear Stress vs. Tip Lateral Displacement

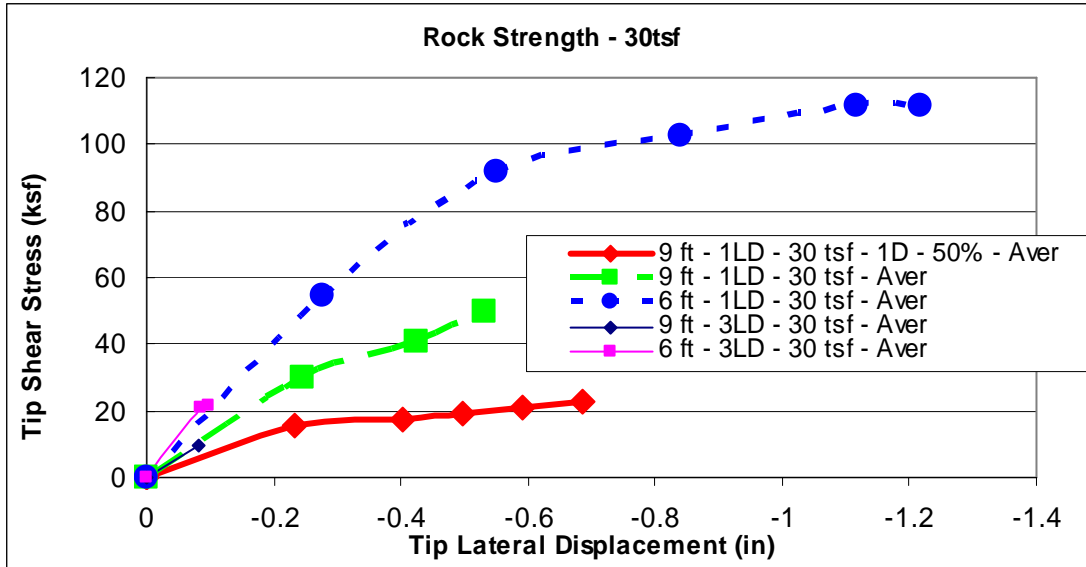


Figure 4.3 Tip Shear Stress vs. Tip Lateral Displacement

As expected, the higher strength rock developed the higher tip shear resistance per unit of lateral tip displacement. Also, the response for the 9 foot shaft was similar to the 6 foot shafts. However, what was not expected was the significantly diminished resistance for the shafts with 50 % recovery located one diameter below the shaft tip. Evidently, the more compressible voided zone resulted in smaller moments developing at the shaft tip, which in turn required larger moments in the overlying rock to resist the applied lateral load. Figures 4.4 and 4.5 show a one to one comparison of the shears and moments with and without the underlying softer (voided) layer. The influence on tip compressibility is shown in Table 4.1 for layered and non-layered systems. Also shown in the table is the influence of rock strength.

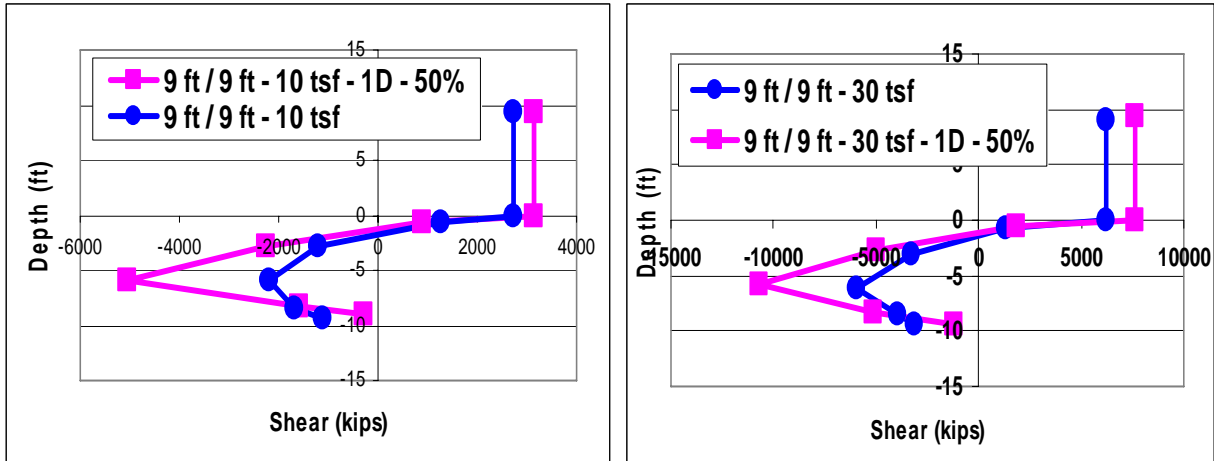


Figure 4.4 Shear in Shafts vs. Depth with and without Underlying Softer Layer

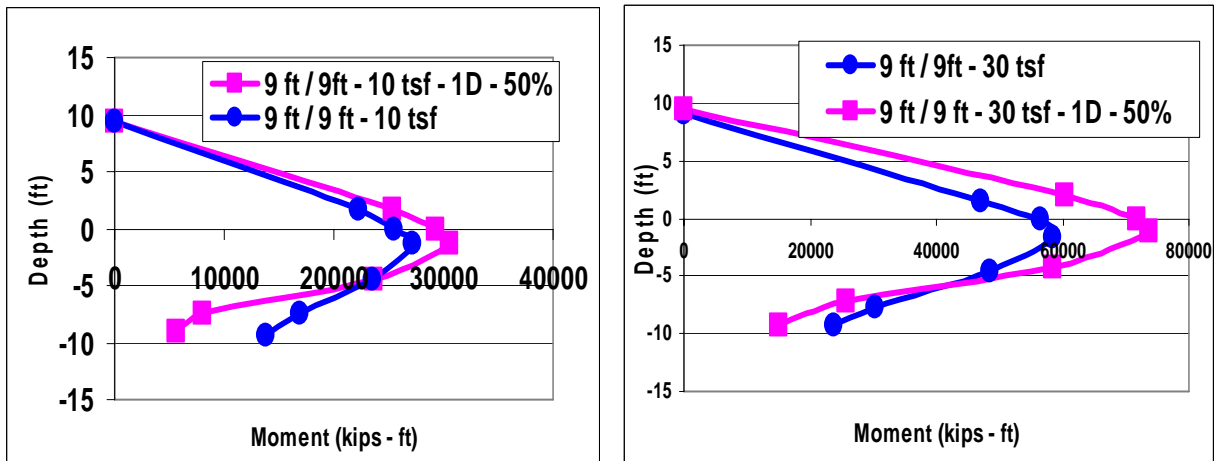


Figure 4.5 Moment in Shafts vs. Depth with and without Underlying Softer Layer

Table 4.1 Comparison of Axial Tip Stresses

		Translated Axial Stress (ksf)
Layered	9 ft / 9 ft - 10 tsf - 1D - 50%	3
Non-Layered	9 ft / 9 ft - 10 tsf	38
Layered	9 ft / 9 ft - 30 tsf - 1D - 50%	12
Non-Layered	9 ft / 9 ft - 30 tsf	60
	9 ft / 27 ft - 10 tsf	32
	9 ft / 27 ft - 30 tsf	82
	6 ft / 18 ft - 10 tsf	25
	6 ft / 18 ft - 30 tsf	60

To develop a tip shear model, the influence of rock strength and normal stress must be taken into account. Shown in Figures 4.6 and 4.7 are the mobilized shear stress minus the rock's strength divided by the mobilized tip resistance versus normalized lateral tip displacement.

Figure 4.6 shows the 10 tsf rock and Figure 4.7, the 30 tsf rock.

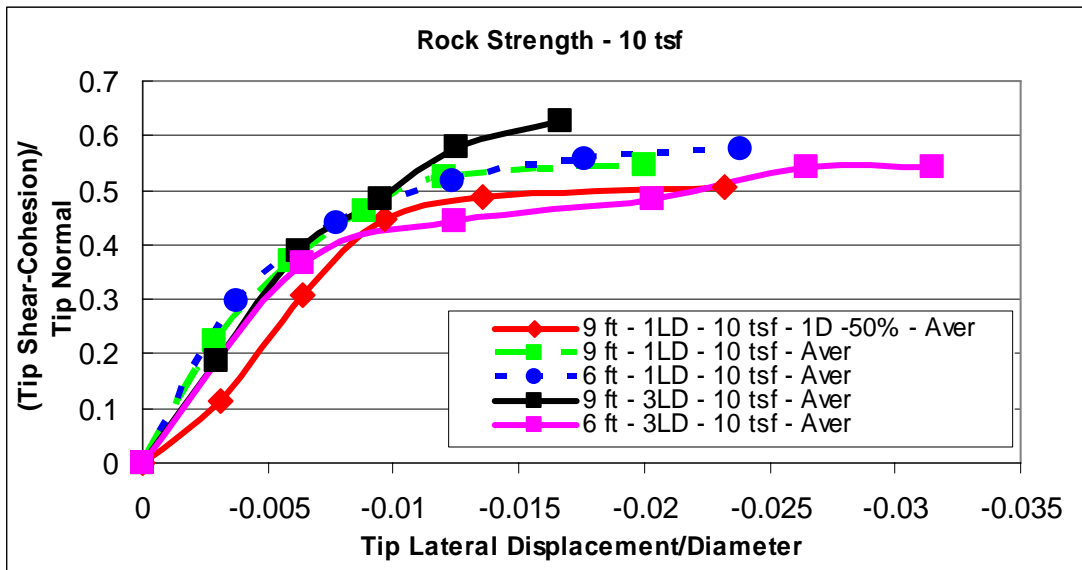


Figure 4.6 Tip Shear Minus Rock Strength Divided by Normal Tip Stress vs. Normalized Lateral Displacement

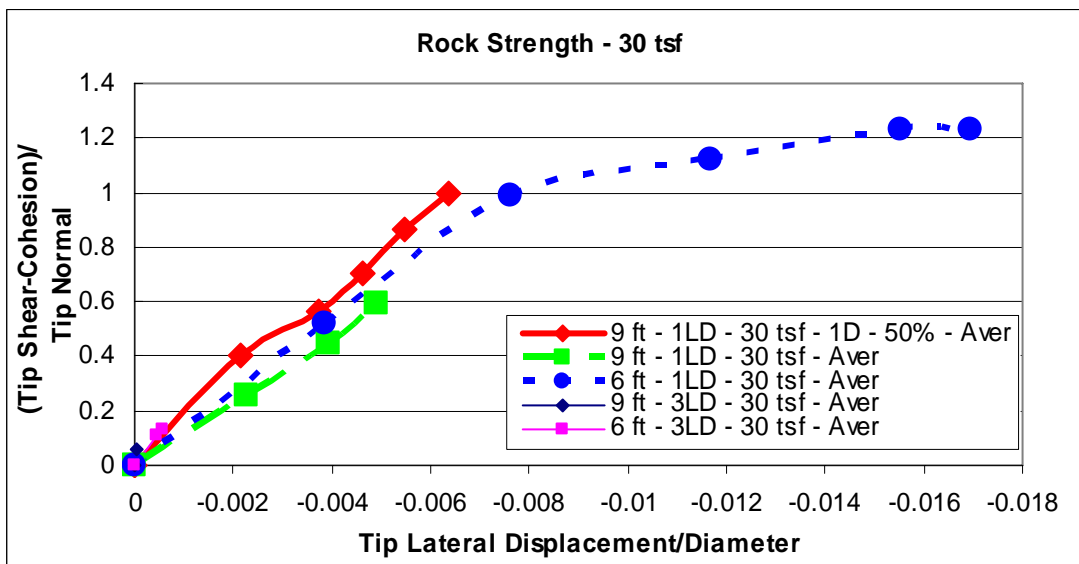


Figure 4.7 Tip Shear minus Rock Strength Divided by Normal Tip Stress vs. Normalized Lateral Displacement

Each plot may be characterized by a bilinear representation, i.e., a linear increasing line, followed by a horizontal or constant line. The linear portion represents the mobilization of tip shear versus normalized lateral tip displacement. The horizontal or maximum value (i.e., 0.55 for 10 tsf rock, and 1.0 for 30 tsf) represents the failure state as shown in Figure 4.8.

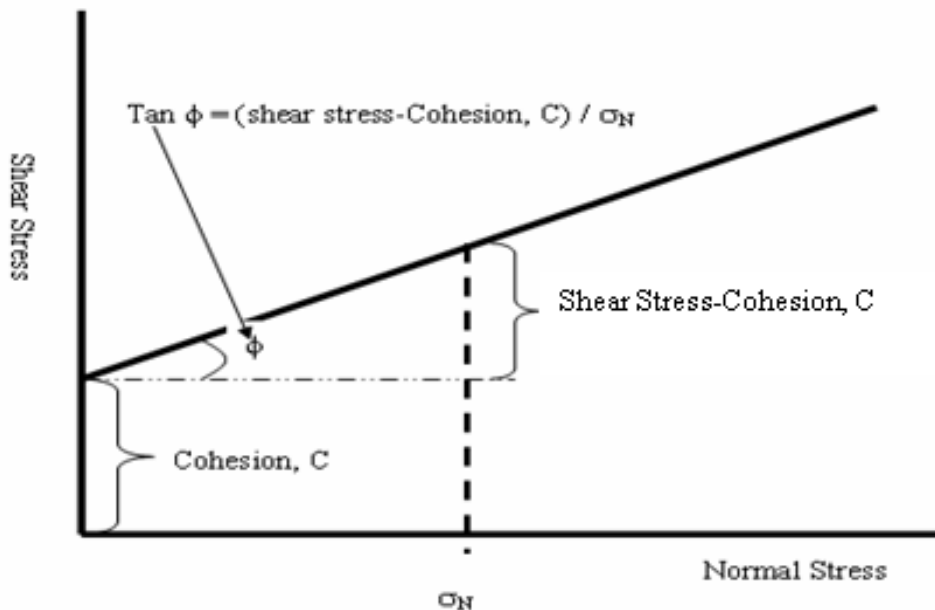


Figure 4.8 Mohr-Coulomb Strength of Florida limestone

Consequently, the failure states represent the shear stresses within the Mohr-Coulomb limit state. That is to say, they are represented by angles of internal friction of 28 and 45 degrees respectively.

The generalized shear model for shaft tip is shown in Figures 4.9 a and b. It is characteristic of an elastic-plastic behavior model. To use the model in a finite element code such as FB-MultiPier, one would do the following:

1. Depending on the strength of the rock, the lateral spring stiffness (Figure 4.9 a) is assessed from the initial slope of the curve (Figure 4.9 b). If the rock strength is not 10 tsf or 30 tsf, the slope is interpolated (e.g., 20 tsf is halfway between 10 and 30).
2. Next, the finite element solution is obtained for the tip displacements;
3. Knowing the tip displacement, the axial tip stress is computed from O'Neill's solution using the geometric mean,  $E_g$ , modulus;
4. Subsequently, Plot 4.9 b is entered with the known lateral tip displacement, and the mobilized tip shear stress is assessed from the curve along with the normal stress and cohesion of the rock

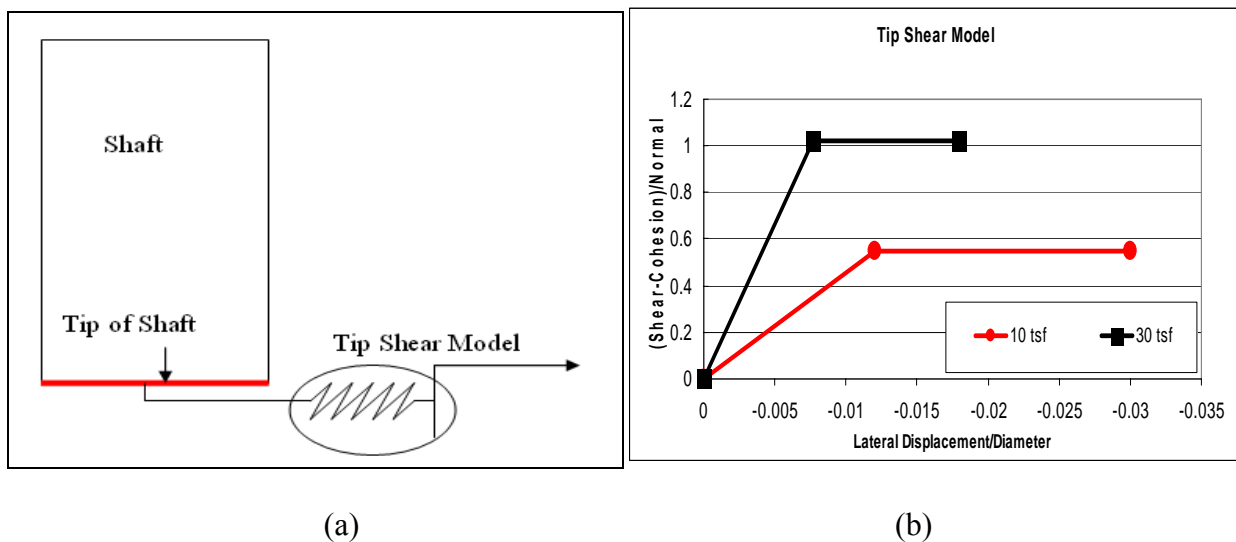


Figure 4.9 Tip Shear Model (a) Tip Shear Model Scheme (b) Tip Shear Model

### 4.3 Lateral Test Results - Moment-Rotation Model

Similar to the tip shear distribution, the moment transfer from the shafts to the underlying rock were plotted versus tip rotation as a function of rock strength, shown in Figures 4.10 and 4.11. Figure 4.10 represents the six and nine foot shaft diameter results in 10 tsf rock while Figure 4.11 shows the same shafts in 30 tsf rock. As expected, the moments for the nine foot

diameter shafts were higher than the six foot shafts due to the greater contact area for similar bending stresses. As discussed earlier, with the lower tip resistance, the layered rock system develops smaller bending stresses due to the lower compressibility modulus.

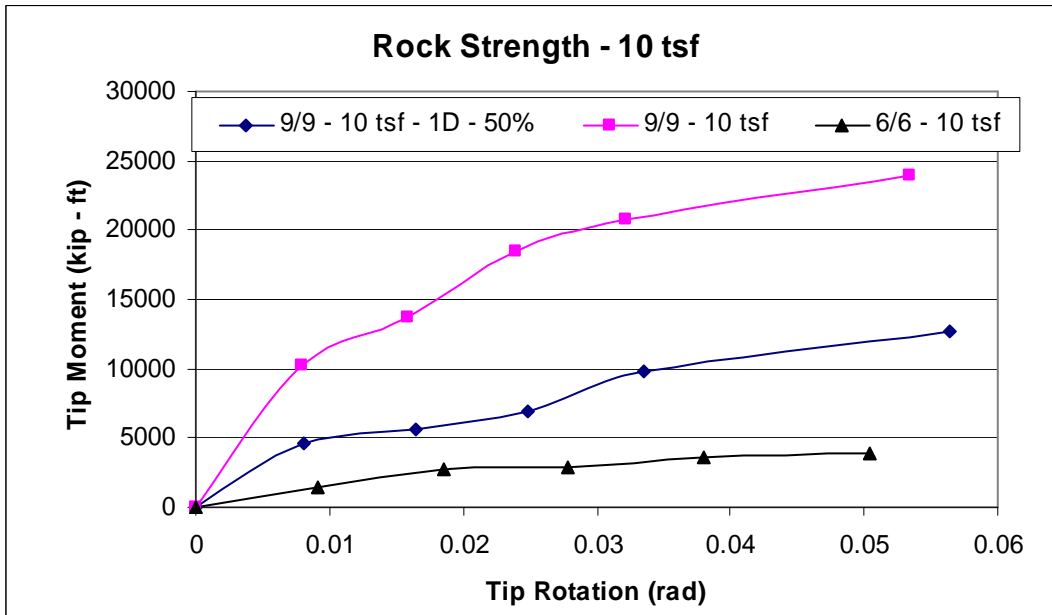


Figure 4.10 Tip Moment Transfer as Function of Tip Rotation

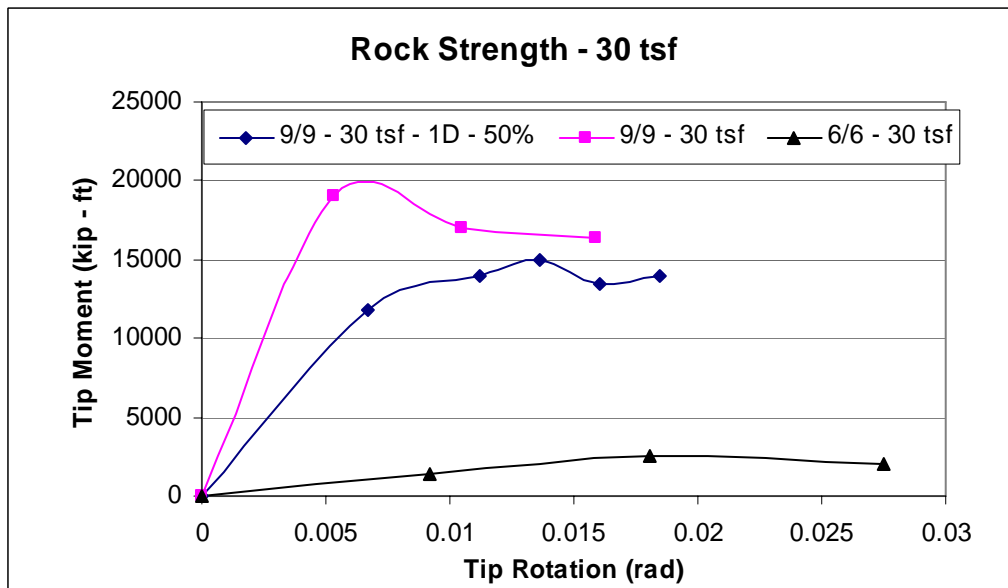


Figure 4.11 Tip Moment Transfer as Function of Tip Rotation

The first reported work on embedded piles in an elastic half space subjected to both lateral tip displacement and rotation was reported by Bell (1991). He performed hundreds of finite element analyses and developed a stiffness matrix [K] relating vertical displacement ( $u_v$ ), horizontal displacement ( $u_H$ ) and rotation ( $\theta_M$ ) to vertical load (V), horizontal load (H) and moment (M) as follows:

$$\begin{bmatrix} V/(G \times R^2) \\ H/(G \times R^2) \\ M/(G \times R^2) \end{bmatrix} = \begin{bmatrix} K_1 & 0 & 0 \\ 0 & K_2 & K_4 \\ 0 & K_4 & K_3 \end{bmatrix} \begin{bmatrix} u_v/R \\ u_H/R \\ \theta_M \end{bmatrix} \quad \text{Eq. 4.1}$$

where G is the Shear Modulus under the tip of shaft and R is the radius of shaft

Evident from Eq.4.1 are cross coupling between the horizontal shear, H, and moment. Bell developed the moment and horizontal stiffness terms from footings located at the ground surface with:

$$\begin{aligned} K_4 &= \frac{H}{GR^2\theta_M} \\ K_3 &= \frac{M}{GR^3\theta_M} \end{aligned} \quad \text{Eq. 4.2}$$

For the case of embedded shafts, the stiffness terms are adjusted due to resistance provided by the shaft's sidewall as described in Figure 4.12. The embedded stiffness terms (superscript, z) are expressed in terms of shaft embedment length  $Z_D$  as follows:

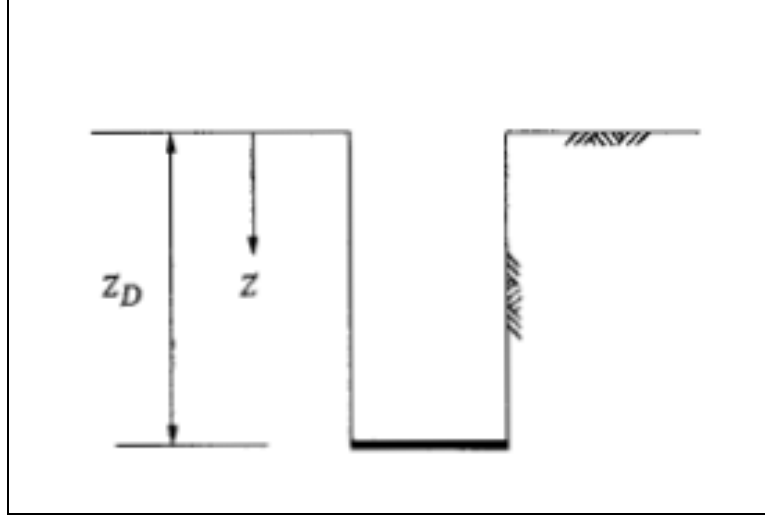


Figure 4.12 Embedded Shaft

$$K_1^z = K_1, K_2^z = K_2, K_4^z = K_4 - K_2 \left( \frac{Z_D}{R} - \frac{Z}{R} \right) \quad \text{Eq. 4.3}$$

$$K_3^z = K_2 \left( \frac{Z_D}{R} - \frac{Z}{R} \right) - 2K_4 \left( \frac{Z_D}{R} - \frac{Z}{R} \right) + K_3$$

Using the metacentre concept, Bell uncoupled the horizontal and moment components by replacing  $K_4^z = 0$  in Eq. 4.3, resulting in an equation for  $Z_m$  as:

$$\frac{Z_m}{R} = \frac{Z_D}{R} - \frac{K_4}{K_2} \quad \text{Eq. 4.4}$$

For the new  $K_3^m$  w/  $K_4^z = 0$ , inserting Eq. 4.4 into Eq. 4.3 for  $K_3^z$  yields:

$$K_3^m = K_2 \left( \frac{Z_D}{R} - \left( \frac{Z_D}{R} - \frac{K_4}{K_2} \right) \right)^2 - 2K_4 \left( \frac{Z_D}{R} - \left( \frac{Z_D}{R} - \frac{K_4}{K_2} \right) \right) + K_3 = K_3 - \frac{K_4^2}{K_2}$$

$$\text{where } K_2 = \frac{H}{GRu_H} \quad \text{Eq. 4.5}$$

Using  $K_3^m$ ,  $\theta_M$  is calculated as:

$$\theta_M = \frac{M}{GR^3 K_3^m} \quad \text{Eq. 4.6}$$

The  $\theta_M$  term is dependent on the horizontal force, horizontal displacement and moment.

Also equations 4.1 to 4.6 are dependent on the shear modulus of the rock. It is assumed that the stress-strain behavior of the rock is linear to failure and Poisson's ratio,  $\mu$ , of the rock is 0.2. Using elastic theory, the shear modulus,  $G$ , was calculated as:

$$G = \frac{E}{2(1 + \mu)} \quad \text{Eq. 4.7}$$

To calculate the shear modulus,  $G$ , in Eq. 4.7, Young's Modulus  $E$ , must be known for the underlying rock. As discussed in Chapter 3, either the harmonic mean modulus,  $E_h$  (Eq. 3.9) or geometric mean modulus,  $E_g$  (Eq. 3.10) may be used. The harmonic mean modulus for both the single and double layered systems was used and the measured versus calculated rotation was assessed for the various rock strengths. Shown in Figure 4.13 are the results for the 10 tsf rock and Figure 4.14, the 30 tsf rock.

It is evident from Figures 4.13 and 4.14, that Bell's representation is quite below the strength of the rock, i.e., within the Mohr-Coulomb strength envelope. The latter occurs at approximately 0.03 radians (Figure 4.13) which wasn't reached in the case of the 30 tsf rock tests. It is important to note that even though the tip rotation,  $\theta$ , was shown as:

$$\theta_{\text{Calculated}} = \frac{M_{\text{measured}}}{GR^3 K_3^m} \quad \text{Eq. 4.8}$$

its stiffness coefficient is not constant, but rather is a function of horizontal loads and displacements as well as moments, as shown in Eq.4.1.

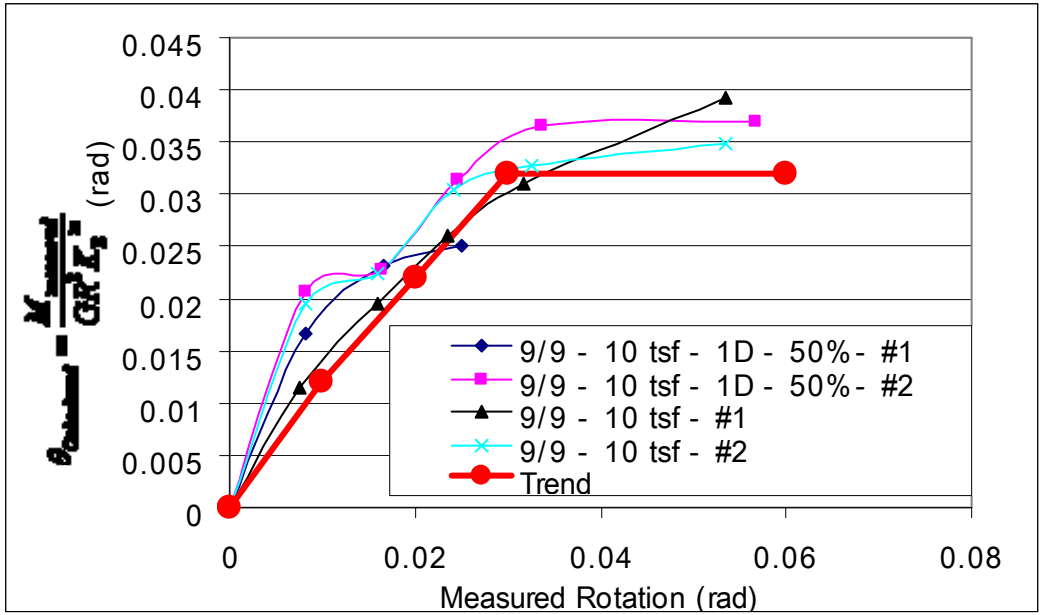


Figure 4.13 Calculated vs. Measured Rotation using Bell (1991) - Trend line is in red

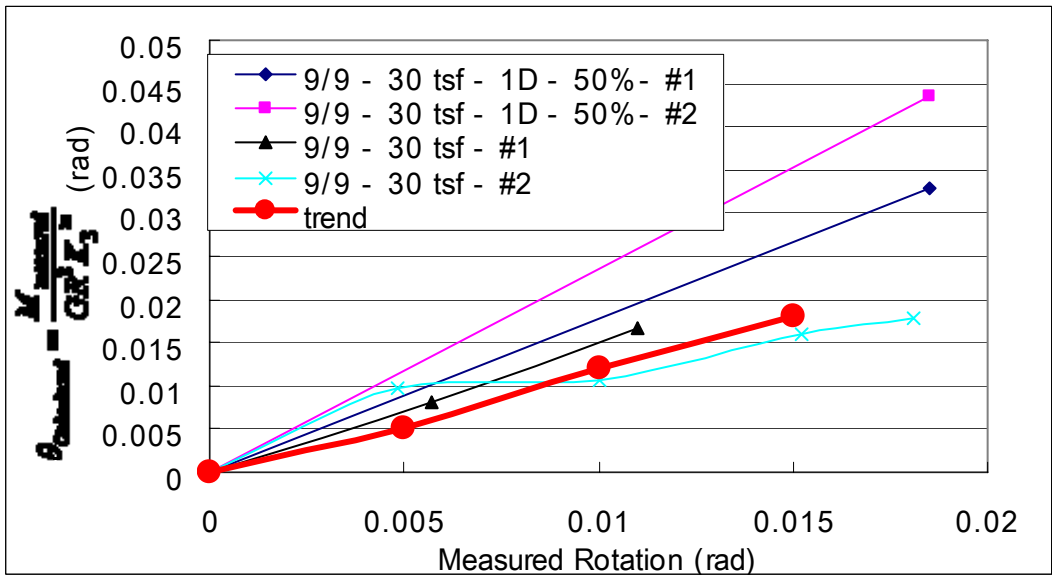


Figure 4.14 Calculated vs. Measured Rotation using Bell (1991) with Trend line in red

A less complicated approach is provided by Doherty and Deeks (2006) for an elastic plate embedded in a Gibson soil and rock medium. This model represents an increasing modulus with depth and is as shown in Figure 4.15. As with Bell (1991), the moment and rotation may be

expressed in an equation similar to Eq. 4.8. However, the stiffness coefficient, K, is determined using a monograph (Figure 4.16) as a function of the plate rigidity parameter, J. The plate rigidity parameter includes Poisson's ratio ( $\nu$ ), Shear modulus ( $G_R$ ) and Poisson's ratio ( $\nu_s$ ) of the soil, Young's modulus( $E_s$ ), radius (R ) and thickness (t) of the footing. The rigidity parameter, J, is shown in Eq. 4.9, as follows:

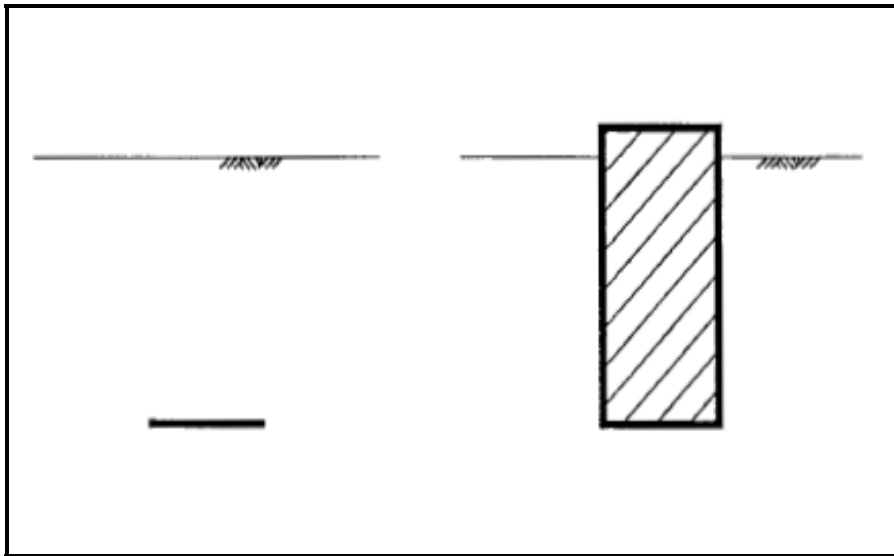


Figure 4.15 Doherty and Deeks (2006) on left, Bell (1991) on Right

$$J = \frac{\pi(3 - 4\nu)}{24(1 - \nu_s)(1 - \nu)} \frac{E_s}{G_R} \frac{t}{R} \quad \text{Eq. 4.9}$$

As identified earlier, the shear modulus in Eq. 4.9 varies with depth (z) according to:

$$G(z) = G_R \left(\frac{Z}{R}\right)^\alpha \quad \text{Eq. 4.10}$$

In the above equation,  $G_R$  is the shear modulus of the rock located at a depth R below the rock surface, and  $\alpha$  is a user defined parameter. For instance,  $\alpha$  was assumed to be equal to 0.5

for the 10 tsf rock (i.e., sensitive to overburden depth), whereas, the 30 tsf rock set  $\alpha$  equal to zero or a constant G.

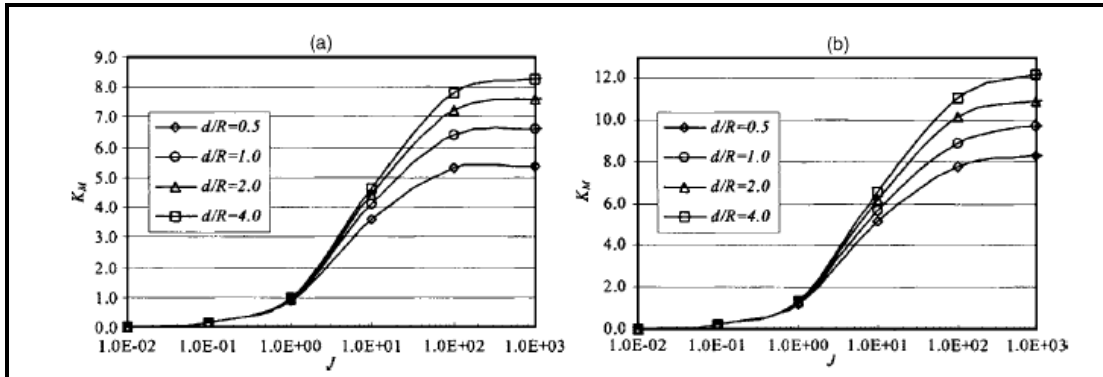


Fig. 14.  $K_M$  for  $\alpha=0$ : (a)  $\nu=0.2$  and (b)  $\nu=0.499$

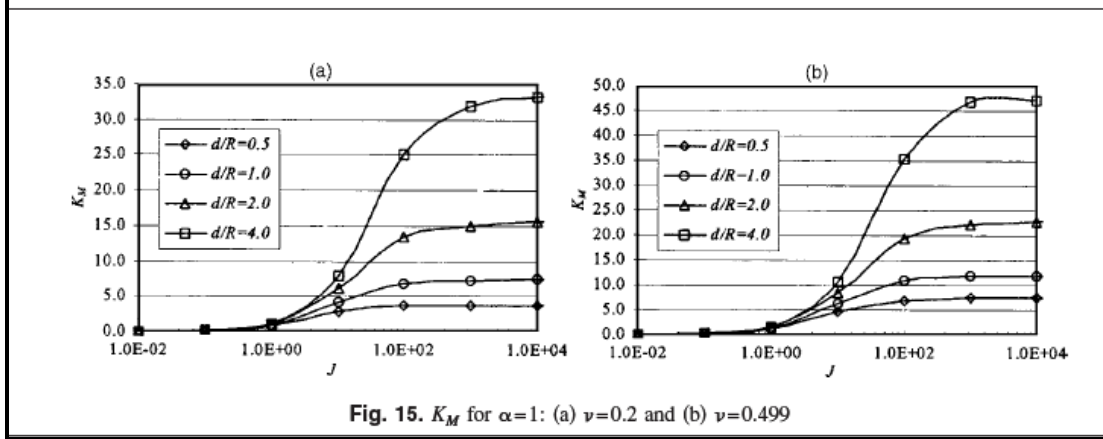


Fig. 15.  $K_M$  for  $\alpha=1$ : (a)  $\nu=0.2$  and (b)  $\nu=0.499$

Figure 4.16 Stiffness Coefficient, K, from Doherty and Deeks (2006)

Using Eq.4.8 with K determined from Figure 4.14 and the rigidity parameter, J, defined from Eq.4.9, the measured and calculated rotations for different rock strengths were found. These are shown in Figures 4.17 and 4.18. The Doherty and Deeks (2006) method also provided acceptable predictions between measured and predicted rotations for the developed moments. However, the Doherty and Deeks (2006) trend lines are in the middle or slightly above the measured results, suggesting that they are slightly less conservative.

Consequently, even though Bell's Moment vs. Rotation model also includes tip shear and lateral translation and hence more complicated than Doherty and Deeks, its procedure recommended for Florida limestone. Figures 4.19 a & b show the model.

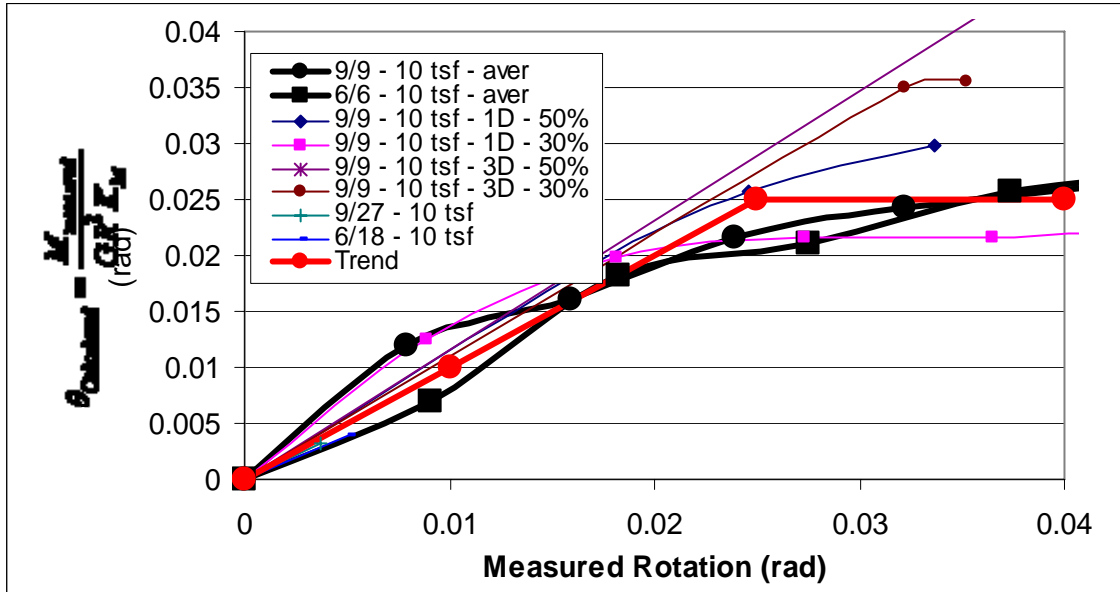


Figure 4.17 Calculated vs. Measured Rotation in 10 tsf Rock using Doherty and Deeks (2006) with Trend Line in Red

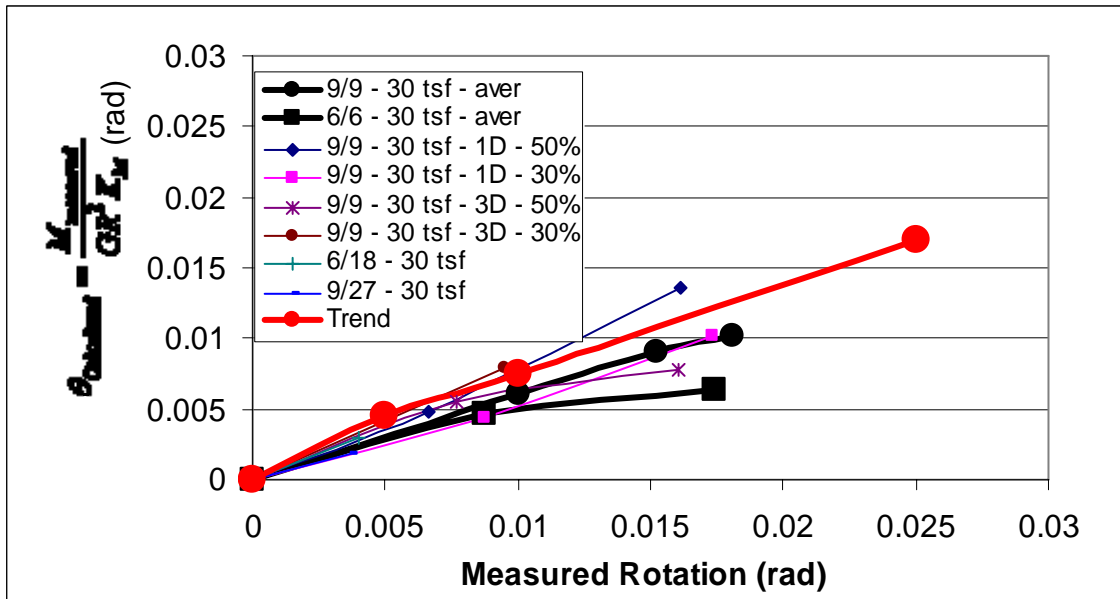


Figure 4.18 Calculated vs. Measured Rotation in 30 tsf Rock using Doherty and Deeks (2006) with Trend Line in red

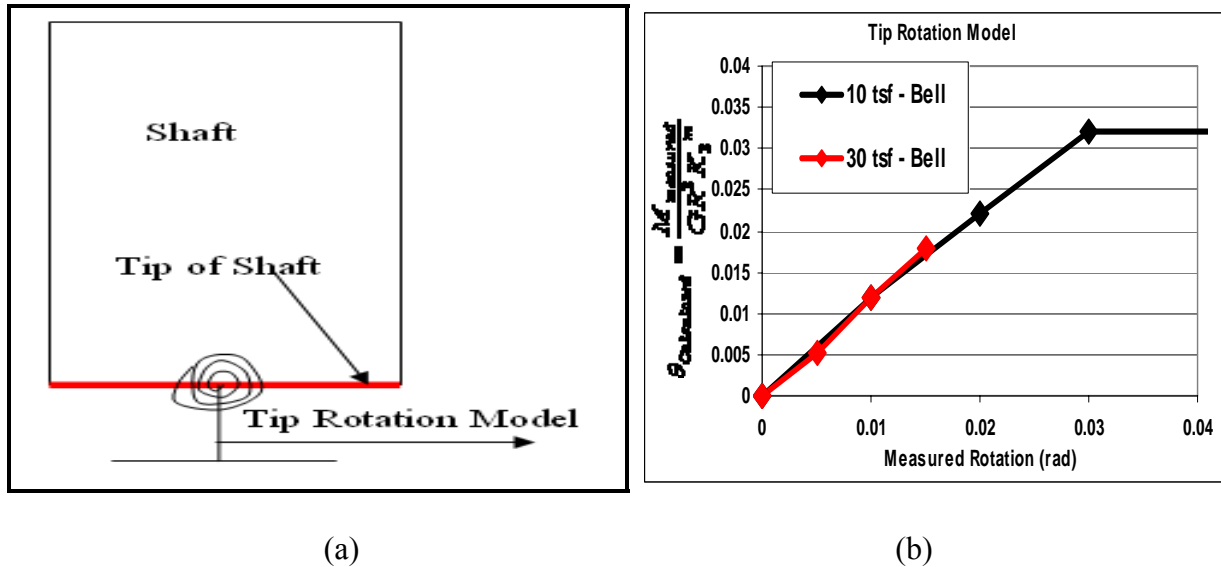


Figure 4.19 Recommended Tip Rotations vs. Moment Model from Bell (1991)  
 (a) Tip Rotation Model Scheme (b) Tip Rotation Model

To use this model the following procedure should be followed:

1. Find the moment and lateral displacement at the tip from FB-MultiPier;
2. Find the tip shear force from the tip shear model in Figure 4.9 with lateral tip displacement;
3. Find the stiffness coefficient,  $K_3^m$ , from Eq. 4.5 and compute the associated tip rotation,  $\theta_M$  from Eq. 4.6.;
4. If  $\theta_M$  from Eq. 4.6 is outside the tolerance (i.e. FB-MultiPier computed) then rerun FB-MultiPier with the new,  $K_3^m$ , from step 3 until tolerance is achieved.

CHAPTER 5  
INFLUENCE OF THREE DIMENSIONAL SOIL/ROCK SPATIAL VARIABILITY ON A  
SHAFT'S CAPACITY

**5.1 Soil and Rock Variability Using Geostatistics**

Geostatistics has been used extensively in mining, water and contaminant transport modeling. According to Deutsch (2002), “Geostatistics is the study of phenomena that vary in space and/or time”, and “Geostatistics offers a way of describing the spatial continuity of natural phenomena and provides adaptations of classical regression techniques to take advantage of this continuity,” Isaaks and Srivastava, (1989).

In the case of Geotechnical Engineering, Geostatistics is very useful for predicting both the values of engineering properties in space as well as their variability. For instance, suppose there is a need to assess a limestone's strength and modulus in the vicinity of a drilled shaft. The designer has the option of boring within the footprint of the shaft, e.g., two borings/core holes approximately three feet apart. It would be expected that their strength and modulus values would be very similar. However, if a third hole was drilled 10 feet away, their strength and modulus values would be expected to be less correlated. As more holes are drilled further and further away, a distance is eventually reached in which the first holes are not correlated (strength and modulus) with the latter values. The study of correlation and predicting nearby values based on an assessment of spatial variability is termed Geostatistics. It employs the following concepts:

- (Semi) variogram analysis – characterization of spatial correlation.
- Kriging – optimal interpolation; generates best linear unbiased estimate at each location; employs semivariogram model.
- Stochastic simulation (e.g., Sequential Gauss Simulation) – generation of multiple equally probable images of the variable; also employs semivariogram model.

A discussion of each of the above concepts along with example data from one of the FDOT bridge sites, i.e., the 17<sup>th</sup> Street Bridge is presented.

### 5.1.1 (Semi) variogram

Establishing the spatial correlation structure of a site having erratic variation in its soil/rock properties would require an extensive amount of subsoil exploration. This may not be feasible for many projects due to the high costs (Fenton & Griffiths 1999) involved. One of the most common methods to estimate the correlation coefficient length is the semivariogram.

The semivariogram is a statistic that appraises the average decrease in similarity between two random variables as the distance between the variables increases. It describes how spatial continuity changes as a function of distance and direction.

Terminology used to describe the important features of the semi-variogram model, shown in Figure 5.1, are:

- **Sill:** The semi variance value at which the variogram levels off. Also it is used to refer to the “amplitude” of a certain component of the semivariogram. For the plot below, “sill” could refer to the overall sill (1.0) or to the difference (0.8) between the overall sill and the nugget (0.2). Meaning depends on context.
- **Range:** The lag distance at which the semivariogram (or semivariogram component) reaches the sill value. Presumably, autocorrelation is essentially zero beyond the range.
- **Nugget:** In theory, the semivariogram value at the origin (0 lag) should be zero. If it is significantly different from zero for lags very close to zero, then this semivariogram value is referred to as the nugget. The nugget represents variability at distances smaller than the typical sample spacing, including measurement error. The ratio of the nugget effect to the sill is often referred to as the relative nugget effect and is usually quoted in percentage.
- **Trend:** If the empirical semivariogram continues climbing steadily beyond the global variance value, this is often indicative of a significant spatial trend in the variable, resulting in a negative correlation between variable values separated by large lags. Three options for dealing with lag include: 1) Fit a trend surface and work with residuals from the trend, 2) Try to find a “trend-free” direction and use the variogram in that direction as the variogram for the “random” component of the variable, 3) ignore the problem and use a linear or power variogram.

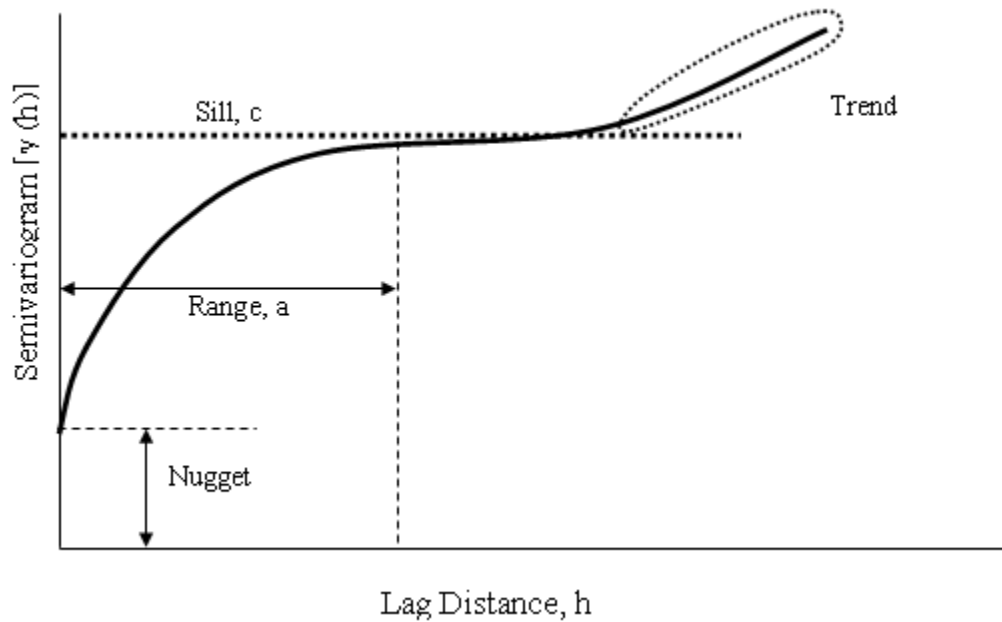


Figure 5.1 Typical Geostatistics Semivariogram

The application of Geostatistics to geotechnical foundation design requires the recovery of core runs, specifically six at the 17<sup>th</sup> Street Bridge site, Pier 10, and subsequent laboratory testing (strength and modulus), Figure 5.2. From laboratory analysis of the rock core samples taken between 52 and 92 ft of depth, a total of 136 rock cohesions,  $q_s = \frac{1}{2} \sqrt{q_u} \sqrt{q_t}$  were obtained. While the numbers in parentheses in Figure 5.2 reflect the means and standard deviations of  $q_s$  at each boring, Figure 5.3 displays the six depth profiles of  $q_s$ . Figures 5.2 and 5.3 do not indicate the presence of a spatial trend (deterministic component, e.g., linear trend) in  $q_s$ , neither do they provide evidence against the assumption of statistical homogeneity (stationarity) over the site. As a consequence, the available data is pooled together and the

resulting histogram is depicted in Figure 5.4 with a respective fit of a lognormal distribution, with a mean of  $m = 21.3$  tsf, a standard deviation of  $\sigma = 10.7$  tsf and a coefficient of variation ( $COV_{qs}$ ) of 0.50.

Figure 5.5 gives examples of experimental variograms and respective variogram model fits, which will be discussed later. The experimental variograms are obtained from the spatial data (dots in Figure 5.5) with a lag interval of 2 ft. The correlation length (range) in the vertical direction may be interpreted between approximately 5 and 10 ft, while the horizontal correlation length may range between 15 and 20 ft. The vertical variogram levels off at a sill of approximately 0.8 and the horizontal sill is not quite well defined between 0.8 and 1. A smaller sill in the vertical direction than in the horizontal direction is indicative of a zonal anisotropy called an areal trend (Deutsch, 2002) and is in agreement with the variability in the mean values of the borings given in Figure 5.2. Due to the sampling geometry (boreholes) the vertical experimental variogram is generally better defined down to small lag distances. For the horizontal variogram no data is available for lag distances smaller than the minimum separation distance between borings. This leaves doubt about the short range behavior at  $h < D$  (e.g., nugget effect).

### **5.1.2 Semivariogram models**

For the sake of kriging (predicting properties at other locations), the empirical semivariogram must be characterized with an analytical function or semivariogram model. Part of the reason for this is that the kriging algorithm will need access to semivariogram values for lag distances other than those used in the empirical semivariogram. More importantly, the

semivariogram models used in the kriging process need to obey certain numerical properties in order for the kriging equations to be solvable. Technically, the semivariogram model needs to be

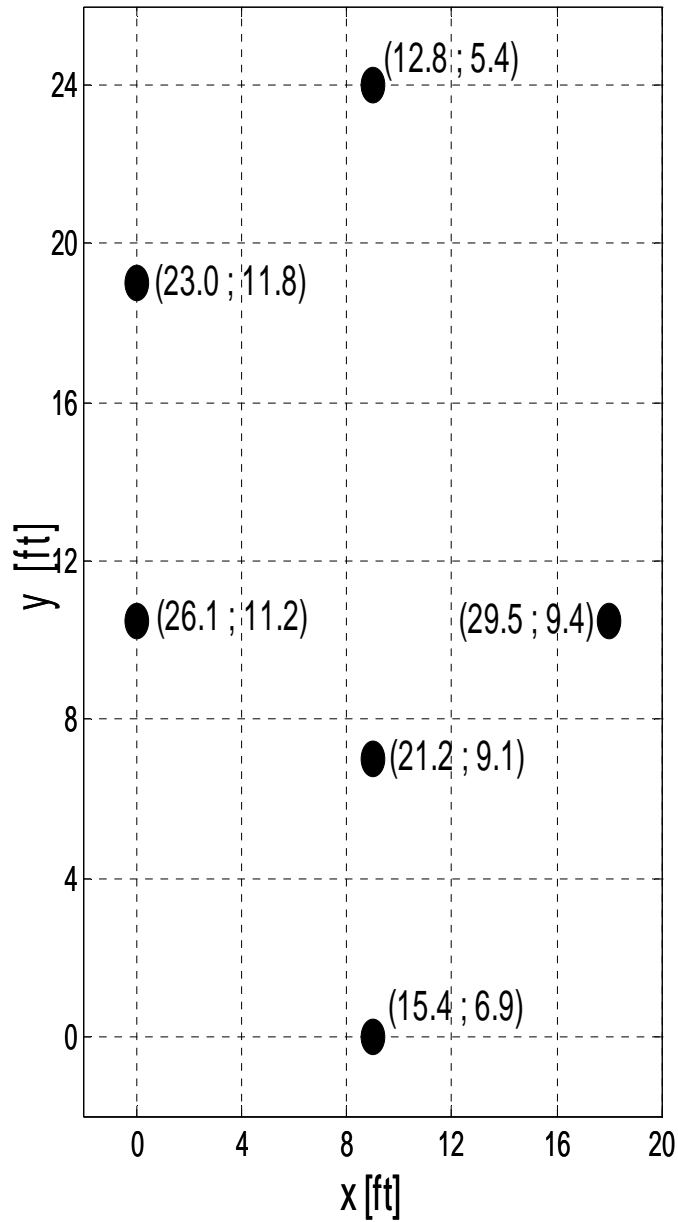


Figure 5.2 Location Map of Core Borings B4 through B9 at 17<sup>th</sup> Street Bridge: Inside Parentheses are Means and Standard Deviations of Measured  $q_s$  per Boring.

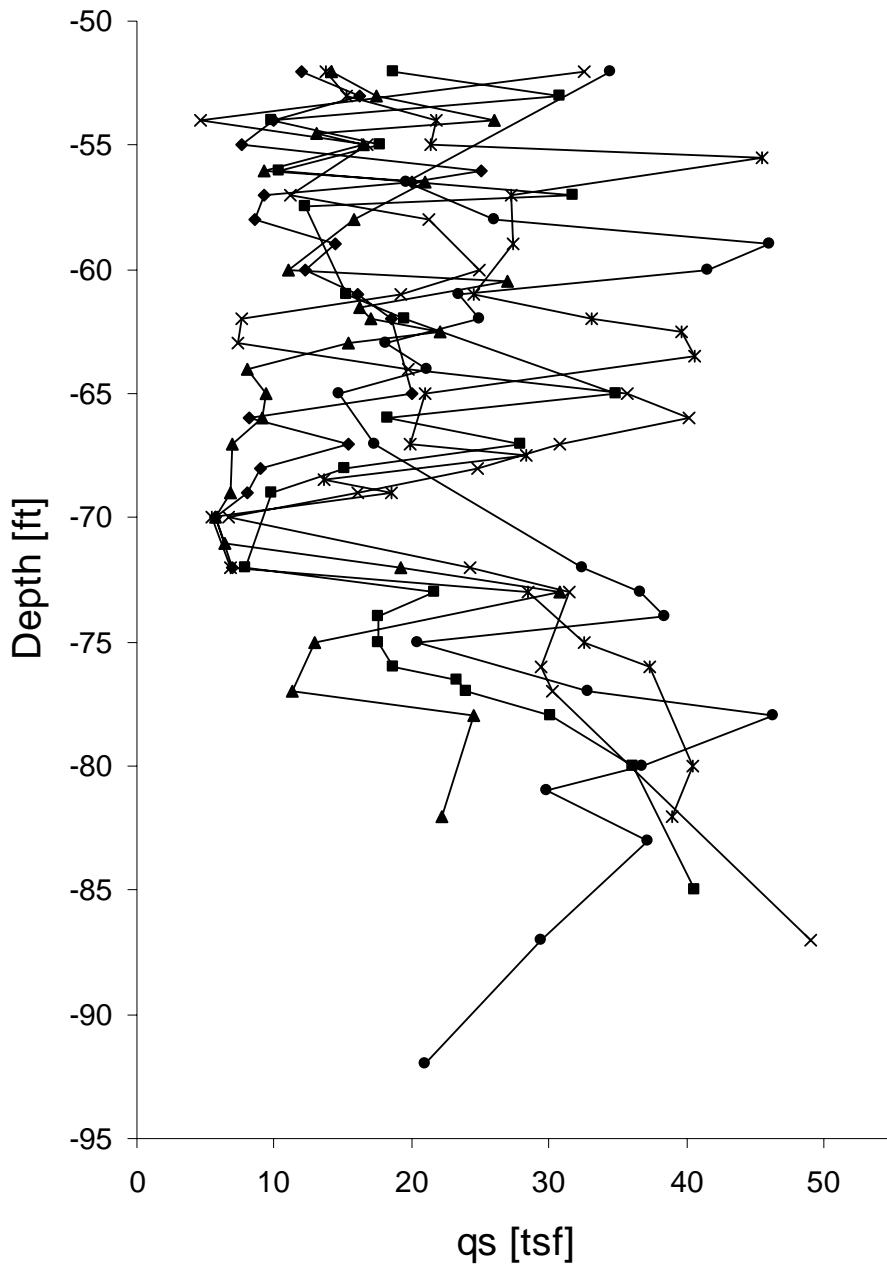


Figure 5.3 17<sup>th</sup> Street Bridge Depth Profiles of  $q_s$  for Borings B4 through B9.

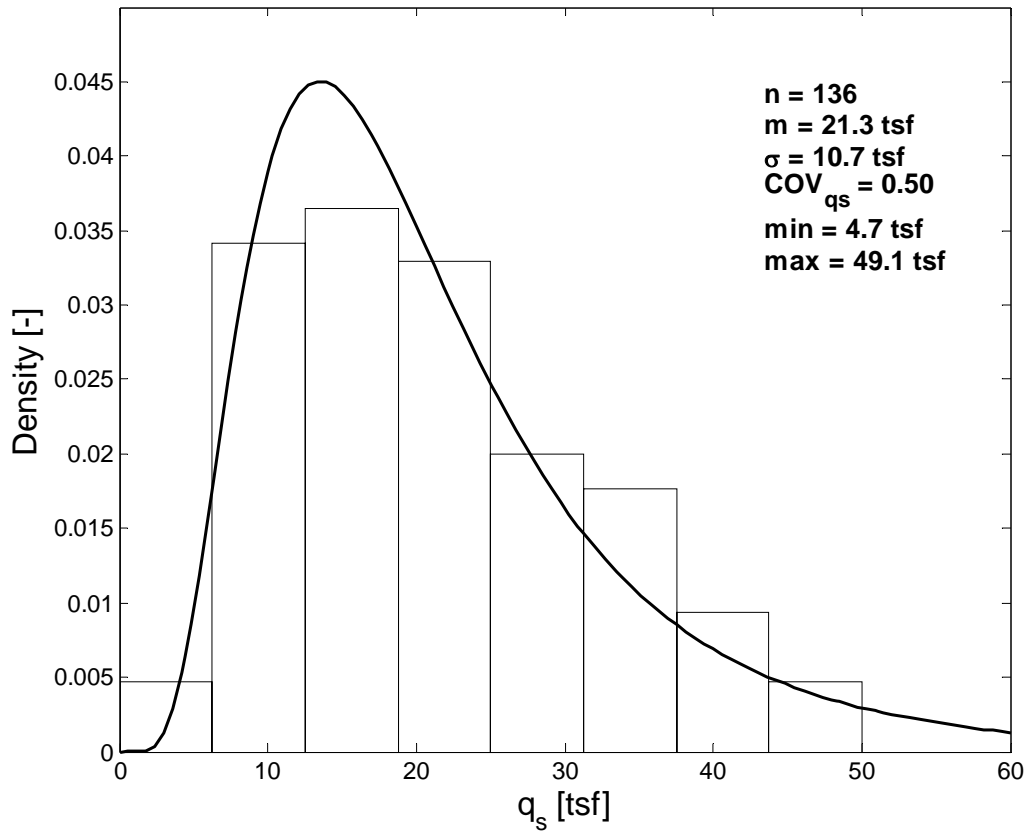


Figure 5.4 17<sup>th</sup> Street Bridge Histogram of  $q_s$  with Log-Normal Distribution Fit.

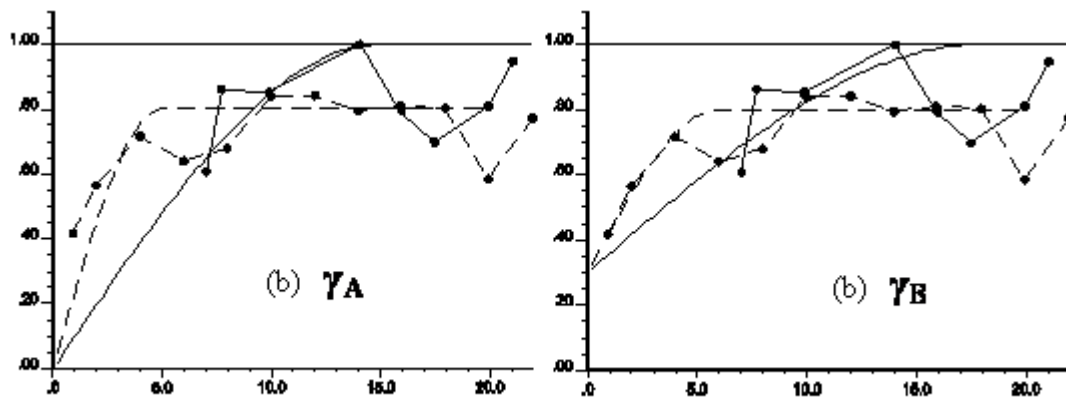


Figure 5.5 Normalized (Unity Sill) Experimental Variograms (Connected Dots) of  $q_s$  with Different Variogram Model Fits (no dots)  $\gamma_A$  &  $\gamma_B$ . Solid line is Horizontal Direction and Dashed Lines are Vertical. Lag Interval in (a) and (b) is 2 ft, X-Axis is in ft.

non-negative definite, in order the system of kriging equations to be non-singular. Therefore, Geostatisticians typically select from a number of acceptable semivariogram models. Using  $h$  to represent lag distance,  $a$  to represent range (i.e., correlation range), and  $c$  to represent sill, the five most frequently used models are, Figure 5.1:

$$\begin{aligned}
 \text{Nugget:} \quad g(h) &= \begin{cases} 0 & \text{if } h = 0 \\ c & \text{otherwise} \end{cases} \\
 \text{Spherical:} \quad g(h) &= \begin{cases} c \cdot \left( 1.5 \left( \frac{h}{a} \right) - 0.5 \left( \frac{h}{a} \right)^3 \right) & \text{if } h \leq a \\ c & \text{otherwise} \end{cases} \\
 \text{Exponential:} \quad g(h) &= c \cdot \left( 1 - \exp\left( \frac{-3h}{a} \right) \right) \\
 \text{Gaussian:} \quad g(h) &= c \cdot \left( 1 - \exp\left( \frac{-3h^2}{a^2} \right) \right) \\
 \text{Power:} \quad g(h) &= c \cdot h^\omega \quad \text{with } 0 < \omega < 2
 \end{aligned}$$

Eq.5.1

The nugget model represents the discontinuity at the origin due to small-scale variation. On its own it would represent a purely random variable, with no spatial correlation. The spherical model actually reaches the specified sill value, “c”, at the specified range, “a”. The exponential and Gaussian approach the sill asymptotically, with “a” representing the practical range, the distance at which the semi variance reaches 95% of the sill value. The Gaussian model, with its parabolic behavior at the origin, represents very smoothly varying properties. (However, using the Gaussian model alone without a nugget effect can lead to numerical instabilities in the kriging process.) The spherical and exponential models exhibit linear behavior the origin, appropriate for representing properties with a higher level of short-range variability.

An omnidirectional semivariogram is one that for which the directional tolerance have been incorporated. That is, it contains all possible directions combined into a single variogram. The calculation of the omnidirectional semivariogram does not imply that the spatial continuity is the same in all directions. It simply provides a starting point for establishing some of the parameters required for sample semivariogram calculations.

In many cases, a random variable shows different autocorrelation structures in different directions, and an anisotropic semivariogram model should be developed to reflect these differences. The most commonly employed model for anisotropy is geometric anisotropy, with the semivariogram reaching the same sill in all directions, but at different ranges. In geological settings, the most prominent form of anisotropy is a strong contrast in ranges in the (stratigraphically) vertical and horizontal directions, with the vertical semivariogram reaching the sill in a much shorter distance than the horizontal semivariogram. In some settings, there may also be significant lateral anisotropy, often reflecting prominent directionality in the depositional setting.

Shown in Figures 5.5 a and b are the semivariogram models fitted to the experimental data at the 17<sup>th</sup> Street Bridge, Pier 10. The models (solid and dashed lines with no points) used spherical models, and both nugget (Figure 5.5 b) and no nugget (Figure 5.5a) effects were considered.

### **5.1.3 Covariance and Correlogram**

There are two other tools used on describing spatial continuity these are the Covariance  $[C(h)]$  and Correlation function  $[\rho(h)]$ . Of the two, the first  $[C(h)]$  is extremely important and is usually obtained from the semivariogram  $[\gamma(h)]$ . Under the condition of second-order stationary

(spatially constant mean and variance), the covariance function, correlogram, and semivariogram obey the following relationships:

$$C(0) = \text{Cov}(Z(u+h(0)), Z(u)) = \text{Var}(Z(u)) \quad \text{Eq. 5.2}$$

$$C(h) = \rho(h) / C(0) \quad \text{Eq. 5.3}$$

$$C(h) = C(0) - \gamma(h) \quad \text{Eq. 5.4}$$

The zero lag covariance ( $h = 0$ ) should be equal to the global variance of the variable under consideration; the Correlogram,  $\rho(h)$ , should look like the covariance function scaled by the variance, and the semivariogram should look like the covariance function inverted.

Unlike time series analysts, who prefer to work with either the covariance function or the correlogram, geostatisticians typically work with the semivariogram. This is primarily because the semivariogram, which averages squared differences of the variable, tends to filter the influence of a spatially varying mean.

#### 5.1.4 Kriging

Kriging technique was named after a South African mining engineer named Daniel Gerhardus Krige who develops the method in an attempt to more accurately predict ore reserves.

Kriging is a group of geostatistical techniques to interpolate the value  $Z(x_0)$  of a random field  $Z(x)$  (e.g., the elevation  $Z$  of the landscape as a function of the geographic location  $x$ ) at an unobserved location  $x_0$  from observations  $z_i = Z(x_i)$ ,  $i = 1, \dots, n$  of the random field at nearby locations  $x_1, \dots, x_n$ . Kriging computes the best linear unbiased estimator  $\hat{Z}(x_0)$  of  $Z(x_0)$  based on a stochastic model of the spatial dependence quantified either by the variogram  $\gamma(x,y)$  or by expectation  $\mu(x) = E[Z(x)]$  and the covariance function  $c(x,y)$  of the random field. It has been demonstrated that kriging is not possible without knowledge of the semivariogram or the covariance.

The kriging estimator is given by a linear combination

$$\hat{Z}(x_0) = \sum_{i=1}^n w_i(x_0)Z(x_i) \quad \text{Eq. 5.5}$$

of the observed values  $z_i = Z(x_i)$  with weights  $w_i(x_0)$ ,  $i = 1, \dots, n$  chosen such that the variance (also called kriging variance or kriging error) is given by

$$\sigma_k^2(x_0) := \text{var}(\hat{Z}(x_0) - Z(x)) = \text{var}\left(\sum_{i=1}^n w_i(x_0)Z(x_i)\right) = \sum_{i=1}^n \sum_{j=1}^n w_i(x_0)w_j(x_0)c(x_i, x_j)$$

Eq. 5.6

(with  $w_0(x_0) = -1$ ) of the prediction error  $\hat{Z}(x) - Z(x)$  is minimized subject to the unbiased ness condition:

$$E[\hat{Z}(x) - Z(x)] = \sum_{i=1}^n w_i(x_0)\mu(x_i) - \mu(x_0) = 0 \quad \text{Eq. 5.7}$$

Depending on the stochastic properties of the random field different types of kriging apply. For the different types of kriging the unbiased ness condition is rewritten into different linear constraints for the weights  $w_i$ .

The kriging variance must not be confused with the variance of the kriging predictor  $\hat{Z}(x_0)$  itself.

$$\text{var}(\hat{Z}(x_0)) = \text{var}\left(\sum_{i=1}^n w_i Z(x_i)\right) = \sum_{i=1}^n \sum_{j=1}^n w_i w_j c(x_i, x_j) \quad \text{Eq. 5.8}$$

There are many types of Kriging:

- **Simple kriging** assuming a known constant trend:  $\mu(x) = 0$ .
- **Ordinary kriging** assuming an unknown constant trend:  $\mu(x) = \mu$ .

$$\mu(x) = \sum_{k=0}^p \beta_k f(x) \quad \text{Eq. 5.9}$$

- **Universal Kriging** assuming a general linear trend model
- **IRFk-Kriging** assuming  $\mu(x)$  to be an unknown polynomial in  $x$ .
- **Indicator Kriging** using indicator functions instead of the process itself, in order to estimate transition probabilities.
- **Multiple indicator kriging** is a version of indicator kriging working with a family of indicators. However, MIK has fallen out of favor as an interpolation technique in recent years. This is due to some inherent difficulties related to operation and model validation. Conditional Simulation is fast becoming the accepted replacement technique in this case.
- **Disjunctive Kriging** is a nonlinear generalization of kriging.
- **Lognormal Kriging** interpolates positive data by means of logarithms.

For this research both Simple and Ordinary Kriging approaches were used. The simple kriging weights,  $w_i$ , have no unbiasedness condition and are given by the by the following system of equations requiring the Covariance function,  $C(h = x_i - x_j)$ :

$$\begin{pmatrix} w_1 \\ \vdots \\ w_n \end{pmatrix} = \begin{pmatrix} c(x_1, x_1) & \cdots & c(x_1, x_n) \\ \vdots & \ddots & \vdots \\ c(x_n, x_1) & \cdots & c(x_n, x_n) \end{pmatrix}^{-1} \begin{pmatrix} c(x_1, x_0) \\ \vdots \\ c(x_n, x_0) \end{pmatrix} \quad \text{Eq. 5.10}$$

Substituting Equation 5.10 into Equation 5.5 for variable estimation, results in

$$\hat{Z}(x) = \begin{pmatrix} z_1 \\ \vdots \\ z_n \end{pmatrix}' \begin{pmatrix} c(x_1, x_1) & \cdots & c(x_1, x_n) \\ \vdots & \ddots & \vdots \\ c(x_n, x_1) & \cdots & c(x_n, x_n) \end{pmatrix}^{-1} \begin{pmatrix} c(x_1, x_0) \\ \vdots \\ c(x_n, x_0) \\ 1 \end{pmatrix} \quad \text{Eq. 5.11}$$

Simple Kriging Error or Variance is given by:

$$\text{var} \left( \hat{Z}(x_0) - Z(x_0) \right) = \underbrace{c(x_0, x_0)}_{\text{var}(Z(x_0))} -$$

$$\underbrace{\begin{pmatrix} c(x_1, x_0) \\ \vdots \\ c(x_n, x_0) \end{pmatrix}' \begin{pmatrix} c(x_1, x_1) & \cdots & c(x_1, x_n) \\ \vdots & \ddots & \vdots \\ c(x_n, x_1) & \cdots & c(x_n, x_n) \end{pmatrix}^{-1} \begin{pmatrix} c(x_1, x_0) \\ \vdots \\ c(x_n, x_0) \end{pmatrix}}_{\text{var}(\hat{Z}(x))}$$

Eq. 5.12

which leads to the generalized least squares version of the Gauss-Markov theorem (Chiles & Delfiner 1999, p.159):

$$\text{var}(Z(x_0)) = \text{var}(\hat{Z}(x_0)) + \text{var} \left( \hat{Z}(x_0) - Z(x_0) \right) \quad \text{Eq. 5.13}$$

Ordinary kriging is an estimation method that is often associated with the acronym B.L.U.E. for “best linear unbiased estimator.” Ordinary kriging is “linear” because its estimates are weighted linear combinations of the available data; it is “unbiased” since it tries to have the mean residual or error,  $m_R$ , equal to 0; it is “best” because it aims at minimizing the variance of the errors,  $\sigma^2_R$ . The distinguish feature of ordinary kriging, is its aim of minimizing the error variance.

### 5.1.5 Stochastic Simulation using Sequential Gaussian Simulation

There are many algorithms that can be devised to create stochastic simulations. For example:

(1) matrix approaches (LU Decomposition), which are not extensively used because of size restrictions (an  $N \times N$  matrix must be solved where  $N$ , the number of locations, could be in the millions);

(2) turning bands methods where the variable is simulated on 1-D lines and then combined into a 3-D model; not commonly used because of artifacts;

(3) spectral methods using FFTs can be CPU fast, but honoring conditioning data requires an expensive kriging step;

(4) fractals which are not used extensively because of the restrictive assumption of self-similarity, and;

(5) moving average methods, which are infrequently used due to CPU requirements. The common approach adopted in recent times is the sequential Gaussian simulation (SGS) approach. This method is simple, flexible, and reasonable efficient.

Sequential Gaussian Simulation is the most straightforward algorithm for generating realizations of multivariate Gaussian fields. It is provided by the sequential simulation principle of including all data available within a neighborhood of the point on question, including the original data and all previously simulated values. Each variable is simulated sequentially according to its normal Cumulative Distribution Function (CDF) fully characterized through a Simple Kriging system.

The detailed steps in Sequential Gaussian Simulation are:

- Determine the univariate CDF representative of the entire study area and not only of the sample data available.
- Transform data to “normal space”, i.e., Gaussian Normal Distribution
- Establish grid network and coordinate system ( $Z_{rel}$ -space)
- Assign data to the nearest grid node (take the closest of multiple data assigned to the same node)

- Determine a random path through all of the grid nodes
- Find nearby data and previously simulated grid nodes
- Construct the conditional distribution by kriging
- Draw simulated value from conditional distribution
- Check results
- Back transform

By using different random number seeds, the order of visiting locations is varied and therefore, multiple realizations can be obtained. In other words, since the simulated values are added to the data set, the values available for use in the simulation are partly dependent on the locations at which simulations have already been made and, because of this, the values simulated at any one location vary as the available data varies.

Sequential Gauss Simulation will be used to simulate variability in rock properties for the 17<sup>th</sup> Street Bridge from which the capacity variability will be assessed. This process uses WINGSLIB (Spatial Variability of Properties) and FLAC3D for assessment of capacities. A discussion of the software follows.

#### **5.1.6 WINGSLIB Stochastic Software**

There exists a wide range of public domain and low cost software for Geostatistics assessment that is readily available to the Geotechnical Engineer. Examples of such software packages include WINGSLIB Geostatistical Software Library, and GSTAT. In addition, several commercial GISystems packages now include Geostatistical Tools (i.e., Variograms, Kriging, etc.). Typical Geostatistical data required for stochastic simulation, such as WINGSLIB analysis include:

- The variable to be simulated (e.g., Cohesion Values), Figure 5.4;

- The Semivariogram structure, Figure 5.5;
- The maximum and minimum of original data that should be used to simulate a grid node.
- The Data Variance, Figure 5.4;
- X, Y and Z coordinates for the measured data, i.e., Figure 5.2;
- Layout of a grid system of interest;
- Type of kriging to be used (Simple Kriging).

Shown in Figure 5.6 is the one of the stochastic simulations of rock strength at the 17<sup>th</sup> Street Bridge using the data provided in Figures 5.2 through 5.5 using the WINGSLIB software. Dark blue is the lowest rock strength ( $c = 0$ ) and red is the highest ( $c = 43,000$  psf).

## **5.2 Numerical Analysis of Shaft Capacity – FLAC3D**

FLAC3D or Fast Lagrangian Analysis of a Continuum is a powerful three-dimensional program for modeling soil, rock and structural behavior subject to static or dynamic loadings. The FLAC3D can model non-linear systems as they evolve in time (Itasca 2002). Used interactively or in batch mode, FLAC is a general analysis and design tool for geotechnical, civil, and mining engineers for broad range of problems including porous media (i.e., fluid analysis). The explicit finite difference formulation employed in the code makes it ideally suited for modeling difficult problems (for example: penetration, excavation, etc.) which are not generally solved with an implicit code (e.g., ADINA). The formulation can handle large displacements and strains, non-linear material behavior, capturing yield as well as failure at a point or over a large area, i.e., a total collapse.

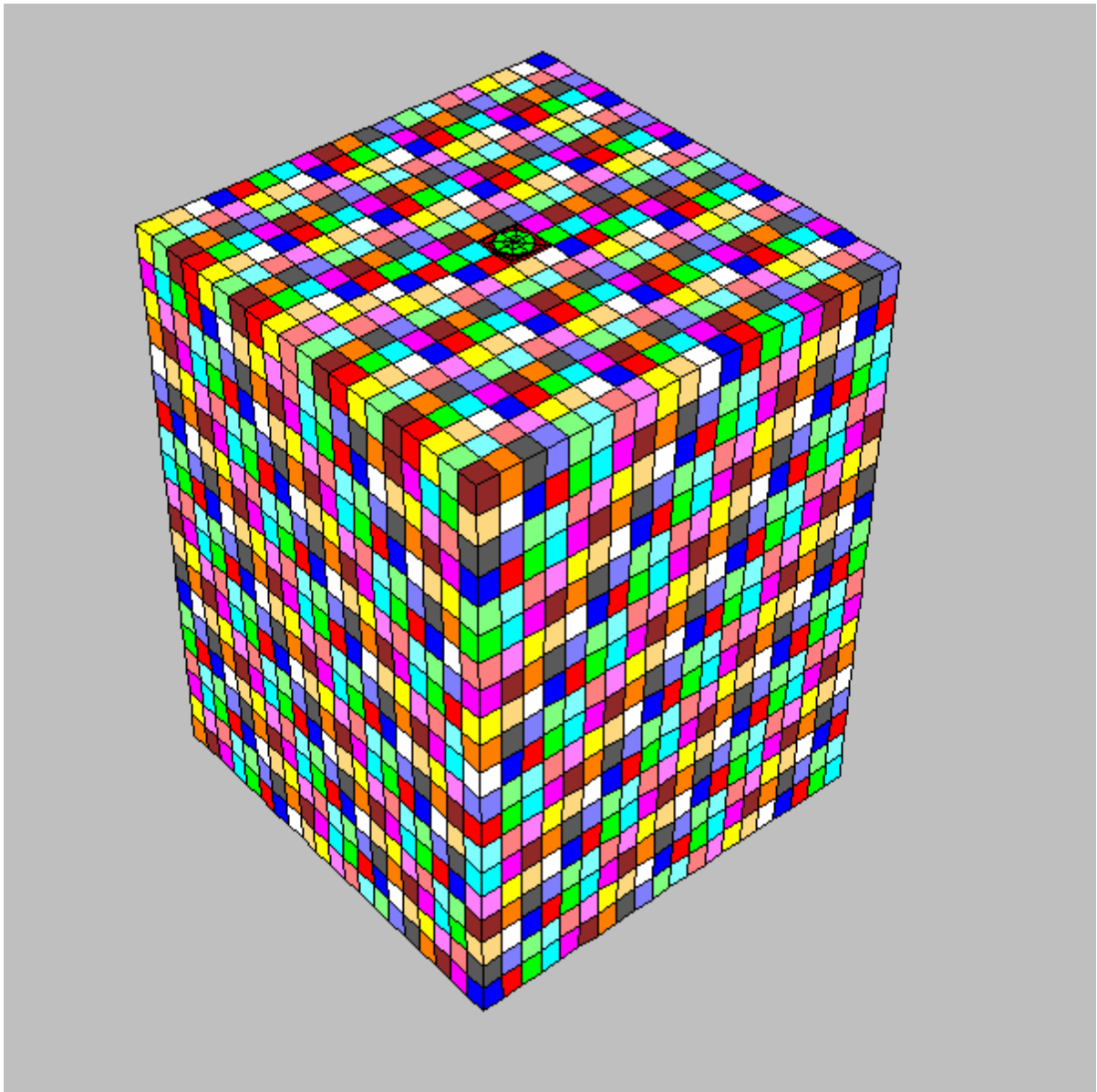


Figure 5.6 Simulation of Rock Strength (i.e., Cohesion) – Red Highest and Blue Lowest

FLAC3D uses an explicit finite difference time-marching scheme to solve the equations of motion or velocities at end of a time step. The velocities are then used to calculate the strains, from which stresses can be calculated through the constitutive equation. These calculations are carried out over individual time steps for which the velocities are assumed to be constant. The advantage of using the explicit formulation is that the numerical scheme stays stable even when

the physical system is unstable. This is particularly advantageous, when modeling “non-linear”, “large strain” behavior and actual “physical instability”. The disadvantage of the time-marching explicit scheme of the FLAC3D is that the time steps must be very small requiring a significant number of steps compared to implicit formulations.

Materials are represented by polyhedral elements within a three-dimensional grid that is adjusted by the user to fit the shape of the object being modeled. Each element behaves according to a prescribed linear or nonlinear stress-strain law in response to applied forces or boundary restraints. The material can yield, flow and in the case of large deformations is updated. The explicit, Lagrangian calculation scheme and the mixed-discretization zoning technique used in FLAC3D ensure that plastic collapse and flow are modeled very accurately.

The FLAC3D has many constitutive models built into it. The user has the option of choosing the most relevant constitutive model for a particular problem.

The following FLAC3D material models are the most used:

- Elastic, isotropic;
- Drucker-Prager plasticity;
- Mohr-Coulomb plasticity;
- Strain-hardening / softening Mohr-Coulomb plasticity;
- Bi-linear strain-hardening / softening ubiquitous-joint plasticity

### **5.3 Simulation of an Axial Loaded Drilled Shaft**

To investigate the influence of spatial variability on the axial capacity of a drilled shaft, the rock strength characterized in Figures 5.2 through 5.6 was used. The only exception was that the correlation length shown in Figure 5.5 which was varied as one, five, ten and twelve feet

respectively. The latter is critical in assessing the influence of spatial correlation. For instance, a correlation length of zero, assumes no correlation, or that homogeneous rock properties are simply randomly arranged.

The shaft modeled was three feet in diameter and twenty feet long shown in Figure 5.6. The rock's constitutive model was characterized as elastic perfectly plastic, or the material behaved linearly, i.e., with a Young's Modulus, E up to failure after which modulus drops to a small or negligible value. Young's Modulus was assessed from the linear regression of strength values given in Figure 5.7 and a sequential gauss simulation as shown in Figure 5.6.

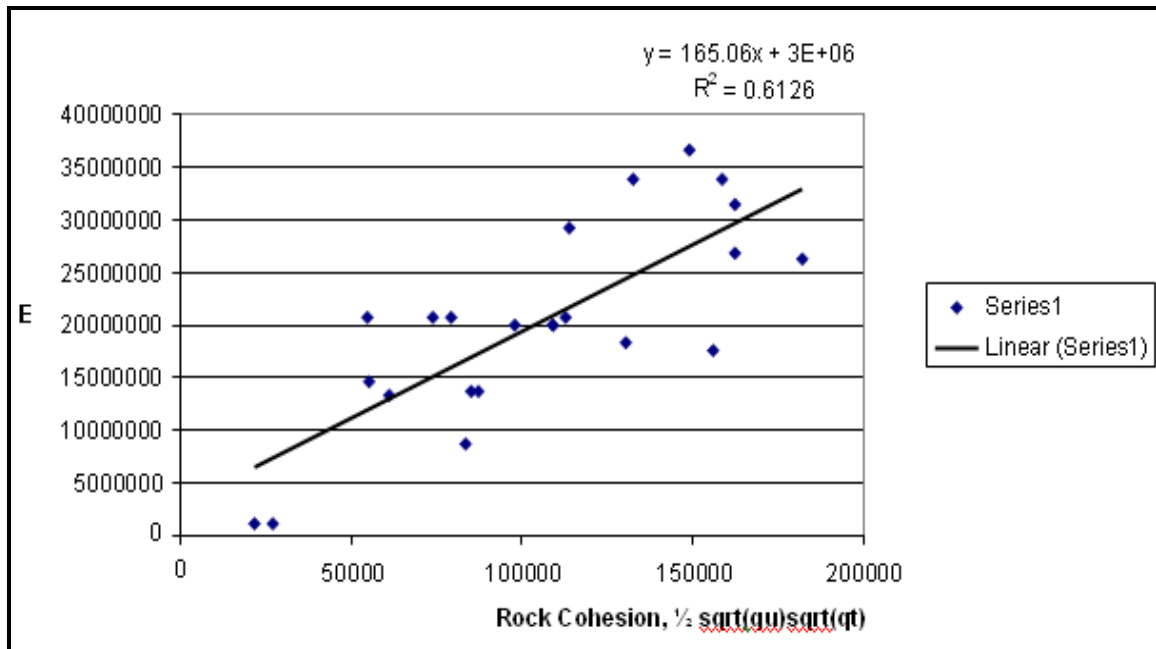


Figure 5.7 Young's Modulus, E, vs. Rock Cohesion

For each spatial correlation range (1, 5, 10 and 12 ft), WINGSLIB was run approximately thirty-five times to obtain 35 spatial distributions of rock properties. For each distribution, FLAC3D was run to assess the shaft's axial load vs. deformation response. Using the FDOT's failure criterion (settlement of 5% of the diameter of the shaft), the shaft capacity was assessed for each of the 35 runs and three correlation ranges (total FLAC3D runs = 140 runs). Shown in Figure 5.8 are the mean total shaft capacities for each of the correlation lengths. Interestingly, as the correlation range increased, the total capacity of the shaft increased. This was first identified by Fenton et al. (2002) who studied the spatial variability of soil/rock properties on the settlement of shallow foundations. They found that the mean settlement,  $\mu_{\delta}$ , of the foundation was the inverse (i.e., exponential) of the mean log settlement,  $\mu_{\ln \delta}$  plus  $\frac{1}{2}$  the variance of the log settlement ( $\frac{1}{2} \sigma_{\ln \delta}^2$ ). The above relationship only applied where the variance of the log settlement was found to be proportional to the variance of the log of the soil/rock's Young's Modulus. The value of the proportionality was found to be equal to Vanmarcke's (1984) variance function,  $\alpha$ , (discussed in Chapter 6) related to the spatial correlation length, "a". Specifically, the higher the correlation length "a", the higher the variance function,  $\alpha$ . This results in a higher variance of Young's Modulus, which subsequently yields a higher mean settlement,  $\mu_{\delta}$ , and higher capacity. Similar results were observed with end bearing, i.e., increased correlation length had increased mean tip resistance. The discussion of spatial variability on end bearing and associated LRFD resistance factors,  $\phi$  is presented in Chapter 6.

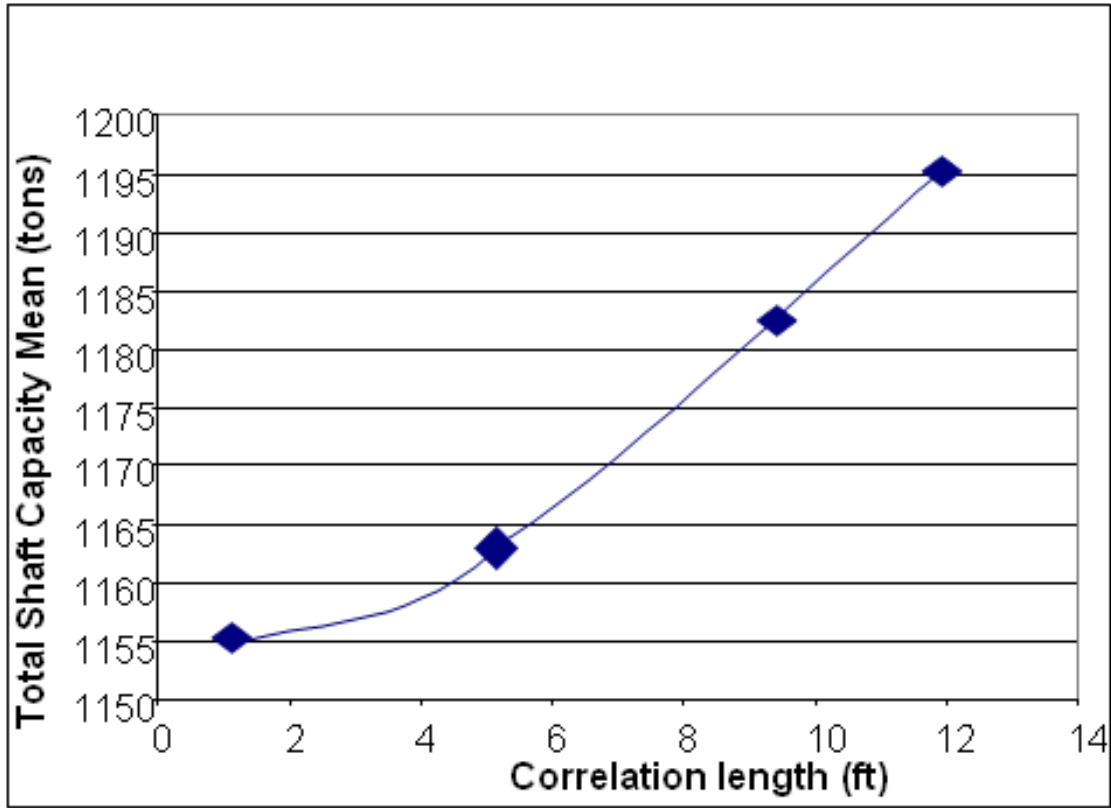


Figure 5.8 Variability of Shaft Total Capacity with Spatial Correlation Length

CHAPTER 6  
LRFD RESISTANCE FACTORS,  $\phi$ , FOR END BEARING

**6.1 Spatial Correlation and Its Influence on LRFD resistance factors,  $\phi$**

A deep foundation's resistance or capacity,  $Q$ , is the summation of side friction,  $Q_s$  and end bearing  $Q_{tip}$ . In the case of cylindrical prismatic shafts of length  $L$  and diameter  $D$  [L], the pile/shaft's side resistance  $Q_s$  may be determined from the product of the pile/shaft's surface area  $A_s = \pi DL$  [units  $L^2$ ] and the mean unit skin friction  $f_s$  [stress] over  $A_s$  or, mathematically,  $Q_s = A_s f_s$ . Consequently,  $f_s$  is related to point unit skin friction  $q_s$  through:

$$f_s = \frac{1}{A_s} \int_{A_s} q_s \cdot dA \quad \text{Eq. 6.1}$$

Since  $q_s$  may be regarded as a spatially random (“regionalized”) variable of a certain distribution (e.g., log-normal) and spatial correlation structure (variogram),  $f_s$  is also a random variable in space and its properties are related to the properties of  $q_s$ . The variable  $q_s$  is defined through summary statistics (mean,  $m$  and variance,  $\sigma^2$ ) and the covariance function  $C(h)$  [stress<sup>2</sup>].  $C(h)$  is a measure of spatial correlation between values of  $q_s$ , which are separated by a distance  $h$  [L], and it is directly related to the variogram  $\gamma(h)$  [stress<sup>2</sup>] by  $\gamma(h) = \sigma^2 - C(h)$ . In practice, this assumption corresponds to situations where  $m$ ,  $\sigma^2$  and  $\gamma(h)$  of a site are known with high confidence (e.g., from exhaustive core sample testing) and the shaft is located at a random location on the site.

In the case of the variance,  $\sigma_s^2$  of the pile/shaft side friction, it is expected that it would be less than the sites variance,  $\sigma^2$  of  $q_s$  as a result of the spatial averaging over the shaft surface or  $\sigma_s^2 < \sigma^2$ . In geostatistics, the problem of determining  $\sigma_s^2$  is known as a “change of support”, “scale up” or “regularization” problem (Isaaks and Srivastava, 1989), since the properties of a

variable are averaged over different support sizes. In the present case,  $q_s$  obtained from core samples may be thought of as a rather small support volume (i.e., points) as opposed to  $f_s$ , which is defined on a support equal to the shaft's side surface  $A_s$ . In fact,  $\alpha = \sigma_s^2/\sigma^2$  [dimensionless] can be introduced as the factor of variance reduction between  $q_s$  and  $f_s$  and it is determined by the relationship (e.g., Journel and Huijbregts, 1978; Isaaks and Srivastava, 1989; Deutsch, 2002) as:

$$\alpha = \frac{1}{A_s^2} \iint_{A_s, A_s} C'(h) \cdot dA_1 dA_2 \quad \text{Eq. 6.2}$$

where  $C'(h) = C(h)/\sigma^2$  [dimensionless] is a covariance function normalized to unit variance. Equation 6.2 contains two integrals over the area  $A_s$  (i.e., in fact a quadruple integral); however, it is nothing but the arithmetic average of the covariance values that correspond to all possible combinations of two points on  $A_s$  (i.e., the side of shaft). If the averaging domain  $A_s$  is not a continuous area but a discrete number of  $n$  [dimensionless] points with statistically independent observations of some random variable, then Eq. 6.2 reduces to the well known formula of the standard error  $\sigma_s^2 = \sigma^2/n$ , where,  $\alpha = 1/n$ .

To assess the variance of side shear,  $\sigma_s^2$ , the covariance  $C'(h)$  in Eq. 6.2 was assumed to be spherical (Isaaks and Srivastava, 1989) with an isotropic correlation length,  $a$  [L] or:

$$C'(h) = 1 - 1.5 \frac{h}{a} + 0.5 \left( \frac{h}{a} \right)^3 \quad \text{Eq. 6.3}$$

Note that  $C'(h)$  takes on a value between 0 and 1 depending on the distance  $h$ . That is to say, when  $h \geq a$ ,  $C'(h) = 0$  (no correlation) and when  $h = 0$   $C'(0) = 1$  (a one to one correlation). The correlation length (or range) "a" is established from the experimental variogram based on available data. Substituting Eq. 6.3 into Eq. 6.2 and integrating over the areas,  $\alpha =$

$\sigma_s^2/\sigma^2$  may be determined. The results are presented in a monograph as a function of L/D and a/D shown in Figure 6.1.

Also shown in the graph is the case of D = 0 (thick dashed line) in which one averages the variability over a length or depth that will subsequently only be used for end bearing.

Next, the LRFD spatial resistance factors  $\phi$  for shaft side shear may be assessed from  $COV_{R_s} = \sigma_s/m_s$  from field and or laboratory soil/rock strength assessment:

$$COV_{R_s} = \frac{\sigma_s}{m_s} = \frac{\sqrt{\alpha\sigma^2}}{m} = \sqrt{\alpha}COV_{q_s} \quad \text{Eq. 6.4}$$

and:

$$\phi = \frac{E[\lambda_R] \cdot \sqrt{\frac{(1 + (COV[QD])^2 + (COV[QL])^2)}{(1 + (COV[R_N])^2)}} \cdot (\gamma_{QD} \cdot \frac{q_D}{q_L} + \gamma_{QL})}{(E[\lambda_{QD}] \cdot \frac{q_D}{q_L} + E[\lambda_{QL}]) \cdot e^{\beta \cdot \sqrt{\ln[(1 + (COV[R_N])^2)(1 + (COV[QD])^2 + (COV[QL])^2])}}} \quad \text{Eq. 6.5}$$

Figure 6.2 shows, the LRFD resistance factors,  $\phi$  for known  $COV_R$  and reliability index,  $\beta$ , values. Using  $COV_{R_s}$  (i.e., side shear) from Eq. 6.4 for  $COV_R$  and typical  $\beta$  values (e.g., 2.5 – 3.0), LRFD resistance factors,  $\phi$  value may be found.

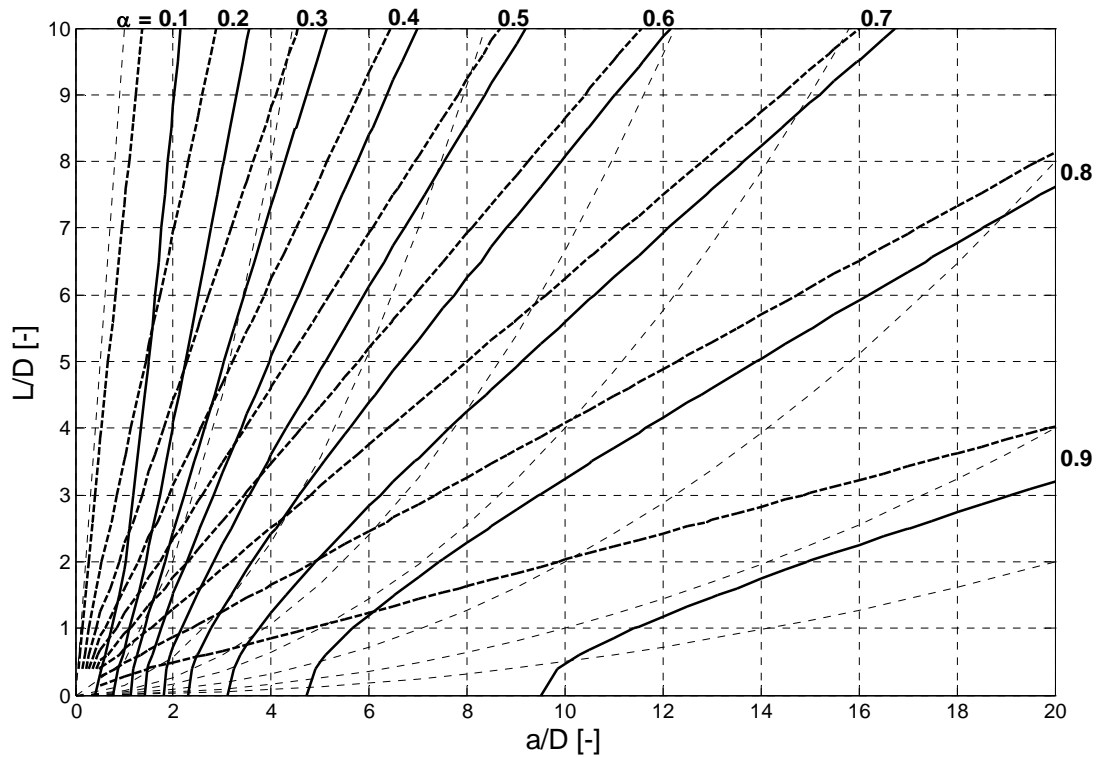


Figure 6.1 Thick Solid Contour Lines Represent  $\alpha = \sigma_s^2/\sigma^2$  for  $a/D = [0, 20]$  and  $L/D = [0,10]$ . Thick Dashed Contour Lines Represent  $\alpha = f(L/a)$  for  $D = 0$ . Thin Dotted Lines are Parabolas, Along Which  $A = \text{const}$ .

## 6.2 Development of LRFD resistance factors, $\phi$ for End Bearing and the 17<sup>th</sup> Street Bridge Case Study

In the case of a shaft's tip resistance,  $Q_{\text{tip}}$ , the shaft's unit tip stress,  $q_b$  must be calculated and then multiplied by the tip's cross-section area. However, the shaft's unit tip resistance is a function of the shaft's displacement, such as found in Eqs. 3.5 to 3.8 as:

$$q_b = \Lambda W_t^{0.67} \quad \text{Eq.6.6}$$

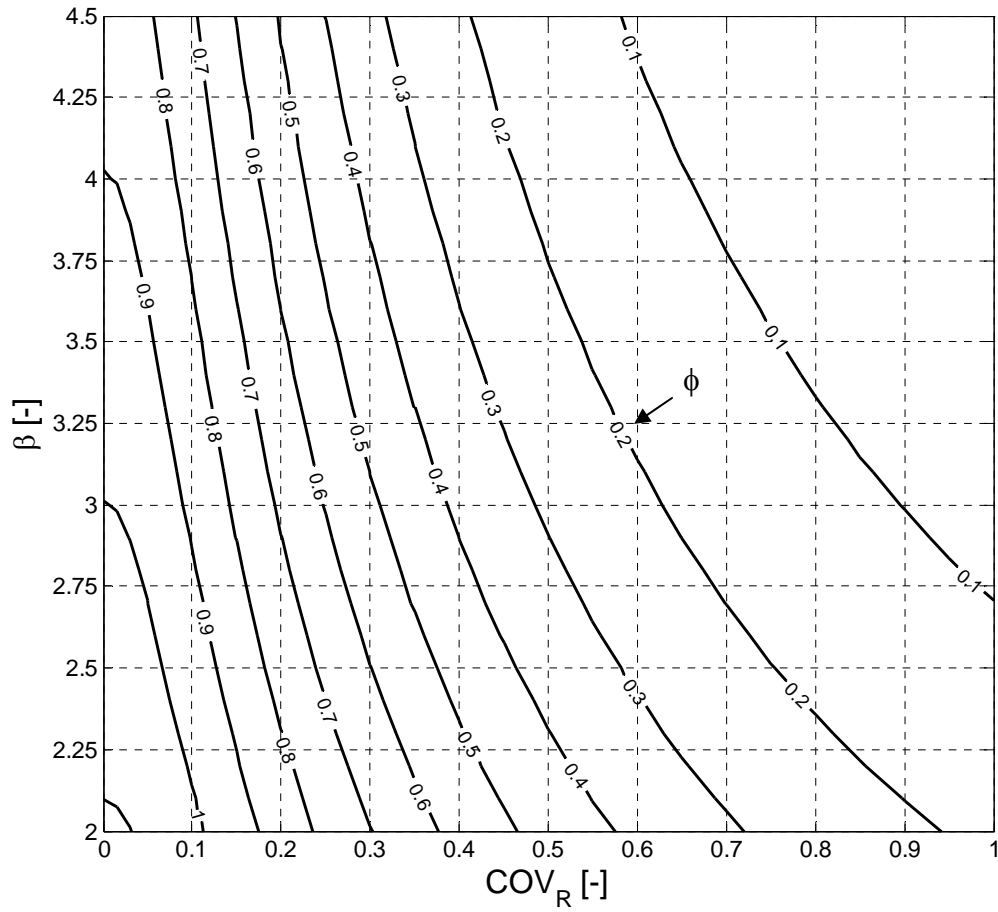


Figure 6.2 LRFD resistance factors,  $\phi$ , as a Function of Reliability Index  $\beta$  and  $COV_R$

Where  $\Lambda$ (Lambda) = Elastic compressibility parameter, and  $W_t$  = Displacement at top of shaft.

The settlement of at the bottom of the shaft,  $W_b$ , is computed from the elastic shortening of the shaft as follows:

$$W_b = W_t - \left[ \frac{2(Q_{top} + Q_{tip})L}{\pi E_c D^2} \right] \quad \text{Eq. 6.7}$$

where  $E_c$  = Young's Modulus of the concrete shaft

$Q_{top}$  = Force at Top of Shaft

$Q_{tip}$  = Force at Bottom of Shaft ( $q_b A_{shaft}$ )

The shaft's tip resistance  $Q_{tip}$  (i.e.,  $q_b$ ), may be found by determining the shaft and rock's compressibility parameter  $\Lambda$ , which is a function of  $\Theta_f$ ,  $\Gamma$ , and  $\Omega$  as shown:

$$\Gamma = 0.37 \left( \frac{L}{D} \right)^{0.5} - 0.15 \left[ \left( \frac{L}{D} \right)^{0.5} - 1 \right] \log_{10} \left( \frac{E_c}{E_m} \right) + 0.13 \quad \text{Eq. 6.8}$$

$$\Omega = 1.14 \left( \frac{L}{D} \right)^{0.5} - 0.05 \left[ \left( \frac{L}{D} \right)^{0.5} - 1 \right] \log_{10} \left( \frac{E_c}{E_m} \right) - 0.44 \quad \text{Eq. 6.9}$$

$$\Lambda = 0.0134 E_m \frac{\left( \frac{L}{D} \right)}{\left( \frac{L}{D} + 1 \right)} \left\{ \frac{200 \left[ \left( \frac{L}{D} \right)^{0.5} - \Omega \right] \left[ \frac{L}{D} + 1 \right]}{\pi L \Gamma} \right\}^{0.67} \quad \text{Eq. 6.10}$$

where  $E_m$  = is the mass modulus of the rock

$L$  = Total length of Shaft

$D$  = Diameter of the shaft

Evident from Eqs.6.8 - 6.10, the Young's Modulus of the rock mass,  $E_m$ , controls the variability of the results. Of interest was the relationship between Florida limestone Mass Modulus and intact Young's Modulus,  $E_i$ . Synthetic Limestone specimens with various strengths were cast with different volume percentage of voids (Styrofoam) reported in Chapter 3. A comparison of no void Young's Modulus,  $E_i$ , vs. Mass Modulus values with different volume percentages (i.e., recovery) was completed. Shown in Figure 6.3 are the  $E_m/E_i$  ratios as reported by O'Neil and UF. As shown, the UF data falls between O'Neil's open and closed joint data.

Also, there exists a linear relationship between  $E_m/E_i$  for Recoveries above 50% and a sharp drop off below 50%.

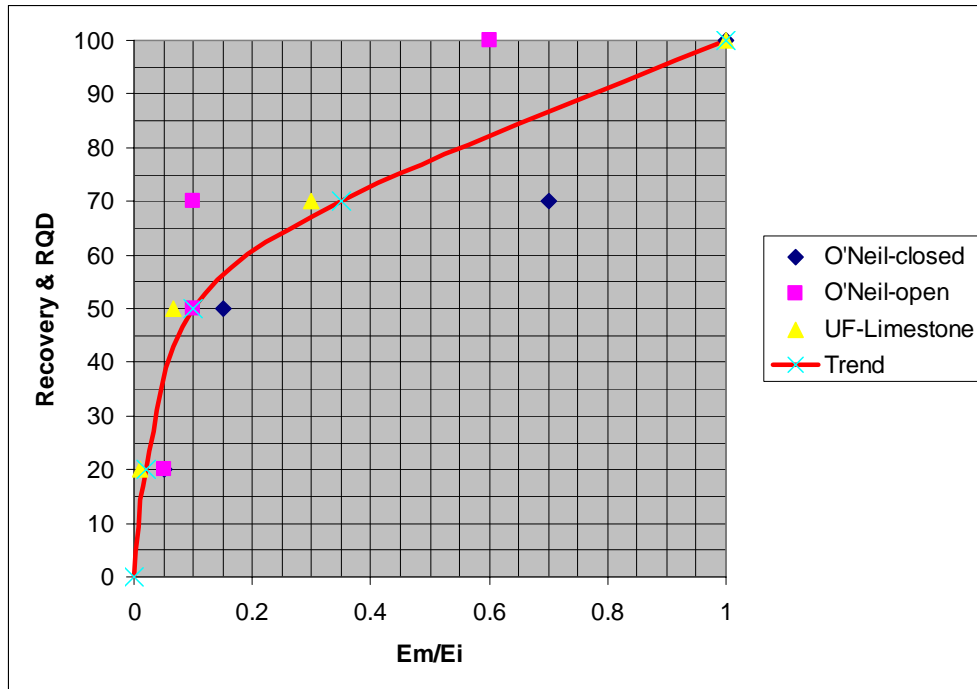


Figure 6.3 O'Neil  $E_m/E_i$  vs. RQD and UF  $E_m/E_i$  vs. Recovery

Of interest is the variability in the field and its impact on the tip resistance of shafts. To study the latter, a series of drilled shaft load tests at a bridge site were investigated. Shown in Figure 6.4 is a typical stress-strain plot from an unconfined test on Florida limestone recovered from the 17<sup>th</sup> Street Bridge near load test LTSO4 at pier 10. A total of 102 unconfined tests were performed by SMO personnel on rock cores recovered in six boreholes at 5 foot spacing near LTSO4. The analysis considered both the Secant Young's Modulus as well as the Tangent Young's Modulus in the assessment. Generally, the secant modulus encompasses end effects as well as micro cracking which induces a reduction in modulus vs. the tangent modulus (Figure 6.4). All observed loss in tangent modulus (i.e. micro cracking) was found to occur beyond 6 to

7% strain which for shafts of interest (6 to 9 ft) equates to a vertical movement greater than two inches or the AASHTO service state.

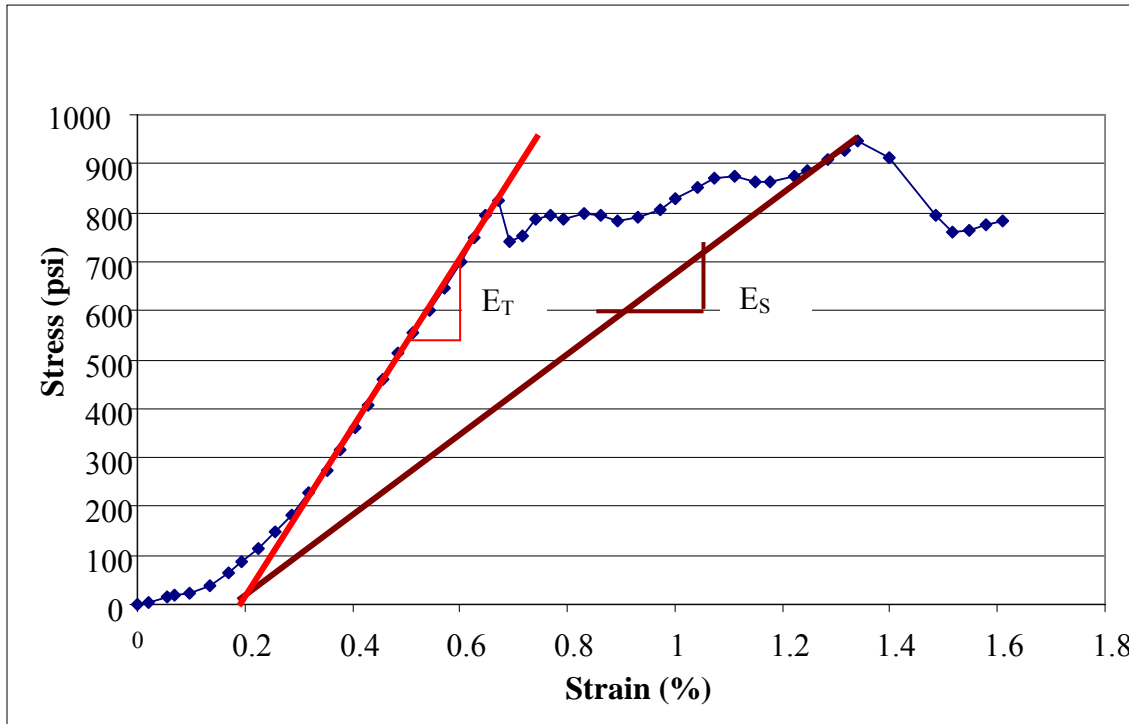


Figure 6.4 Secant vs. Tangent Young's Modulus on 17<sup>th</sup> Street Bridge Data from LTSO4

Also shown in each Figure are summary statistics (median, mean, standard deviation, and COV), of the data as well as a lognormal distribution fit to the data. From a comparison of Figures 6.5 and 6.6, the mean of the tangent modulus is approximately 1.8 times the secant mean modulus, but the variation, COV of each are quite similar.

From the boring logs, the recoveries varied from 65% to 95% with a mean value of 75%. Based on Figure 6.3, an  $E_m/E_i$  ratio of 0.45 was selected, and the Mass Modulus was computed using both the secant and tangent  $E_i$  moduli. Figure 6.5 and 6.6 show the probability density

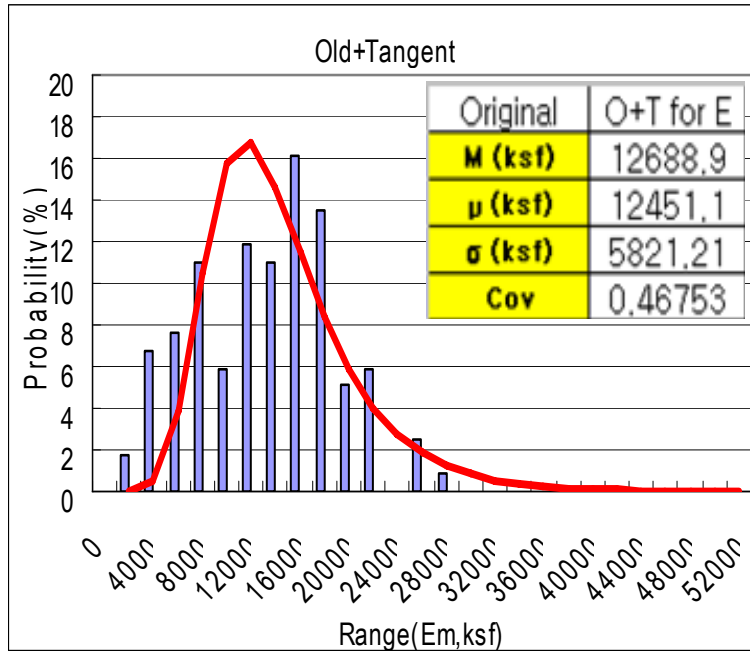


Figure 6.5 Tangent Mass Modulus of 17<sup>th</sup> Street Bridge (118 Values)

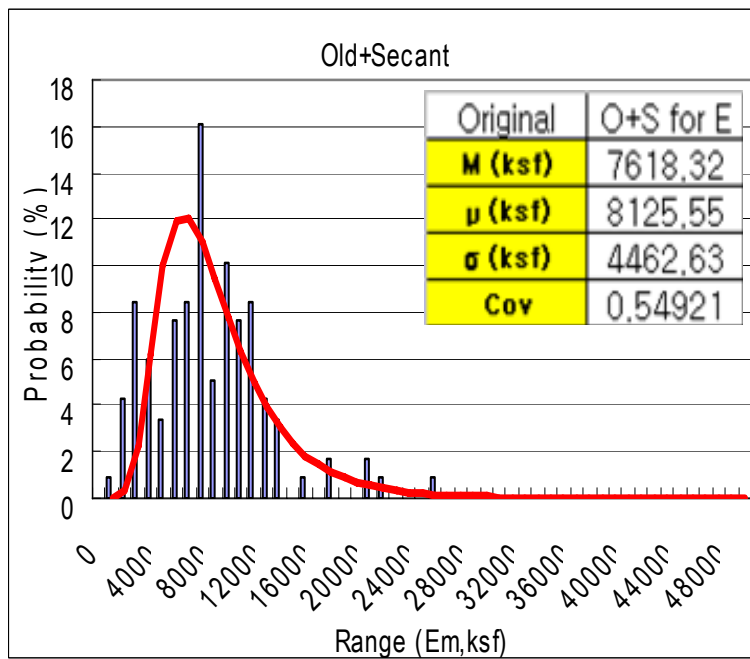


Figure 6.6 Secant Mass Modulus of 17<sup>th</sup> Street Bridge (118 values)

distribution for the Tangent and Secant Mass Modulus, using both the recent LTSO4 data (102), as well as the original design data (16) set.

Clearly, from Figures 6.5 and 6.6, the mass modulus of the rock varies over the site as well as within 3D below the shaft and must be accounted for in Eqs. 6.8 - 6.10. As identified in Chapter 3, one may use the harmonic mean modulus,  $E_h$ , or:

$$\frac{n}{E_h} = \left[ \frac{1}{E_1} + \frac{1}{E_2} \dots \frac{1}{E_n} \right] \quad \text{Eq. 6.11}$$

In the case of different layer thicknesses:

$$E_h = \left[ \frac{1}{H} \int_0^H \frac{dz}{E(z)} \right]^{-1} \quad \text{Eq. 6.12}$$

Fenton (2005) showed an excellent correlation with FEM analysis using the geometric mean,  $E_g$ , or:

$$E_g = \left( \prod_{i=1}^n E_i \right)^{1/n} = \exp \left( \frac{1}{n} \sum_{m=1}^n \ln(E_m) \right) \quad \text{Eq. 6.13}$$

It should be recognized that the geometric mean generally lies between the arithmetic and harmonic mean and is used in this project to assess contact stresses (Eq. 6.6). The next question is the influence of geospatial correlation on the geometric mean modulus,  $E_g$ . Specifically, Eq. 6.13 requires the sum or average of  $\ln(E_m)$  over a distance (3D) below the shaft. If  $Y = \ln(E_m)$ , then the term inside the parenthesis in Eq. 6.13 becomes the simple arithmetic average, i.e.,  $1/n \sum Y = F$ . Note, that because  $Y [\ln(E_m)]$  is a random variable, so is  $F$  and it will have the general summary statistics, i.e.,  $m_F$ , and  $\sigma_F^2$  as well. As discussed for side friction, the mean of  $F$ ,  $m_F$ , will be the same as  $m_Y$ ; however the variance of  $F$  will be reduced by the averaging process (i.e.,

$1/n \sum Y = F$ ) or  $\sigma_F^2 = \alpha \sigma_Y^2$ , where  $\sigma_Y^2$  represents the variance of  $\ln(E_m)$  over the site. As was found with side friction, Eq. 6.2 for  $\alpha$  or the monograph, Figure 6.1, may be used to assess  $\alpha$  for the case of  $D = 0$  and an appropriate correlation length, “a”. Once the value of  $\alpha$  has been assessed then the random function,  $F$  ( $m_F = m_Y$ ; and  $\sigma_F^2 = \alpha \sigma_Y^2$ ) is also known and it may be substituted back into Eq. 6.13 to obtain  $E_g$ , also a random function.

In the case of the 17<sup>th</sup> Street Bridge, the  $\ln(E_m)$  was calculated for all the new and old tangent data. The mean of  $\ln(E_m) = m_Y = 9.2697$  and the standard deviation of  $\ln(E_m) = \sigma_Y = 0.4053$  was obtained. Next,  $\alpha$  was obtained for  $L/D = 3$ , and  $a = 5, 10$ , and  $15$  from Figure 6.1, from which  $\sigma_F^2 = \alpha \sigma_Y^2$  was found. Subsequently, a Monte Carlo simulation was performed to generate typical  $F$  values which were substituted into Eq. 6.13, to generate the distributions shown in Figures 6.7, 6.8, and 6.9.

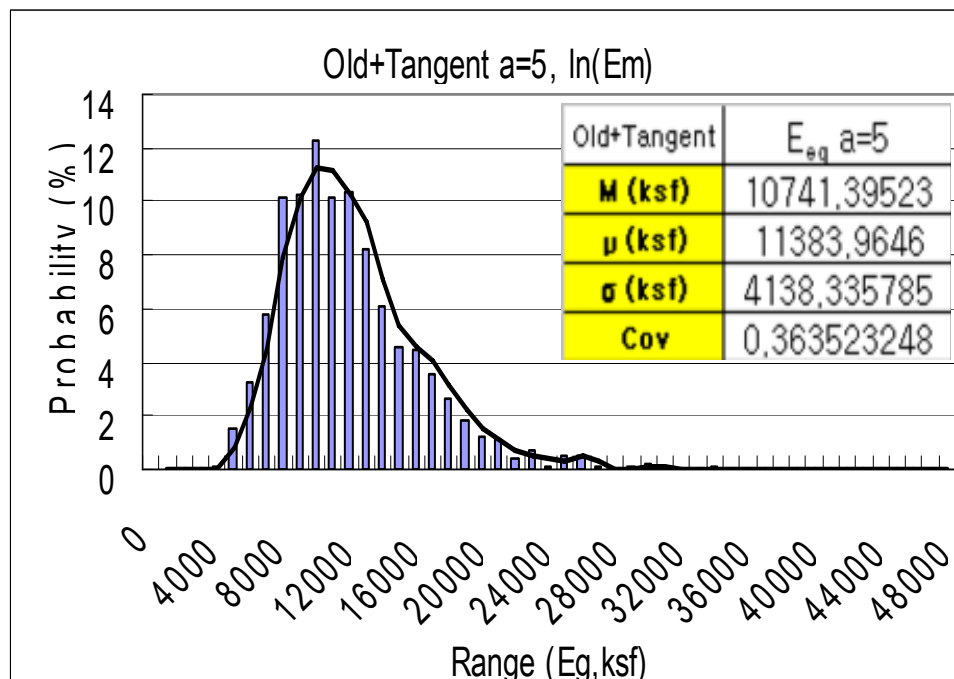


Figure 6.7 Geometric Mean Modulus,  $E_g$ , Assuming Correlation Length,  $a = 5$  ft from 17<sup>th</sup> Street Bridge Data

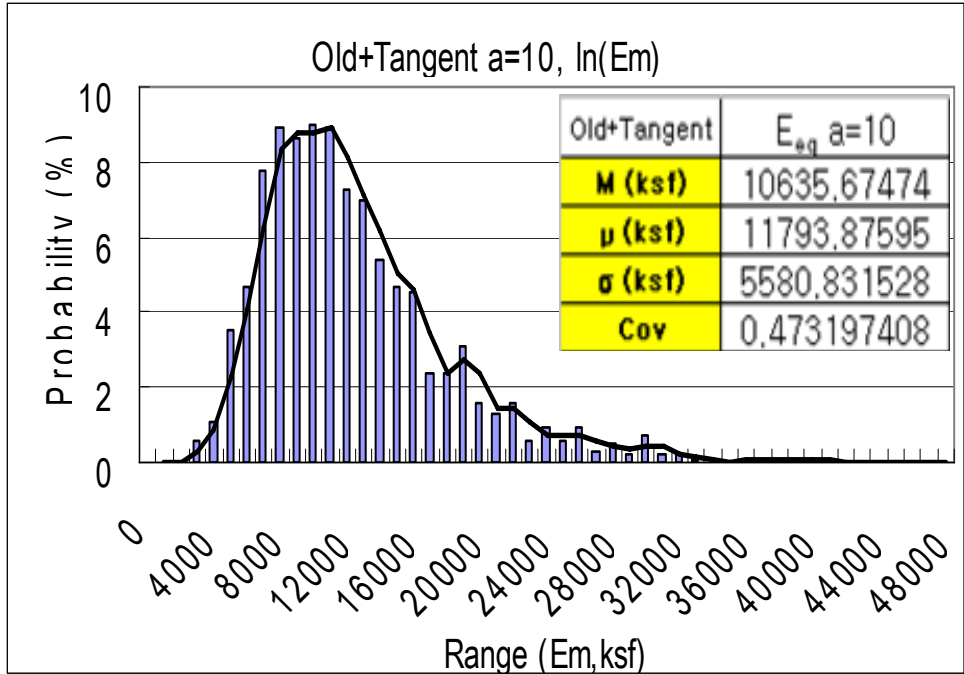


Figure 6.8 Geometric Mean Modulus,  $E_g$ , Assuming Correlation Length,  $a = 10$  ft from 17<sup>th</sup> Street Bridge Data

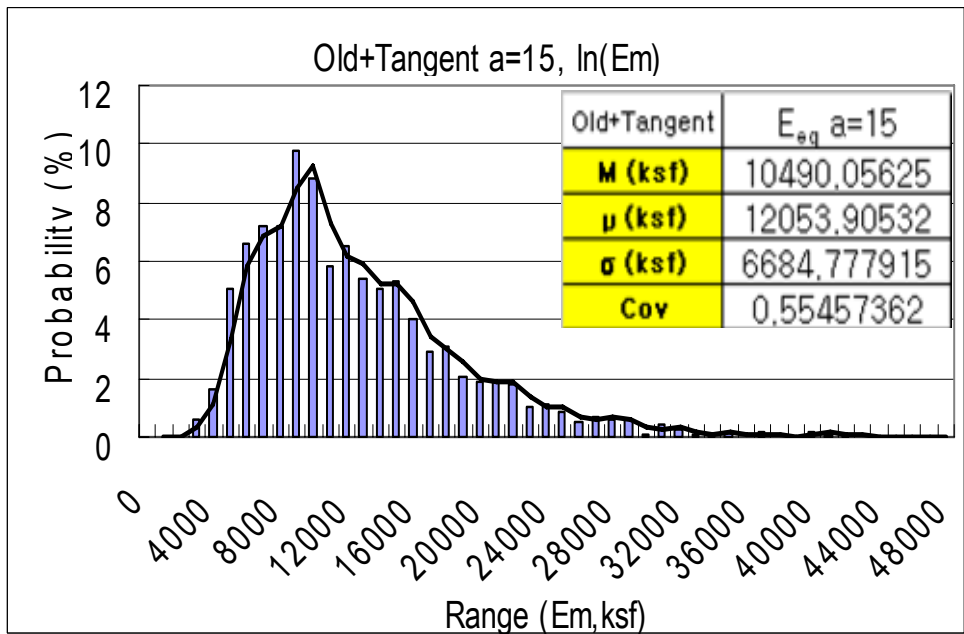


Figure 6.9 Geometric Mean Modulus,  $E_g$ , Assuming Correlation Length,  $a = 15$  ft from 17<sup>th</sup> Street Bridge Data

Of particular interest is a comparison of the Geometric Mean Modulus,  $E_g$ , with the original field data,  $E_m$ , as well as the inverted lognormal distribution which is shown as the red curve in Figure 6.5. Its summary statistics show a mean of 13,140 ksf, a standard deviation,  $\sigma$  of 10,326 ksf, and a COV equal to 0.785. The red curve represents what the field samples should look like if enough samples were recovered and the mass modulus,  $E_m$ , was lognormally distributed. As expected, the Geometric mean,  $E_g$  is reduced from both the field sample mean (12,689 ksf), and the assumed inverted lognormal mean (13,140 ksf). The major difference occurs in the COV of the  $E_g$  versus the field (0.4675) and its inverted lognormal COV (0.785). Specifically, due to spatial correlation represented in the Covariance function as correlation lengths of five, ten and fifteen feet, the COV of  $E_g$  was reduced to 0.3635, 0.4732, and 0.5545 respectively, from the COV of  $E_m$ . The highest reduction in COV of  $E_g$  to 0.3635 is due to the lack of correlation between  $E_m$  over short distances (i.e., the data are more random), which results in lower variability in  $E_g$  when averaged geometrically.

Using the Geometric Mean Function,  $E_g$  (Figures 6.7 - 6.9), in Eqs. 6.8 - 6.10 and subsequently Eq. 6.6, the distribution of the contact stress,  $q_b$  at the bottom of the drilled shaft was obtained for a top shaft movement of 1.6 inches. This is shown in Figures 6.10, 6.11, and 6.12. Note that the Figures represent the expected distribution of end bearing on the east side of the site where all the data were collected (i.e., in the vicinity of LTSO4). Variograms developed for the data showed a typical vertical correlation length of approximately eight feet, which from Figures 6.10 and 6.11 suggest a mean tip resistance of between 120 to 125 ksf and a standard deviation above and below the mean of 75 ksf to 173 ksf. The actual recorded tip resistance was

120 ksf for LTSO4 and the other east side shaft LTSO3 was 110 ksf. Both were close to the mean and well within the one standard deviation (75 to 173 ksf).

Knowing the distribution of the end bearing, the LRFD resistance factors,  $\phi$  may be assessed for the shafts from Eq.6.5 for multiple reliability index values,  $\beta$  (e.g.,  $\beta = 2.5$  and 3). The computed  $\phi$  values are also shown in each Figure depending on the correlation length, “a”. It is apparent, that there is a significant effect of “a”, on the  $\phi$  factor for a specific reliability index,  $\beta$ . For example, in the case of  $\beta$  equal 3.0, the  $\phi$  varies from 0.51 to 0.32, and the design end bearing goes from  $0.51 (124 \text{ ksf}) = 63.2 \text{ ksf}$  to  $0.32 (124 \text{ ksf}) = 39.7 \text{ ksf}$ .

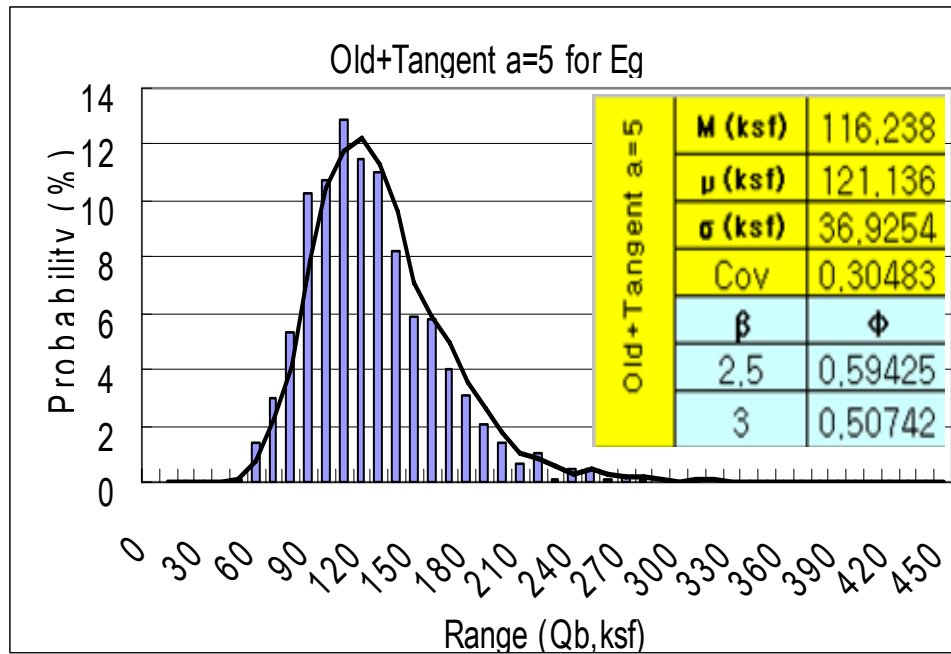


Figure 6.10 Histogram/PDF of Contact Stress,  $q_b$ , Using  $E_g$  with Correlation Length,  $a = 5$ ft from 17<sup>th</sup> Street Bridge Data

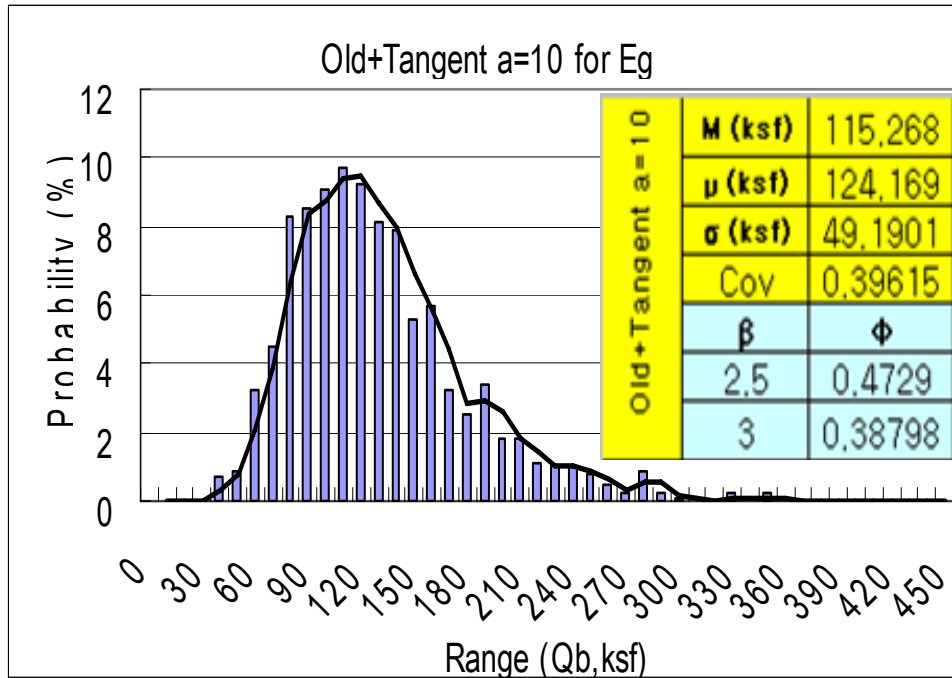


Figure 6.11 Histogram/PDF of Contact Stress,  $q_b$ , Using  $E_g$  with Correlation Length,  $a = 10$  ft from 17<sup>th</sup> Street Bridge Data

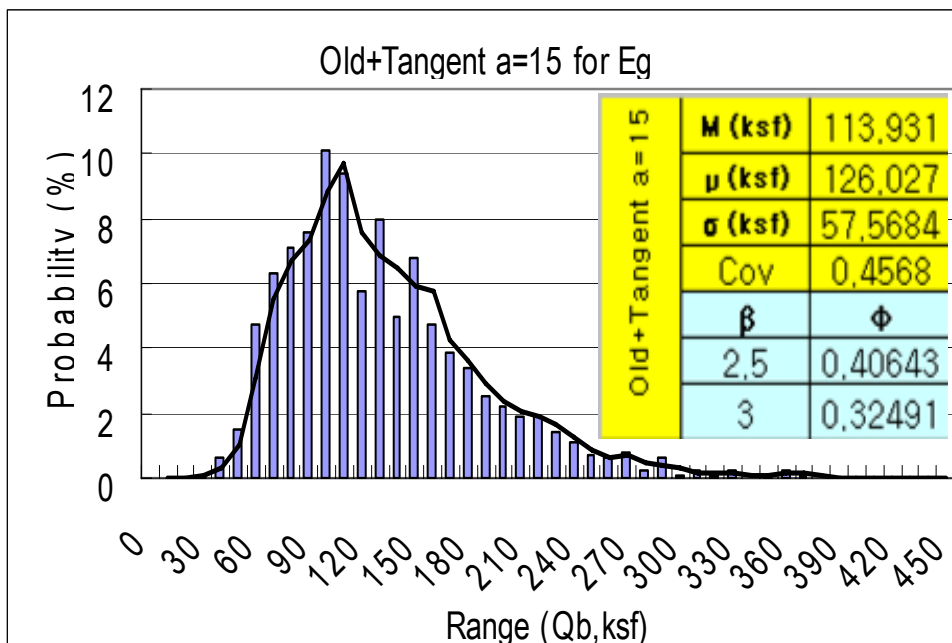


Figure 6.12 Histogram/PDF of Contact Stress,  $q_b$ , Using  $E_g$  with Correlation Length,  $a = 15$  ft from 17<sup>th</sup> Street Bridge Data

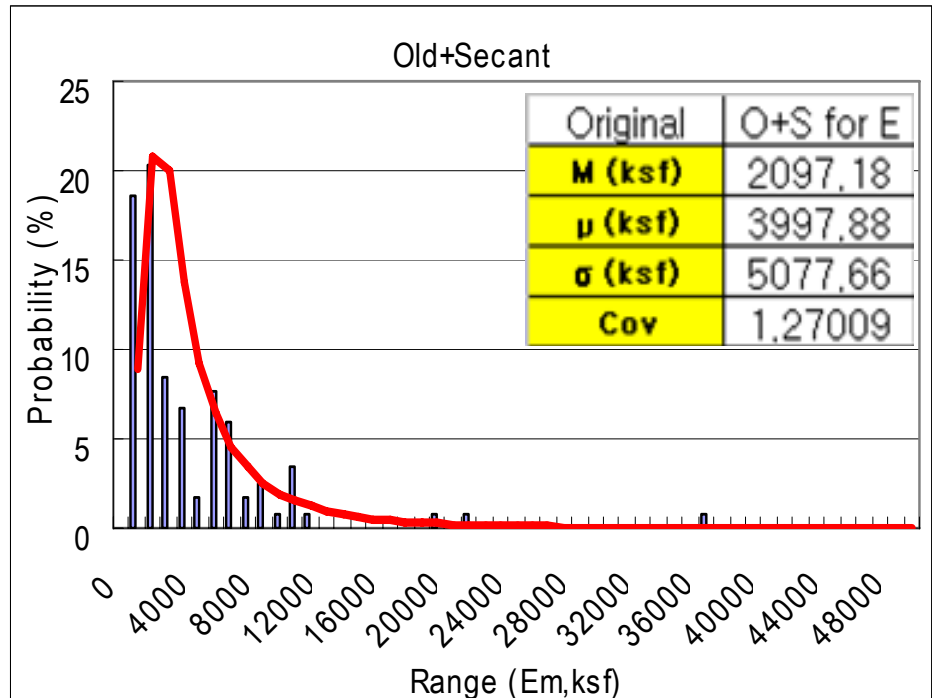


Figure 6.13 Secant Mass Modulus of Fuller Warren Bridge (96 values)

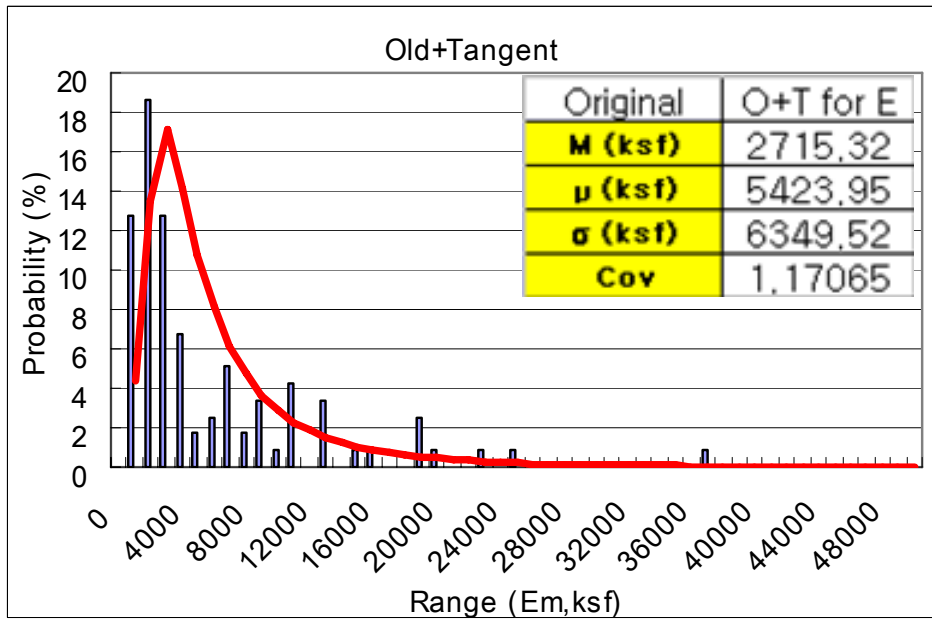


Figure 6.14 Tangent Mass Modulus of Fuller Warren Bridge (96 values)

### 6.3 LRFD resistance factors, $\phi$ for End Bearing at the Fuller Warren Bridge

Like the 17<sup>th</sup> Street Bridge, the Fuller Warren Bridge site was revisited and three new borings along with sixty-three samples were recovered and tested by the State Materials Office. Similar to the 17<sup>th</sup> Street Bridge data, the mean of the tangent modulus was approximately 1.7 times the secant mean modulus. However, the COV of each are quite different: 0.47 & 0.55 for 17<sup>th</sup> Street Bridge and 1.27 and 1.17 for the Fuller Warren Bridge. The latter will have a profound effect on the LRFD resistance factors,  $\phi$  for the two sites.

From the boring logs, the recoveries varied from 58% to 94% with a mean value of 77%. Based on Figure 6.3, an  $E_m/E_i$  ratio of 0.5 was selected, and the Mass Modulus was computed using both the secant and tangent  $E_i$  moduli. Figures 6.13 and 6.14 show the probability density distribution for the Tangent and Secant Mass Modulus, using data between LTSO3 and LTSO4 (63), as well as the original design data (33).

In the case of Fuller Warren, the  $\ln(E_m)$  was calculated for all the new and old tangent data and is shown Figure 6.13. The results showed a mean of  $\ln(E_m) = m_Y = 8.03$ , and a standard deviation of  $\ln(E_m) = \sigma_F = 1.14$ . Next,  $\alpha$  was obtained for  $L/D = 3$ , with a correlation range,  $a = 5, 10, \text{ and } 15$  feet from which  $\sigma_F^2 = \alpha \sigma_Y^2$  was found. Subsequently, a Monte Carlo simulation was performed to generate typical F values which were then substituted into Eq. 6.13 to generate the distributions shown in Figures 6.16, 6.17, and 6.18.

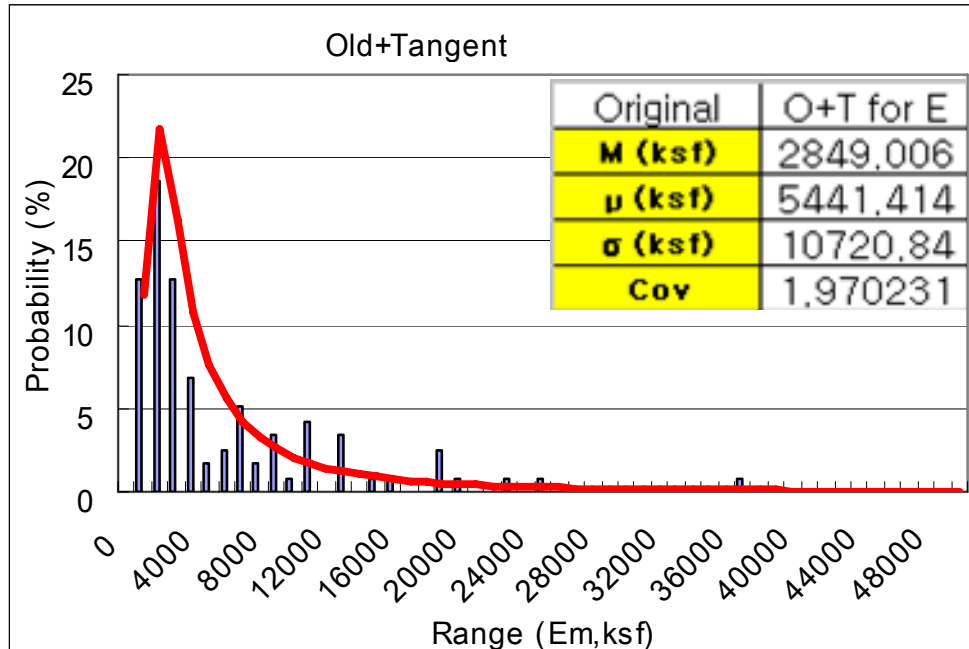


Figure 6.15 Tangent Mass Modulus for the Fuller Warren Bridge Site (96 values)

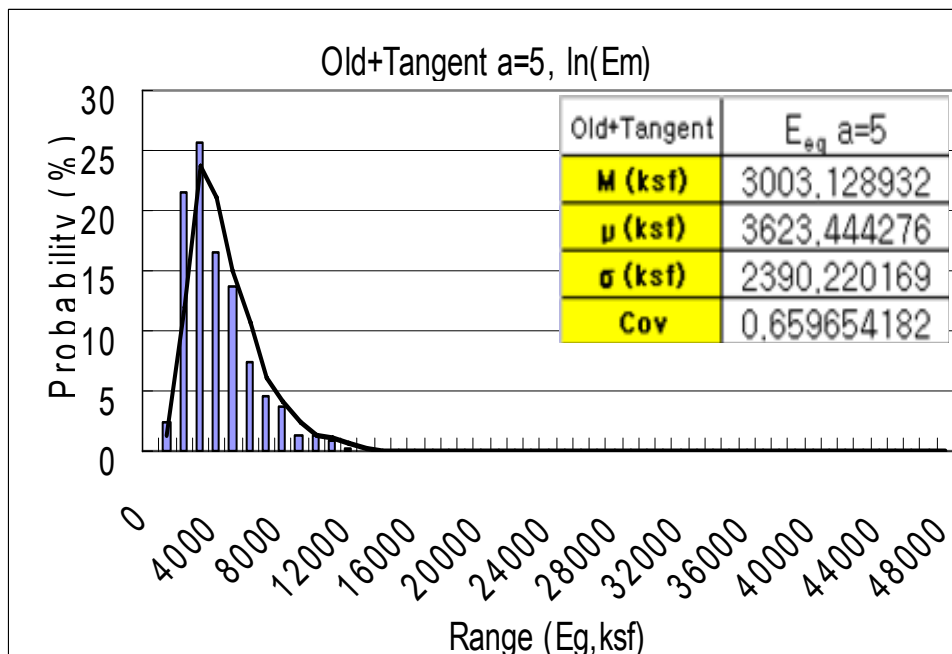


Figure 6.16 Geometric Mean Modulus,  $E_g$ , Assuming a Correlation Length,  $a = 5$  ft from Fuller Warren Bridge Data

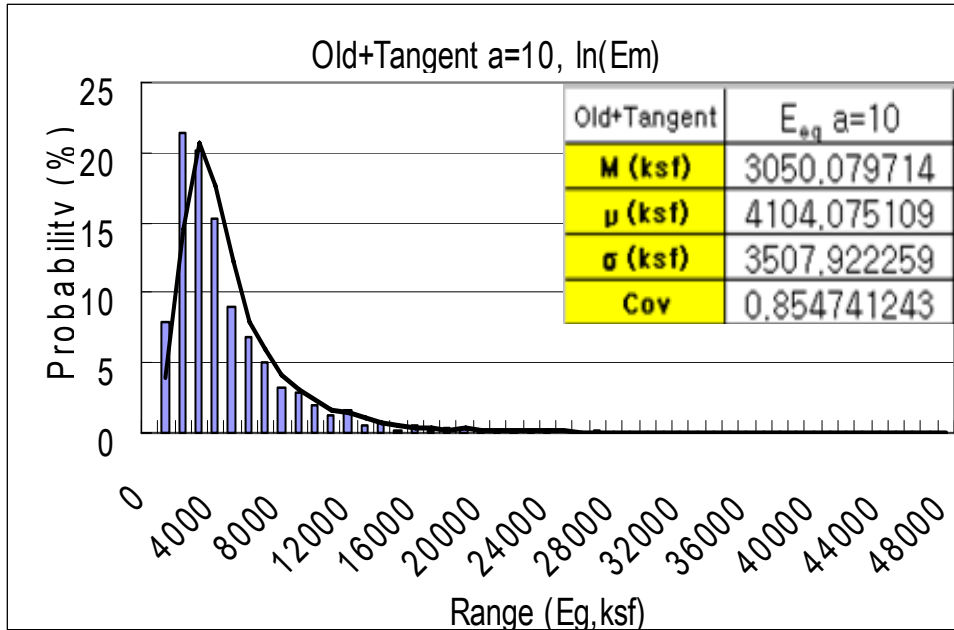


Figure 6.17 Geometric Mean Modulus, E<sub>g</sub>, Assuming a Correlation Length, a = 10 ft from Fuller Warren Bridge Data

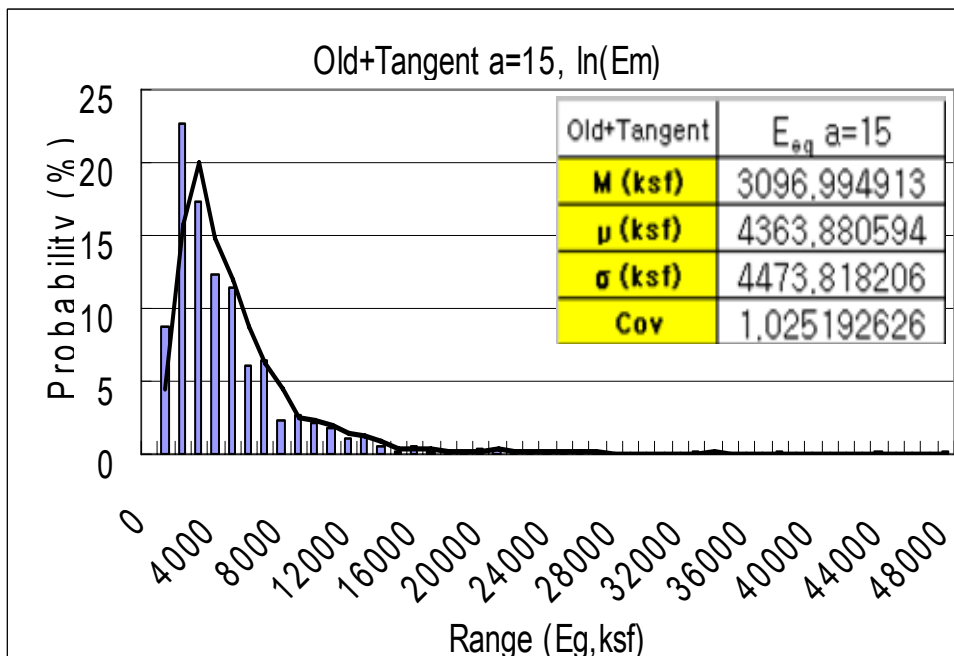


Figure 6.18 Geometric Mean Modulus, E<sub>g</sub>, Assuming a Correlation Length, a = 15 ft from Fuller Warren Bridge Data

Of interest is a comparison of the Geometric Mean Modulus,  $E_g$ , with the original field data,  $E_m$  as well as with the inverted lognormal distribution shown as the red curve in Figure 6.15. It has a summary statistics of mean = 5441.414 ksf, standard deviation,  $\sigma = 10720.84$  ksf, and a COV = 1.97 as shown inside Figure 6.15. The red curve represents what the field samples should look like if enough samples were recovered and the mass modulus,  $E_m$ , was lognormally distributed. The large difference occurs in the COV of the  $E_g$  versus the field (0.8465) and inverted lognormal COV (1.97). Specifically, due to spatial correlation represented in the Covariance function as correlation length, “a”, the COV of  $E_g$  was reduced to 0.65965, 0.85474, and 1.0252, respectively, from the COV of  $E_m$ . The highest reduction in the COV of  $E_g$  to 0.3635 is due to the lack of correlation between  $E_m$  over short distances (i.e., more random), which results in lower variability in  $E_g$  when averaged geometrically.

Using the Geometric Mean Function,  $E_g$  and Eq. 6.6, the distribution of the contact stress,  $q_b$  at the bottom of the drilled shaft was obtained for a top shaft movement of 3.2” (field data), as shown in Figures 6.19, 6.20, and 6.21. Note, the Figures represent the expected distribution of end bearing at the site where the data were collected (LT2 ~ LT 4). Variograms developed for the data showed typical vertical correlation lengths of approximately 14 feet, which from Figures 6.19 ~ 6.21 suggest a mean tip resistance of between 73 to 88 ksf and one standard deviation above and below the mean of 33 ksf to 160 ksf, respectively. The actual recorded tip resistances were 68 ksf for LTSO3, 108 ksf for LTSO 4 and 160 ksf for LTSO2. Evident, the results were close to the mean and well within the one standard deviation (33 ksf to 160 ksf). Sixty-three of the Moduli for the analysis were from locations between LTSO 4 and LTSO 3 and the other thirty-three values were from the entire site.

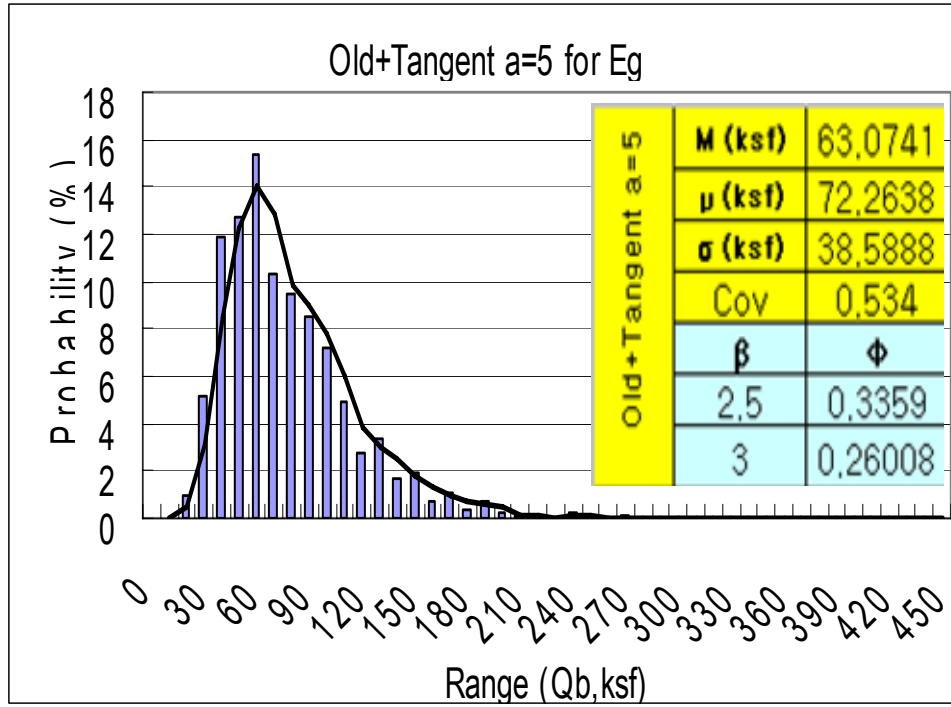


Figure 6.19 Histogram/PDF of Contact Stress,  $q_b$ , Using  $E_g$  with a Correlation Length,  $a = 5$  ft from Fuller Warren Bridge Data

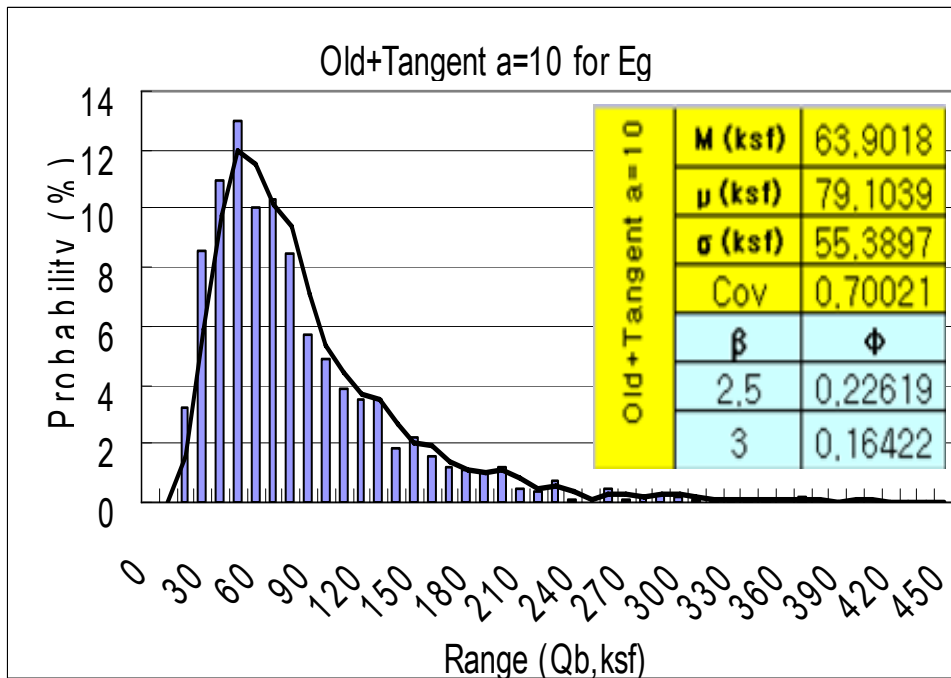


Figure 6.20 Histogram/PDF of Contact Stress,  $q_b$ , Using  $E_g$  with a Correlation Length,  $a = 10$  ft from Fuller Warren Bridge Data

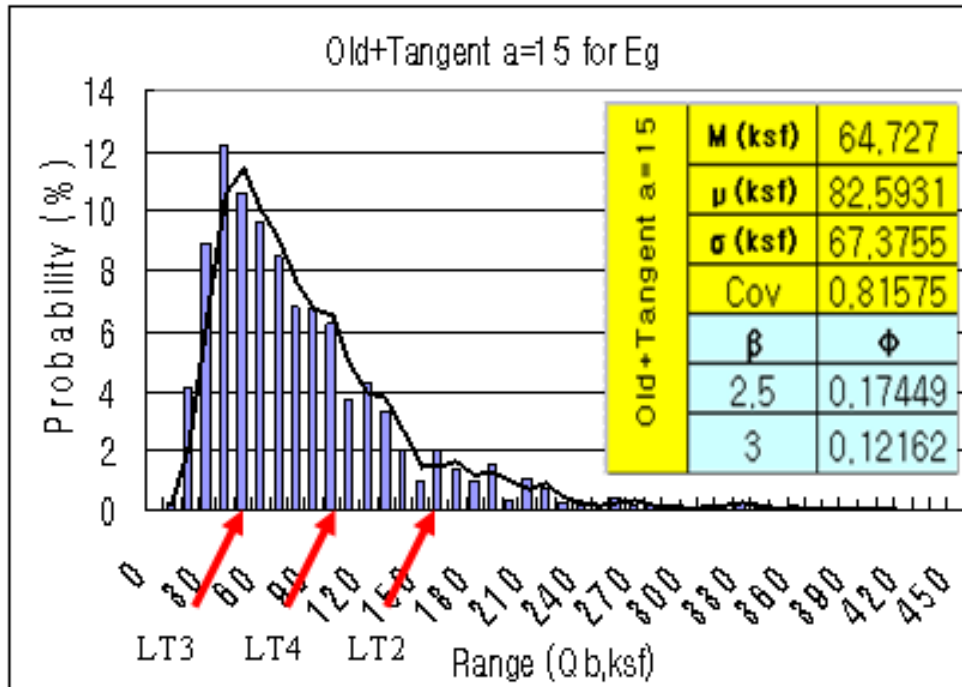


Figure 6.21 Histogram/PDF of Contact Stress,  $q_b$ , Using  $E_g$  with a Correlation Length,  $a = 15$  ft from Fuller Warren Bridge Data

A comparison of LRFD resistance factors from the 17<sup>th</sup> Street and Fuller Warren Bridges are quite interesting, i.e., Figures 6.10 ~ 6.12 and Figures 6.19 ~ 6.21. What controlled the variability of the resistance factors was the variability of  $E_g$ . For example, the data from Fuller Warren had much higher variability ( $E_g$  of 0.65 ~ 1.02 shown in Figures 6.16 ~ 6.18) versus the lower 0.36 ~ 0.55 for the 17<sup>th</sup> Street Bridge data (Figures. 6.7 - 6.9). The latter affected the variability in contact stresses which in turn affected the  $\phi$  values. For instance, the  $\phi$  values ranged from 0.50 ~ 0.32 ( $\beta = 3$ ) and 0.59 ~ 0.4 ( $\beta = 2.5$ ) for the 17<sup>th</sup> Street Bridge data, whereas Fuller Warren's  $\phi$  values ranged from 0.26 ~ 0.12 ( $\beta = 3$ ) and 0.33 ~ 0.17 ( $\beta = 2.5$ ) as shown in Figures 6.19 ~ 6.21. Evidently, the design end bearing for both sites are quite different. In addition, if sufficient data was collected at any single pier/shaft, an individual

LRFD resistance factor could be assessed and its value would most likely be higher than the value assigned to the entire site.

## CHAPTER 7 CONCLUSIONS AND RECOMMENDATIONS

This project focused on the development of axial, shear, and moment tip models for drilled shafts founded in Florida limestone. Specific interest was large shafts with short embedment lengths which undergo tip movements (i.e., translation and rotation).

Controlling much of the tip resistance (e.g., shear and moment) was the axial response which is in turn controlled by the material's Young's Modulus. To study this relationship a total of 16 centrifuge tests were performed, which varied shaft dimensions, rock strengths, rock recovery, Young's Modulus as well as layering. To ensure repeatability, each test was repeated twice. To assist with repeatability, artificial homogeneous limestone was used in the tests, which was constructed from ground limestone and cement. The following conclusions on axial tip resistance were found:

- Florida Limestone's mass modulus, i.e.,  $E_m$ , is very sensitive to recoveries or voids and is proportional to intact Young's Modulus,  $E_i$ , from core samples. Comparison of  $E_m$  vs  $E_i$  has shown values that fall between O'Neill's (1995) open joint and close jointed recommendations shown in Figure 7.1. The latter may be expressed as two bilinear curves that break at approximately 60% recoveries;
- The Mass Modulus,  $E_{mi}$  should be assessed from the tangent Young's Modulus,  $E_{i,t}$ ; use of secant Young's Modulus will generally be 1.8 to 2.0 times lower than tangent values (Fuller Warren & 17<sup>th</sup> Bridge sites);
- The axial tip resistance is very sensitive to mass modulus,  $E_m$  within a zone of three diameters below the tip of the shaft;
- Variable layered rock modulus, as well as numerical simulations (e.g., Fenton 2005) has suggested that the use of either the Harmonic Mean or the Geometric Mean provide reasonable predictions of axial tip resistance (e.g., O'Neill, FHWA 1995).

The Harmonic mean of the mass modulus may be assessed as:

$$\frac{n}{E_h} = \left[ \frac{1}{E_1} + \frac{1}{E_2} \dots \frac{1}{E_n} \right] \quad \text{Eq. 7.1}$$

or in the case of different layer thicknesses;

$$E_h = \left[ \frac{1}{H} \int_0^H \frac{dz}{E(z)} \right]^{-1} \quad \text{Eq. 7.2}$$

The geometric mean,  $E_g$ , may be expressed as:

$$E_g = \left( \prod_{i=1}^n E_i \right)^{1/n} = \exp \left( \frac{1}{n} \sum_{m=1}^n \ln(E_m) \right) \quad \text{Eq. 7.3}$$

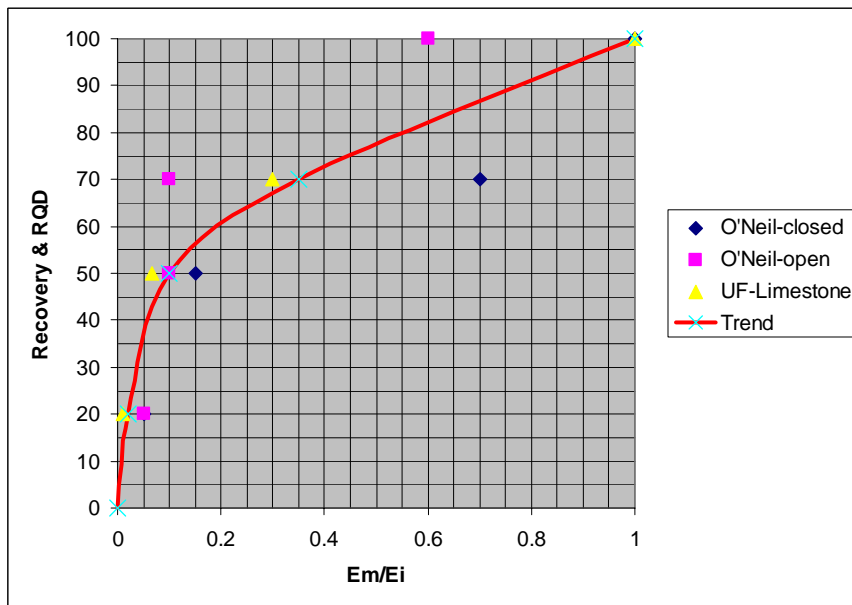


Figure 7.1 Ratio of Mass Modulus,  $E_m$  to Intact Young's Modulus,  $E_i$ , for Florida Limestone

Examples of predicting the tip axial contact stresses versus tip displacement using the FHWA method (O'Neill 1995) and both harmonic and geometric means are shown in Figure 7.2. These are assessed over a depth of 3D below the shaft tip. Since geometric moduli gave slightly better results it is recommended that further investigation of LRFD resistance factors be conducted as more data are collected.

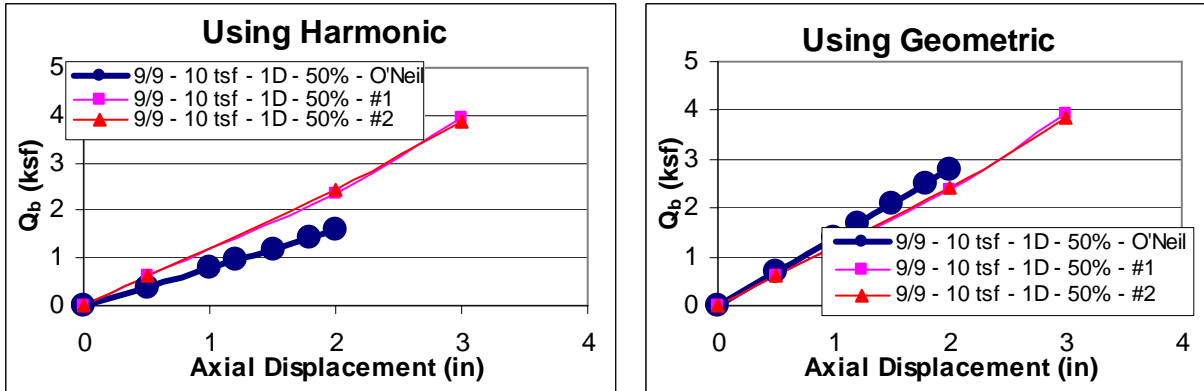


Figure 7.2 Tip Resistance from Field Data vs. Tip Resistance from O'Neill's Equation with Harmonic Average Method (left) and Geometric Average Method (right) for 10 tsf Rock with 50% Recovery at 1D

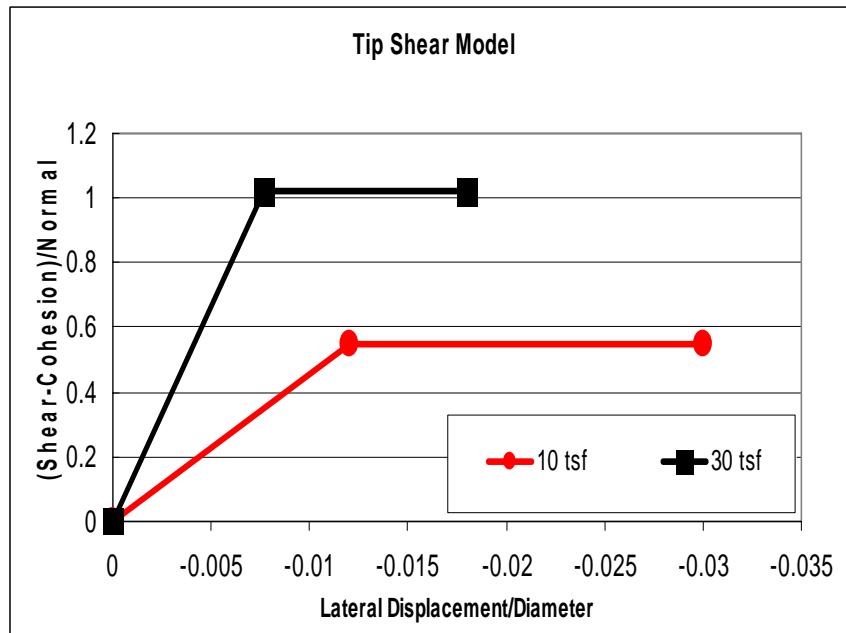


Figure 7.3 Drilled Shaft Tip Shear Model in Florida Limestone

After assessing the axial tip resistance, the shaft's tip shear resistance versus displacement may be found from Figure 7.3. For instance, knowing the lateral tip displacement and rock strength, Figure 7.3 is entered to obtain the normalized tip shear (i.e., shear stress minus cohesion divided by axial tip stress). Multiplying the normalized tip shear by axial tip stress and adding

cohesion will equal the mobilized tip shear. The bilinear representation covers typical rock strengths from 10 to 30 tsf and was obtained from 16 different types of boundaries conditions, e.g., L/D = 1 and 3 as well as homogeneous and layered scenarios. The bilinear characterization represents elastic behavior up to failure at which point no additional shear is mobilized. The values of the normalized shear failure, suggest rock angles of internal friction of 28 and 45 degrees with unconfined strengths,  $q_u$ , of 10 and 30 tsf, respectively.

Once the axial and shear resistance of the tip has been determined, the moment versus rotation model suggested by Bell (1991) is recommended, as shown in Figure 7.4. The relationship between moment and rotation is given by:

$$\theta_M = \frac{M}{GR^3 K_3^m} \quad \text{Eq. 7.4}$$

where G = Shear Modulus, R = shaft radius, M = applied moment, and  $K_3$  is a stiffness term which is a function of lateral tip shear and displacement.

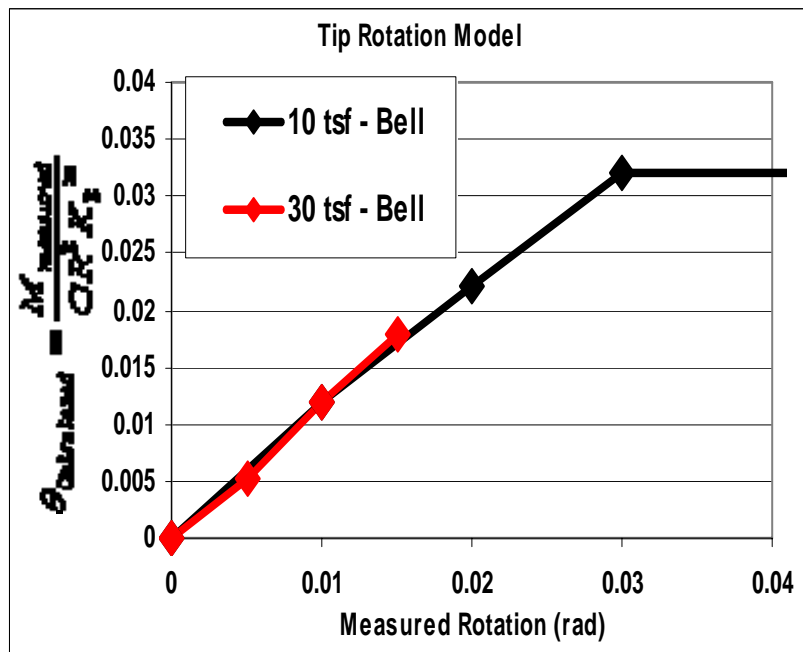


Figure 7.4 The Tip Rotation Model

In summary, the drilled shaft tip model characterized by Figure 7.5 requires that the axial tip resistance ( $q_b$ ) versus axial displacement be found first, followed by the tip shear vs. lateral tip displacement and ultimately, the tip moment vs. tip rotation.

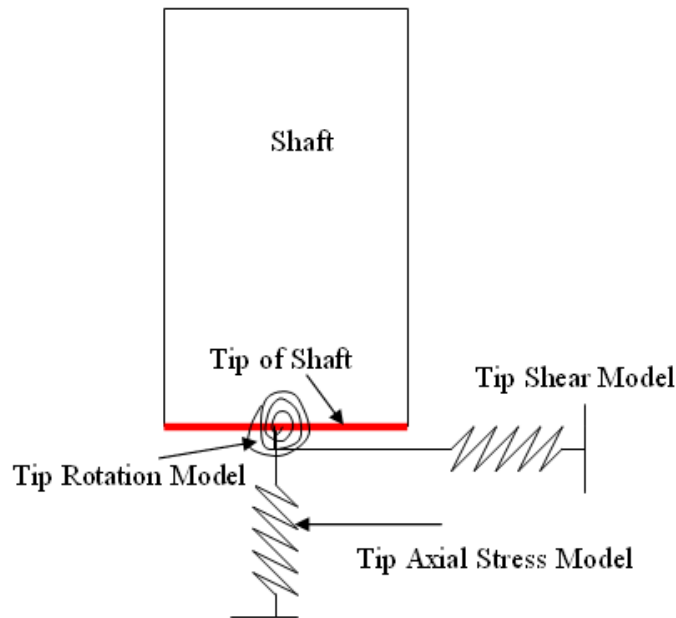


Figure 7.5 Drilled Shaft Tip Model

Besides developing a tip model, the question as to the appropriate LRFD resistance factors,  $\phi$  to use was investigated. Presently, one set of fixed resistance factors are used for drilled shafts in Florida. Unfortunately, spatial variability and associated correlation lengths (i.e., covariance function), suggest that LRFD resistance factors should vary from site to site. Specifically, the geometric mean, Eq.7.3 requires the sum or average of  $\ln(E_m)$  over a distance (3D) below the tip. If one lets  $Y = \ln(E_m)$  then the term inside the parenthesis in Equation. 7.3 becomes the simple arithmetic average, i.e.,  $1/n \sum Y = F$ . Note, because  $Y [\ln(E_m)]$  is a random variable, so is  $F$  and it will have the general summary statistics, i.e.,  $m_F$ , and  $\sigma_F^2$ . As discussed in

Chapter 6, the mean of  $F$ ,  $m_F$ , will be the same as  $m_Y$ ; however the variance of  $F$ , i.e.,  $\sigma_F^2$  will be reduced by the averaging process (i.e.,  $1/n \sum Y = F$  or  $\sigma_F^2 = \alpha \sigma_Y^2$ , where  $\sigma_Y^2$  represents the variance of  $\ln(E_m)$ ) over the site or pier location. The value of  $\alpha$  may be obtained from Figure 6.1 which is the integral of the covariance function over a distance of three times the shaft diameter,  $D$ . It was found that this distance strongly influenced the correlation length, “ $a$ ”. Once the value of  $\alpha$  has been assessed then the random function,  $F$  ( $m_F = m_Y$ , and  $\sigma_F^2 = \alpha \sigma_Y^2$ ) is also known and a Monte Carlo simulation may be performed to generate typical  $F$  values. The  $F$  values, which when substituted into Eq.7.3, yield the geometric mean modulus,  $E_g$  (Figure 7.6). When the distribution for  $E_g$  is substituted into O’Neill’s mobilized tip resistance model, a distribution of axial tip resistance develops shown in Figure 7.7. Using end bearing, i.e.,  $q_b$ , summary statistics (mean, COV), the LRFD resistance factors,  $\phi$  values for different levels of reliability may be determined.

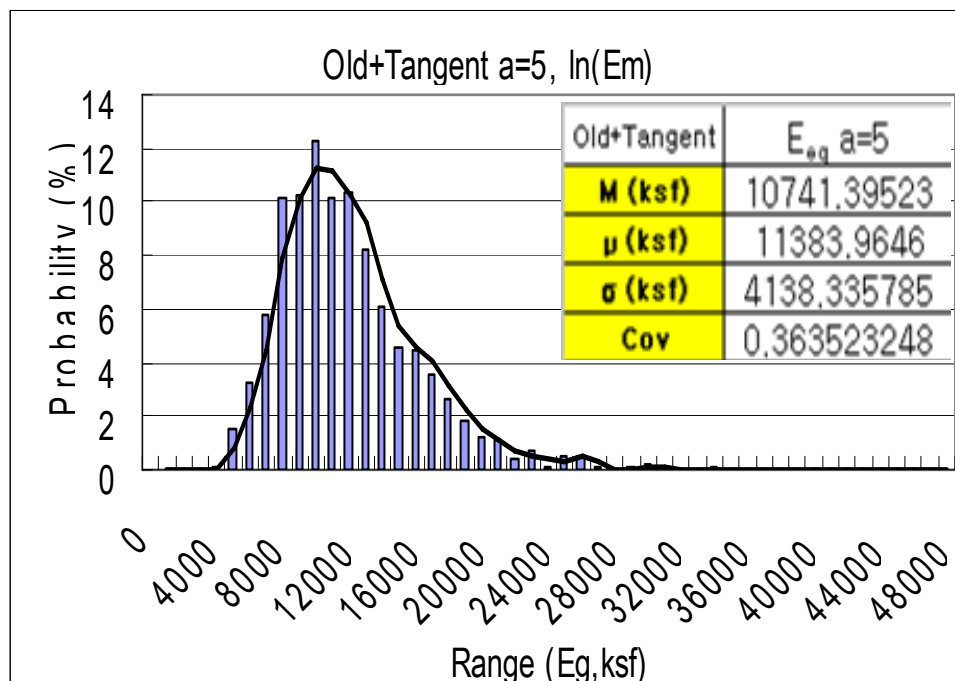


Figure 7.6 Estimated Variability of Geometric Mean Modulus at 17<sup>th</sup> Street Bridge

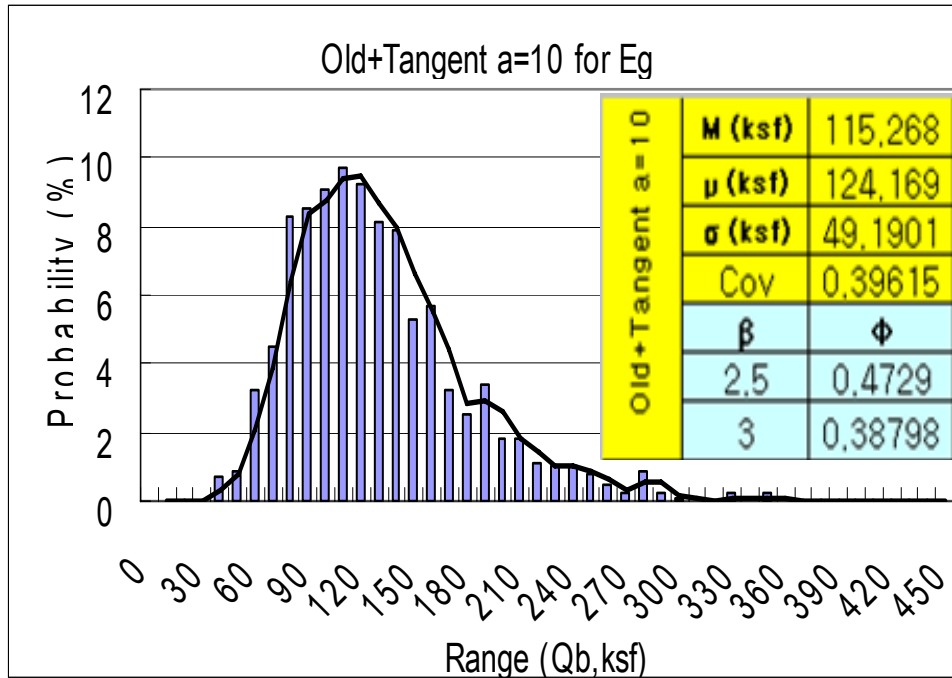


Figure 7.7 Histogram/PDF of Contact Stress,  $q_b$ , Using  $E_g$  with Correlation Length,  $a = 10$  ft at 17<sup>th</sup> Street Bridge

An assessment of LRFD resistance factors,  $\phi$  for two separate field sites, i.e., 17<sup>th</sup> Street and Fuller Warren Bridges showed quite dissimilar LRFD resistance factors,  $\phi$  values due to each sites Geostatistics. Consequently, the LRFD assessment process must be analyzed on a site by site basis. The latter has been coded into an Excel spreadsheet (Appendix E) and is available for standard design use.

## REFERENCES

- Bell, R.W., 1991. "The Analysis of Offshore Foundations Subjected to Combined Loading." MSc Thesis, Univ. of Oxford, Oxford, U.K.
- Chiles, J.P., Delfiner, P., 1999. "Modeling: Spatial Uncertainty." Wiley, New York
- Doherty, J.P., and Deeks, A.J., 2006. "Stiffness of a Flexible Circular Footing Embedded in an Elastic Half Space." *J. Geomechics*, Vol(6), 46-54.
- Fenton, G.A., and Griffiths, D.V., 1999. "Estimation for Stochastic Soil Models." *J. Geotech. Eng.*,125(6), 470-485.
- Fenton, G.A., and Griffiths, D.V., 2002. "Probability Foundation Settlement on Spatially Random Soil." *J. Geotech. Eng.*,128(5), 381-390.
- Fenton, G.A., and Griffiths, D.V., 2003. "Bearing Capacity of Spatially Random  $c-\phi$  Soils." Canadian Geotechnical Journal, 40(1), 54-65.
- Fenton, G.A., and Griffiths, D.V., 2005. "Three-Dimensional Probabilistic Foundation Settlement." *J. Geotech. Eng.*,131(2), 232-239.
- Hassan, K.M., O'Neill, M.W., Sheikh, S.A., and Ealy, C.D., 1997. "Design Method For Drilled Shafts in Soft Argillaceous Rock." *J. Geotech. Eng.*,123(3), 272-280.
- Hoit, M.I, McVay M.C., 1996. "FB-Pier User's Manual." Department of Civil & Coastal Engineering, University of Florida, Gainesville, Florida
- Isaaks, E.H, Srivastava R.M., 1989. "Applied Geostatistic" Oxford University Press.
- Kim, Myoung-Ho, 2001. "Analysis of Osterberg and Statnamic Axial Load Testing and Conventional Lateral Load Testing." Master's Thesis, University of Florida, Gainesville, Florida.
- McVay, M.C., Townsend, F.C. and Williams R.C, 1992. "Design of Socketed Drilled Shafts in Limestone." ASCE, Journal of Geotechnical Engineering, 118(10),1626-1637.
- National Instruments, 1999. "DAQ 6034E/6035E User Manual." National Instruments Corporation, Austin Texas.
- Niraula, Lila Dhar, 2004. "Development of Modified T-Z Curves For Large diameter Piles/Drilled Shafts In Limestone For FB-PIER." Master's Thesis, University of Florida, Gainesville, Florida.
- Reese, L. C., and O'Neil, M. W., 1999. "Drilled Shafts: Construction Methods and Design Procedures," FHWA-IF-99-025, U.S. Department of Transportation, ADSC, Dallas, Texas.

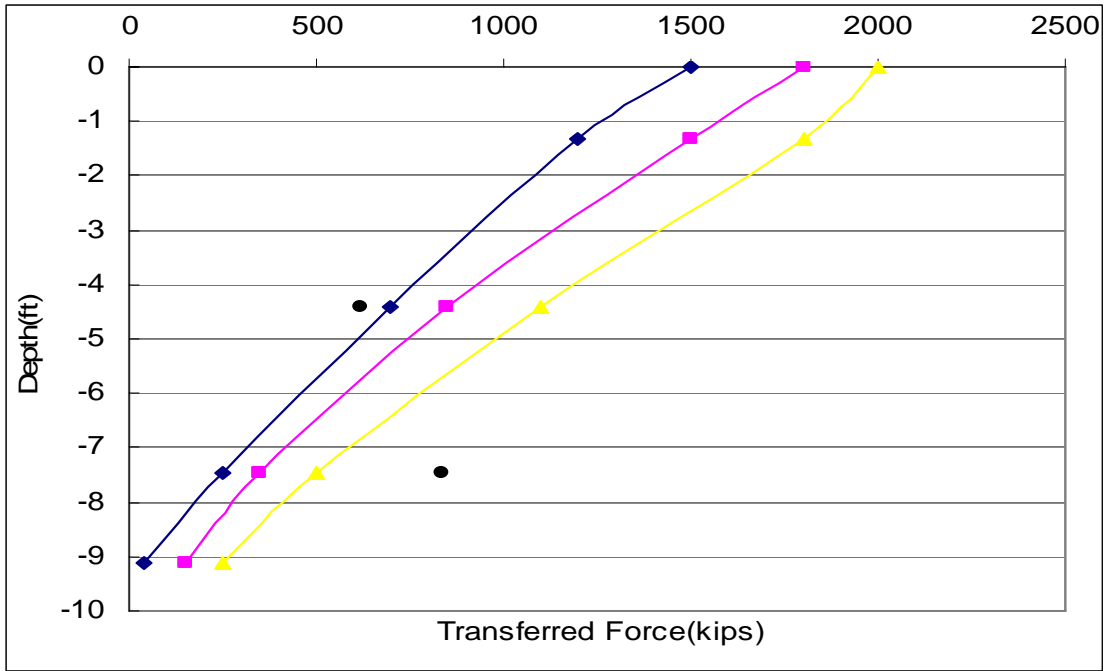
Styler, Mark.Anthony, 2006. "Development and Implementation of the Diggs Format to Perform LRFD Resistance Factor Calibration of Driven concrete Piles in Florida." Master's Thesis, University of Florida, Gainesville, Florida.

Ueshita. K, and Meyerhof, G. G., 1967. "Deflection of Multilayer Soil System," *J. Soil Mechs. Fndns. Divn., ASCE*, Vol.93, No. SM5, pp.257-282.

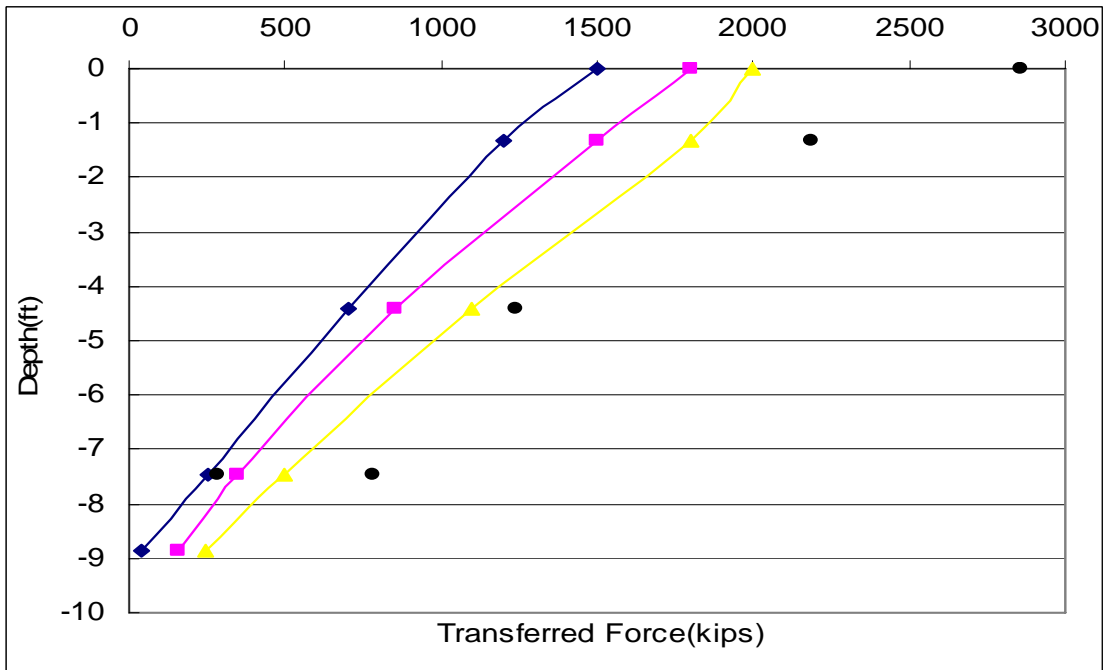
Vanmarcke, E, 1983. "Random Fields: Analysis and Synthesis." MIT Press, Cambridge, Mass

APPENDIX A

Compressive Force (Q) along Depth from Each Pair of Strain Gage with Trend Line

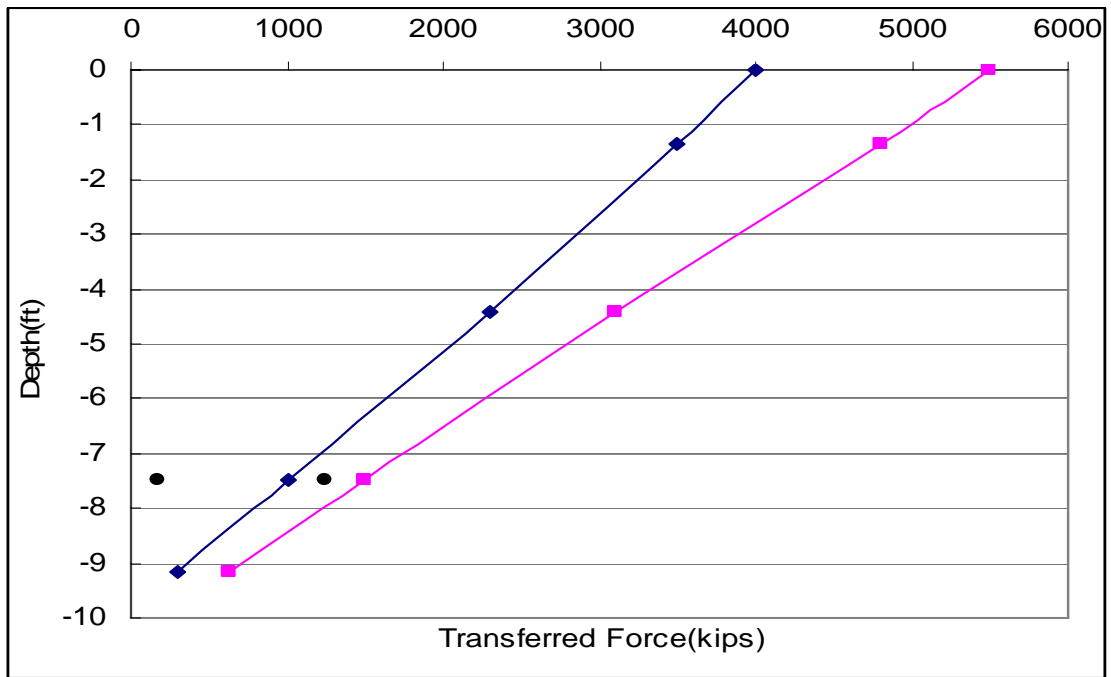


a)

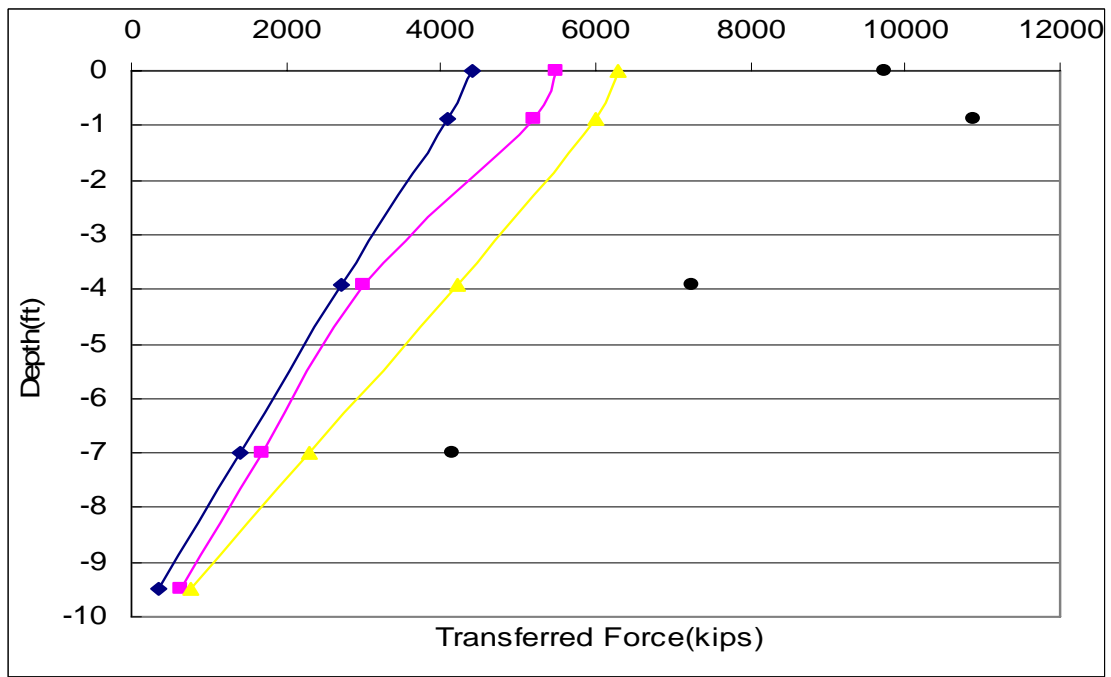


b)

Figure A.1 Result from 9 ft Diameter 9 ft Embedded Length in 10 tsf Rock with 50 % Styrofoam Layering below 1D below from Tip of Shaft a) Test No. 1 b) Test No. 2

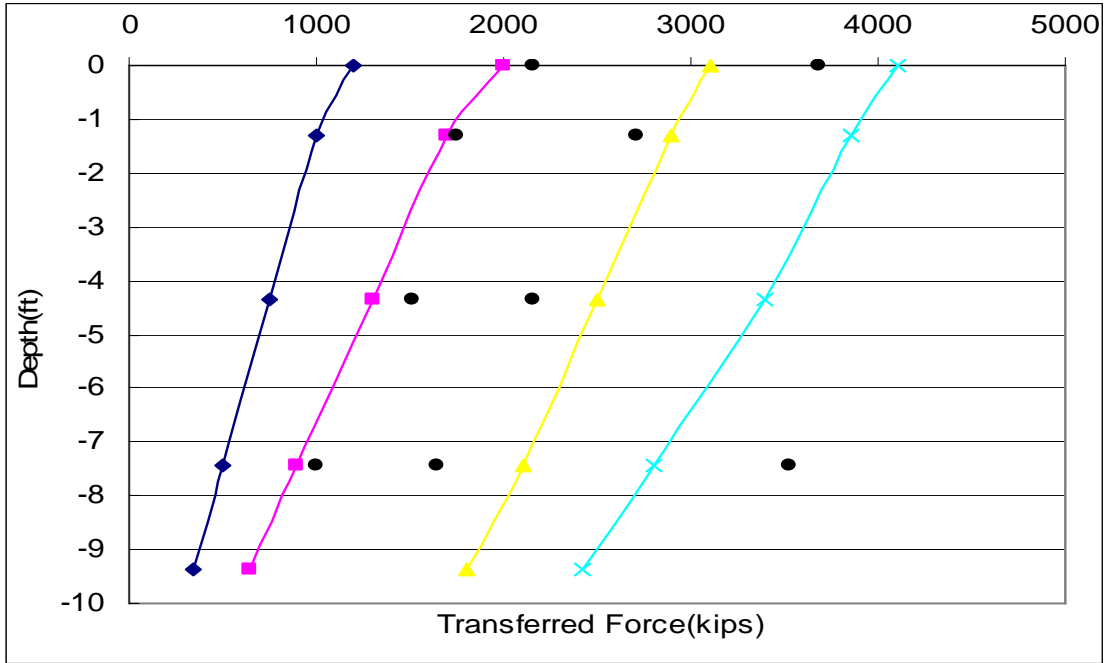


a)

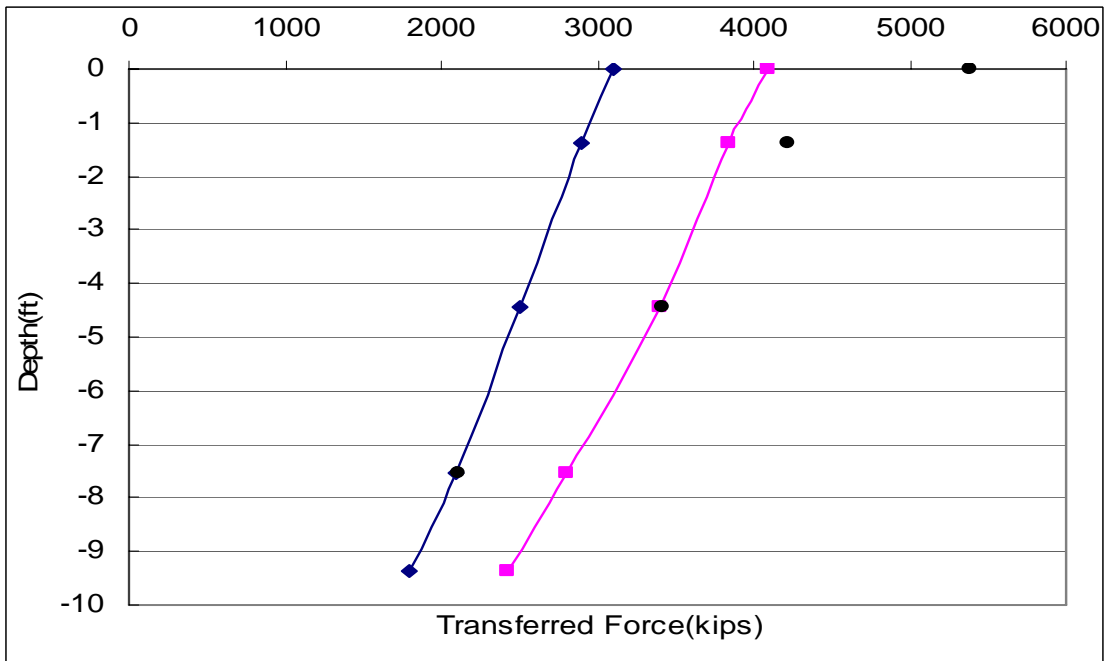


b)

Figure A.2 Result from 9 ft Diameter 9 ft Embedded Length in 30 tsf Rock with 50 % Styrofoam Layering below 1D below from Tip of Shaft a) Test No. 1 b) Test No. 2

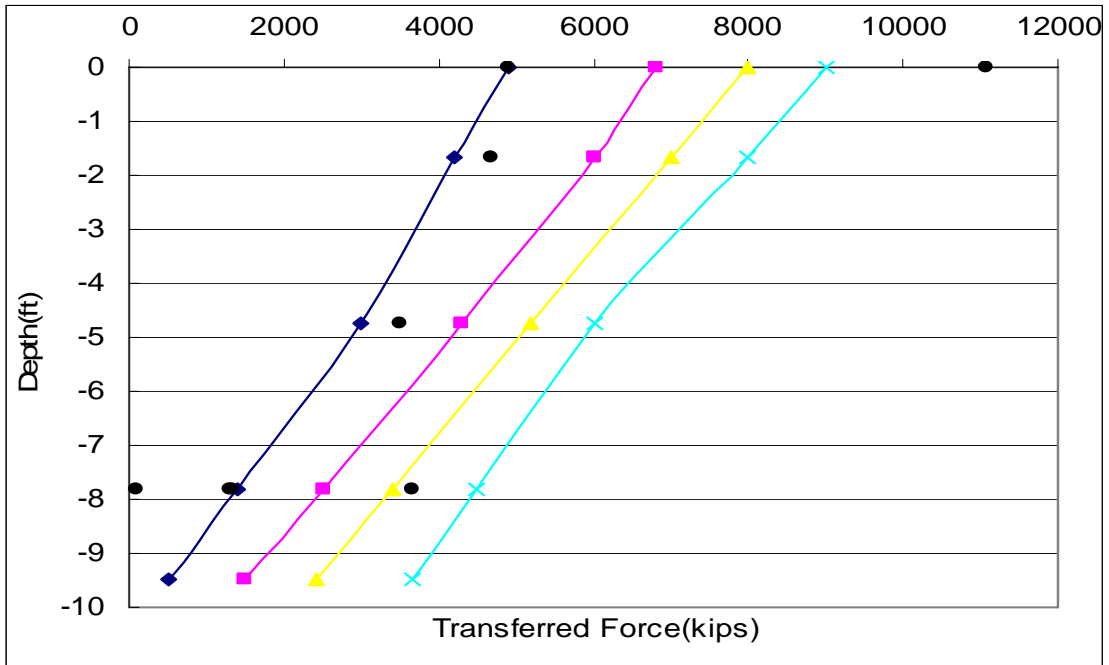


a)

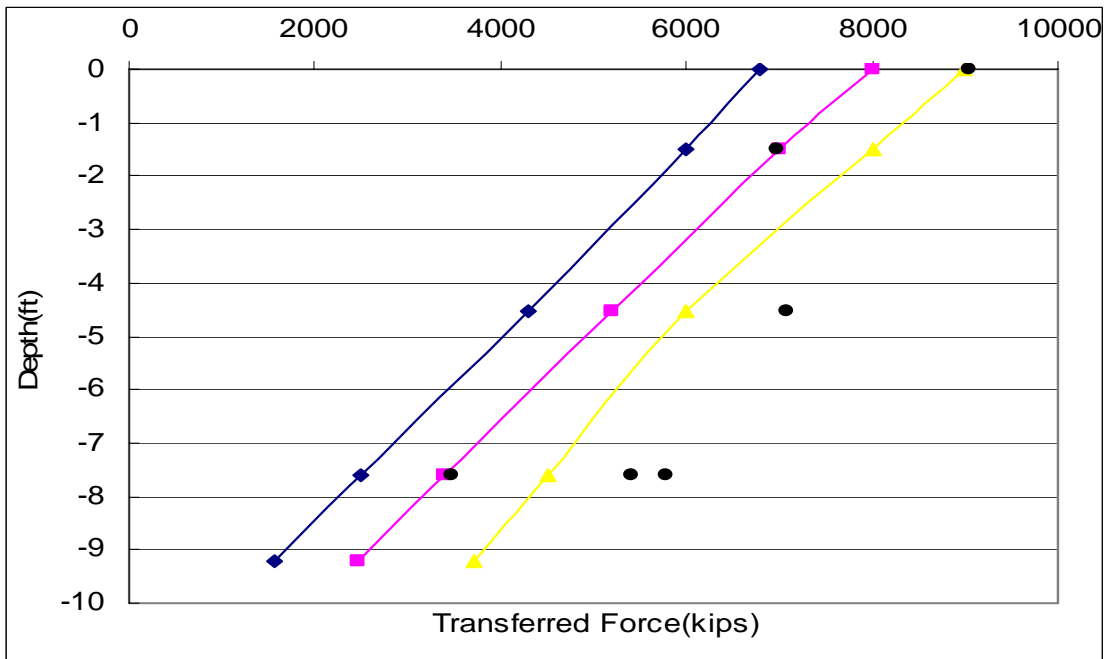


b)

Figure A.3 Result from 9 ft Diameter 9 ft Embedded Length in 10 tsf Rock a) Test No. 1 b) Test No. 2

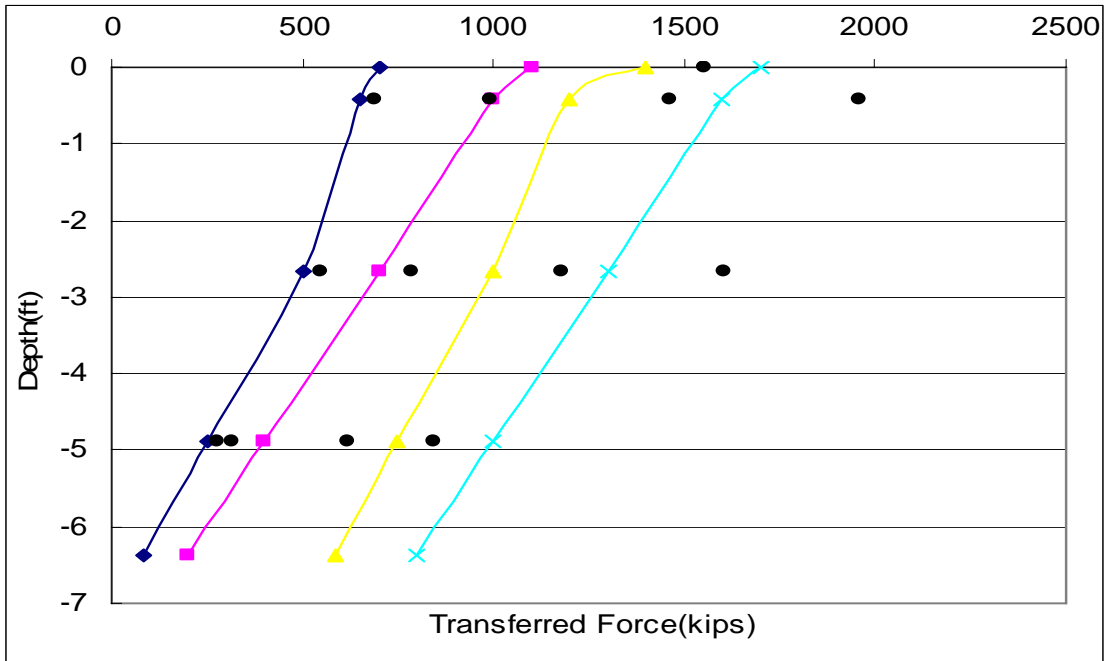


a)

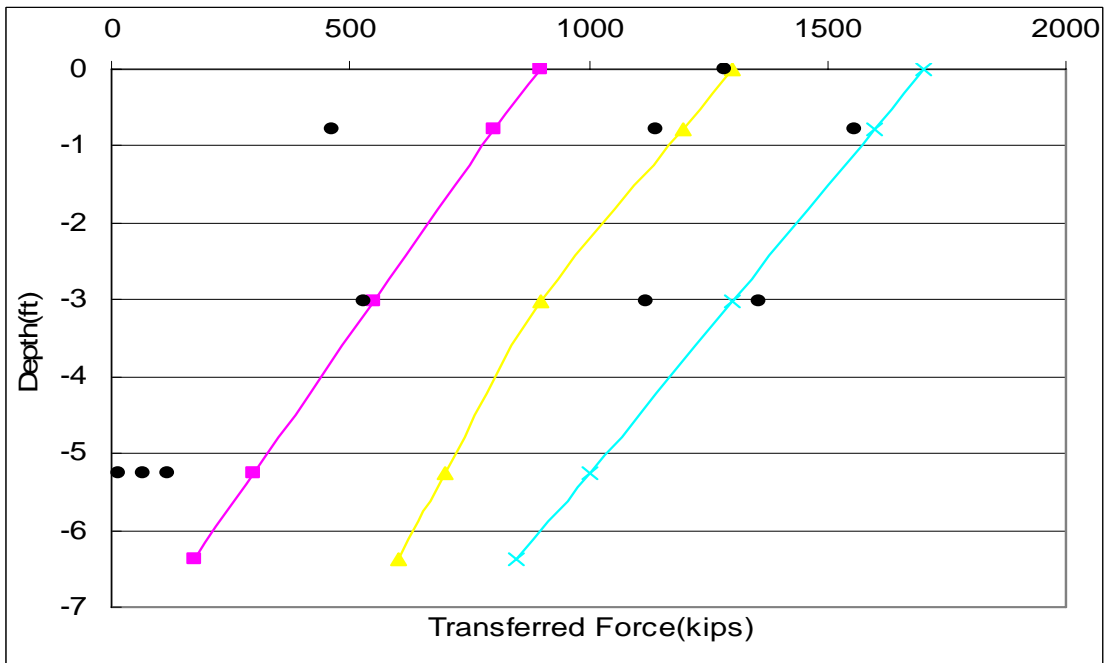


b)

Figure A.4 Result from 9 ft Diameter 9 ft Embedded Length in 30 tsf Rock a) Test No. 1 b) Test No. 2

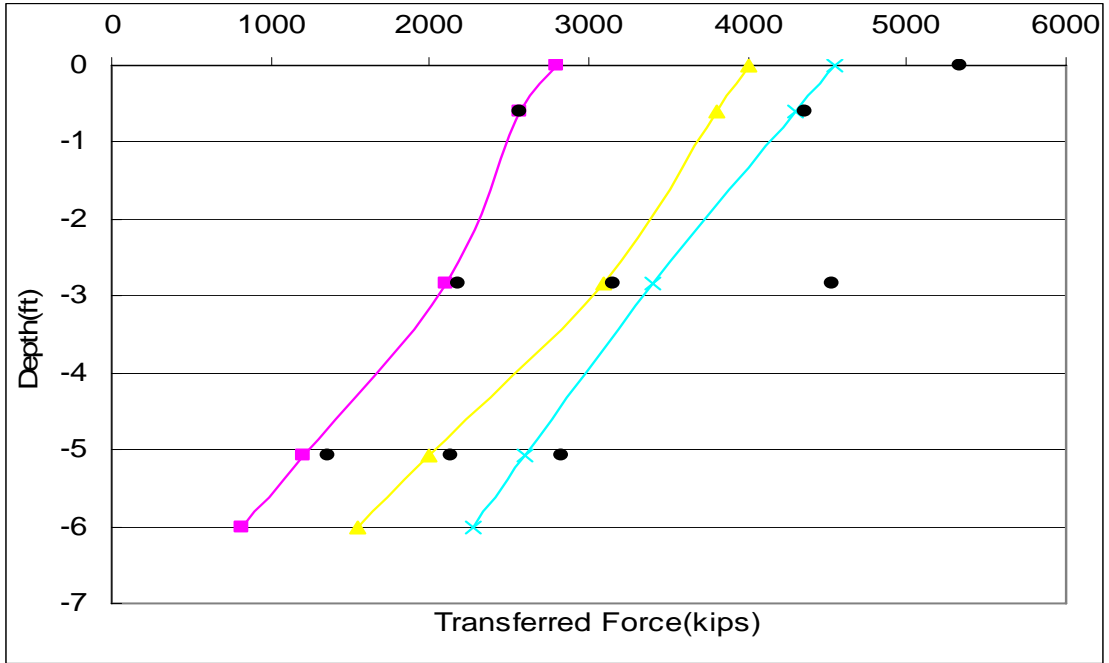


a)

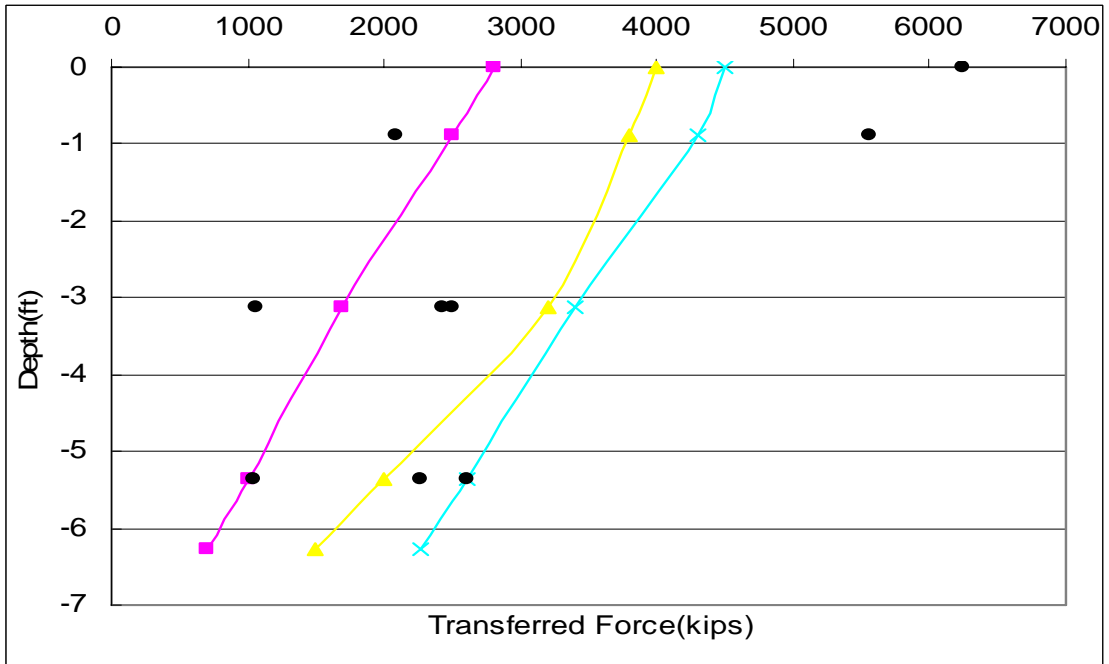


b)

Figure A.5 Result from 6 ft Diameter 6 ft Embedded Length in 10 tsf Rock a) Test No. 1 b) Test No. 2

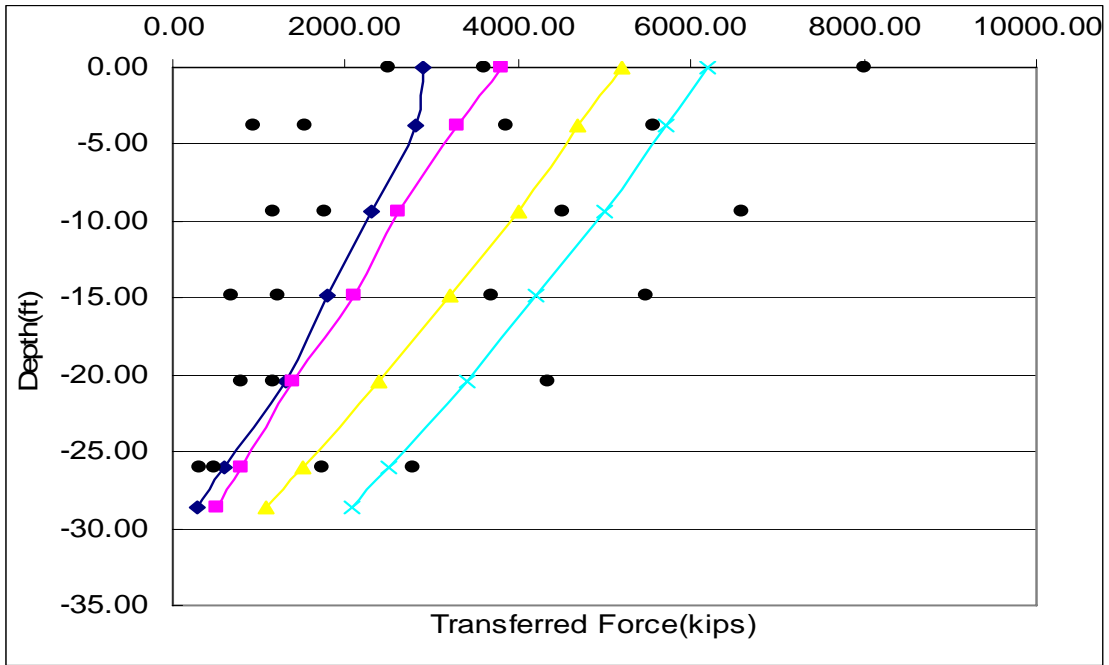


a)

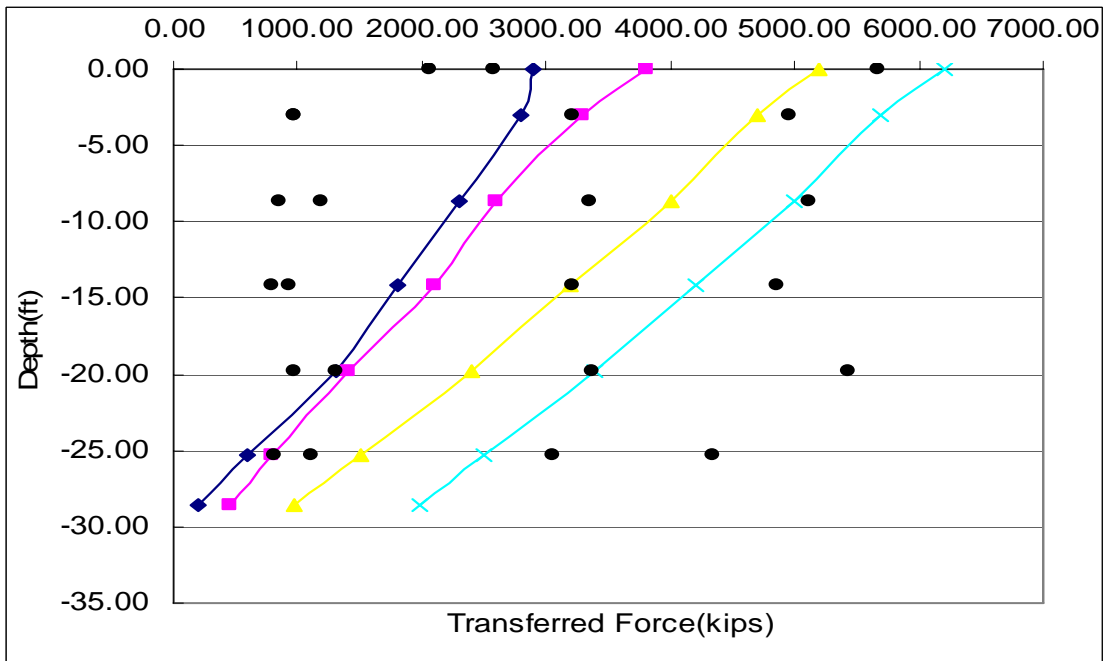


b)

Figure A.6 Result from 6 ft Diameter 6 ft Embedded Length in 30 tsf Rock a) Test No. 1 b) Test No. 2

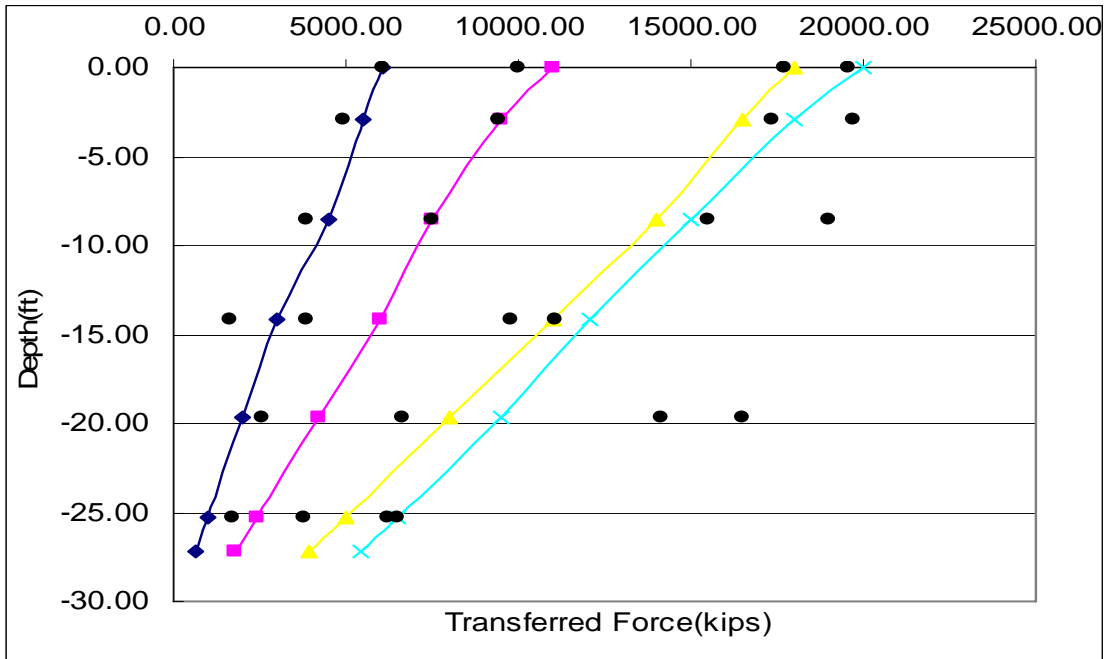


a)

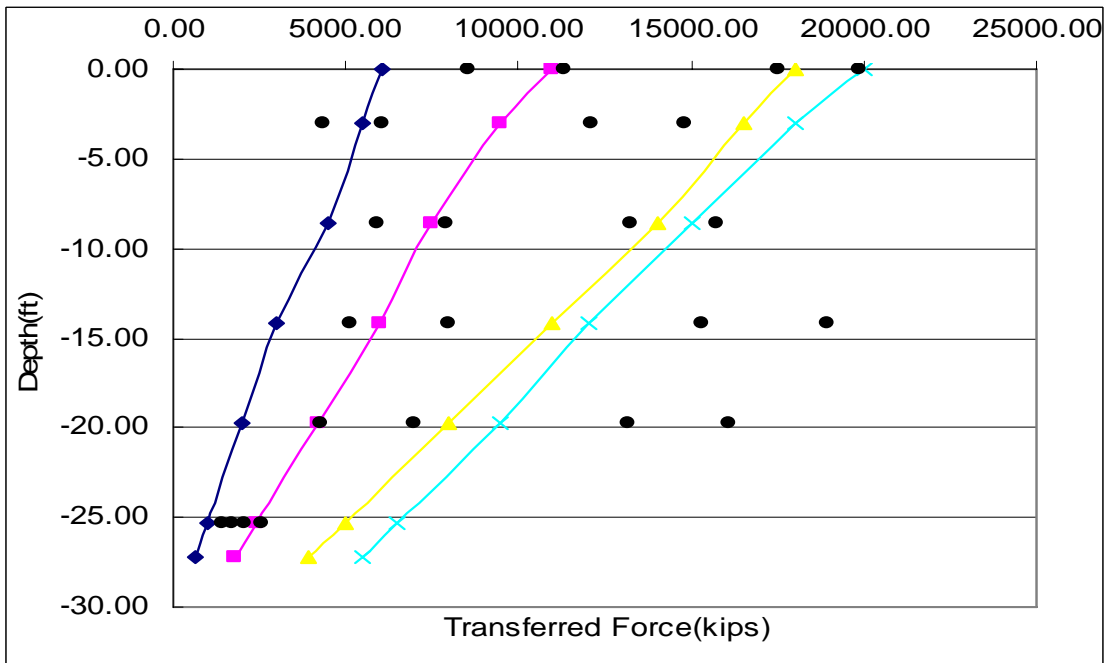


b)

Figure A.7 Result from 9 ft Diameter 27 ft Embedded Length in 10 tsf Rock a) Test No. 1 b) Test No. 2

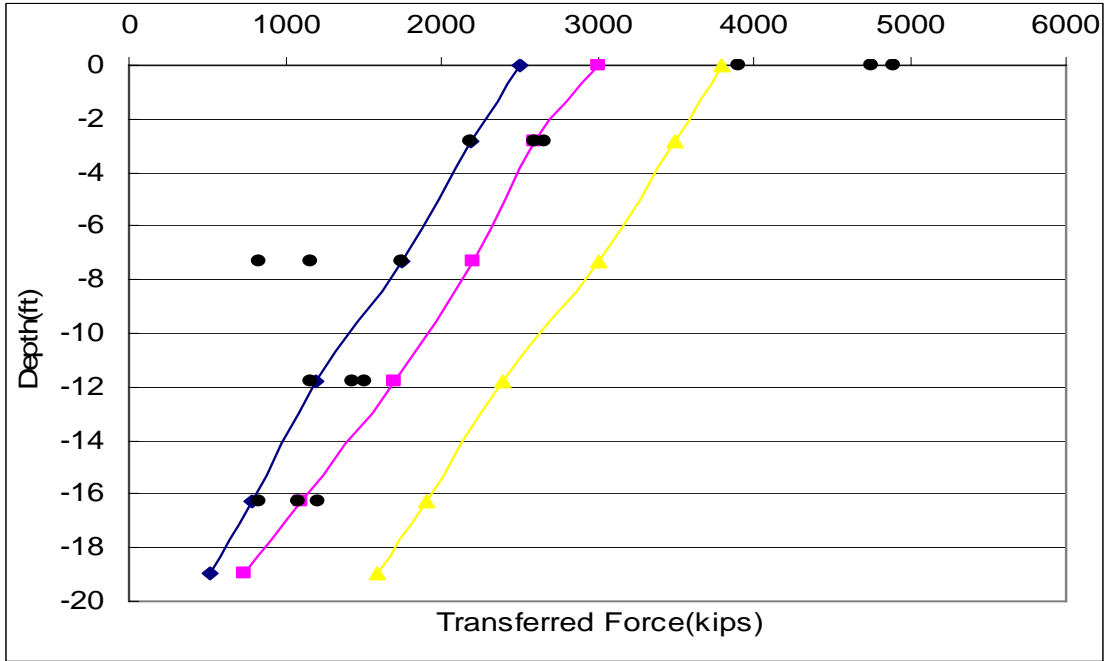


a)

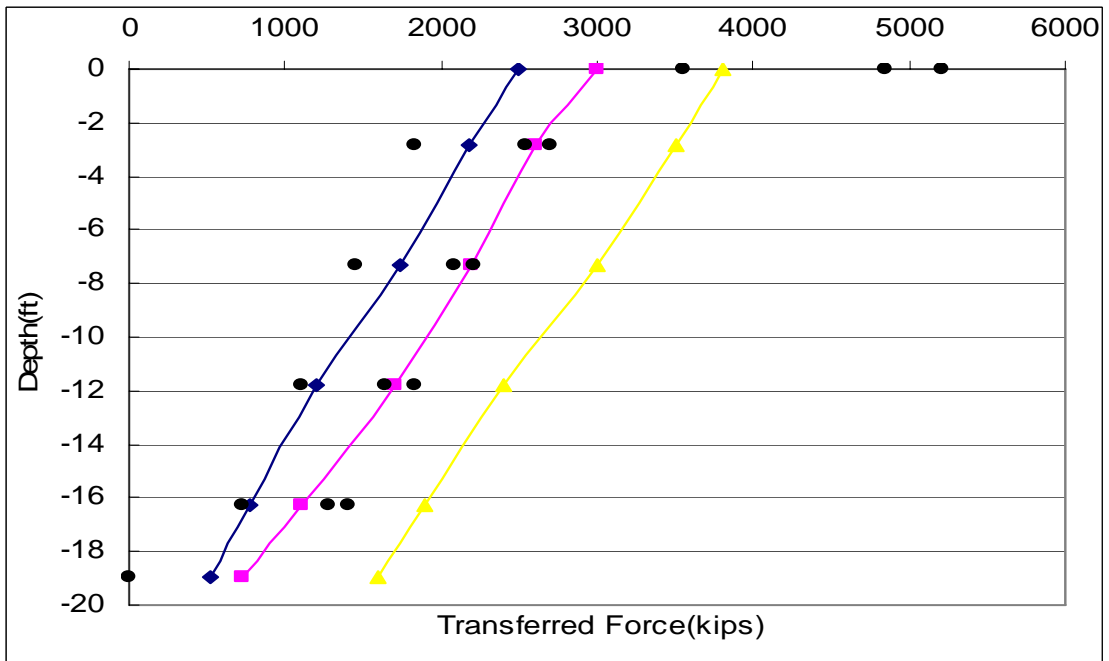


b)

Figure A.8 Result from 9 ft Diameter 27 ft Embedded Length in 30 tsf Rock a) Test No. 1 b) Test No. 2

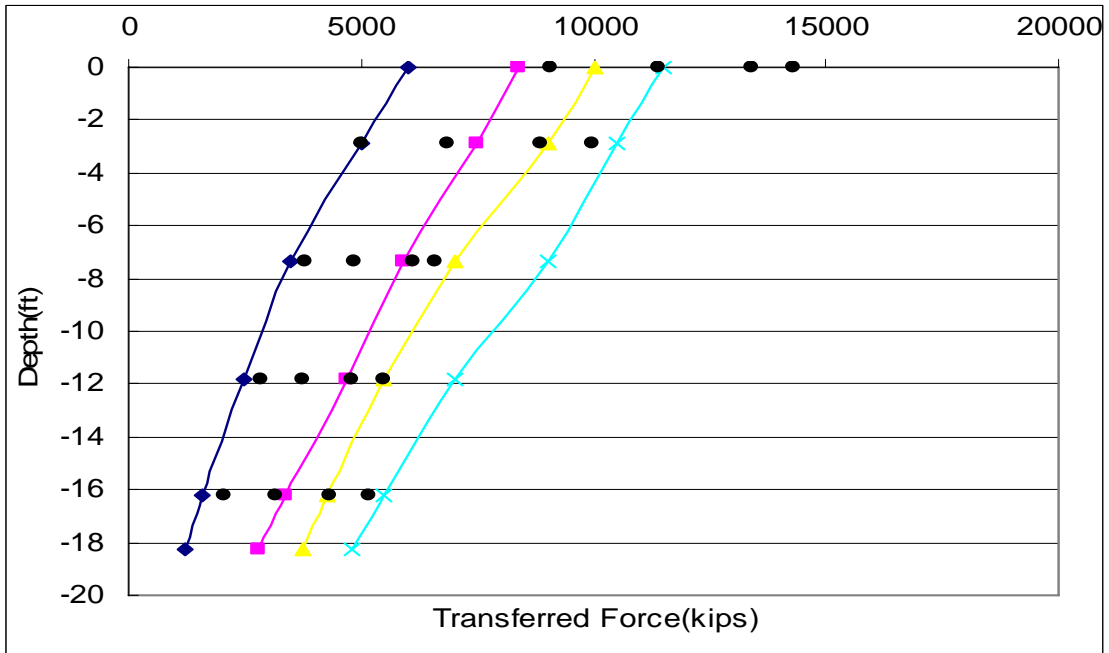


a)

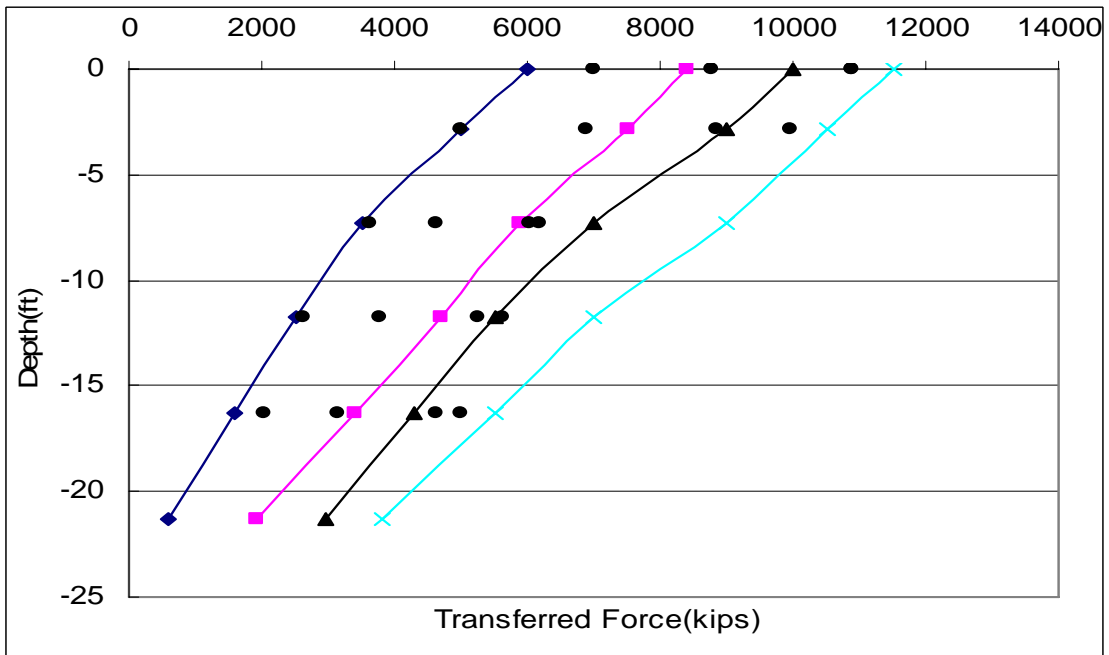


b)

Figure A.9 Result from 6 ft Diameter 18 ft Embedded Length in 10 tsf Rock a) Test No. 1 b) Test No. 2



a)

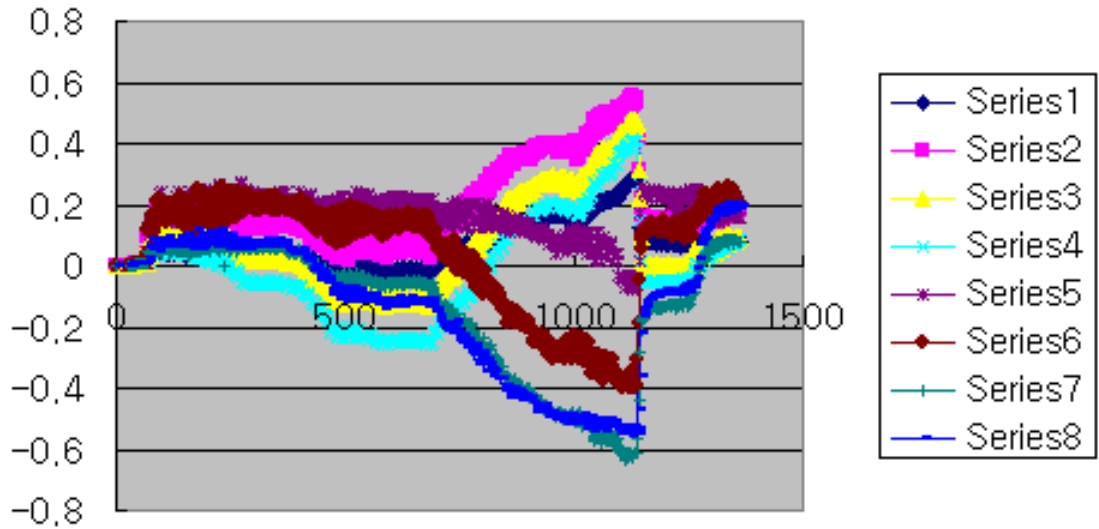


b)

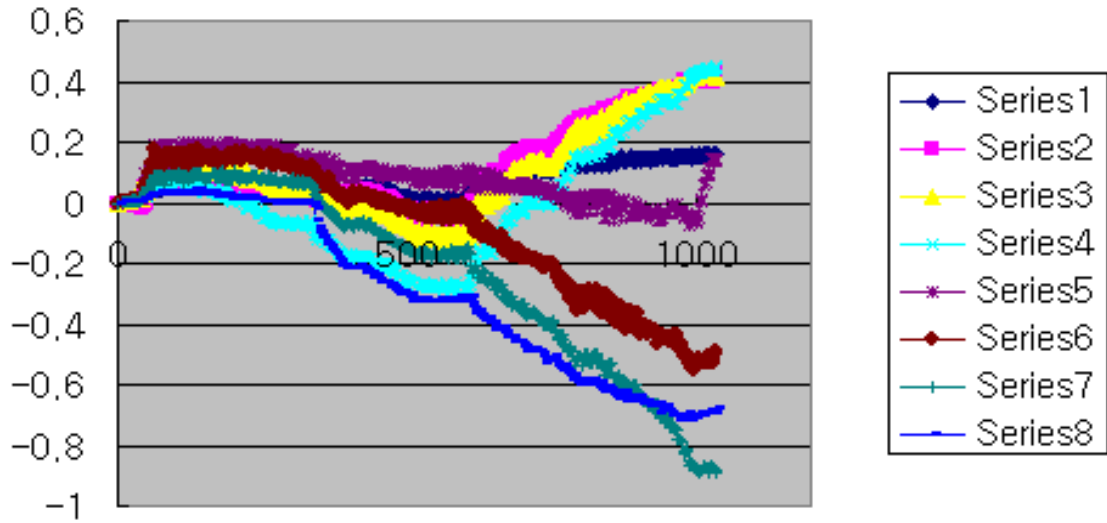
Figure A.10 Result from 6 ft Diameter 18 ft Embedded Length in 30 tsf Rock a) Test No. 1 b) Test No. 2

APPENDIX B

**Output Voltage (Volt on Y-Axis) from Gages vs. Time (Sec on X-Axis) with Loadings**

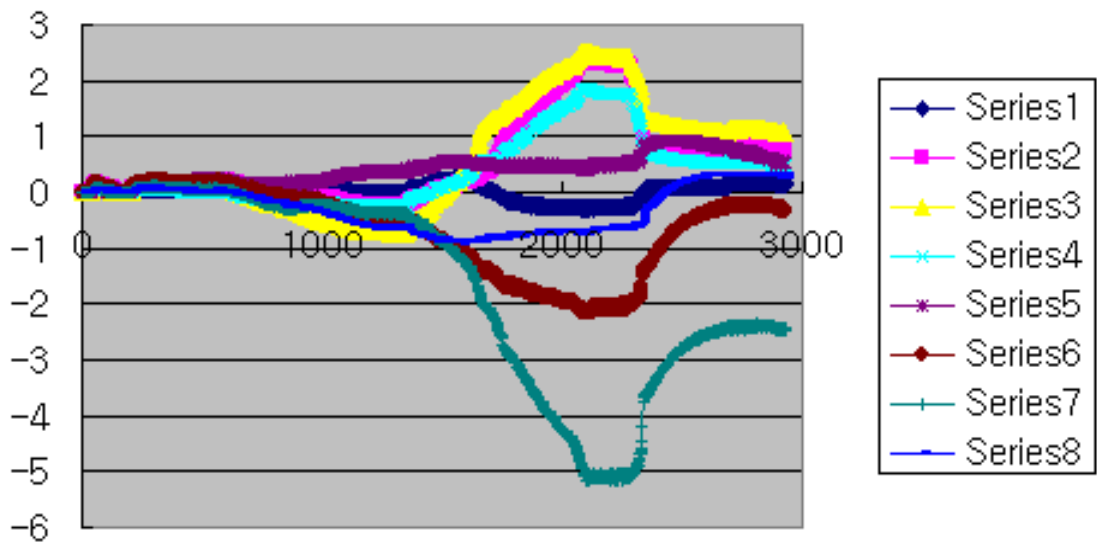


a)

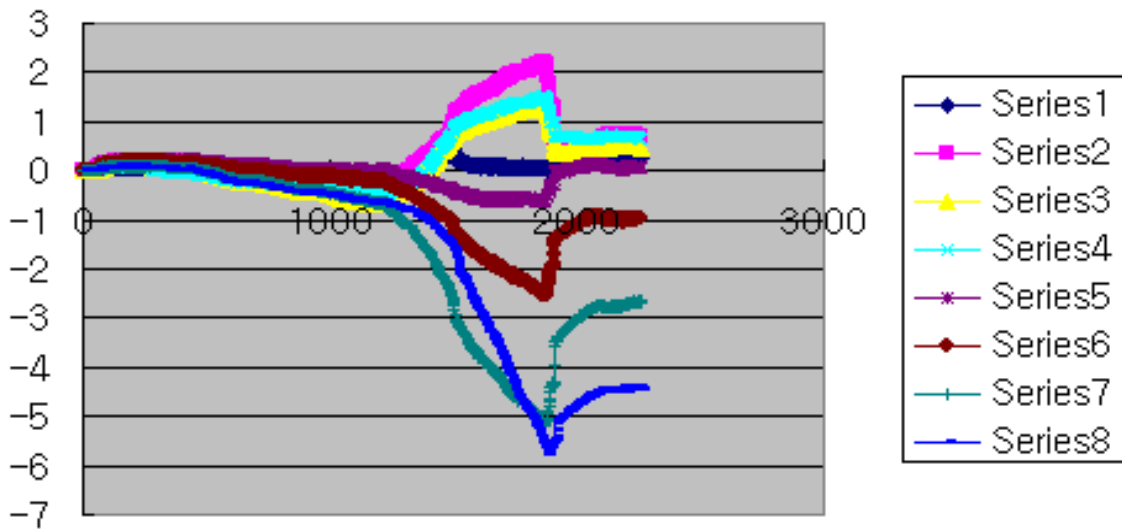


b)

Figure B.1 Output Voltage from 9 ft Diameter 9 ft Embedded Length in 10 tsf Rock with 50 % Styrofoam Layering below 1D below from Tip of Shaft a) Test No. 1 b) Test No. 2

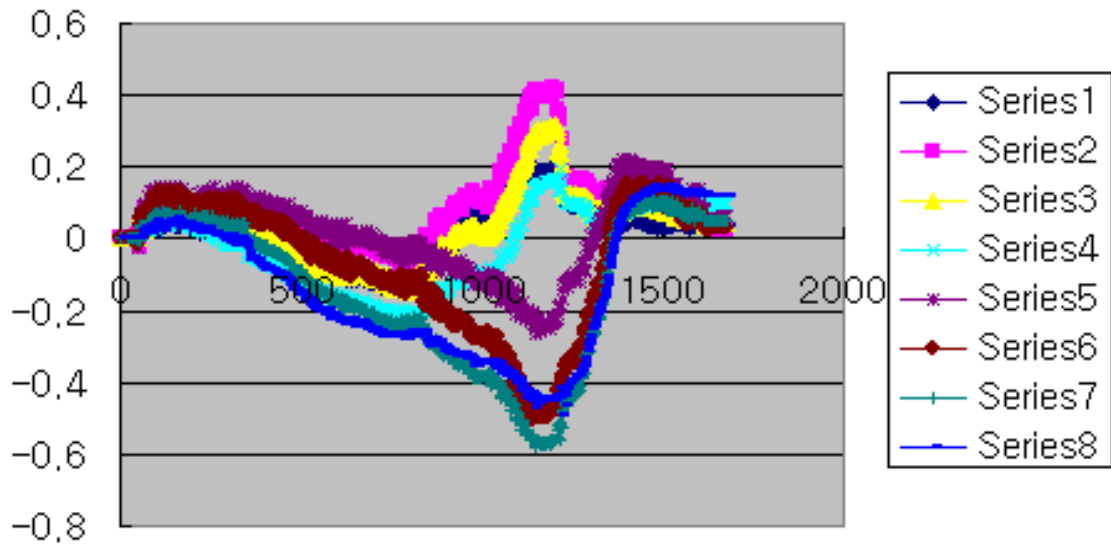


(a)

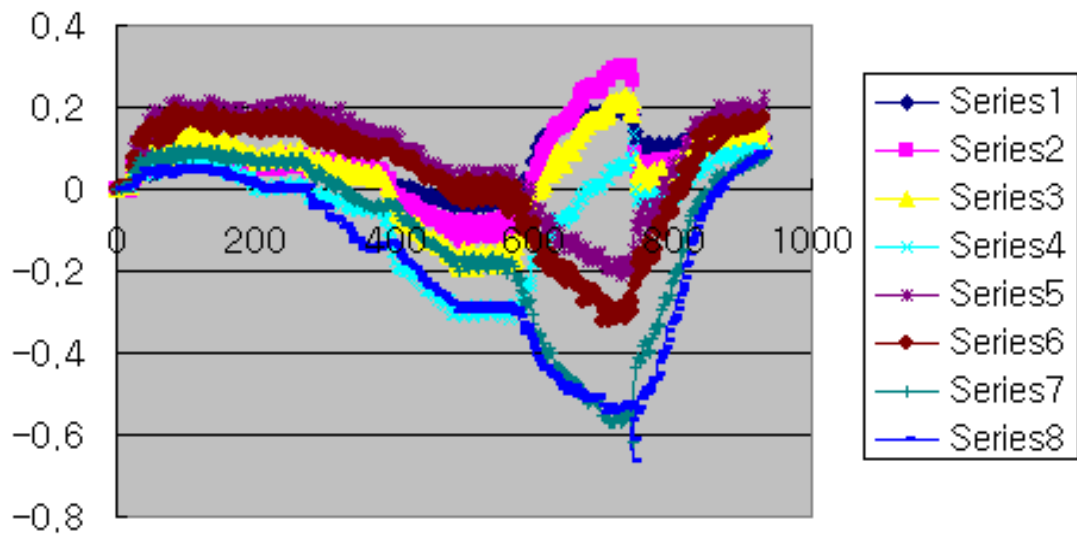


(b)

Figure B.2 Output Voltage from 9 ft Diameter 9 ft Embedded Length in 30 tsf Rock with 50 % Styrofoam Layering below 1D below from Tip of Shaft a) Test No. 1 b) Test No. 2

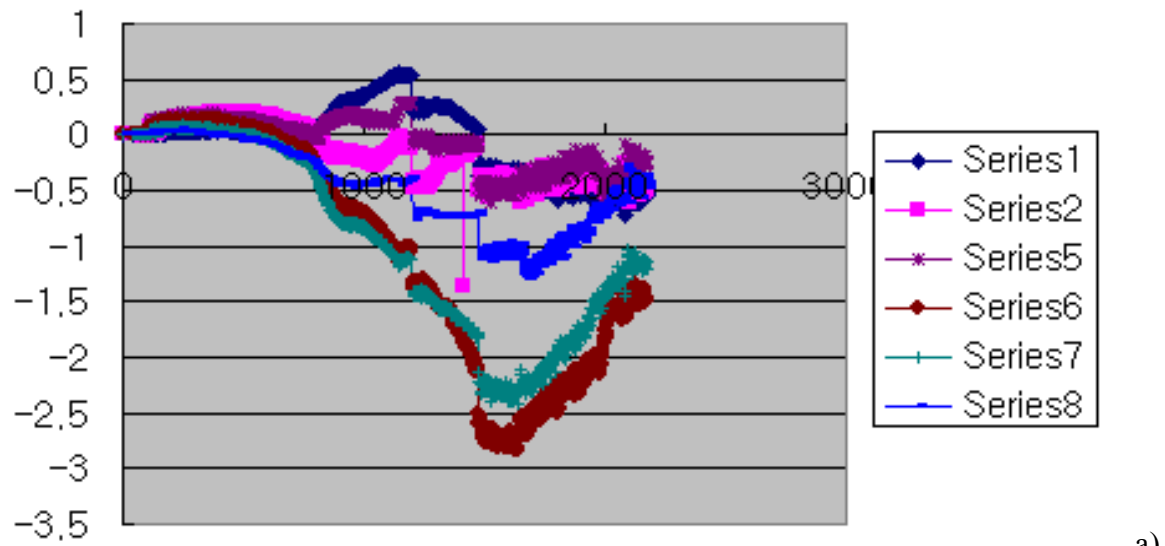


a)

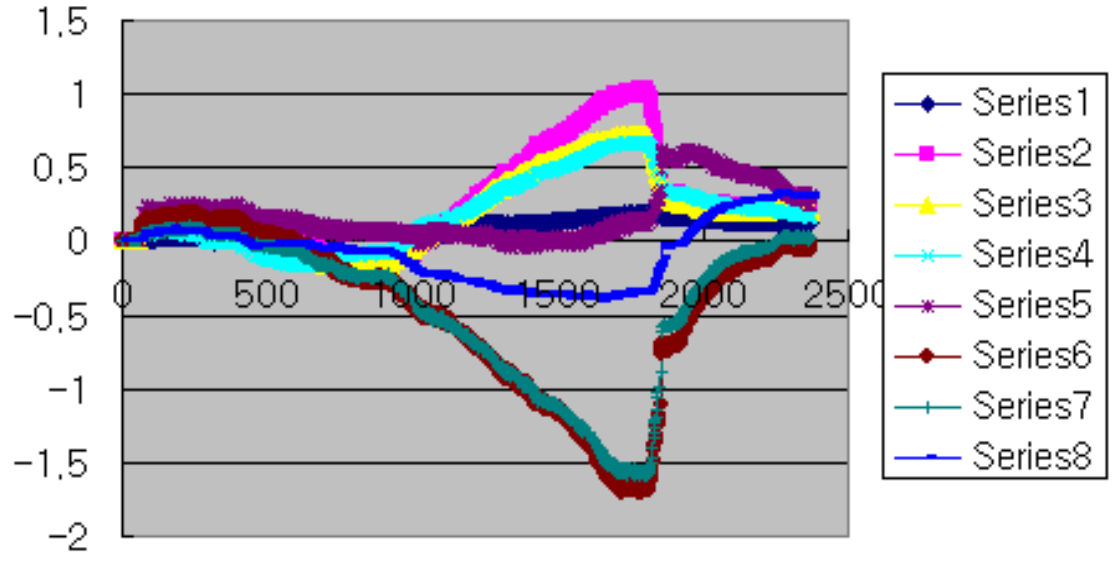


b)

Figure B.3 Output Voltage from 9 ft Diameter 9 ft Embedded Length in 10 tsf Rock a) Test No. 1 b) Test No. 2

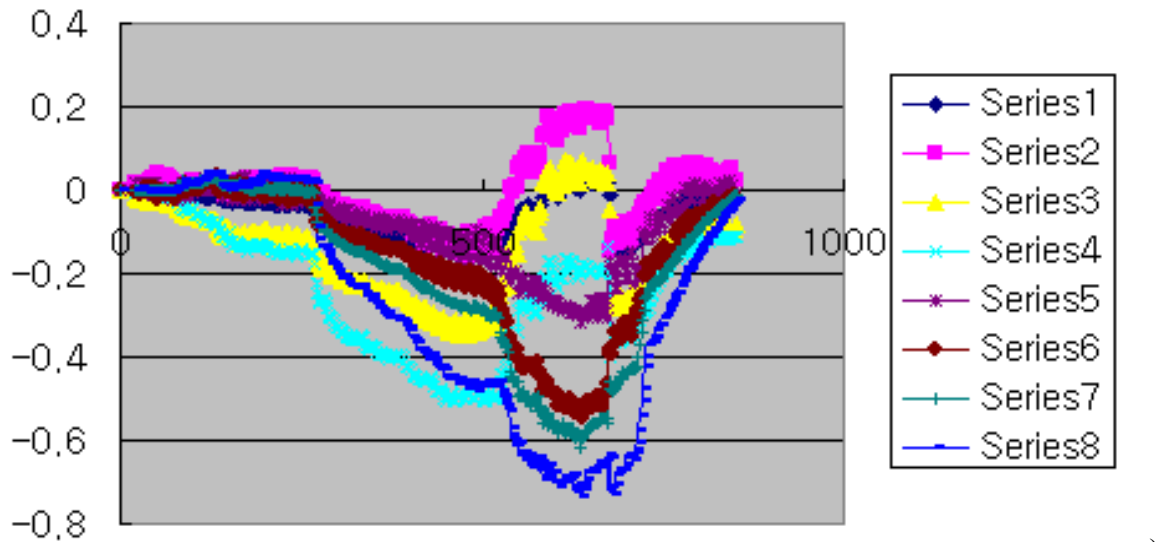


a)

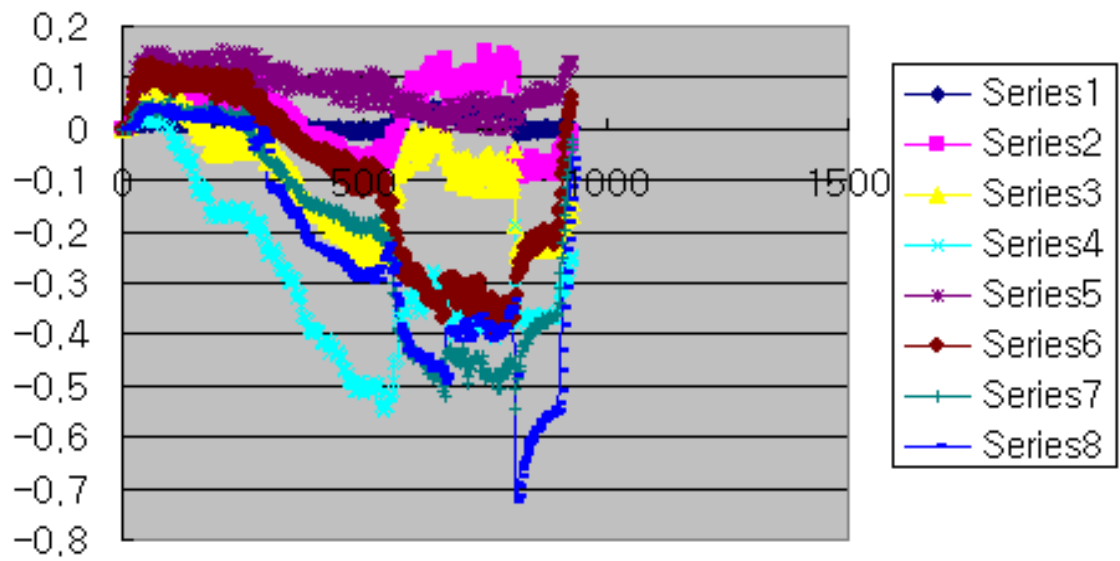


b)

Figure B.4 Output Voltage from 9 ft Diameter 9 ft Embedded Length in 30 tsf Rock a) Test No. 1 b) Test No. 2

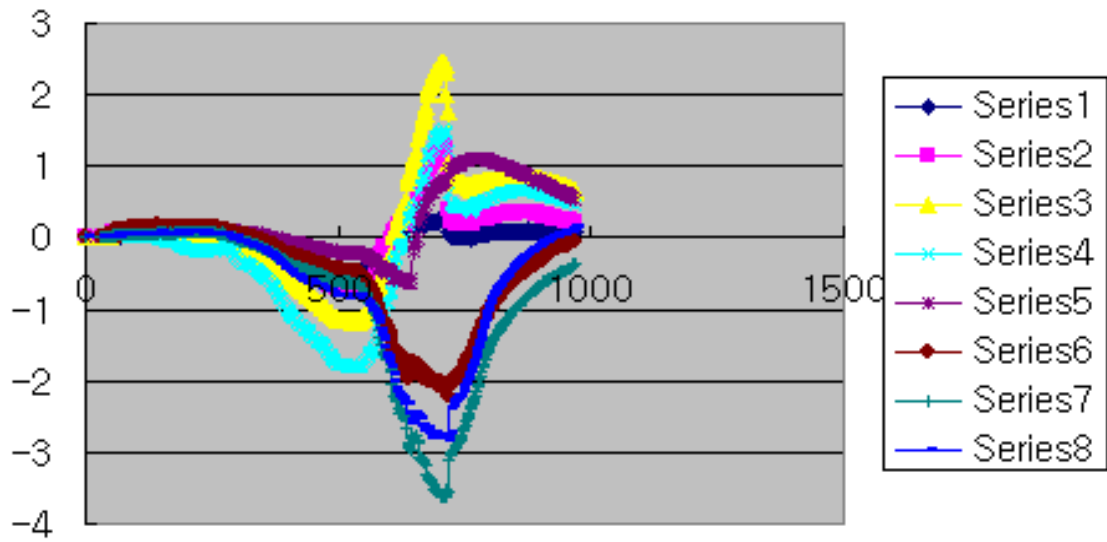


a)

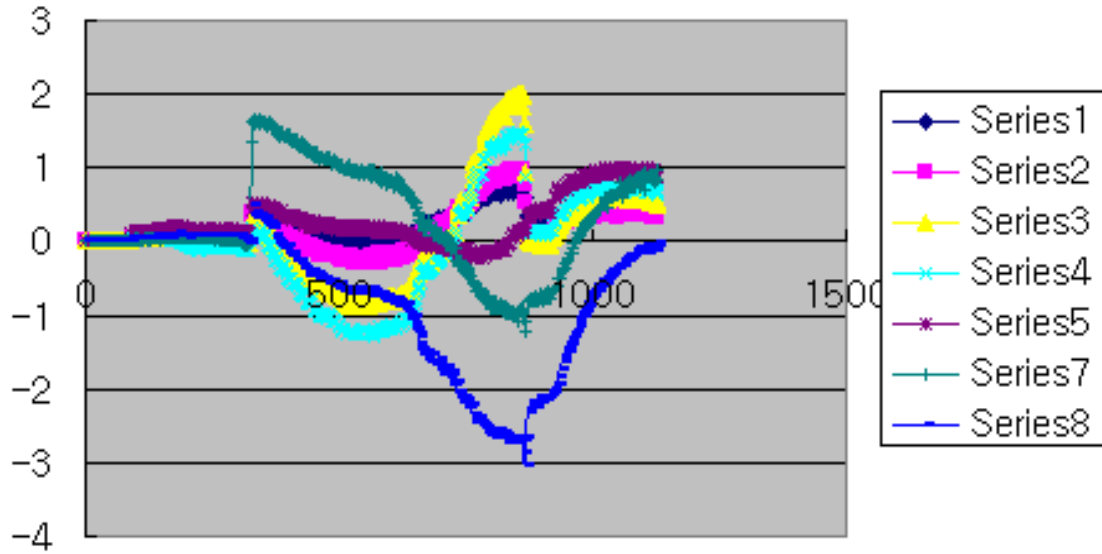


b)

Figure B.5 Output Voltage from 6 ft Diameter 6 ft Embedded Length in 10 tsf Rock a) Test No. 1 b) Test No. 2

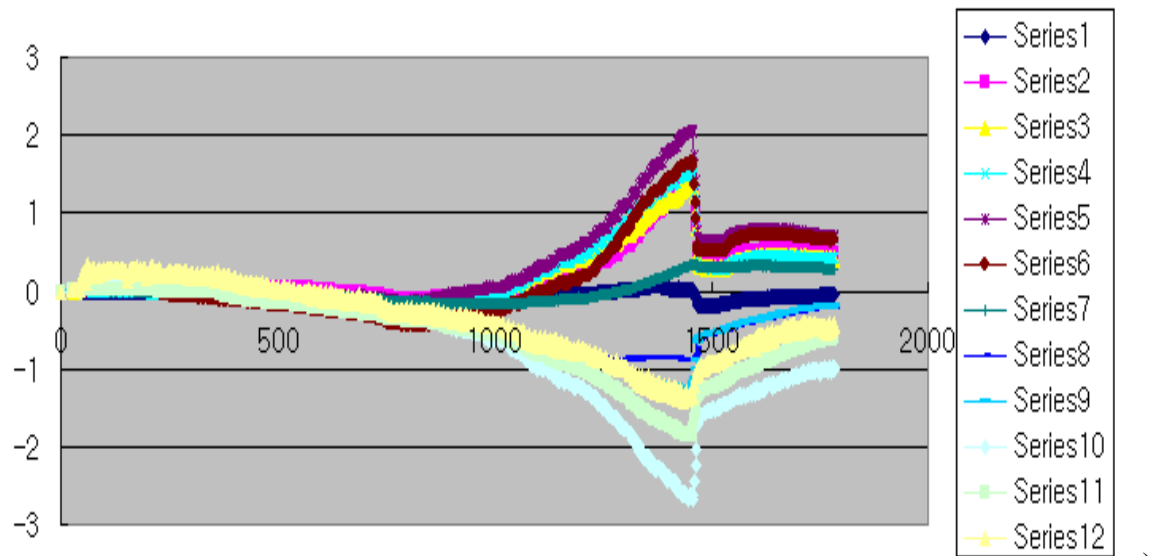


a)

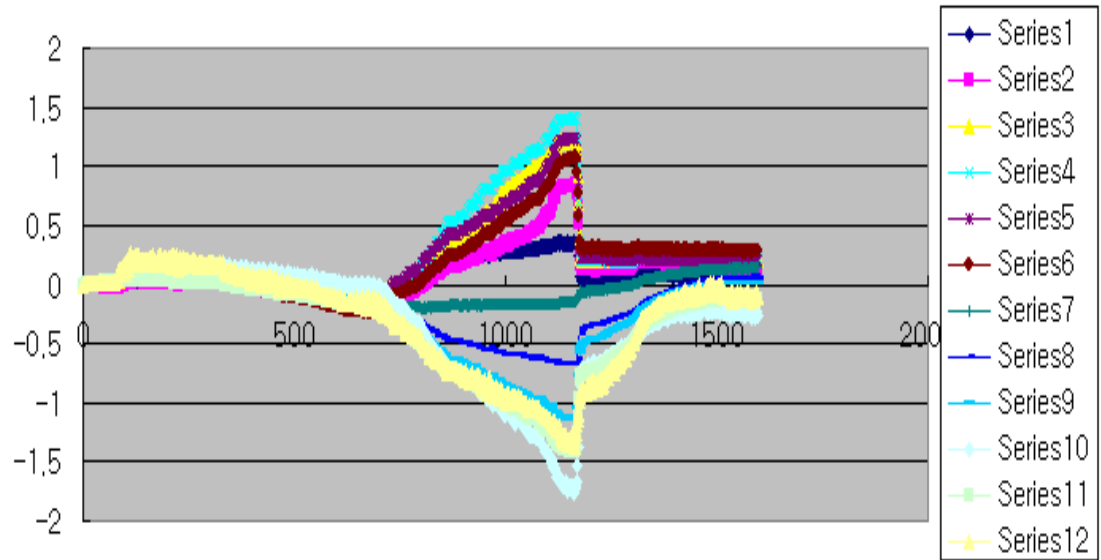


b)

Figure B.6 Output Voltage from 6 ft Diameter 6 ft Embedded Length in 30 tsf Rock a) Test No. 1 b) Test No. 2



a)



b)

Figure B.7 Output Voltage from 9 ft Diameter 27 ft Embedded Length in 10 tsf Rock a) Test No. 1 b) Test No. 2

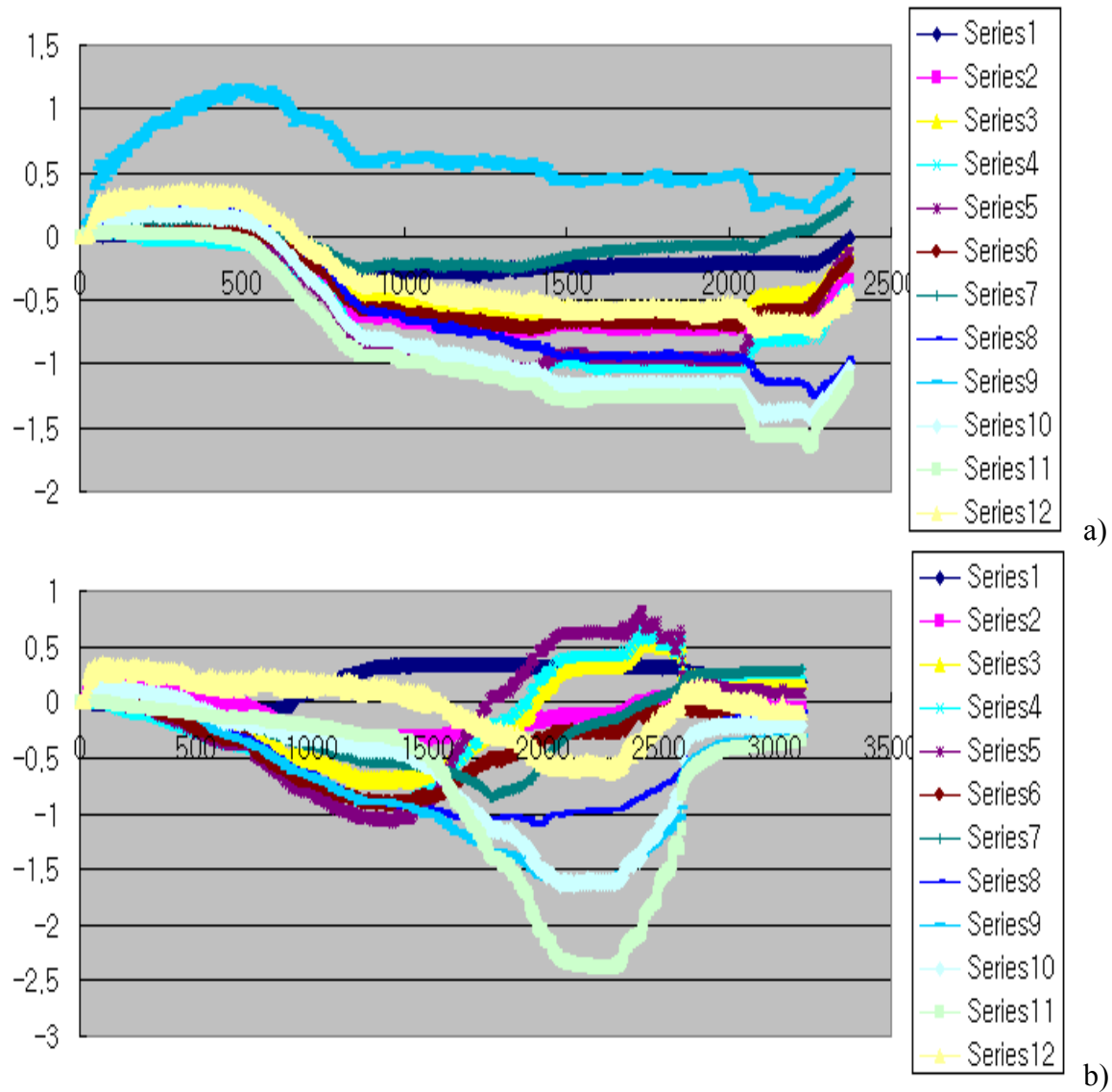
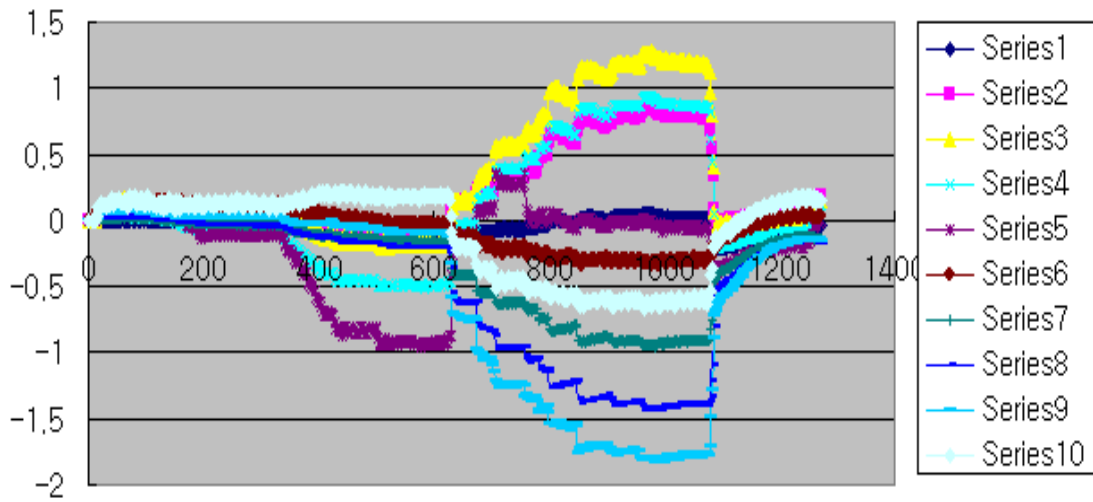
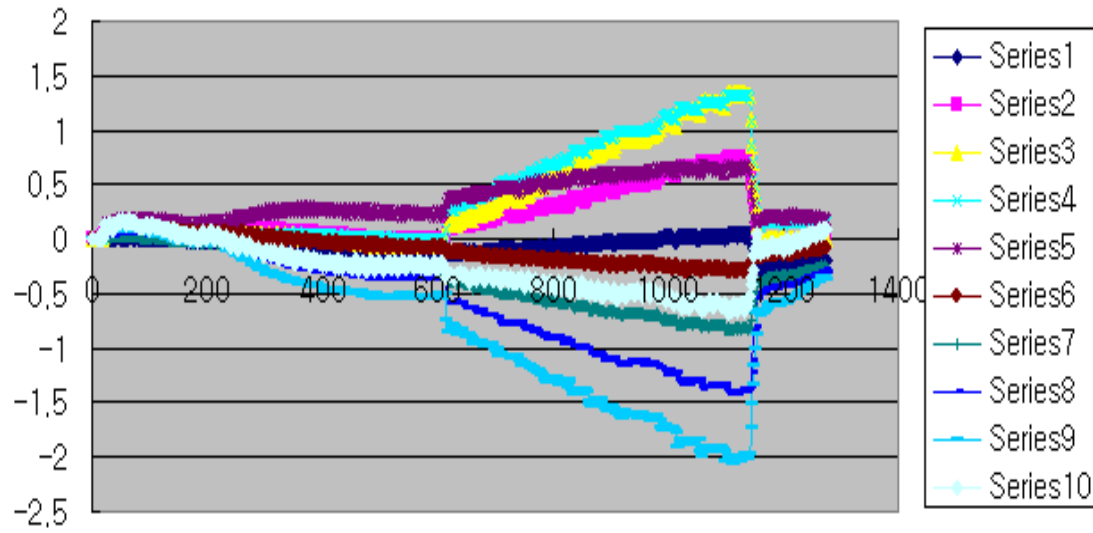


Figure B.8 Output Voltage from 9 ft Diameter 27 ft Embedded Length in 30 tsf Rock a) Test No. 1 b) Test No. 2

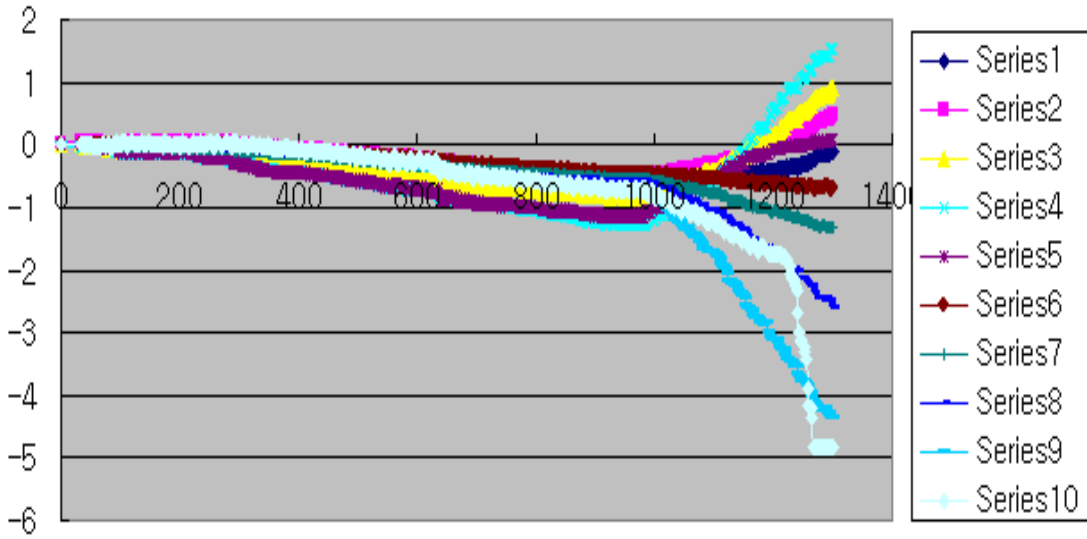


a)

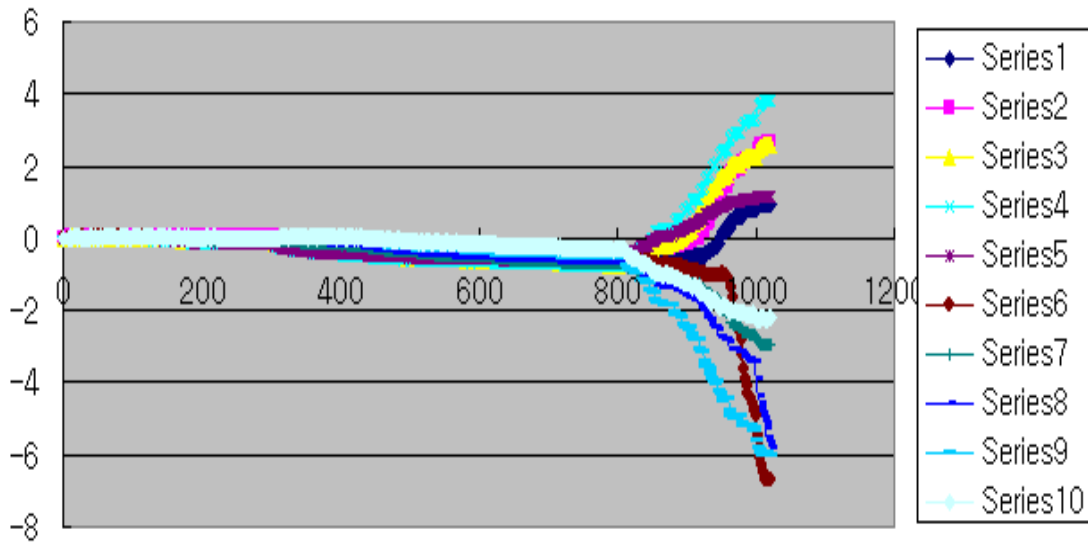


b)

Figure B.9 Output Voltage from 6 ft Diameter 18 ft Embedded Length in 10 tsf Rock a) Test No. 1 b) Test No. 2



a)

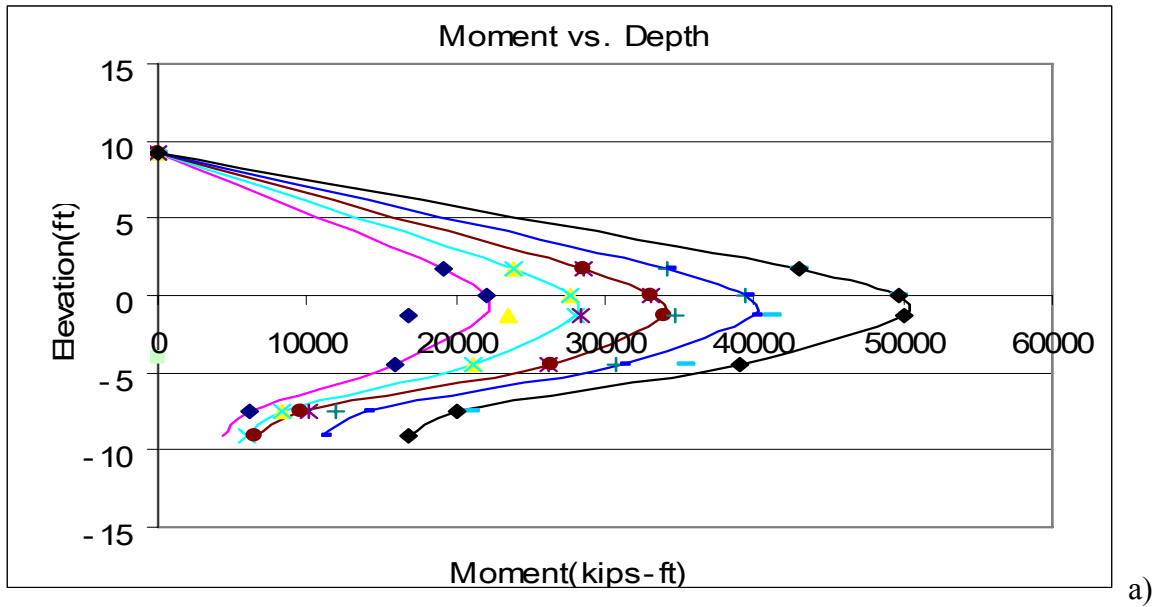


b)

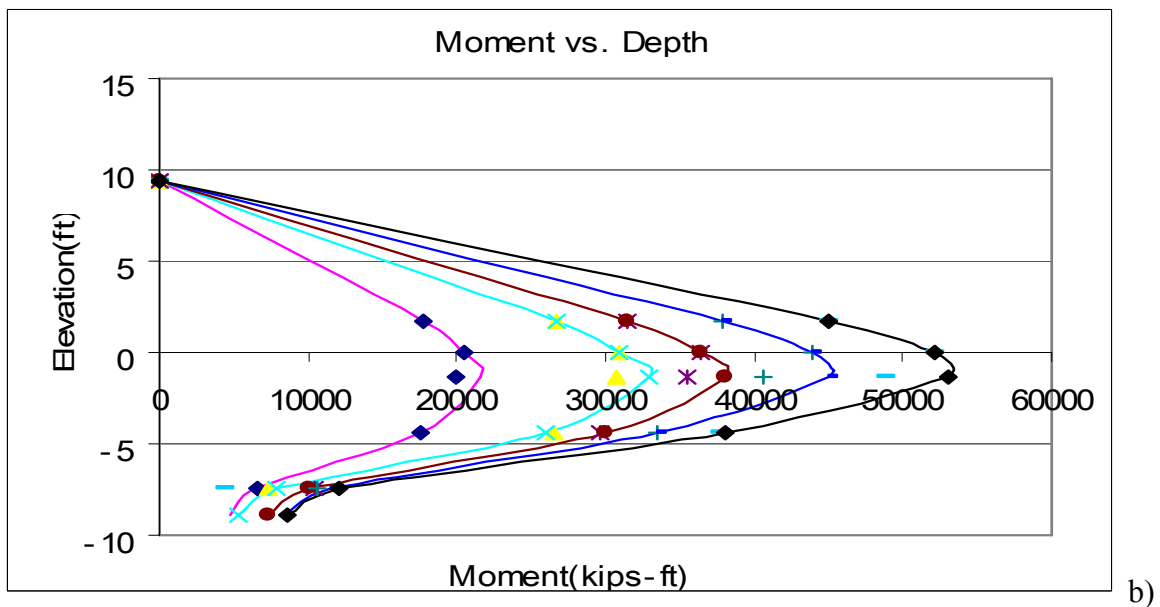
Figure B.10 Output Voltage from 6 ft Diameter 18 ft Embedded Length in 30 tsf Rock a) Test No. 1 b) Test No. 2

APPENDIX C

Moment Curve

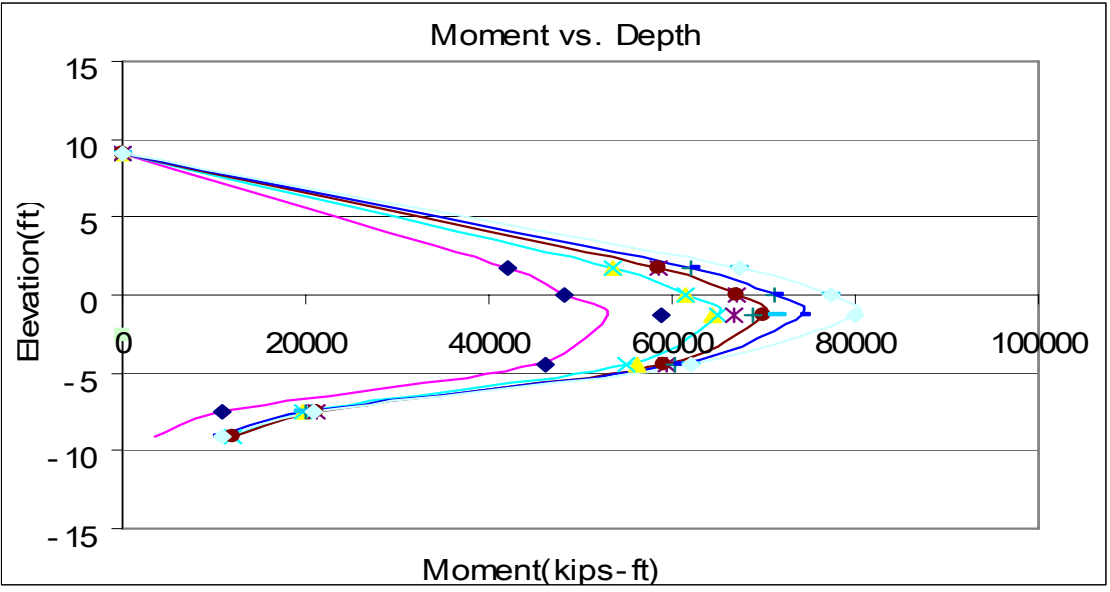


a)

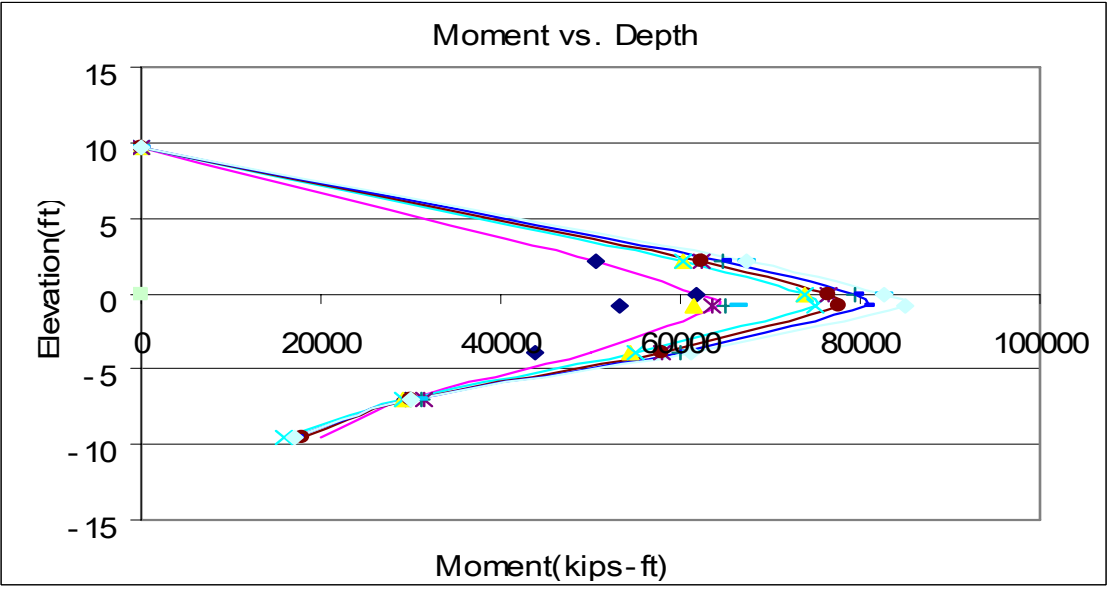


b)

Figure C.1 Moment Curve with Different Top Lateral Displacement from 9 ft Diameter 9 ft Embedded Length in 10 tsf Rock with 50 % Styrofoam Layering below 1D below from Tip of Shaft a) Test No. 1 b) Test No. 2

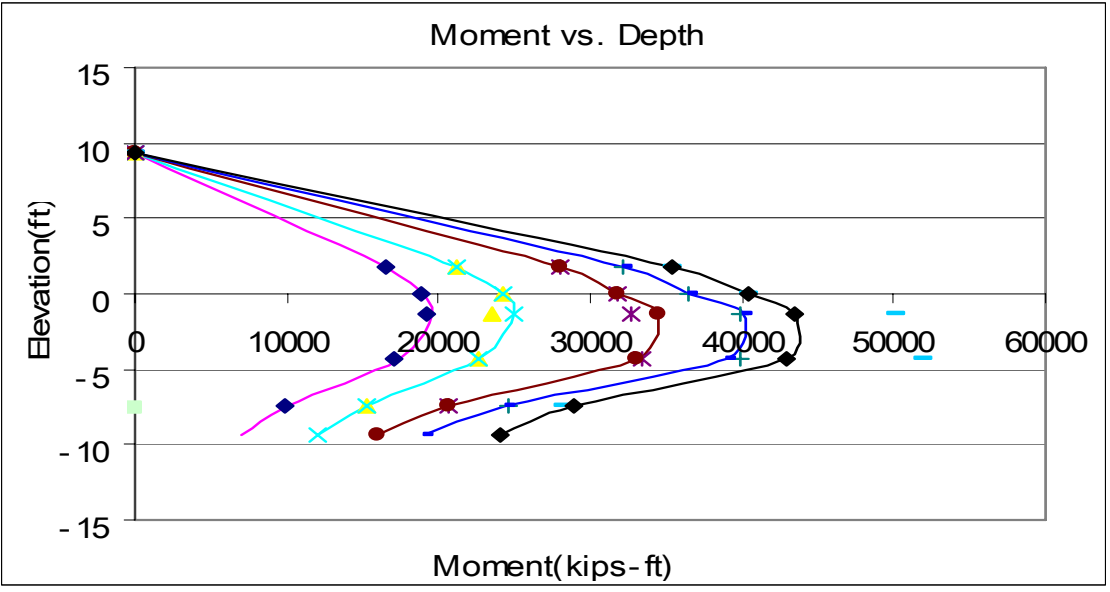


a)

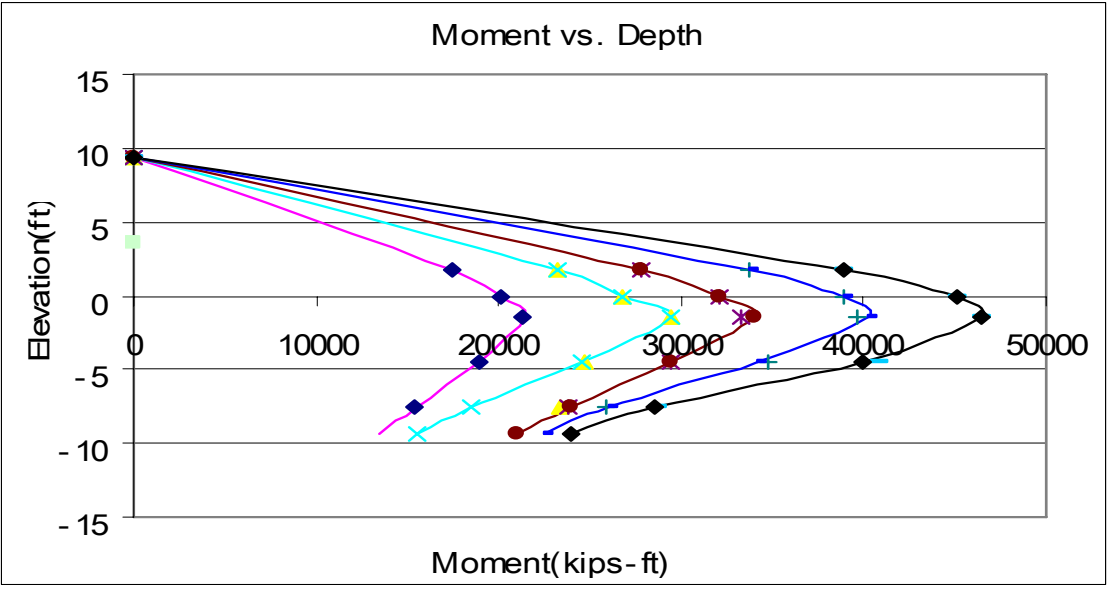


b)

Figure C.2 Moment Curve with Different Top Lateral Displacement from 9 ft Diameter 9 ft Embedded Length in 30 tsf Rock with 50 % Styrofoam Layering below 1D below from Tip of Shaft a) Test No. 1 b) Test No. 2

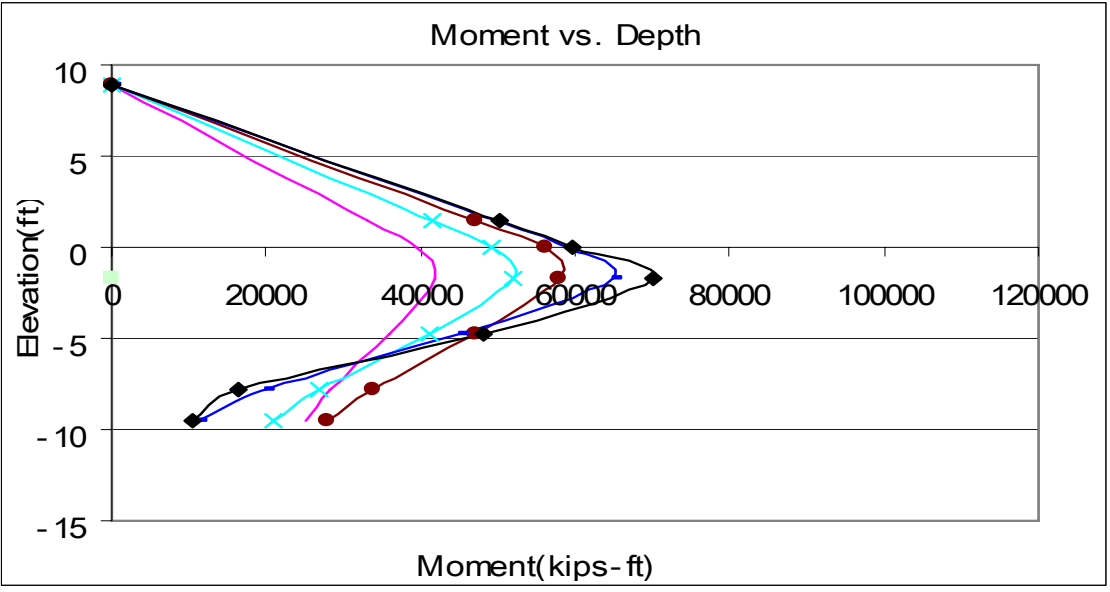


a)

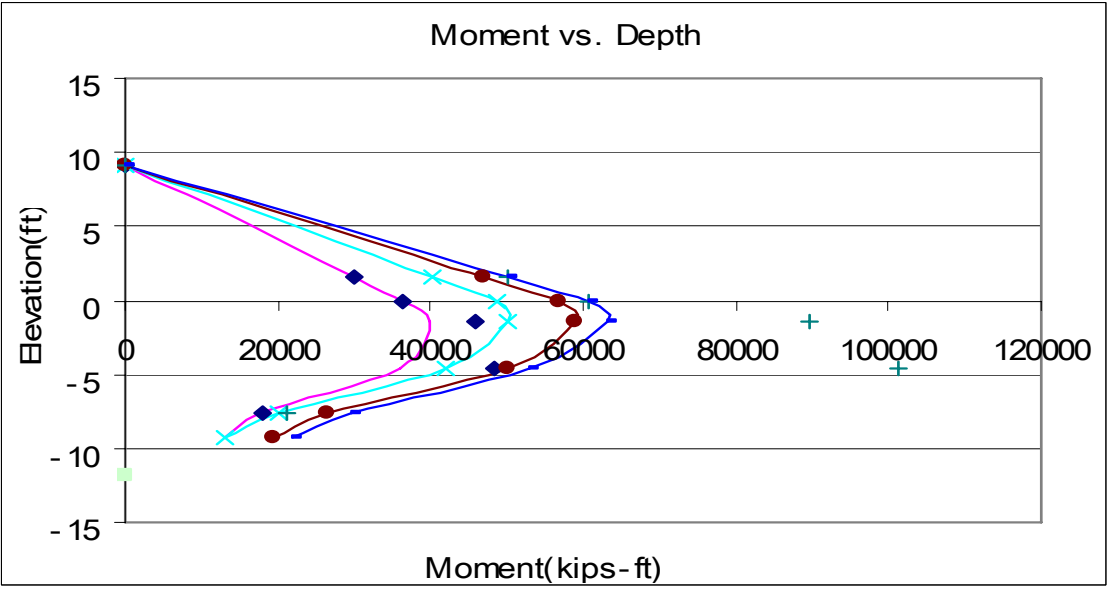


b)

Figure C.3 Moment Curve with Different Top Lateral Displacement from 9 ft Diameter 9 ft Embedded Length in 10 tsf Rock a) Test No. 1 b) Test No. 2

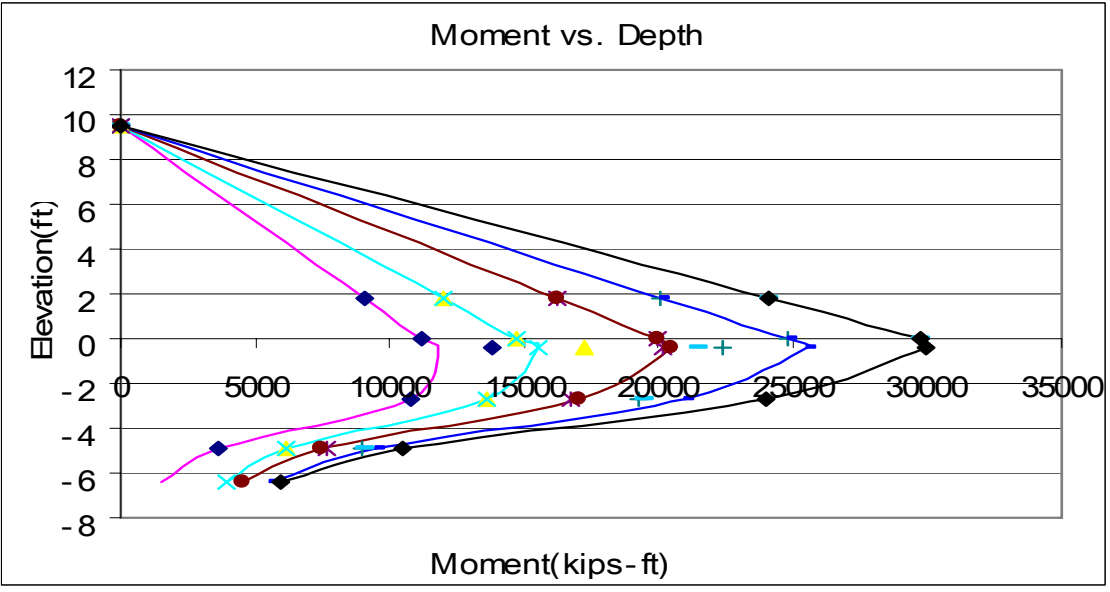


a)

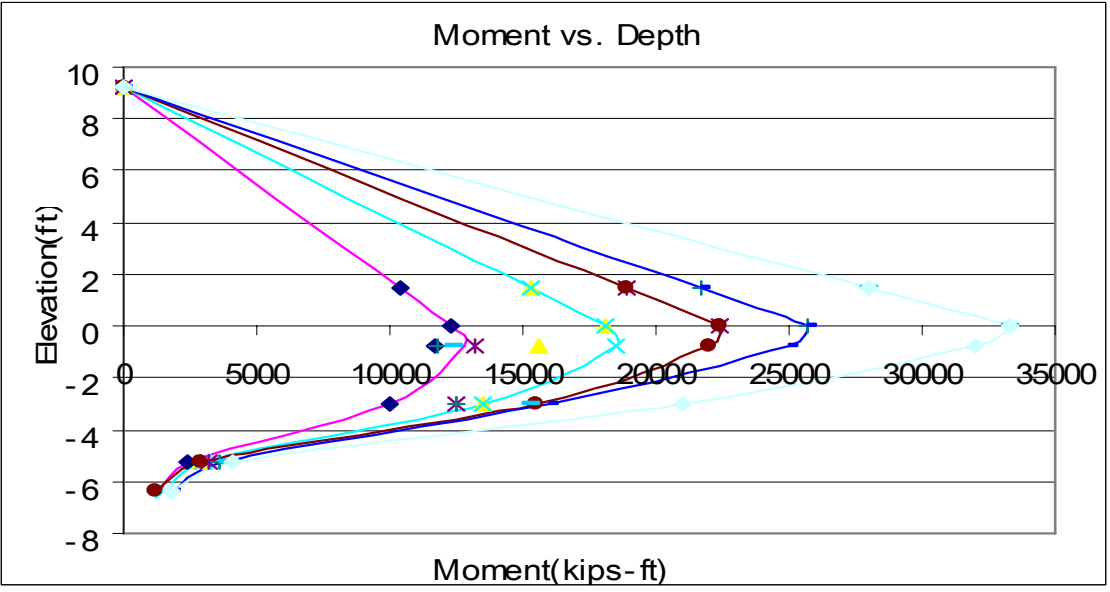


b)

Figure C.4 Moment Curve with Different Top Lateral Displacement from 9 ft Diameter 9 ft Embedded Length in 30 tsf Rock a) Test No. 1 b) Test No. 2

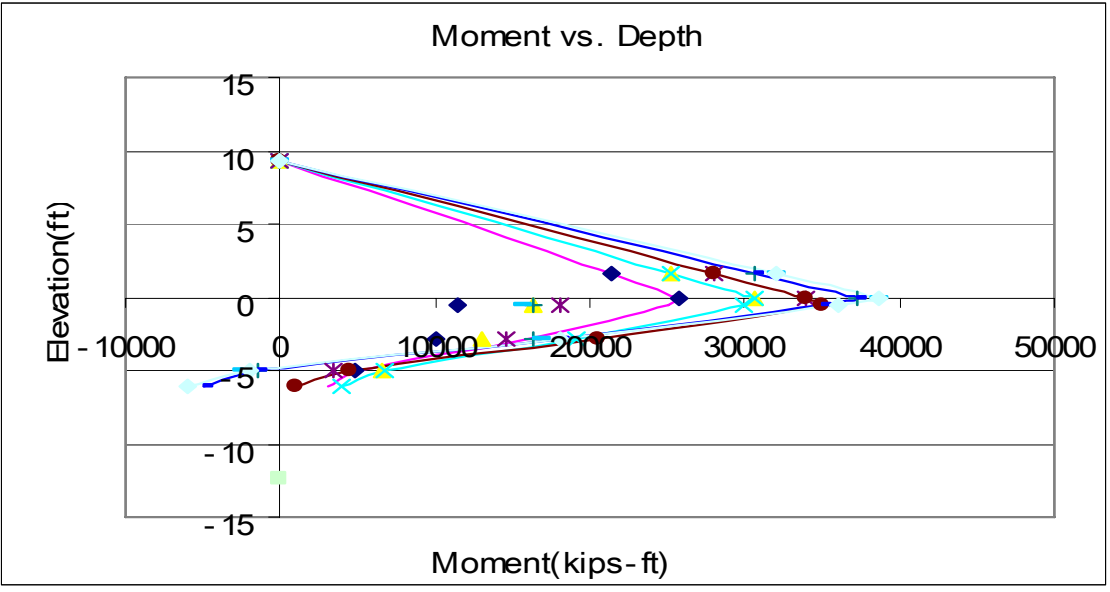


a)

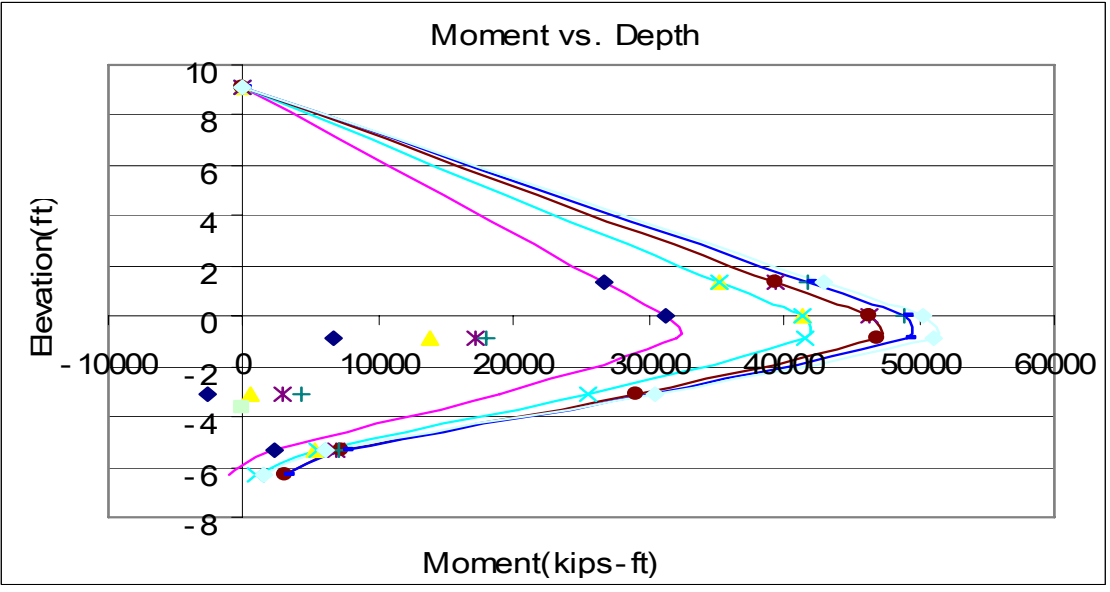


b)

Figure C.5 Moment Curve with Different Top Lateral Displacement from 6 ft Diameter 6 ft Embedded Length in 10 tsf Rock a) Test No. 1 b) Test No. 2

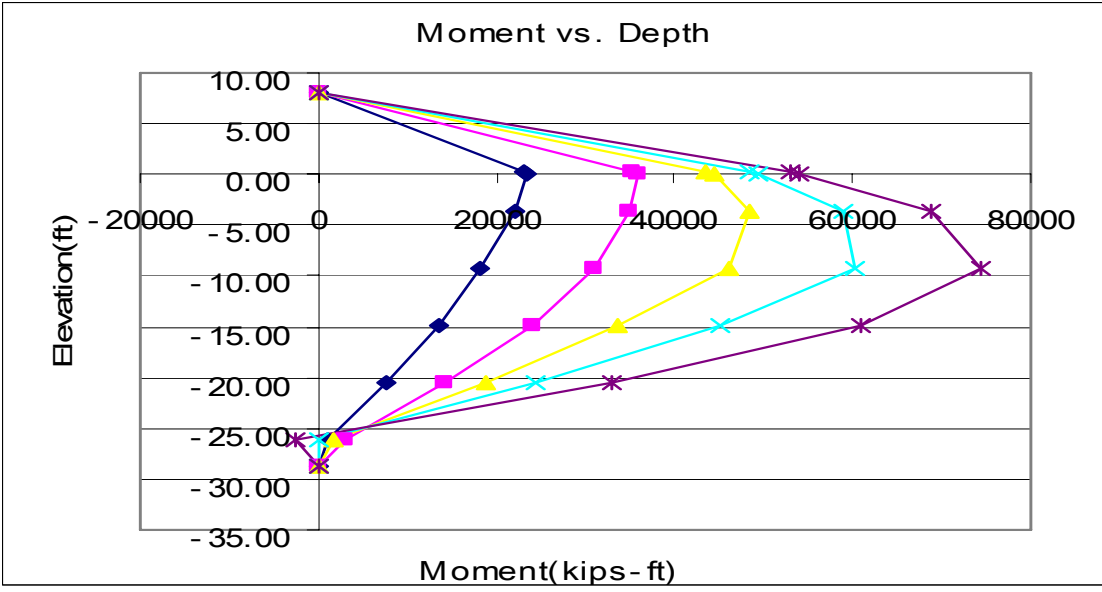


a)

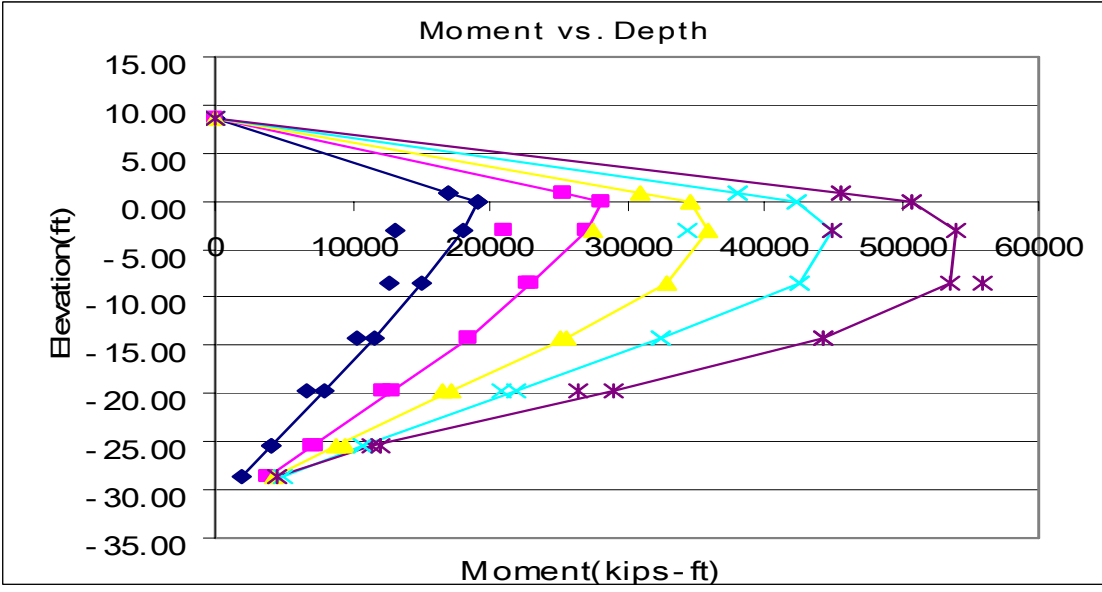


b)

Figure C.6 Moment Curve with Different Top Lateral Displacement from 6 ft Diameter 6 ft Embedded Length in 30 tsf Rock a) Test No. 1 b) Test No. 2

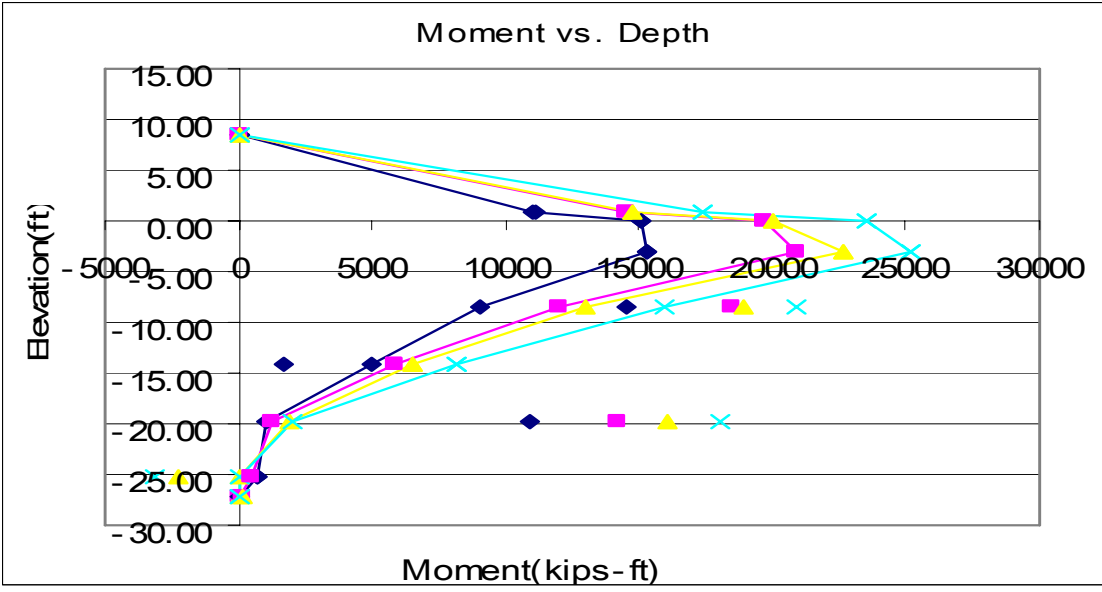


a)

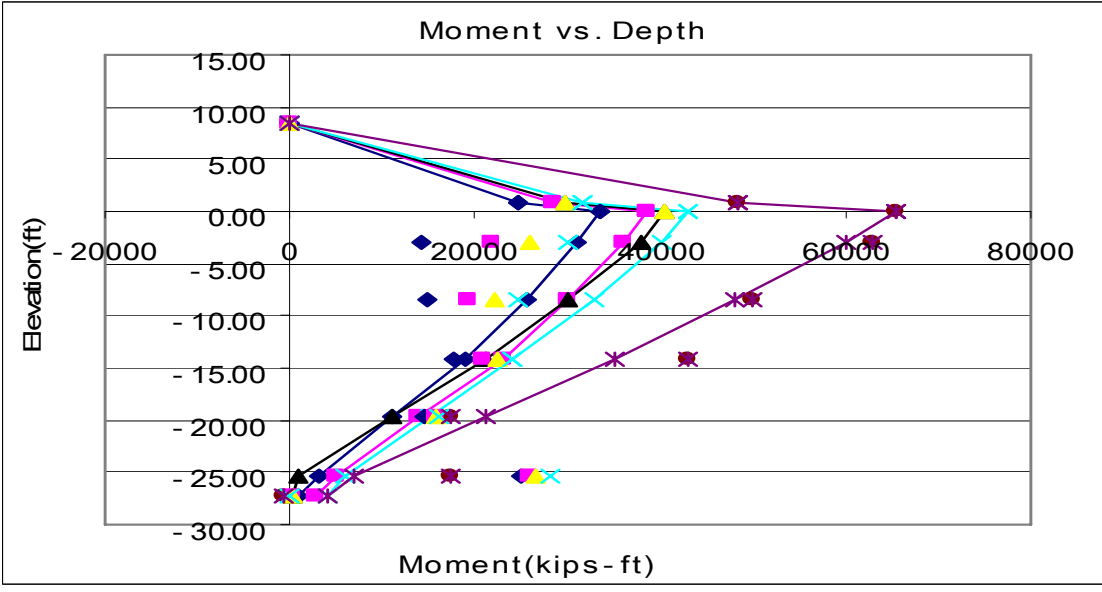


b)

Figure C.7 Moment Curve with Different Top Lateral Displacement from 9 ft Diameter 27 ft Embedded Length in 10 tsf Rock a) Test No. 1 b) Test No. 2

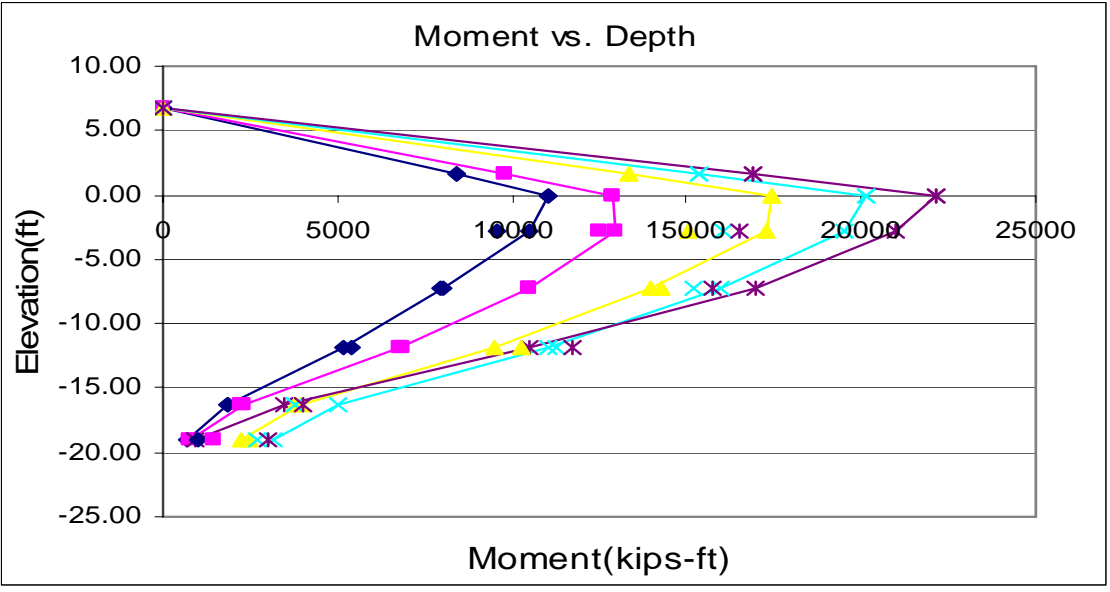


a)

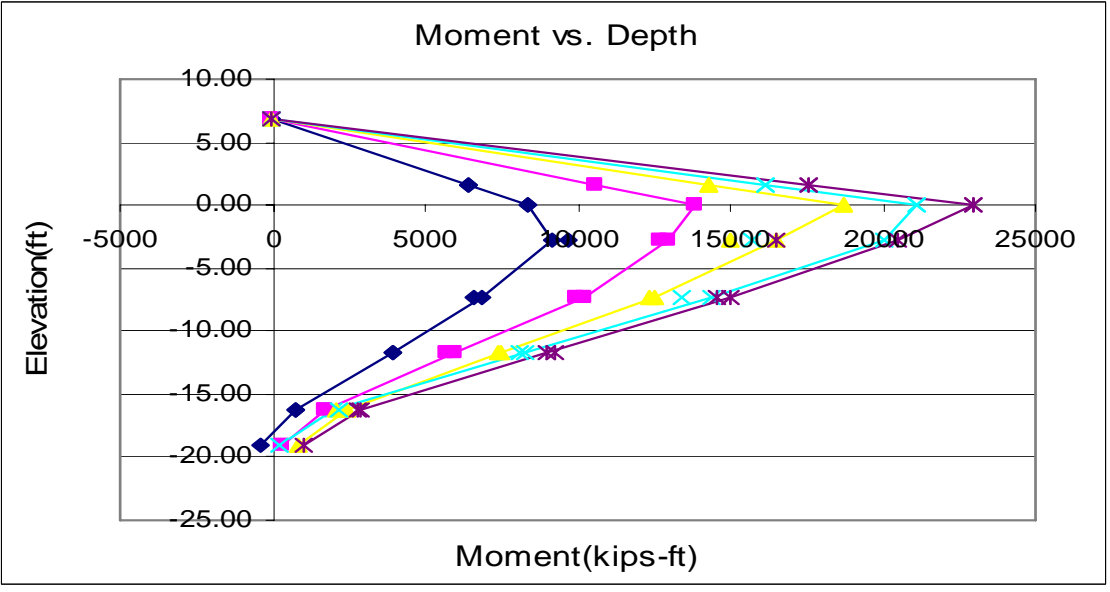


b)

Figure C.8 Moment Curve with Different Top Lateral Displacement from 9 ft Diameter 27 ft Embedded Length in 30 tsf Rock a) Test No. 1 b) Test No. 2

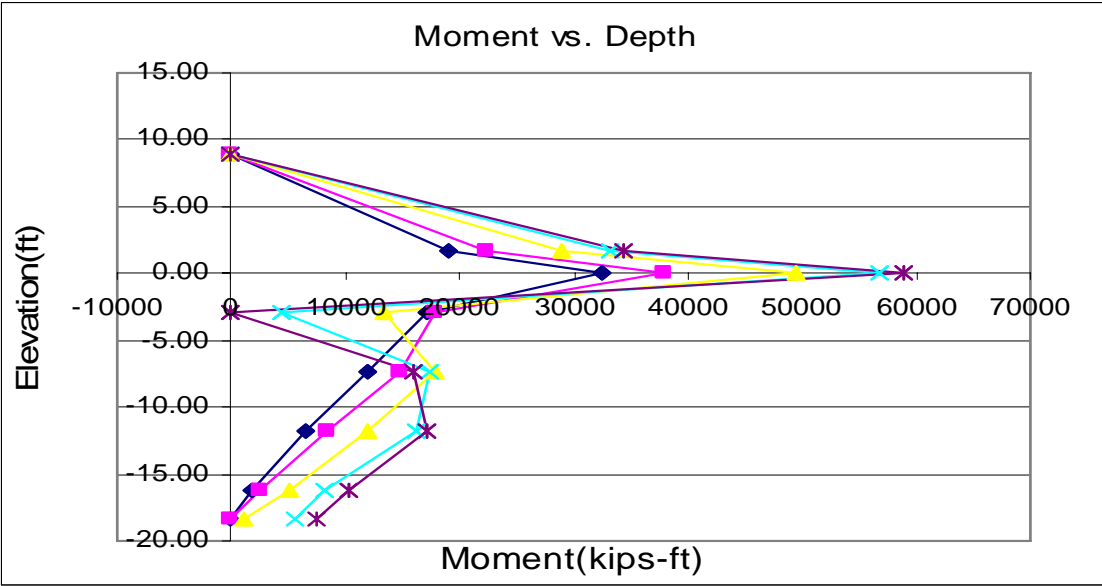


a)

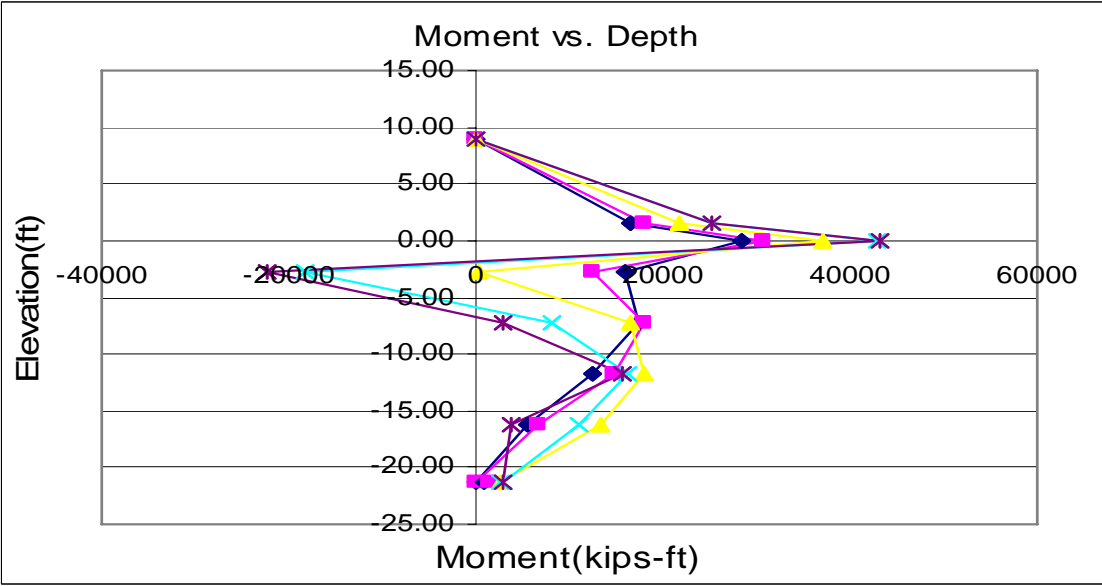


b)

Figure C.9 Moment Curve with Different Top Lateral Displacement from 6 ft Diameter 18 ft Embedded Length in 10 tsf Rock a) Test No. 1 b) Test No. 2



a)

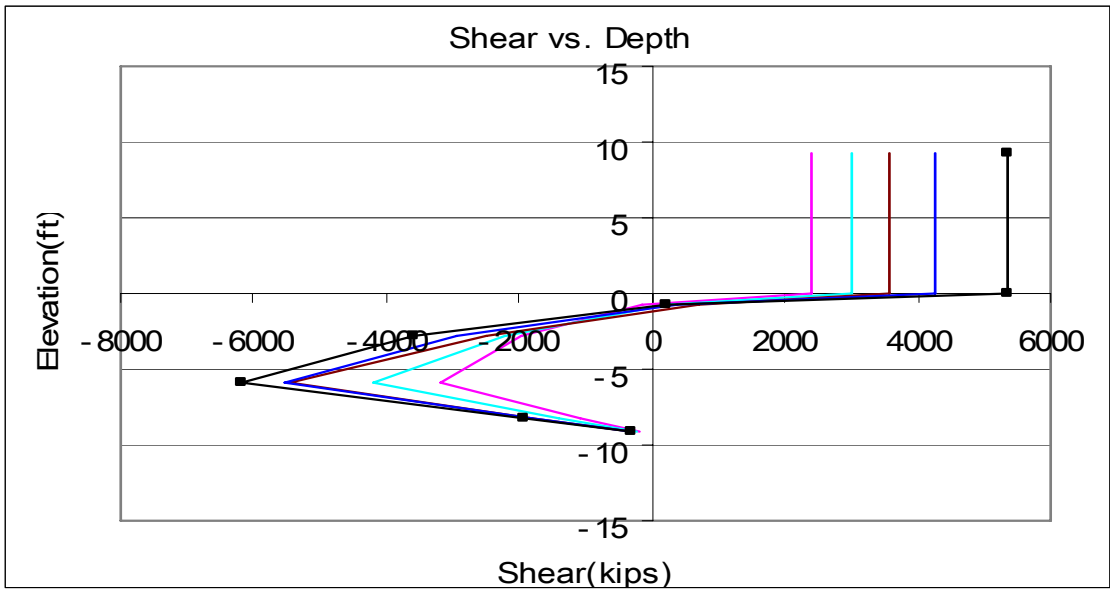


b)

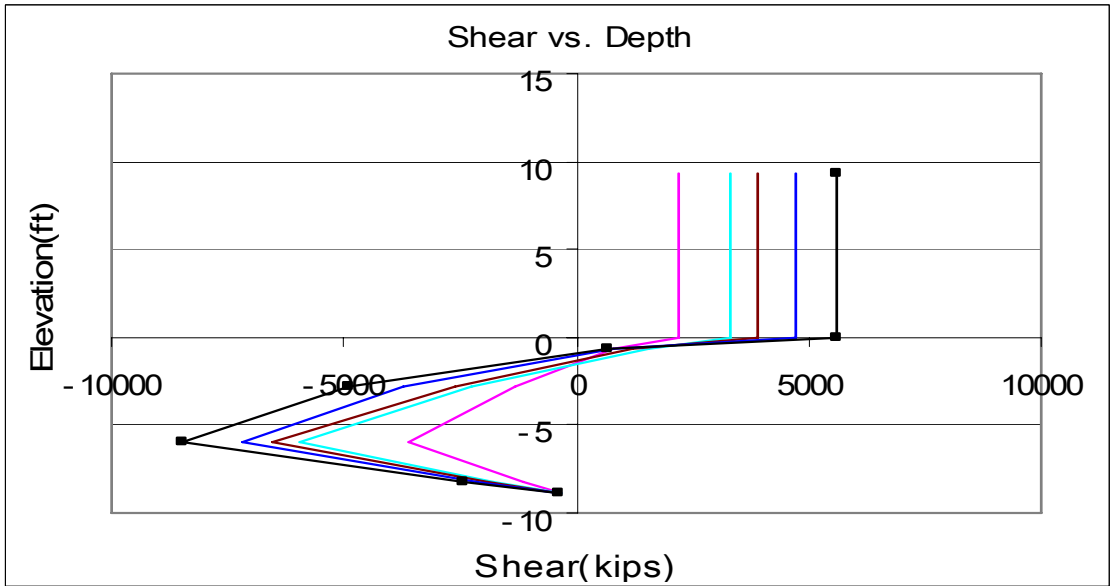
Figure C.10 Moment Curve with Different Top Lateral Displacement from 6 ft Diameter 18 ft Embedded Length in 30 tsf Rock a) Test No. 1 b) Test No. 2

APPENDIX D

Shear Curve

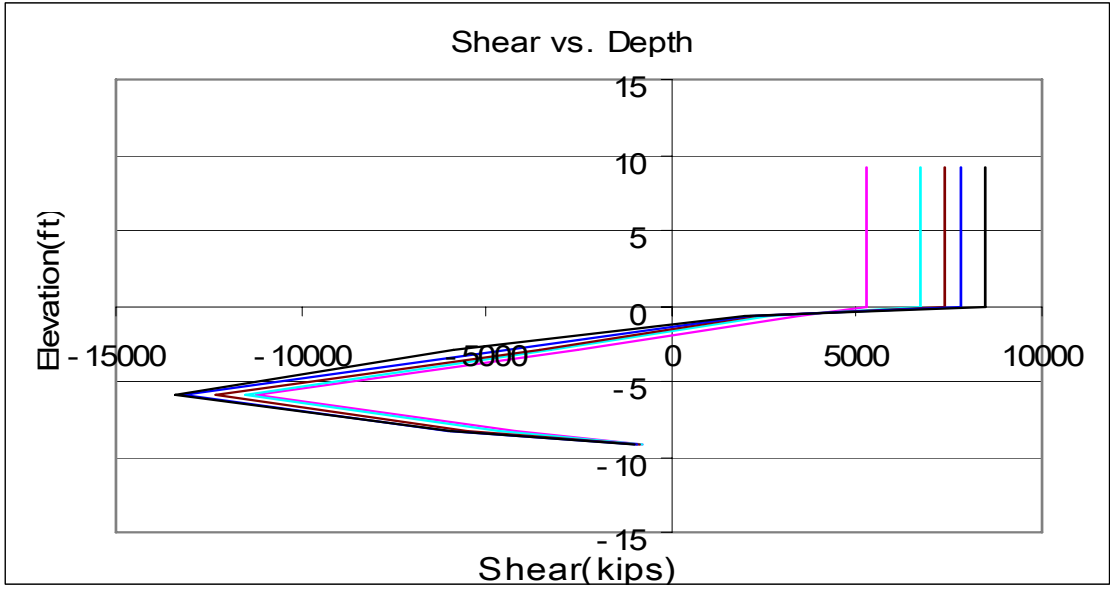


a)

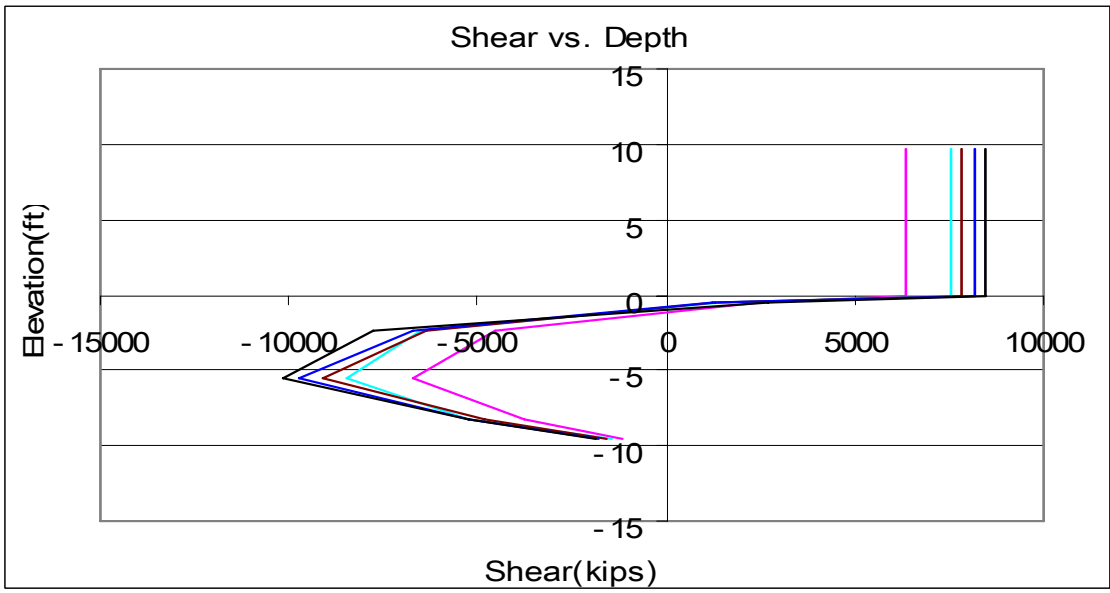


b)

Figure D.1 Shear Curve with Different Top Lateral Displacement from 9 ft Diameter 9 ft Embedded Length in 10 tsf Rock with 50 % Styrofoam Layering below 1D below from Tip of Shaft a) Test No. 1 b) Test No. 2

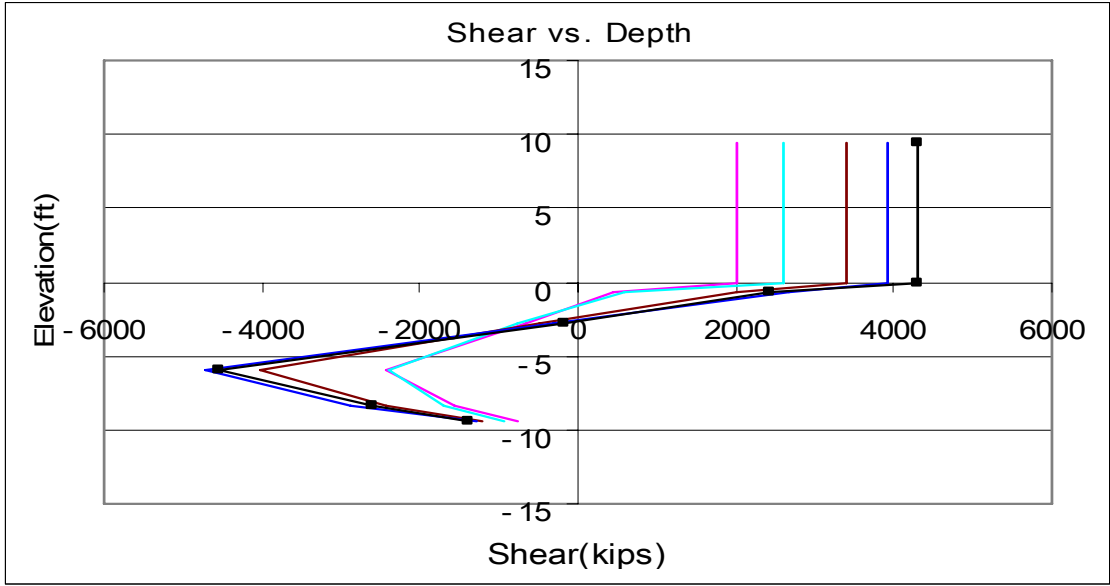


a)

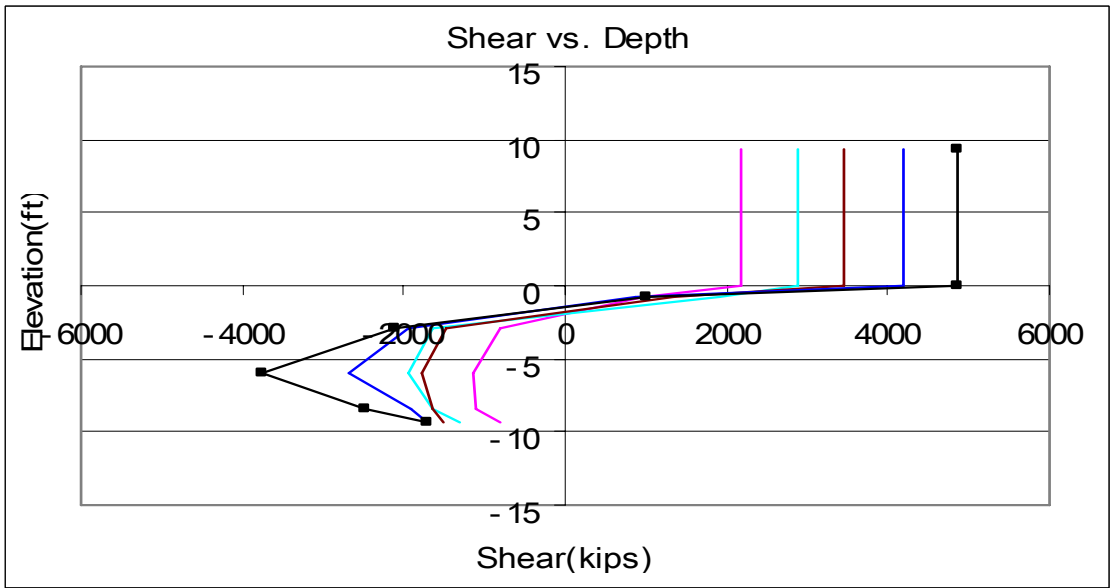


b)

Figure D.2 Shear Curve with Different Top Lateral Displacement from 9 ft Diameter 9 ft Embedded Length in 30 tsf Rock with 50 % Styrofoam Layering below 1D below from Tip of Shaft a) Test No. 1 b)Test No. 2

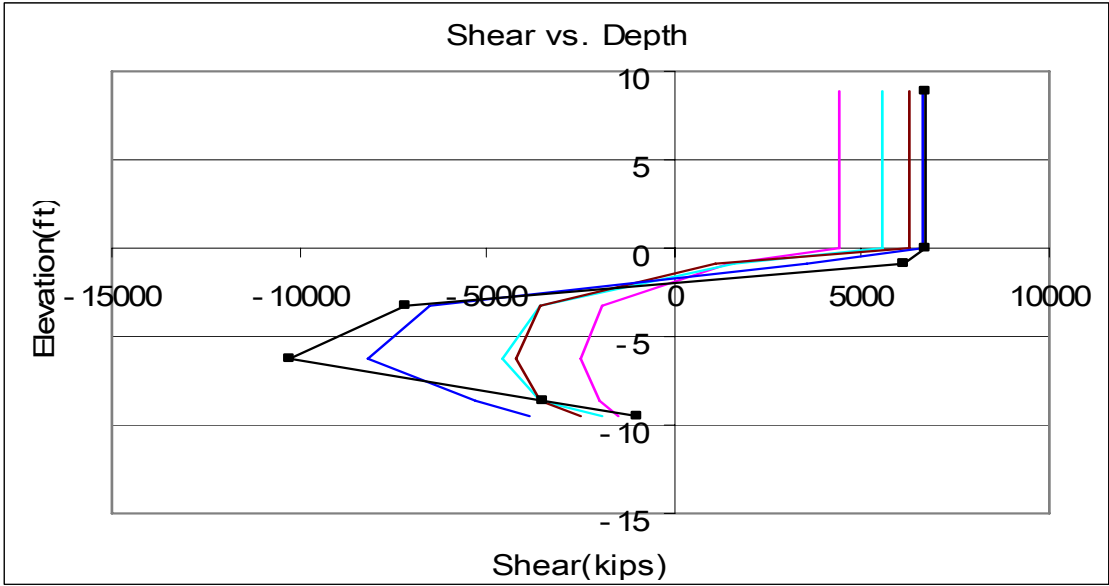


a)

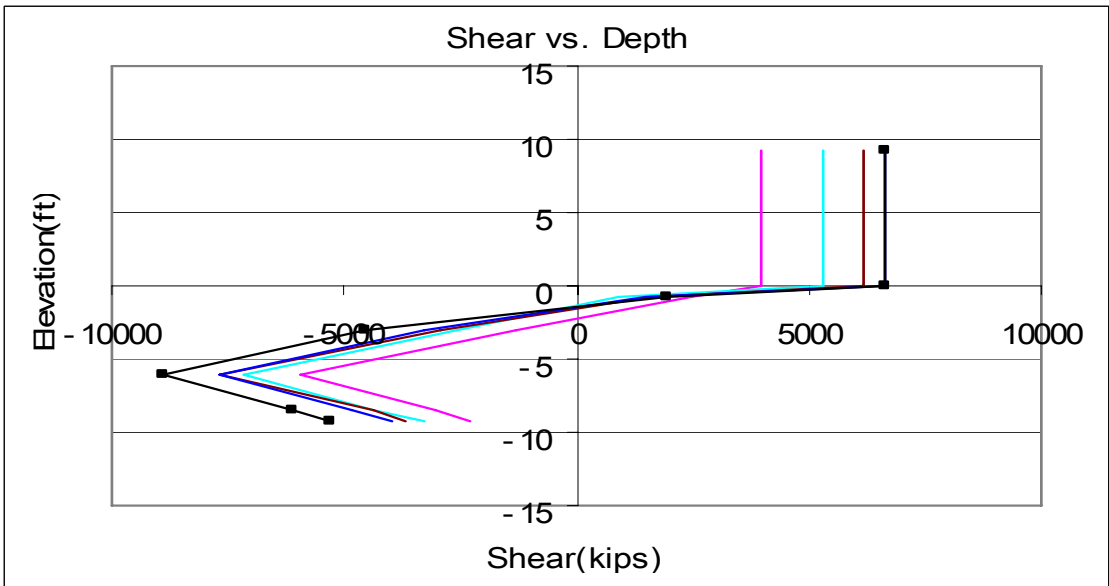


b)

Figure D.3 Shear Curve with Different Top Lateral Displacement from 9 ft Diameter 9 ft Embedded Length in 10 tsf Rock a) Test No. 1 b) Test No. 2

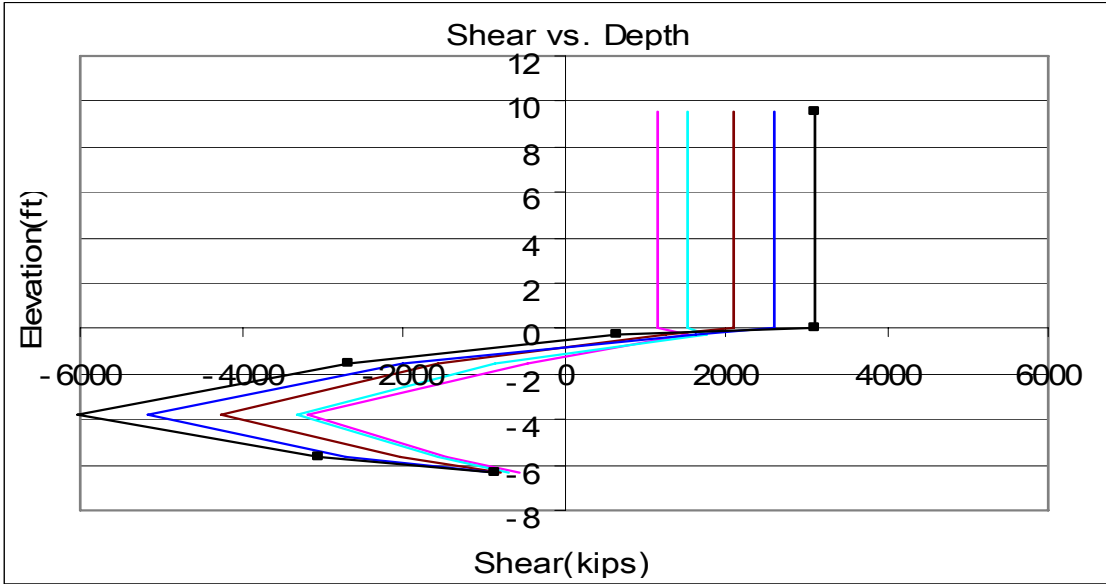


a)

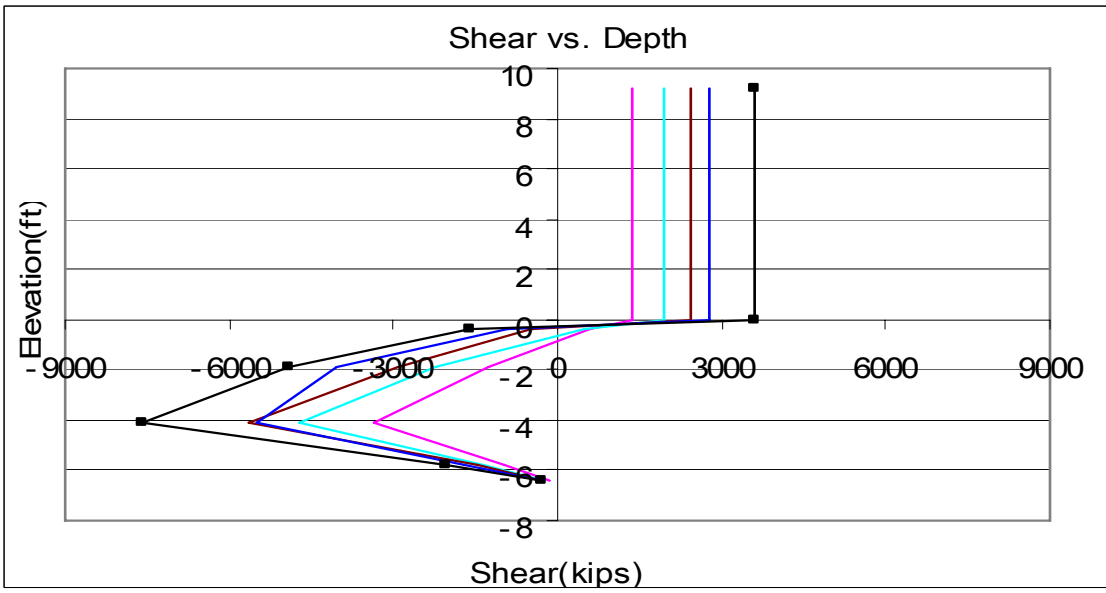


b)

Figure D.4 Shear Curve with Different Top Lateral Displacement from 9 ft Diameter 9 ft Embedded Length in 30 tsf Rock a) Test No. 1 b) Test No. 2

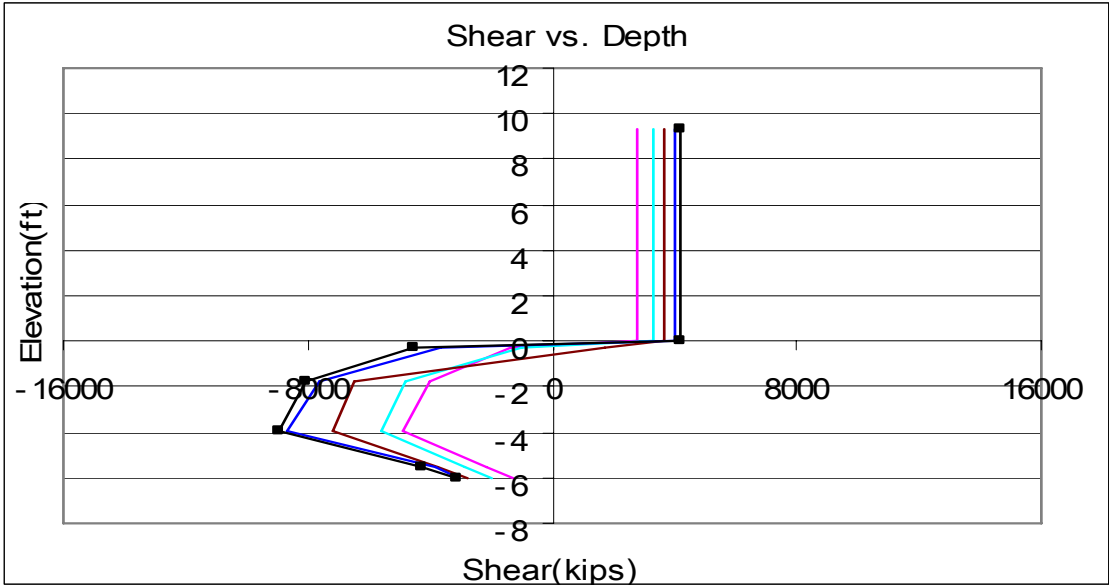


a)

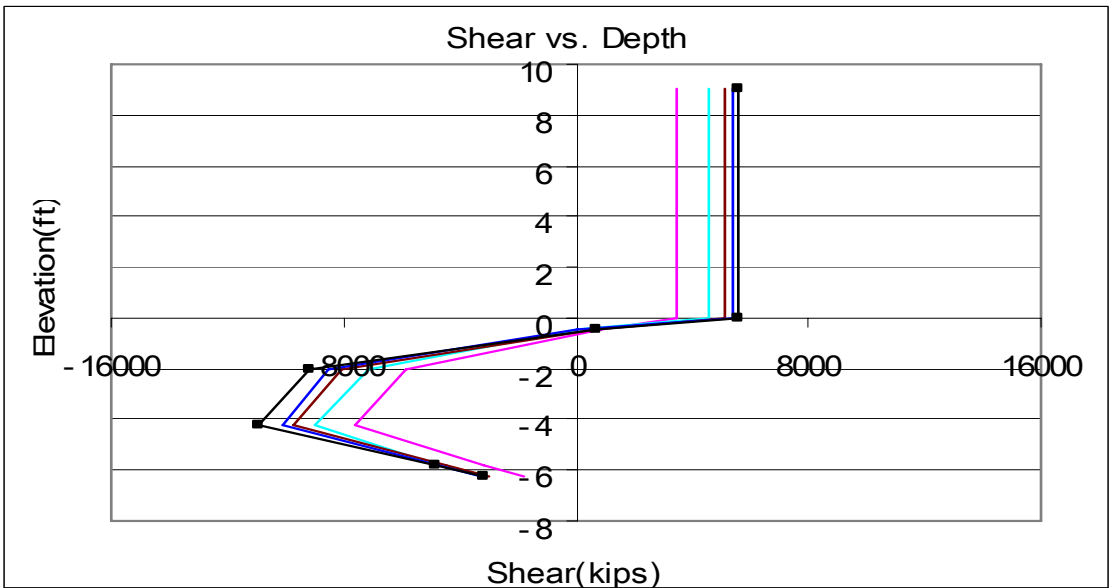


b)

Figure D.5 Shear Curve with Different Top Lateral Displacement from 6 ft Diameter 6 ft Embedded Length in 10 tsf Rock a) Test No. 1 b) Test No. 2

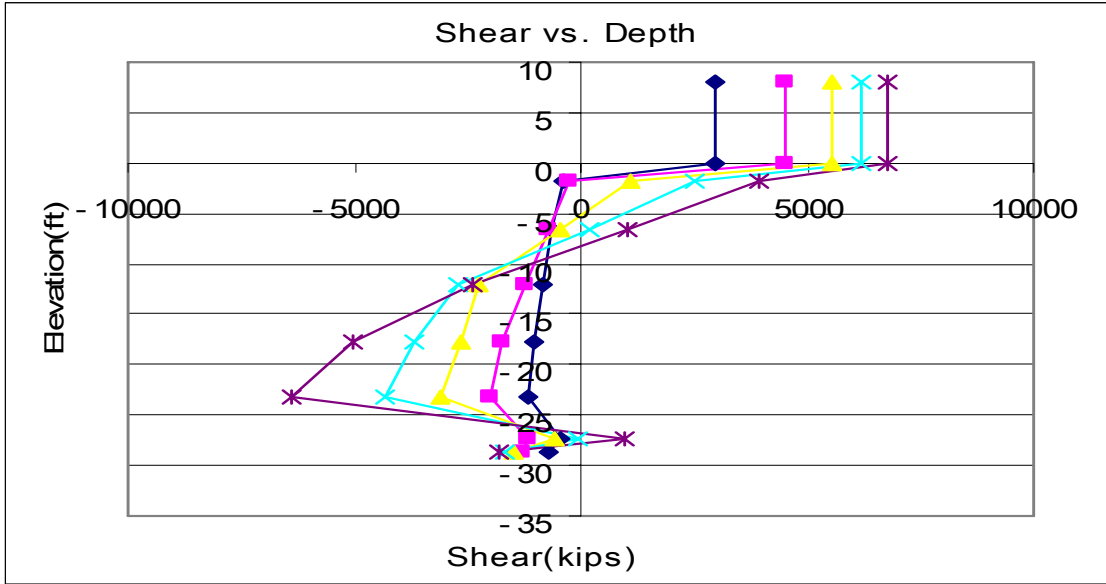


a)

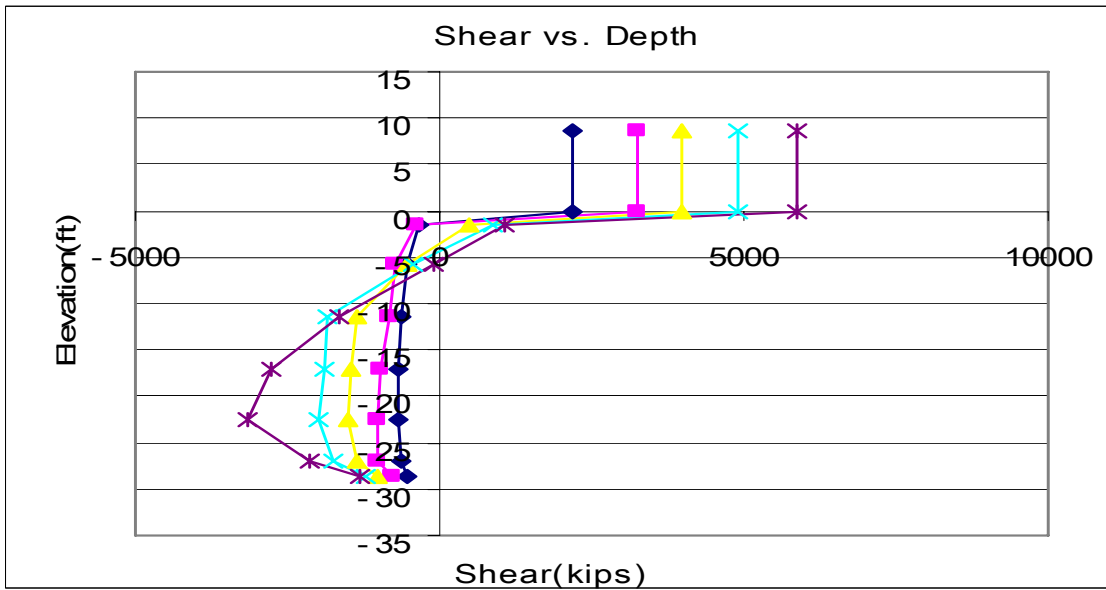


b)

Figure D.6 Shear Curve with Different Top Lateral Displacement from 6 ft Diameter 6 ft Embedded Length in 30 tsf Rock a) Test No. 1 b) Test No. 2

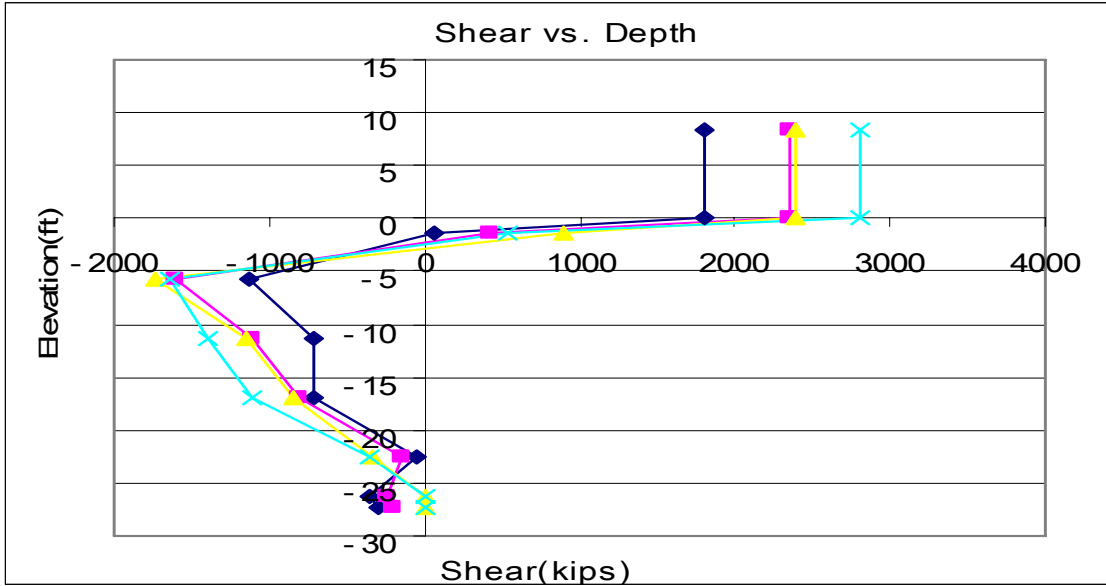


a)

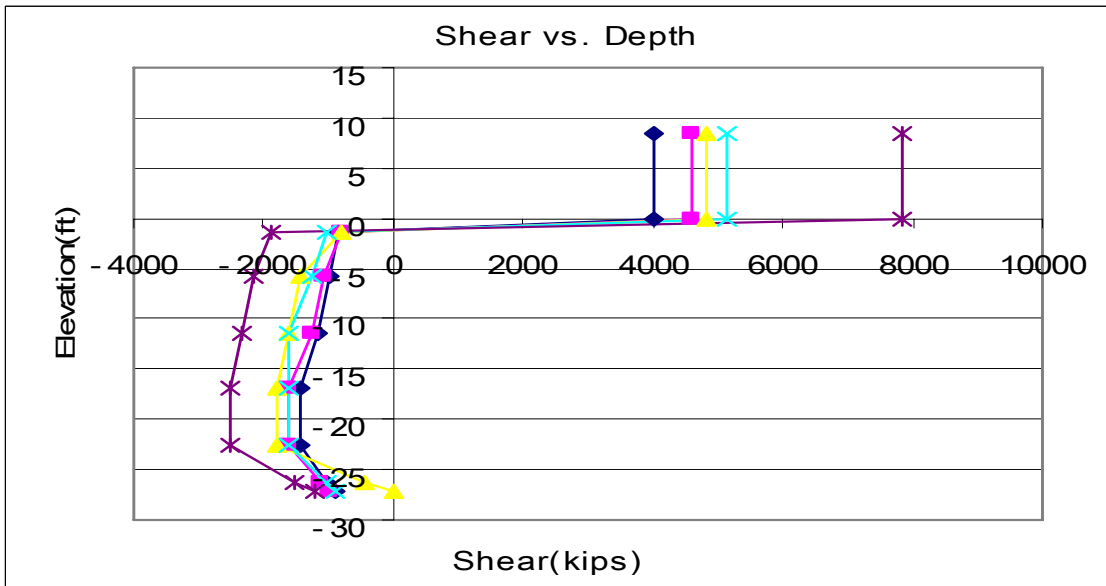


b)

Figure D.7 Shear Curve with Different Top Lateral Displacement from 9 ft Diameter 27 ft Embedded Length in 10 tsf Rock a) Test No. 1 b) Test No. 2

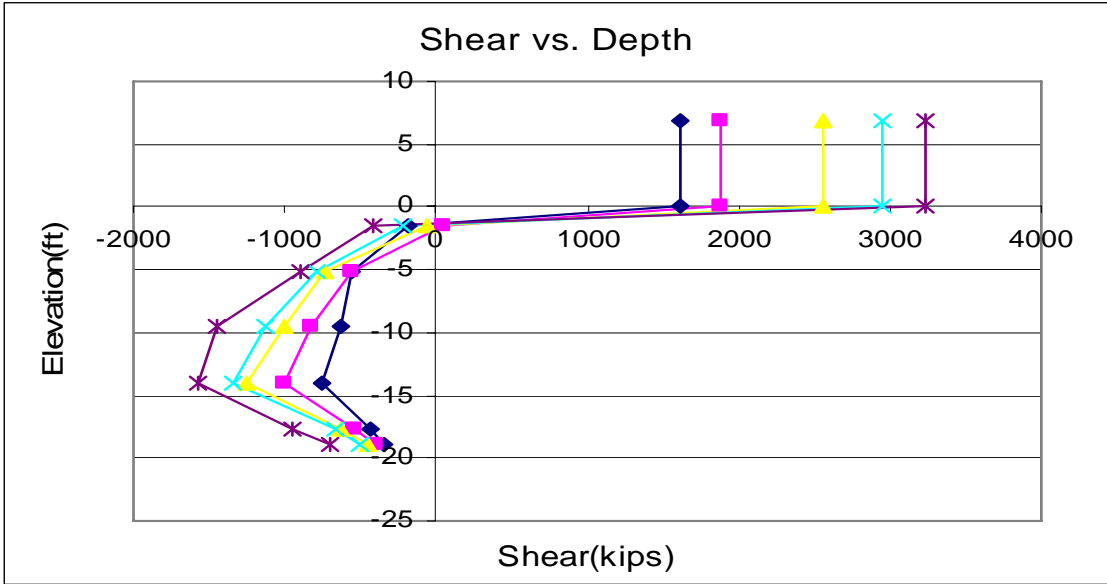


a)

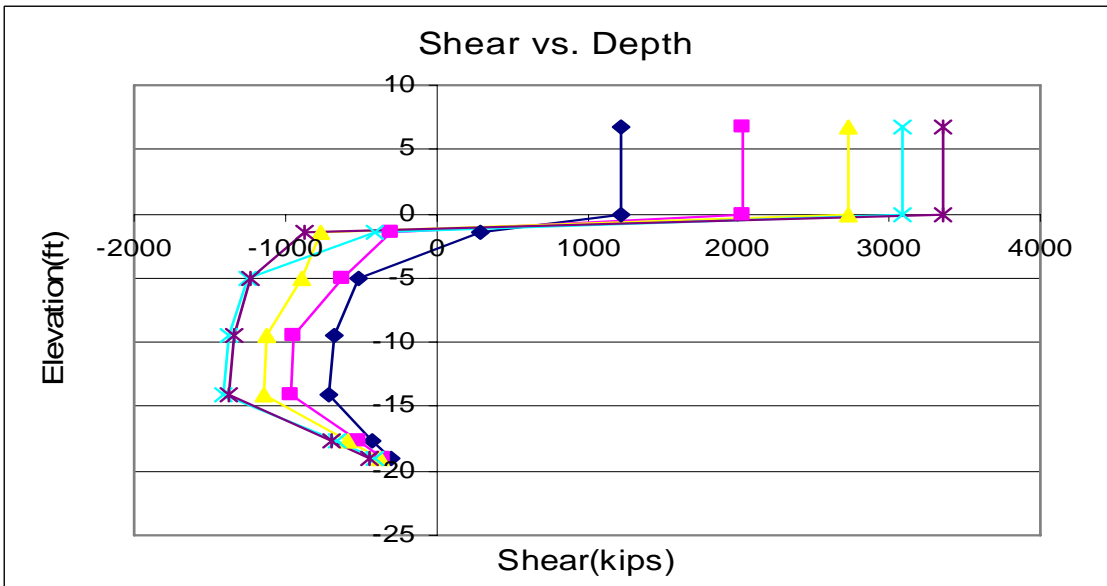


b)

Figure D.8 Shear Curve with Different Top Lateral Displacement from 9 ft Diameter 27 ft Embedded Length in 30 tsf Rock a) Test No. 1 b) Test No. 2

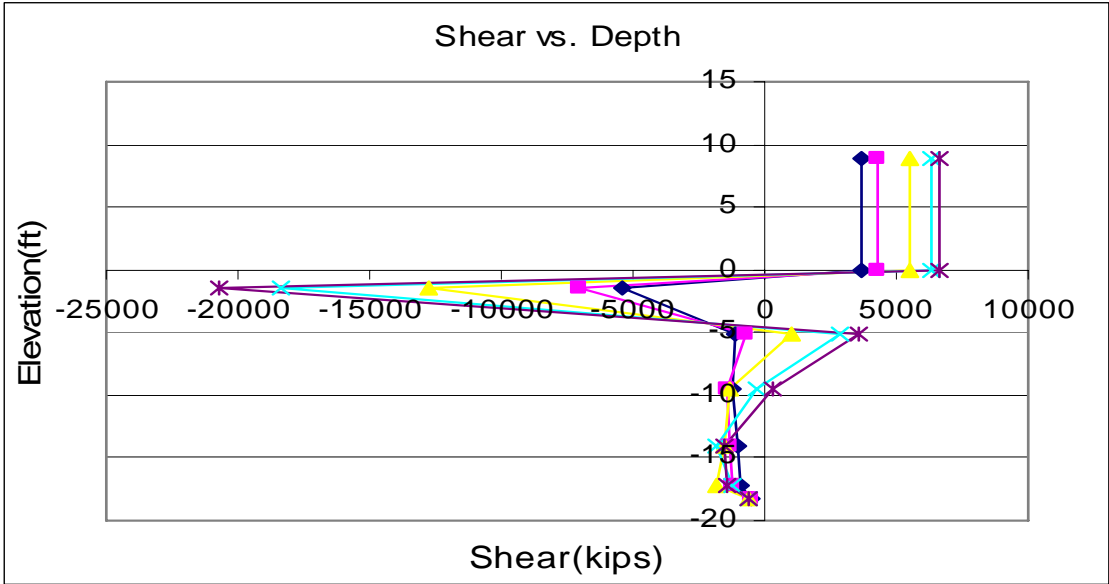


a)

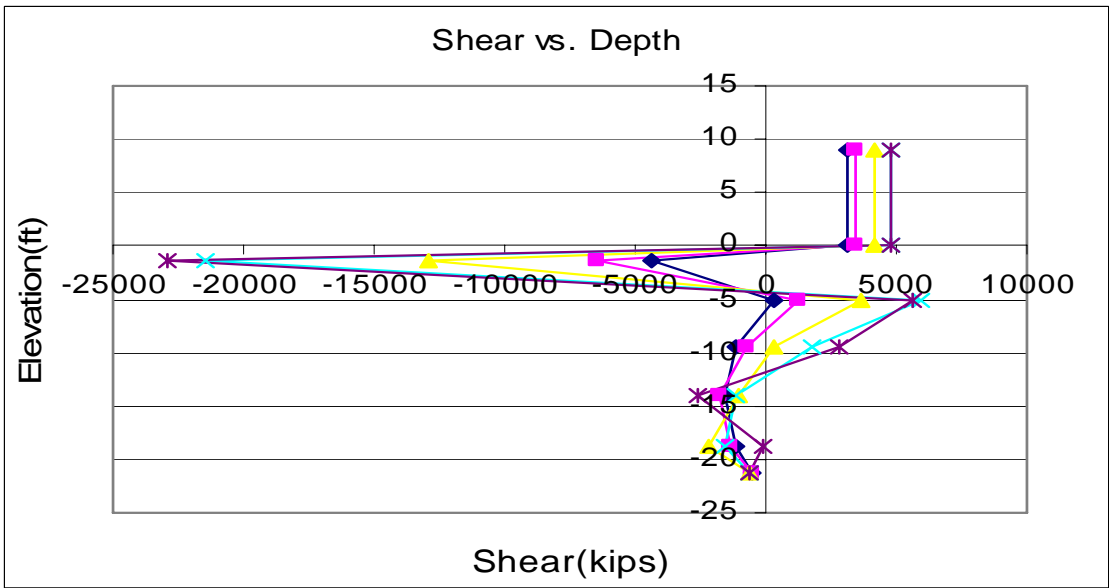


b)

Figure D.9 Shear Curve with Different Top Lateral Displacement from 6 ft Diameter 18 ft Embedded Length in 10 tsf Rock a) Test No. 1 b) Test No. 2



a)



b)

Figure D.10 Shear Curve with Different Top Lateral Displacement from 6 ft Diameter 18 ft Embedded Length in 30 tsf Rock a) Test No. 1 b) Test No. 2



APPENDIX E

**Example for LRFD resistance factors,  $\phi$  to Be Calculated From Field Test**

1. Load the Data( $E_i$ -ksf), i.e., Fuller Warren (First 63 data is “New” and last 33 data is “Existing”)

4799.95	7542.96	21182	4579.2	3062.06	2183.18	1197.01	37402.6	30000.1	
29647.1	6252.88	21788.4	4089.25	36924	7997.76	1727.74	50086.9	12307.7	
25980.1	2365.09	25146	3582.72	12369	5069.76	2426.11	90000	5647.1	
21355.6	1449.3	9533.93	5457.97	21857	3160.67	367660	6193.44	12521.8	
15474.1	1902.27	31879.8	2104.38	18069.6	1834.1	192000	7058.88	16551.6	30315.7
25703.1	2448.12	3649.65	4066.39	24778.5	1898.35	11076.9	66976.7	8089.92	22857.1
45109	2845.14	16248.6	2679.4	36269.2	2377.15	30320.9	83478.2	56470.6	29690.6
49347.3	922.625	5465.71	2232.86	15236.9	2059.69	66976.7	85970	26181.8	9350.64
37817.9	12490.4	5403.32	2774.47	5680.5	1997.93	102857	61935.4	66976.7	5179.82
2700.33	8747.86	4325.2	3004.34	3508.32	1414.51	35121.9	21176.4	22500	50086.9

Using the Built-In function, get the statistic of  $E_i$  as like below:

Mean(ksf)	25189.7
STD(ksf)	45433.5
Cov(ksf)	1.80365

2. Calculate the  $E_m$ -ksf, i.e., Fuller Warren

From field, RQD or Recovery has been measured. Using that RQD and Figure 6.3, get the  $E_m/E_i$ , i.e., 0.5 for RQD=77% for first 63 data and 0.1 for RQD=50% for last 33data.

2399.976	3771.481	10591.008	2289.6	1531.0325	1091.592	598.5072	3740.256	3000.0096	
14823.529	3126.438	10894.19	2044.6272	18462.017	3998.88	863.856	5008.6944	1230.768	
12990.049	1182.5446	12572.976	1791.36	6184.4918	2534.8788	1213.0546	9000	564.7104	
10677.8	724.64832	4766.9652	2728.984	10928.488	1580.3371	36765.95	619.344	1252.1808	3031.5744
7737.0394	951.13584	15939.924	1052.1878	9034.8091	917.0496	19199.995	705.888	1655.1648	2285.712
12851.544	1224.0576	1824.8242	2033.1958	12389.226	949.17312	1107.6912	6697.6704	808.992	2969.064
22554.48	1422.5681	8124.3094	1339.7018	18134.612	1188.576	3032.0928	8347.824	5647.0608	935.064
24673.672	461.31264	2732.8572	1116.432	7618.4741	1029.8434	6697.6704	8597.0016	2618.1792	517.9824
18908.968	6245.1922	2701.6596	1387.2355	2840.2486	998.964	10285.704	6193.5408	6697.6704	517.9824
1350.1663	4373.9316	2162.6025	1502.1698	1754.1583	707.256	3512.1888	2117.6352	2250	5008.6944

Using the Built-In function, get the statistic of  $E_m$  as like below:

<b>Mean(ksf)</b>	<b>5423.95</b>
<b>STD(ksf)</b>	<b>6349.52</b>
<b>Cov(ksf)</b>	<b>1.17065</b>

3. The data obtained from Step 2 was converted to  $\ln(x)$ .

7.783214	8.235223	9.2677607	7.7361324	7.3336976	6.9953925	6.3944386	8.2269093	8.0063708	
9.603971	8.0476496	9.2959849	7.6229708	9.8234708	8.2937696	6.7614061	8.5189306	7.1153936	
9.4719389	7.0754238	9.439305	7.4907304	8.7298001	7.8379011	7.1008969	9.1049799	6.336313	
9.2759221	6.5856865	8.4694652	7.9116847	9.2991282	7.3653934	10.512327	6.4286609	7.132642	8.0168374
8.9537744	6.8576569	9.6765822	6.9586269	9.1088401	6.8211616	9.8626653	6.5594566	7.4116559	7.7344329
9.4612193	7.1099265	7.5092389	7.6173641	9.4245825	6.8555912	7.0100331	8.809515	6.695789	7.996002
10.023689	7.260219	9.002616	7.2002024	9.8055777	7.0805112	8.0170084	9.0297562	8.6388905	6.840615
10.113492	6.134076	7.9131029	7.0178932	8.9383314	6.937162	8.809515	9.0591688	7.8702344	6.2499413
9.8473916	8.7395672	7.9016215	7.2350682	7.9516469	6.9067187	9.2385102	8.7312622	8.809515	8.5189306
7.2079831	8.3834176	7.6790676	7.3146659	7.4697444	6.5613927	8.1639947	7.6580553	7.7186855	

Using the Built-In function, get the statistic of  $\ln(E_m)$  as like below:

<b>Mean(ksf)</b>	<b>8.03189</b>
<b>STD(ksf)</b>	<b>1.06962</b>
<b>Cov(ksf)</b>	<b>0.13317</b>

4. Using the statistic from Step 3 and  $\alpha$  from Figure 6.1 with correlation length( $a=5, 10$  and  $15$ ), get the new Cov with same mean(i.e., 8.03189) and new STD like below:

	<b>a=5</b>	<b>a=10</b>	<b>a=15</b>
<b>Mean(ksf)</b>	<b>8.032</b>	<b>8.032</b>	<b>8.032</b>
<b>STD(ksf)</b>	<b>0.58585</b>	<b>0.75633</b>	<b>0.78598</b>
<b>Cov(ksf)</b>	<b>0.07294</b>	<b>0.09417</b>	<b>0.09786</b>

5. With above statistic, Monte Carlo Simulation was performed to generate Typical  $F$  values which were substituted into Equation  $E_g = \exp(F)$  to give the distributions.

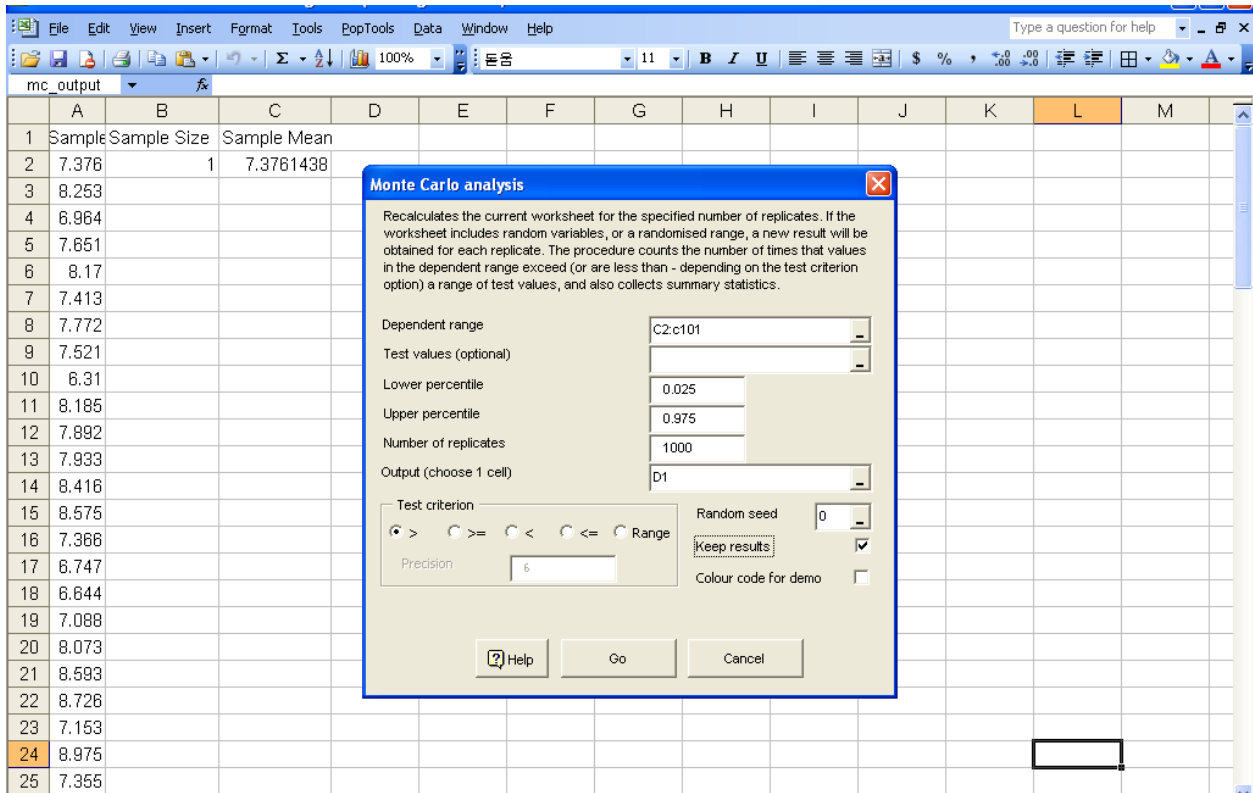
The step for Monte Carlo Simulation is below

- a. Install "POPTOOL" which is for handling statistic problem in Excel

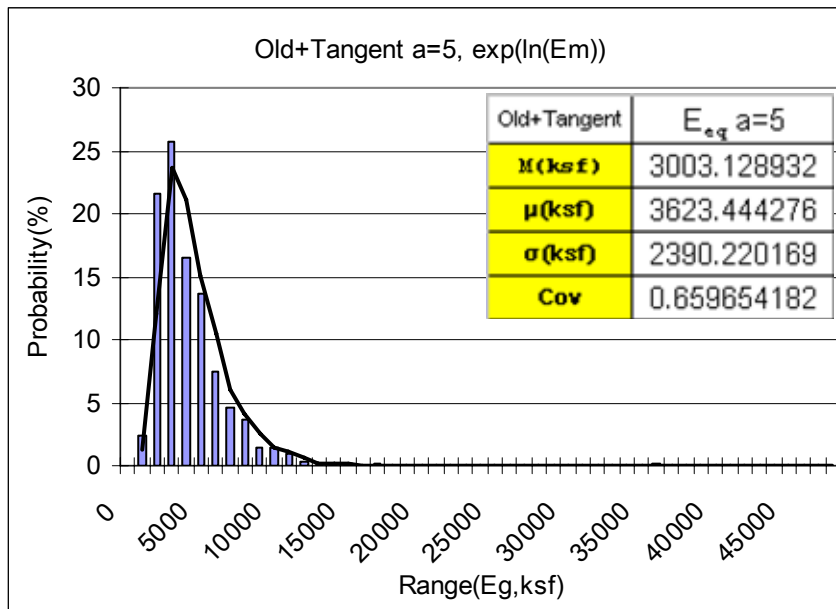
- b. Open a new Workbook
- c. Enter “Sample” in Cell A1 and Enter=dnNormalDev(mean, std) in Cell A2 for generating a random number with given statistics.
- d. Fill this down to row 101.
- e. Enter “Sample Size” in Cell B1 and Enter “Sample Mean” in Cell C1
- f. Enter “=Average(A\$2:A2)” in Cell C2
- g. That looks like below:

	A	B	C	D	E	F
1	Sample	Sample Size	Sample Mean			
2	9.34	1	9.33988784			
3	7.603					
4	8.055					
5	9.399					
6	8.086					
7	7.422					
8	8.697					
9	6.961					
10	7.306					
11	7.967					
12	7.338					
13	7.386					
14	8.198					
15	8.817					

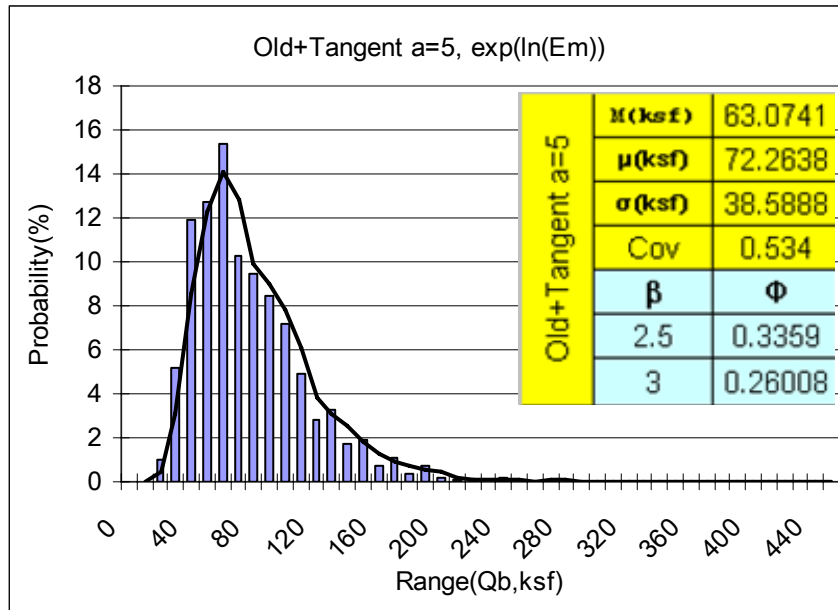
- h. Now we want the computer to go through the process of repeatedly calculation new random numbers, calculating the sample means, and recording them.
  - i. Select “Monte Carlo Analysis in Poptool.
  - ii. Put input as like below:



6. From Step 5, new generated data sets (F) have been obtained.
7. Typical F values which were substituted into Equation  $E_g = \exp(F)$  to give the distributions. That distribution is shown below:



8. These data ( $E_g$ ) have been applied into O'Neil Equation to get end bearing distributions. That distribution is shown below:



As same as Fuller Warren Data, 17<sup>th</sup> street data is below

Load the Data ( $E_i$ -ksf), i.e., 17<sup>th</sup> Street Data (First 102 data is “New” and last 16 data is “Existing”)

								40563.4
20611.7	12083.9	18441.2	29047	37351.4	39514	48977.1	34624.7	92903.2
32368.2	53760	23705	62635	18006.8	17524.1	39528.4	54704.3	51428.4
37565.1	28379.5	43056	45237.6	21568.9	11425.4	19882.1	42859.3	84705.8
26354.7	52508	26528.3	27366	22078.1	30612.5	10610.1	27050.8	62608.6
38769.3	35987.6	42487.3	38157.4	36271.9	44654	10041.4	41253.4	20000
45163.6	61447.1	29578.5	37606.9	34758.1	12661.6	38513.5	5710.32	49655.1
21600	34143.7	25935	50276	28254.5	37736.1	41659.9	46228.5	137143
10622.9	44640	29767	41522.1	17060	17412.9	43209.8	33588.4	24000
12000	36649.7	30528	25642.9	13273.1	28117.4	44164.4	65729.7	16363.6
27257.2	30302.6	43244.9	39437.3	14235.8	31651.2	18944.4	38544.6	5393.23
48738.5	42471.1	36216.3	41753.2	6746.4	15144.6	24350.4	44841.2	17560.9
31680	53383.4	38748	26913.6	6576.48	8708.11	35347	9729.79	144000
17280	41152.3	36602.4	39104.5	31638.7	47750.4	40770	47213.1	169412

Using the Built-In function, get the statistic of  $E_i$  as like below:

Mean(ksf)	36279.7
STD(ksf)	24207.4
COV(ksf)	0.66725

Calculate the  $E_m$ -ksf, i.e., 17<sup>th</sup> Street Data

From field, RQD or Recovery has been measured. Using that RQD and Figure 6.3, get the  $E_m/E_i$ , i.e., 0.4 for RQD=75% for first 102 data and 0.15 for RQD=50% for last 16 data.

								<b>6084.5</b>
<b>8244.69</b>	<b>4833.56</b>	<b>7376.49</b>	<b>11618.8</b>	<b>14940.6</b>	<b>15805.6</b>	<b>19590.9</b>	<b>13849.9</b>	<b>13935.5</b>
<b>12947.3</b>	<b>21504</b>	<b>9482</b>	<b>25054</b>	<b>7202.71</b>	<b>7009.63</b>	<b>15811.4</b>	<b>21881.7</b>	<b>7714.27</b>
<b>15026.1</b>	<b>11351.8</b>	<b>17222.4</b>	<b>18095</b>	<b>8627.56</b>	<b>4570.16</b>	<b>7952.83</b>	<b>17143.7</b>	<b>12705.9</b>
<b>10541.9</b>	<b>21003.2</b>	<b>10611.3</b>	<b>10946.4</b>	<b>8831.23</b>	<b>12245</b>	<b>4244.03</b>	<b>10820.3</b>	<b>9391.29</b>
<b>15507.7</b>	<b>14395</b>	<b>16994.9</b>	<b>15263</b>	<b>14508.7</b>	<b>17861.6</b>	<b>4016.56</b>	<b>16501.4</b>	<b>3000</b>
<b>18065.4</b>	<b>24578.8</b>	<b>11831.4</b>	<b>15042.8</b>	<b>13903.3</b>	<b>5064.65</b>	<b>15405.4</b>	<b>2284.13</b>	<b>7448.26</b>
<b>8640</b>	<b>13657.5</b>	<b>10374</b>	<b>20110.4</b>	<b>11301.8</b>	<b>15094.4</b>	<b>16664</b>	<b>18491.4</b>	<b>20571.4</b>
<b>4249.15</b>	<b>17856</b>	<b>11906.8</b>	<b>16608.8</b>	<b>6823.99</b>	<b>6965.16</b>	<b>17283.9</b>	<b>13435.4</b>	<b>3600.01</b>
<b>4799.98</b>	<b>14659.9</b>	<b>12211.2</b>	<b>10257.2</b>	<b>5309.22</b>	<b>11247</b>	<b>17665.7</b>	<b>26291.9</b>	<b>2454.54</b>
<b>10902.9</b>	<b>12121.1</b>	<b>17298</b>	<b>15774.9</b>	<b>5694.34</b>	<b>12660.5</b>	<b>7577.74</b>	<b>15417.8</b>	<b>808.985</b>
<b>19495.4</b>	<b>16988.4</b>	<b>14486.5</b>	<b>16701.3</b>	<b>2698.56</b>	<b>6057.85</b>	<b>9740.16</b>	<b>17936.5</b>	<b>2634.14</b>
<b>12672</b>	<b>21353.4</b>	<b>15499.2</b>	<b>10765.4</b>	<b>2630.59</b>	<b>3483.24</b>	<b>14138.8</b>	<b>1459.47</b>	<b>21600</b>
<b>6912</b>	<b>16460.9</b>	<b>14640.9</b>	<b>15641.8</b>	<b>12655.5</b>	<b>19100.2</b>	<b>16308</b>	<b>7081.97</b>	<b>25411.8</b>

Using the Built-In function, get the statistic of  $E_m$  as like below:

Mean(ksf)	12451.1
STD(ksf)	5821.21
COV(ksf)	0.46753